A Multi-Wavelength Study of Cataclysmic Variable Stars

Tracey Suzanne Poole

Mullard Space Science Laboratory
Department of Space and Climate Physics
University College London

A thesis submitted to the University of London
for the degree of Doctor of Philosophy

Abstract

This thesis investigates the properties of two cataclysmic variables which have previously been considered to be non-magnetic systems. The goal of this work is to constrain the component star masses and other physical parameters of these systems using multi-wavelength observations.

I carry out spectroscopic studies on the eclipsing nova-like system RW Tri in the ultraviolet, far red, and near infrared. I produce a simple absorption model to show that one possible scenario for the origin of ultraviolet narrow absorption features, seen in *Hubble Space Telescope* observations, is a ring-like structure with height above the orbital plane, centred on the primary star. I re-analyse far red data from the *Issac Newton Telescope*, using the tomographic technique of 'skew-mapping' to obtain the radial velocity amplitude of the secondary star. I have made new observations of RW Tri in the near infrared using the *United Kingdom Infra-Red Telescope* to determine the accuracy of the secondary star radial velocity amplitude. The measured secondary star radial velocity has been combined with ultraviolet absorption line analysis and existing optical emission line data, to calculate the mass ratio, and hence the mass of the component stars. The rotational velocity of the secondary star has also been obtained from the infrared observations, and combined with the radial velocity of the secondary star to calculate more reliable component star masses.

OY Car, an eclipsing dwarf nova, was observed at X-ray wavelengths using *XMM-Newton*. I study the light curves, and measure the extent of the boundary layer in the system. I also observe significant quasi-sinusoidal variations with an underlying periodicity of 2233 seconds, which may be the spin period of the white dwarf primary star. These results imply that OY Car may be weakly magnetic, and could therefore belong to a new class of intermediate polars below the period gap. Investigations of the eclipse profile lead to an estimate of the component star masses.

Contents

List of Figures

List of Tables

Chapter 1

Introduction

The two objects studied in this thesis, RW Tri and OY Car, are members of a class of binary system called cataclysmic variables (CVs). The standard CV model contains a compact white dwarf primary and a late type (K-M) secondary star that fills its Roche lobe, transferring mass to the white dwarf via an accretion disc in the majority of cases. A bright spot, where the accretion stream impacts the disc, is sometimes visible at optical wavelengths. This is illustrated in Figure 1.1.

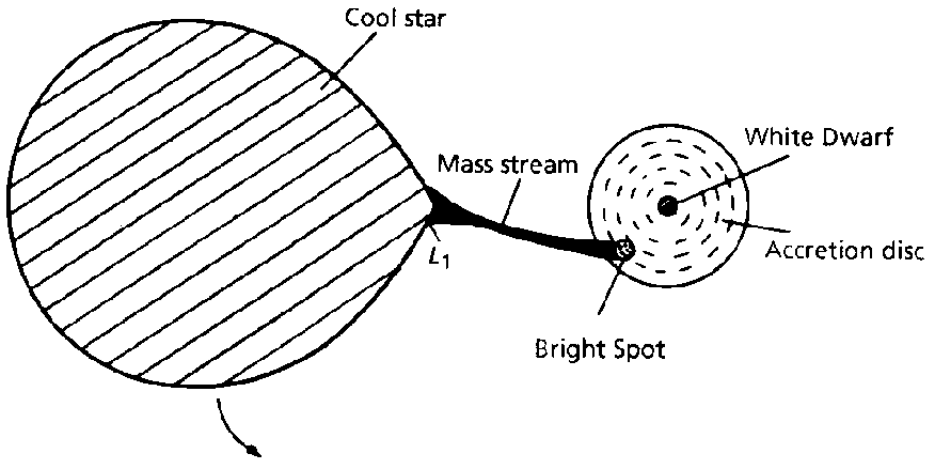

Figure 1.1: An illustration of the standard model of a non-magnetic CV from Warner (1995).

A boundary layer forms in the region where the accretion disc material is decelerated and merges with the white dwarf. The boundary layer is seen at X-ray wavelengths. If the magnetic field of the white dwarf is strong enough, material will become frozen on to the field lines of the white dwarf, and accretion will occur via accretion streams governed by the magnetic field lines. In this case the material accretes on to discrete regions on the surface of the white dwarf, which are seen in X-rays.

1.1 The Physics of CV Systems

In this section the method of calculating the component star masses, the geometry of a CV, the formation of the accretion disc, and the luminosity of the boundary layer are discussed. These topics are an important part of understanding the mechanism of mass transfer, which makes CV systems so variable.

Close binary systems like RW Tri and OY Car have circular orbits due to the tidal interactions between the component stars (Section 1.1.2). Kepler's third law defines the circular orbit of these binary systems, and is given by

$$a^3 = GM\frac{P_{orb}^2}{4\pi^2}, \tag{1.1}$$

where a is the binary separation, G is the gravitational constant (6.673×10^{-11} $\mathrm{Nm^2kg^{-2}}$), M is the sum of the primary (M_1) and secondary (M_2) star masses ($M = M_1 + M_2$), and P_{orb} is the orbital period of the binary system.

The system geometry is shown in Figure 1.2. The separation of the component stars (a) is defined as

$$a = a_1 + a_2, \tag{1.2}$$

where a_1 and a_2 are the radii of the primary and secondary orbits around the centre of mass of the system. The inclination of the system (i) is the angle subtended from the perpendicular of the orbital plane to the orbital plane of the system, and defines the observers' line of sight to the system.

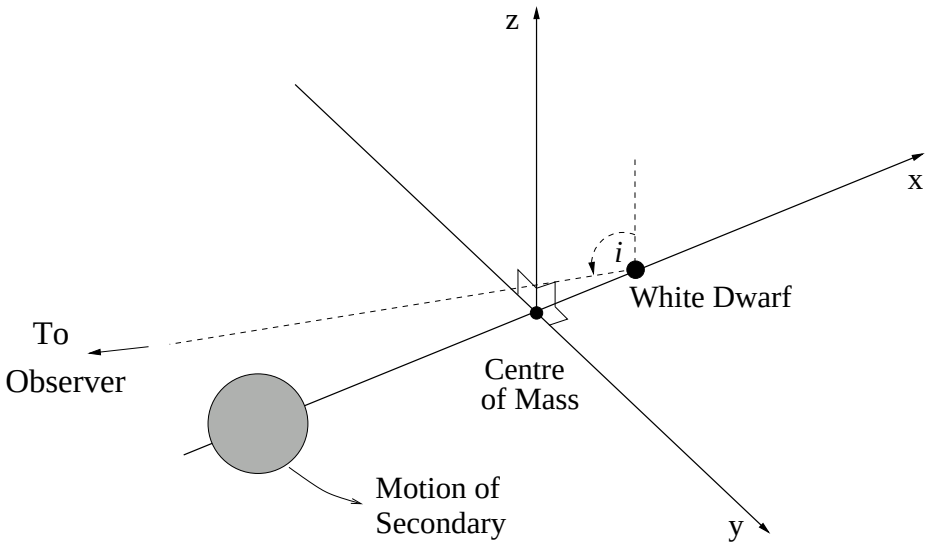

Figure 1.2: Binary coordinate system. The dashed line points to the observer and defines the inclination angle (i).

The individual stars in a close binary system can only be resolved spectroscopically.

1.1.1 Spectroscopic Binary Solution

A spectroscopic binary system has spectral lines that oscillate in a periodic manner revealing the presence of one or both of the component stars. The period of these oscillations provide the orbital period (P_{orb}) of the system. The change in wavelength ($\Delta\lambda$) of a spectral line with respect to its rest wavelength (λ_o) can be used to calculate the radial velocity[1] (v_r) of the source producing the spectral line using the Doppler shift equation

$$\frac{\Delta\lambda}{\lambda_o} = \frac{\lambda - \lambda_o}{\lambda_o} = \frac{v_r}{c}, \tag{1.3}$$

where λ is the observed wavelength, and c is the speed of light (2.99×10^5 km/s). In this way spectral lines at different wavelengths can be used to measure the radial velocity of the component stars, leading to velocity curves over an orbital period.

[1]The component of relative velocity that lies along the line of sight of the observer.

Figure 1.3 shows the velocity curve of a spectroscopic binary system over one orbital period, with an illustration showing the rest frame of the centre of mass of the system. v_1, v_2 and v_{cm} are the circular velocities of the primary star, the secondary star, and the centre of mass respectively. K_1 and K_2 are the radial velocity amplitudes of the primary and secondary star.

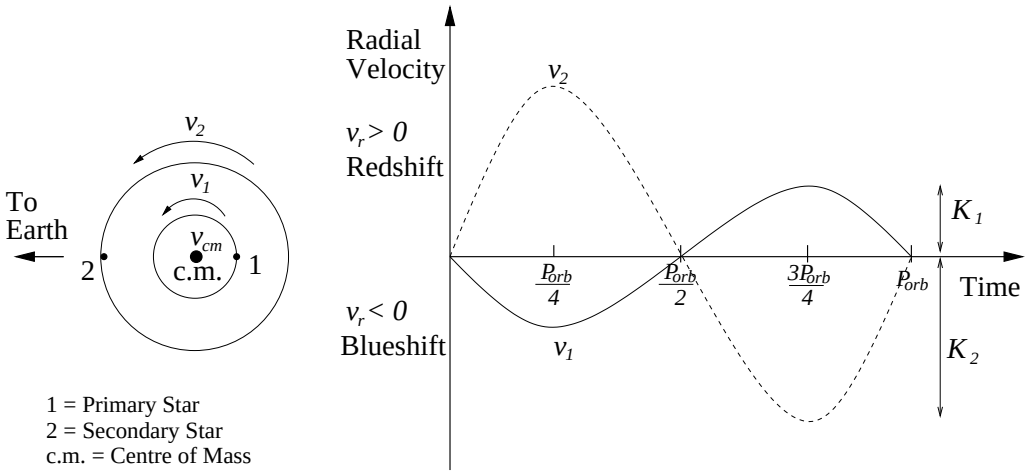

Figure 1.3: Velocity curve of a spectroscopic binary system over one orbital phase adapted from Zeilik, Gregory & Smith (1992). Left: Illustration of the circular velocities in the binary system with respect to the rest frame of the centre of mass (c.m.). Right: The radial velocity curve of the component stars of orbital period (P_{orb}) in the rest frame of the observer.

The inclination angle (i) of the system directly influences the measured radial velocities of the component stars, as can be seen in Figure 1.4. So far an inclination angle of $i = 90^o$ has been considered, and hence the radial velocity of each star equals the circular velocity[2]of each star at $P_{orb}/4$ and $3P_{orb}/4$. If the direction of motion of the star is perpendicular to the line of sight ($i = 0^o$), then the radial velocity is zero. If the inclination angle is less than 90^o, the maximum radial velocities of the primary ($v_{1r|max|}$) and the secondary ($v_{2r|max|}$) become

[2]The speed at which an object must travel to maintain uniform circular motion around a gravitational body.

$$v_{1r|max|} = v_1 \sin i = K_1, \tag{1.4}$$

$$v_{2r|max|} = v_2 \sin i = K_2. \tag{1.5}$$

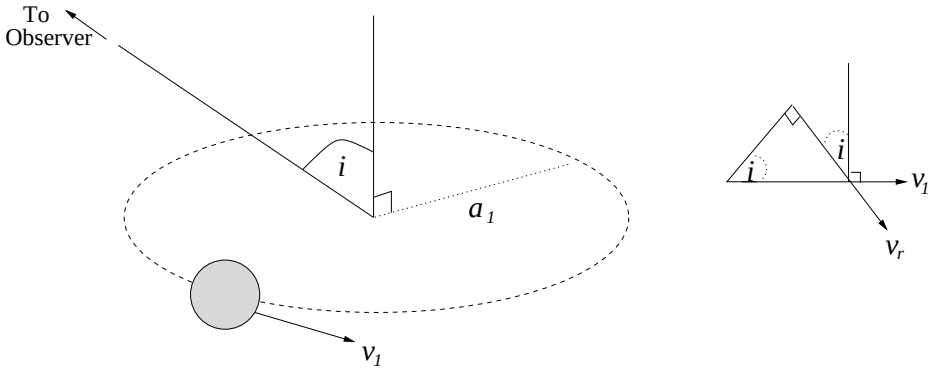

Figure 1.4: Inclination angle in the rest frame of the centre of mass with respect to the primary star motion.

The velocities of the two component stars rotating in circular orbits are given by

$$v_1 = \omega a_1 = \frac{2\pi a_1}{P_{orb}} = \text{constant}, \tag{1.6}$$

$$v_2 = \omega a_2 = \frac{2\pi a_2}{P_{orb}} = \text{constant}, \tag{1.7}$$

where ω is the angular velocity. Hence the radial velocity amplitudes of the primary and secondary stars are

$$K_1 = \frac{2\pi a_1}{P_{orb}} \sin i, \tag{1.8}$$

$$K_2 = \frac{2\pi a_2}{P_{orb}} \sin i. \tag{1.9}$$

Consider the gravitational forces in the binary system (Figure 1.5).

$$M_1 a_1 = M_2 a_2. \tag{1.10}$$

By substituting $a = a_1 + a_2$ and $M = M_1 + M_2$ into Equation 1.10, the radii of the primary and secondary star orbits can be defined as

$$a_1 = M_2 \frac{a}{M}, \tag{1.11}$$

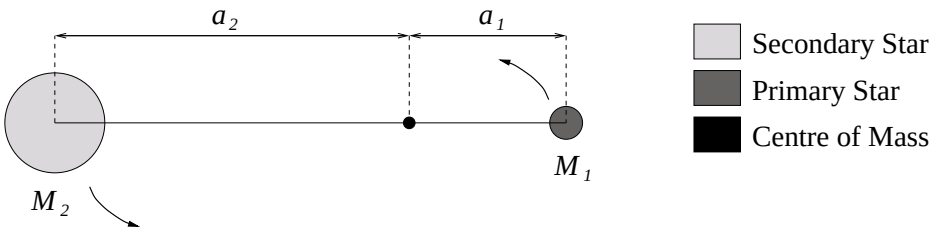

Figure 1.5: Two stars orbiting in a plane about the centre of mass.

$$a_2 = M_1 \frac{a}{M}. \tag{1.12}$$

Substituting Kepler's third law (Equation 1.1), and the radii of the primary and secondary orbits (Equations 1.11 and 1.12) into the radial velocity amplitude of each star (Equations 1.8 and 1.9) gives

$$f_1 = \frac{M_2^3 \sin^3 i}{(M_1 + M_2)^2} = \frac{P_{orb}}{2\pi G} K_1^3, \tag{1.13}$$

$$f_2 = \frac{M_1^3 \sin^3 i}{(M_1 + M_2)^2} = \frac{P_{orb}}{2\pi G} K_2^3. \tag{1.14}$$

These two equations are known as the *mass function* equations. On the right hand side of the equations are the observable quantities, and on the left hand side of the equations are the mass functions. If K_1 and K_2 are known, a ratio of the mass function equations can be used to determine the mass ratio (q) of the system

$$q = \frac{\sqrt[3]{f_1}}{\sqrt[3]{f_2}} = \frac{M_2}{M_1} = \frac{K_1}{K_2}. \tag{1.15}$$

The mass function equations (Equations 1.13 and 1.14) can be rearranged in terms of the radial velocity amplitudes of the component stars and the mass ratio of the system, using the mass ratio (Equation 1.15). Equation 1.13 can be written in the form

$$M_2 \sin^3 i = \frac{P_{orb}}{2\pi G} K_1 (K_1 + K_2)^2, \tag{1.16}$$

or

$$M_2 \sin^3 i = \frac{P_{orb}}{2\pi G} K_1^3 \frac{(1+q)^2}{q^2}. \tag{1.17}$$

Equation 1.14 can be written in the forms

$$M_1 \sin^3 i = \frac{P_{orb}}{2\pi G} K_2 (K_1 + K_2)^2, \tag{1.18}$$

or

$$M_1 \sin^3 i = \frac{P_{orb}}{2\pi G} K_2^3 (1 + q)^2. \tag{1.19}$$

Using the mass function (Equation 1.13) the mass of the secondary star is

$$M_2 = \frac{f_1}{\sin^3 i} \frac{(M_1 + M_2)^2}{M_2^2}, \tag{1.20}$$

when $\sin^3 i \leq 1$, and $(M_1 + M_2)^2 / M_2^2 > 1$, then

$$M_2 > f_1. \tag{1.21}$$

Similarly

$$M_1 > f_2. \tag{1.22}$$

Therefore the mass function gives a lower limit to the masses of the component stars in the system.

1.1.2 Roche lobe overflow Geometry

To find an accurate value of the individual masses of the component stars, the inclination angle of the system must be known. The inclination angle can be calculated using Roche lobe geometry. The secondary star is influenced by the gravitational effects of the primary, and therefore becomes tidally distorted producing a tidal bulge. Viscosity in the outer envelope of the secondary star causes the tidal bulge to either lag or lead the rotating material in the envelope, setting up a tidal torque. This torque acts to synchronise the rotation of the secondary star, and also reduces any eccentricity in its orbit (Hut 1981).

The total potential (Φ_o) at any point in the binary system is the sum of the gravitational potentials of the two stars and the effective potential of the centrifugal effect, defined by Warner (1995) as

$$\Phi_o = \frac{GM_1}{a} f\left(\frac{x}{a}, \frac{y}{a}, \frac{z}{a}, q\right), \tag{1.23}$$

where x, y, and z define the coordinate system (Figure 1.2). The Roche lobe equipotentials are a function of the mass ratio and the binary separation (Equation 1.23).

The surface of a synchronously rotating secondary star lies on Φ_R =constant, if the secondary fills its Roche lobe (Warner 1995). The equipotentials define the shape of the secondary star. Rotation will flatten the secondary star along the rotational axis, and tidal forces will elongate the secondary star in the direction of the primary star. The Roche lobe equipotentials in the plane of the orbit ($z = 0$) are shown in Figure 1.6.

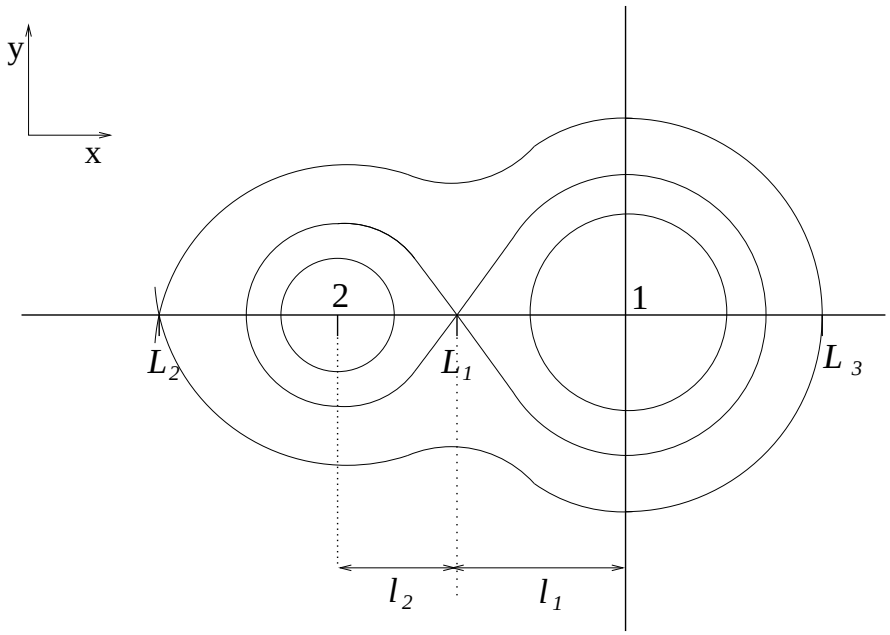

Figure 1.6: Roche lobe potentials adapted from Warner (1995). 1 and 2 represent the primary and secondary stars, and L_1 is the inner Lagrangian point.

In Figure 1.6, 1 and 2 represent the primary and secondary stars, l_1 and l_2 are the distances from the primary and secondary stars to the inner Lagrangian point (L_1) respectively. The inner Lagrangian point (L_1) is the saddle-point of Φ_o, and lies at the point where

$$\frac{\delta \Phi_R}{\delta x} = 0. \tag{1.24}$$

1.1.3 Driving Mass Transfer in CV Systems

In a CV system mass is transferred from the secondary star to the more massive primary star via Roche lobe overflow. The transferred material must lose angular momentum to accrete on to the primary star, which is closer to the centre of mass of the system. To compensate for the loss in angular momentum the binary separation will increase to conserve the angular momentum of the binary system, causing the secondary star to detach from its Roche lobe, and stopping further mass transfer (Hellier 2001). This can be explained by considering the orbital angular momentum of the system (J). From Figure 1.5

$$J = M_1 a_1 K_1 + M_2 a_2 K_2. \tag{1.25}$$

Using Equations 1.10, 1.8, 1.9, $a = a_1 + a_2$, $M = M_1 + M_2$ and Kepler's third law (Equation 1.1) gives

$$J = M_1 M_2 \left(\frac{Ga}{M}\right)^{1/2}. \tag{1.26}$$

Logarithmically differentiating (Hellier 2001) leads to

$$\frac{\dot{J}}{J} = \frac{\dot{M}_1}{M_1} + \frac{\dot{M}_2}{M_2} - \frac{1}{2}\frac{\dot{M}}{M} + \frac{1}{2}\frac{\dot{a}}{a}. \tag{1.27}$$

The total mass of the binary system is conserved, so $\dot{M} = 0$. If the orbital angular momentum is conserved ($\dot{J} = 0$), then material transferred from the secondary ($-\dot{M}_2 > 0$) leads to an increase in the binary separation ($\dot{a} > 0$), provided that the secondary star is less massive than the primary star ($M_2 < M_1$). Consider the simple form of the secondary star Roche lobe given by Paczynski (1971)

$$R_L \propto a \left(\frac{q}{1+q}\right)^{1/3} = a \left(\frac{M_2}{M}\right)^{1/3}, \tag{1.28}$$

where R_L is the volume radius of the Roche lobe (the radius of a sphere having the same volume as the Roche lobe). Logarithmically differentiating Equation 1.28, combining it with Equations 1.27 and 1.15, and considering total mass conservation in the system ($\dot{M} = 0$), leads to

$$\frac{\dot{R}_L}{R_L} = \frac{2\dot{J}}{J} + \frac{2(-\dot{M}_2)}{M_2}\left(\frac{5}{6} - q\right), \tag{1.29}$$

where -$\dot{M}_2$ is the instantaneous mass transfer rate.

If $q > 5/6$, conservative mass transfer ($\dot{M} = 0$) will shrink the Roche lobe ($\dot{R_L} < 0$) down on to the secondary star (Equation 1.29). Any loss in angular momentum ($\dot{J} < 0$) will accelerate the shrinkage of the Roche lobe. The mass transfer process will become violent and unstable ($-\dot{M}_2 > 0$) unless the secondary star can contract rapidly to keep its radius smaller than the radius of the Roche lobe. The overflow will stop once the mass ratio has reversed to $q < 5/6$.

If the angular momentum of the system is conserved ($\dot{J} = 0$) the mass transfer in the system causes the Roche lobe to expand ($\dot{R_L} > 0$) when $q < 5/6$ (Equation 1.29). The expansion of the Roche lobe reduces the mass transfer ($-\dot{M}_2 < 0$), and the system becomes stable. In order to sustain long lived mass transfer either 1) the secondary star must expand in size relative to the Roche lobe, otherwise the lobes detach from the star and mass transfer stops, or 2) the Roche lobe must decrease in size ($-\dot{R_L} < 0$). Evolution of the secondary star is one possibility, but for the secondary to evolve within the age of the Galaxy it must be spectral type G0 or earlier (Patterson 1984). Most CV secondary stars have spectral types later than G0, so a more likely solution for stable mass transfer is angular momentum loss, which shrinks the binary separation, and hence the size of the Roche lobe. Angular momentum loss is due to either gravitational radiation and/or magnetic braking in a CV system.

Gravitational Radiation

General relativity predicts that matter causes space to curve; therefore the orbital motion in a binary system will cause space to warp rhythmically. This warping produces gravitational radiation, which ripples outwards as a periodic wave. The energy needed to generate this wave is extracted from the binary orbit causing the stars to reduce their separation. Therefore, gravitational radiation becomes significant in the shortest period systems (Hellier 2001).

Magnetic Braking

The secondary star in a CV system is forced to co-rotate with orbital motion due to the tidal effects of the primary star (Section 1.1.2). The secondary star therefore has a rotational period of hours (rather than days as for a single star). This rapid rotation generates strong magnetic fields in the secondary star. Particles in the stellar wind[3] of the secondary star flow along the magnetic field lines of the star, and therefore co-rotate with the secondary star and its magnetic field. This rotation accelerates the particles into space due to the long lever-arm of the field lines, therefore taking with them a substantial amount of angular momentum. This angular momentum drain brakes the rotation of the secondary star, but the tidal torques of the primary are so efficient that angular momentum is rapidly transferred from the orbit to keep the secondary star in synchronism. In this way angular momentum is drained from the binary orbit, reducing the binary separation. Magnetic braking does not always occur in a CV system, it depends upon the strength of the secondary star's magnetic field. For systems with $P_{orb} \leq 3$hrs, the secondary star ($M_2 \leq 0.25 M_\odot$) is fully convective, therefore quenching the strong magnetic field of the star and switching magnetic braking off (Hellier 2001).

If mass loss is slow, the secondary star will stay close to thermal equilibrium, and will remain close to a main sequence type star, keeping its radius, R_2, approximately proportional to its mass, M_2 (Frank, King & Raine 1992). For stable mass transfer, the secondary star remains in contact with its Roche lobe, so

$$R_L = R_2 \propto M_2. \tag{1.30}$$

Logarithmically differentiating Equation 1.30 gives

$$\frac{\dot{R_L}}{R_L} = \frac{\dot{R_2}}{R_2} = \frac{\dot{M_2}}{M_2}. \tag{1.31}$$

[3]Stream of energetic ionised particles ejected from a star.

Substituting this into Equation 1.29 leads to

$$-\frac{\dot{J}}{J} = -\frac{\dot{M}_2}{M_2}\left(\frac{4}{3} - q\right), \tag{1.32}$$

and a critical upper mass limit (q_{crit}) of 4/3 for conservative mass transfer on a thermal time scale.

When $q < 4/3$ then $\dot{J} < 0$, therefore for sustained mass transfer angular momentum must be lost from the system. When $q > 4/3$ mass transfer becomes unstable and there will be a spontaneous overflow.

The secondary star in a CV is a late type low mass convective star, loosing mass on a dynamical time scale governed by the star's adiabatic response. The polytropic model of a star is defined by

$$\frac{R_2}{R_\odot} = \left(\frac{M_2}{M_\odot}\right)^{\frac{(1-n)}{(3-n)}}, \tag{1.33}$$

where n is the polytropic index. Considering the adiabatic response for a fully convective secondary star of $n = 3/2$ (Hjellming & Webbink 1987), leads to the mass-radius relation of

$$R_L = R_2 \propto M_2^{-1/3}, \tag{1.34}$$

and hence

$$\frac{\dot{R}_L}{R_L} = \frac{\dot{R}_2}{R_2} = -\frac{\dot{M}_2}{3M_2}, \tag{1.35}$$

by logarithmically differentiating Equation 1.34. Substituting Equation 1.35 into Equation 1.29 leads to

$$-\frac{\dot{J}}{J} = -\frac{\dot{M}_2}{M_2}\left(\frac{2}{3} - q\right), \tag{1.36}$$

producing a lower mass ratio limit for an adiabatic fully convective star of $q_{ad,fc} = 2/3$. When $q > 2/3$ the star cannot remain within its Roche lobe in hydrostatic equilibrium, and mass transfer occurs on dynamical time scales. When $q < 2/3$, the star becomes stable on a dynamical time scale and mass transfer occurs due to the slow expansion of the star via nuclear evolution or angular momentum loss, causing the Roche lobe to contract.

The secondary star in most CVs is not fully convective so the true adiabatic mass ratio will be higher. In the case where the secondary star has a convective envelope and a radiative core, the mass-radius relation becomes $R_2 \propto M_2^{1/3}$, leading to a mass ratio of $q_{ad,rc} = 1$ for the adiabatic response (Hjellming & Webbink 1987).

1.1.4 Accretion Disc Formation

The secondary star fills its Roche lobe causing mass to be transferred through the inner Lagrangian point (L_1) on to the primary star. In the primary star's rest frame the material appears to be expelled from a point which is rotating in the binary plane. In this non-rotating frame the material will have velocities parallel ($v_{\|}$) and perpendicular ($v_{\perp}$) to the line passing through both component star centres of mass. The secondary star's stellar atmosphere pushes the material through L_1 at roughly the speed of sound in a gas (c_s) leading to

$$v_{\|} \sim c_s \sim 10 km/s, \tag{1.37}$$

assuming T $< 10^5$ K for stellar envelopes (Frank, King & Raine 1992). The orbital motion of L_1 leads to

$$v_{\perp} \sim a_1 \frac{2\pi}{P_{orb}} > 100 km/s. \tag{1.38}$$

$v_{\perp} >> v_{\|}$, therefore the stream swings into an orbit around the white dwarf rather than flowing directly towards it (Frank, King & Raine 1992).

The stream of material follows along a ballistic trajectory determined by the gravity of the primary because $v_{\|} << v_{ft}$, where v_{ft} is the velocity the material gains during free fall towards the primary star. Figure 1.7 illustrates the trajectory that the stream of material will take, showing that it intersects itself. This intersection causes turbulent shocks, which dissipate energy. The gas in the stream does not have an opportunity to reduce the angular momentum it had when passing through L_1. Therefore it settles into the orbit of lowest energy for a given angular momentum, a circular orbit of radius r_{cir} in the binary plane. This initial Keplerian orbit has the

same angular momentum as the material passing through L_1 (Frank, King & Raine 1992).

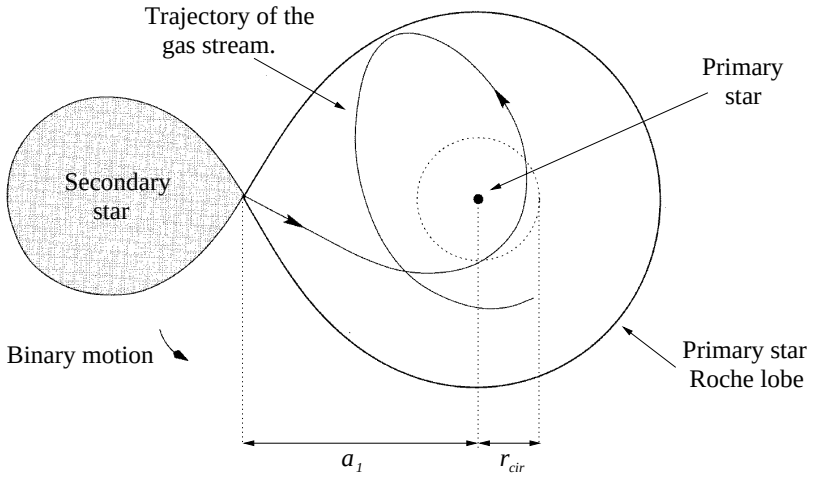

Figure 1.7: The trajectory of the gas stream (solid line) coming from the secondary star, adapted from Hellier (2001). The stream will collide with itself, ultimately forming a ring of material at the *circularisation radius*, r_{cir} (dotted line).

The ring of material formed at the *circularisation radius* (r_{cir}) will eventually radiate energy (due to viscosity); material in the ring will move towards the primary to compensate for this loss of energy, forming an *accretion disc* (Figure 1.8). For material to orbit the primary star more closely it must lose angular momentum, therefore angular momentum will flow outwards, causing the outer parts of the disc to spiral outwards. The original ring of material at radius r_{cir} will therefore expand towards and away from the primary star.

1.1.5 Boundary Layer

The boundary layer is the region between the inner edge of the accretion disc and the surface of the white dwarf. In this region the accretion disc material is decelerated to match the surface velocity of the white dwarf, so accretion on to the white dwarf can occur.

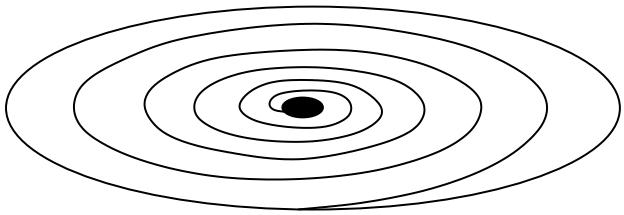

Figure 1.8: Formation of an accretion disc from Frank, King & Raine (1992). Material will spiral towards the white dwarf to compensate for the loss of energy due to radiation.

The gravitational potential energy (PE) released by a mass, m, from infinity to the surface of the white dwarf is

$$\mathrm{PE}_{inf} = -\int_{R_1}^{\infty} \frac{GM_1 m}{r^2} dr = \frac{GM_1 m}{R_1}. \tag{1.39}$$

The kinetic energy of the mass circulating just above the surface of the white dwarf is given by $\frac{1}{2}mv_k^2$, where $v_k = (GM_1/R_1)^{1/2}$ is the Keplerian velocity, giving

$$\mathrm{KE} = \frac{GM_1 m}{2R_1}. \tag{1.40}$$

Therefore at the surface of the white dwarf KE=$\mathrm{PE}_{inf}/2$ (from Equations 1.39 and 1.40); the kinetic energy of the material is converted into heat and irradiated, emitting up to half the total luminosity of the system.

At high accretion rates, the boundary layer contains enough material to obscure the emerging radiation, causing it to be optically thick. Figure 1.9 shows an illustration of an optically thick boundary layer. In this optically thick case the luminosity must diffuse through a distance H before emerging over an area given by

$$\mathrm{Area} \sim 2\pi R_1 2H, \tag{1.41}$$

(Warner 1995). The optically thick boundary layer can be approximated to a black body

$$4\pi H \sigma T_{BL}^4 = \frac{GM_1 \dot{M}}{2R_1}, \tag{1.42}$$

where $\dot{M}$ is the accretion rate, and will therefore have an effective boundary layer temperature (T_{BL}) of

$$T_{BL} \sim 1 \times 10^5 M_1^{11/32} \left(\frac{\dot{M}}{10^{16}}\right)^{7/32} \left(\frac{R}{10^9}\right)^{-25/32} \text{ K} \tag{1.43}$$

(Frank, King & Raine 1992). $T_{BL} \sim 10^5$K indicates that the bulk of radiation from an optically thick boundary layer is emitted at soft X-ray and extreme ultraviolet wavelengths (~ 0.1keV).

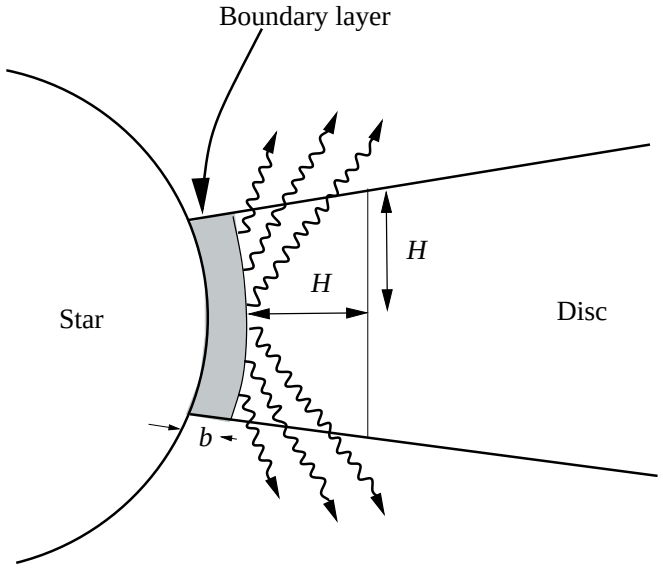

Figure 1.9: Schematic view of an optically thick boundary layer in the plane perpendicular to the plane of the disc, from Frank, King & Raine (1992).

When the boundary layer is optically thin, radiation can escape directly from the shock front formed when the highly supersonic accretion disc material meets the surface of the white dwarf. For a perfect gas, the temperature of the post-shock gas (T_s) is given by

$$T_s = \frac{3}{16}\frac{\mu m_H}{k} v_p^2 \sim 1.9 \times 10^8 M_1 \left(\frac{R_1}{10^9}\right)^{-1} \text{ K}, \tag{1.44}$$

where μ is mean molecular weight , m_H is the mass of a hydrogen atom, k is the Boltzmann constant, and $v_p = (GM_1/R_1)^{1/2}$ is the pre-shock velocity (Frank, King

& Raine 1992). Therefore an optically thin boundary layer should radiate hard X-rays with energies $\sim$ 10keV.

At $T \sim 10^8$K, cooling of the gas via bremsstrahlung radiation is ineffective. If the cooling time (t_{cool}) of the gas exceeds the adiabatic time scale (t_{ad}) the boundary layer will expand to form a hot X-ray emitting corona (Figure 1.10). The formation of this hot corona ($t_{cool} > t_{ad}$) is a condition of the accretion rate ($\dot{M}$). At low mass transfer rates there is not enough material for effective cooling via particle collisions, therefore the boundary layer will expand to a hard X-ray emitting corona. At higher mass transfer rates, the boundary layer becomes optically thick producing softer X-rays.

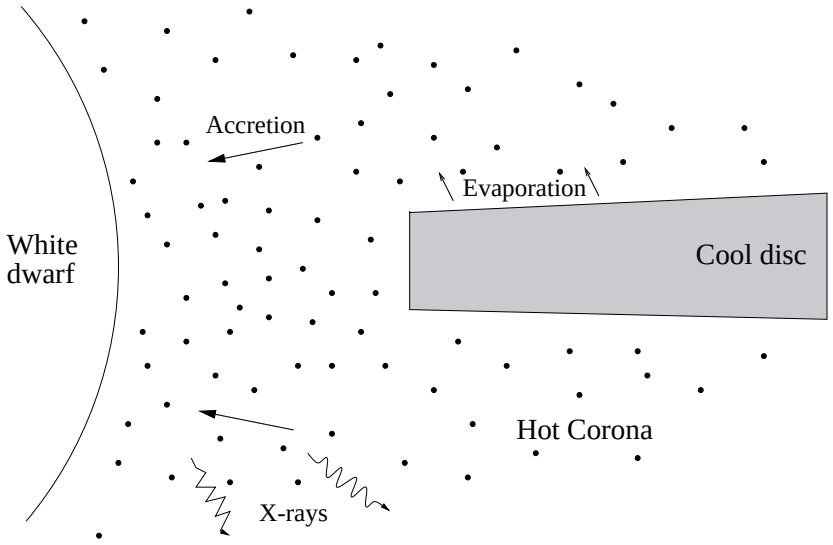

Figure 1.10: Schematic view of an optically thin boundary layer in the plane perpendicular to the plane of the disc, from Hellier (2001) based on a diagram in Meyer (1999).

1.1.6 Evolution into a CV System

The starting point of a CV system is a widely separated binary system ($a \geq 50R_\odot$ - Warner 1995), containing two main sequence stars with a large orbital period

($P_{orb} \geq 1$ years - Patterson 1984). The primary star is more massive than the secondary star ($M_1 > M_2$), and has a mass of $0.95 < M_1 < 10 M_\odot$ to enable it to evolve off the main sequence and form a white dwarf.

The primary star will evolve off the main sequence to become a red giant before the secondary star, because the greater mass of the primary core ensures higher pressure and temperature, and therefore more vigorous nuclear burning. Evolution of the primary star initialises the transfer of mass from the primary to the secondary ($-\dot{M}_2 < 0$). This mass transfer is *unstable* (Section 1.1.3, Equation 1.29) because the transferred material gains angular momentum as it moves closer to the centre of mass of the system. To compensate for this increase the binary separation shrinks, reducing the size of the Roche lobe and therefore increasing the mass transfer. The stars will spiral together causing the Roche lobe to shrink around the primary star. This results in a runaway feedback as the entire envelope of the red giant primary star accretes on to the secondary star in only a few years (Rasio & Livio 1996).

The accreting secondary star is unable to adjust its structure at the rate at which mass is arriving, therefore the material overflows both of the Roche lobes, eventually producing an extended atmosphere around both of the stars. This *common envelope* phase in which the degenerate core of the primary and the main sequence secondary share a common gaseous envelope was first suggested by Ostriker (1976) and Paczynski (1976). The gaseous envelope causes a drag force on the binary stars, draining their orbital energy and causing them to spiral inwards. The separation of the stars reduces to a few solar radii over ~ 1000 years (Meyer & Meyer-Hofmeister 1979).

The heat dissipated in the envelope via the drag force eventually exceeds its binding energy and the envelope ejects as a planetary nebula, exposing the centrally detached binary. After this *propeller phase* the detached binary consists of a main sequence secondary star orbiting a hot sub dwarf primary; this end point has been simulated by Taam & Bodenheiner (1991). A numerical investigation by Hjellmung & Taam (1991) has also shown that the secondary star is only $\sim 0.01 M_\odot$, more

massive than before mass transfer began.

Eventually the secondary star will fill its Roche lobe and transfer mass to the primary star ($-\dot{M}_2 > 0$), giving birth to a CV system.

1.2 Observational Phenomena in CV Systems

Both RW Tri and OY Car have high inclination angles and therefore are eclipsing systems. This eclipsing phenomenon is observed as a periodic dip in the light curves of each system. The eclipse profile of a system is important because it constrains the size of the component stars.

1.2.1 Eclipsing Systems

An eclipse occurs when the secondary star occults the continuum source in the binary system. The eclipse profile can be studied to provide information about the size of the component stars, the accretion disc, the bright spot, and the boundary layer. Figure 1.11 shows an idealised eclipse profile where the secondary star occults only the primary star; it defines four phases of contact, along with an illustration of the position of the secondary star at each of the contact phases.

The eclipse profile of a CV system may alter in different wavelength regions. At optical wavelengths the accretion disc, bright spot, and primary star contribute to the continuum and can therefore be eclipsed; this produces a complex profile of staggered steps. Figure 1.12 shows an example of an optical eclipse where the white dwarf and bright spot contact phases are clearly visible. In the ultraviolet the continuum source consists of the inner accretion disc and the white dwarf. Whereas in X-rays the eclipsed continuum region is either the boundary layer or the accretion region on the surface of the white dwarf, depending upon the magnetic field strength of the primary star. The secondary star is eclipsed by the primary star and accretion disc at infrared wavelengths. This secondary star eclipse produces a much shallower profile.

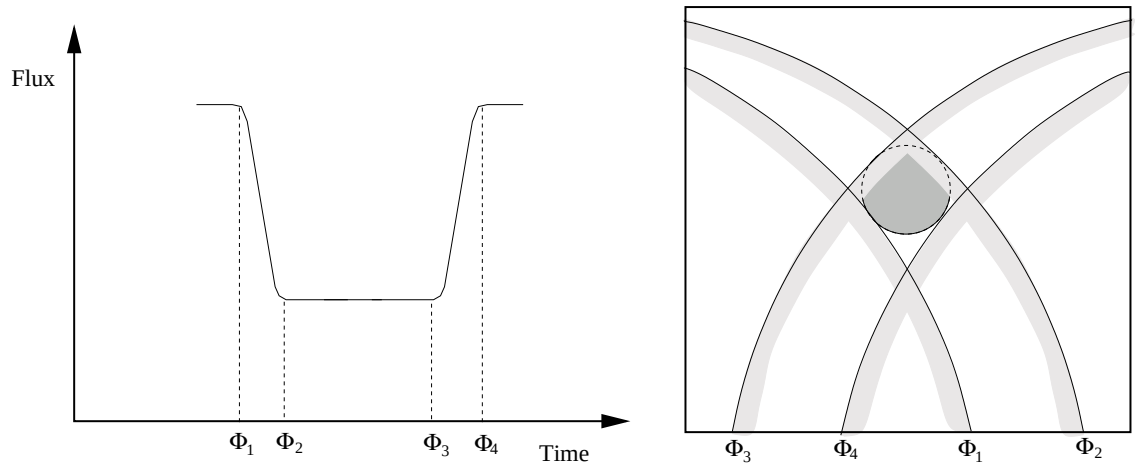

Figure 1.11: Illustration of an eclipse profile and eclipse contact phases. Left: Eclipse profile with the four contact phases defined as Φ_1, Φ_2, Φ_3 and Φ_4. Right: Illustration of the position of the Roche lobe of the secondary star at the four contact phases. The solid dark grey circle represents the continuum source, and the solid black arc lines with light grey shading represent the outer edge of the secondary star Roche lobe.

The inclination angle (i) of a system affects the eclipse profile of that system. High inclination systems ($i \sim 75-90^o$) are seen nearly edge on, so the secondary star totally eclipses the continuum source (Figure 1.13, left). Grazing eclipses produce a 'U'-shaped eclipse profile and occur when $i \sim 70^o$ depending upon the size of the component stars (Figure 1.13, middle). Partial eclipse profiles occur for systems with smaller inclination angles and are 'V'-shaped (Figure 1.13, right). As the inclination angle decreases further, the eclipse profile reduces until no eclipse is seen.

Eclipse Timings

The eclipse of the primary star is crucial in determining its radius (R_1). The full eclipse duration of the primary star is measured from 1st to 4th contact (Φ_1 to Φ_4), and can be found at most wavelengths as long as sharp steps are observed for the primary eclipse (Figure 1.11 and 1.12). The primary eclipse full width half

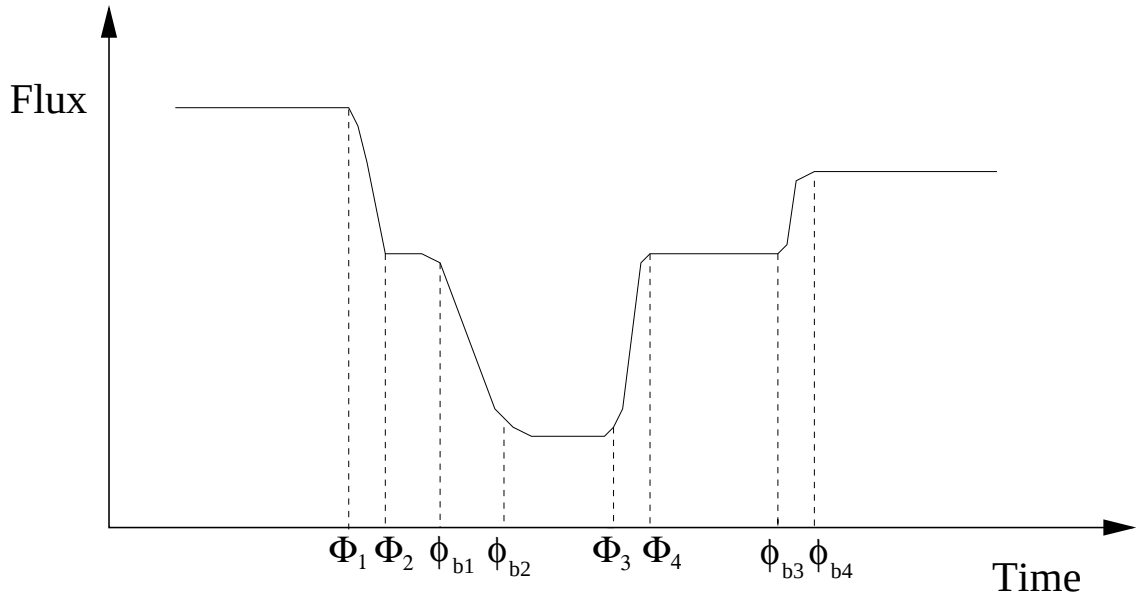

Figure 1.12: Illustration of an optical eclipse profile. The four white dwarf contact phases are defined as Φ_1, Φ_2, Φ_3 and Φ_4. The four bright spot contact phases are defined as $\phi_{b1}, \phi_{b2}, \phi_{b3}$ and ϕ_{b4}.

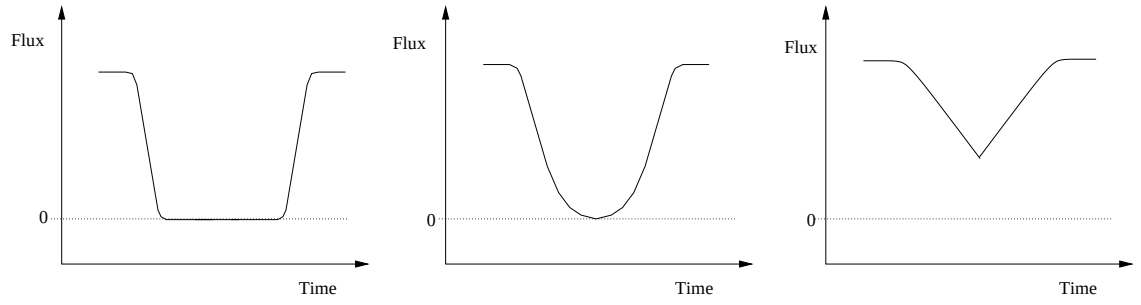

Figure 1.13: Inclination angle effect on the eclipse profile. Left: Total eclipse. Middle: Grazing eclipse. Right: Partial eclipse.

maximum (FWHM), $\Delta\Phi$, is related to the mass ratio (q) and the inclination angle (i) due to the Roche lobe geometry of the system (further discussed in Chapter 4, Section 4.1.1).

The time in which the primary star is in total eclipse is measured from 2nd to 3rd contact (Φ_2 to Φ_3). The total eclipse time is inclination angle dependent, and

is zero for grazing or partial eclipses.

The time taken for the primary star to be fully eclipsed (Δw_d) is defined as

$$\Delta w_d = \frac{1}{2}(t_i + t_e), \tag{1.45}$$

where t_i is the ingress time of eclipse, and t_e is the egress time of eclipse. t_i is measured between Φ_1 and Φ_2 (Figure 1.11), and is the time taken for the continuum to be fully eclipsed. t_e is measured between Φ_3 and Φ_4 (Figure 1.11), and is the time taken for the continuum to emerge out of eclipse. If the continuum source is symmetric the egress and ingress of eclipse will be equal; this is what should be seen in the case of non-magnetic CVs. In the case of magnetic CVs, where material is accreting directly on to one or both poles of the white dwarf, the shape of ingress and egress will differ.

Magnetic Eclipse Profiles

Although not the subject of this thesis, the eclipse profiles of magnetic systems are briefly considered for completeness. In magnetic systems material is accreted via the white dwarf's strong magnetic field, producing 'accretion spot' regions on the surface of the white dwarf. Figure 1.14 shows how the profile of the eclipse changes as these accretion regions move through the observers' line of sight. Each eclipse profile in Figure 1.14 has two illustrations to show where the limb of the secondary star is in relation to the accretion region and the white dwarf.

In optical light curves of non-magnetic systems a similar phenomenon is seen when eclipsing the bright spot on the edge of the accretion disc.

1.2.2 P Cygni Winds

P Cygni is an emission line star, which has a specific line profile that is formed in the expanding envelope of the star (Van Blerkom 1970). Figure 1.15 shows an illustration of P Cygni, and the emission line profile expected from such a star.

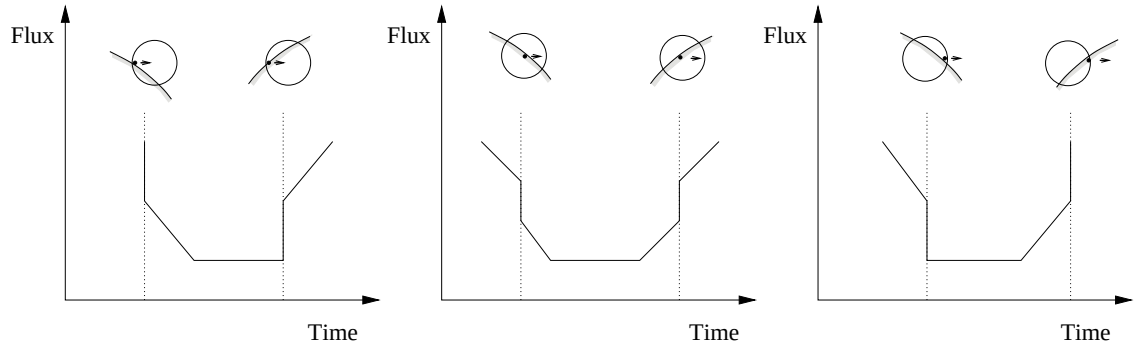

Figure 1.14: Eclipse ingress and egress of the accretion region in magnetic CVs depending on the accretion region position relative to the white dwarf surface, along the line of sight. Each accretion region is represented by a black spot in the illustrations. Left: Accretion region on the left side of the white dwarf. Middle: Accretion region in the middle of the white dwarf. Right: Accretion region on the right of the white dwarf. The two illustrations for each profile show the accretion region going into and out of eclipse.

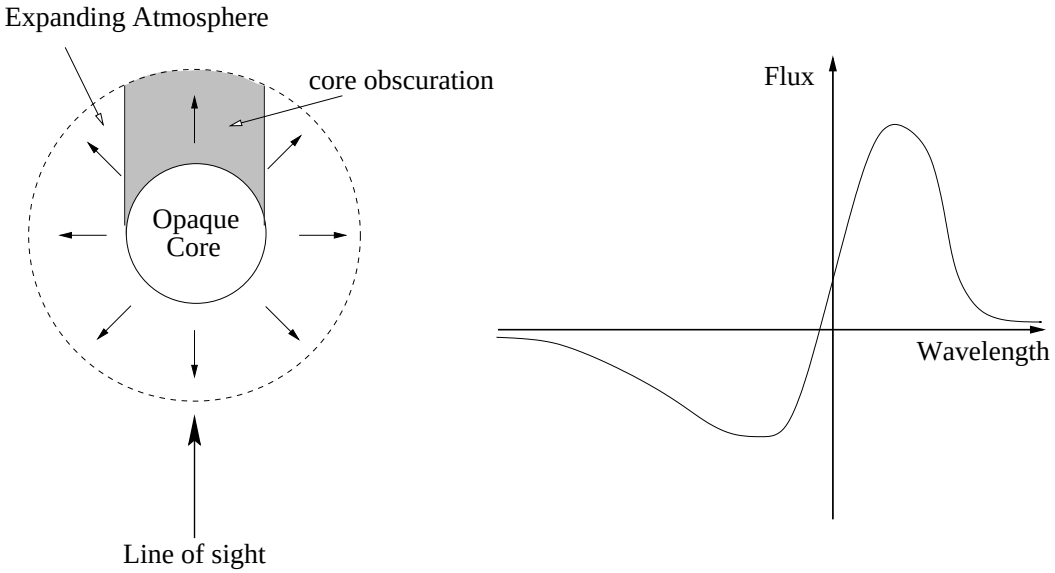

Figure 1.15: Illustration of P Cygni and its characteristic line profile. Left: Opaque core and expanding envelope of P Cygni. Right: A typical emission line profile from P Cygni.

P Cygni is a spherical system with an opaque core (the continuum source) surrounded by a radially expanding atmosphere. Photons escape from the continuum source producing an emission line in the expanding envelope. Absorption is seen in the region between the core and the observer, due to scattering. This absorption is also produced at the greatest line of sight velocity towards the observer, and is

therefore blue shifted. Part of the envelope with the greatest line of sight velocity away from the observer lies directly behind the continuum core, and is therefore occulted. This causes a reduction in the red wing of the emission line. The emission line itself is also red shifted, due to the motions of the expanding envelope.

In an accretion disc system, the white dwarf and accretion disc act as the continuum source, and emission lines are formed at the interface between the disc and the wind. A wind surrounding the disc in some configuration acts as the scattering medium, altering the profile of the emission lines due to expansion effects. This is shown in Figure 1.16.

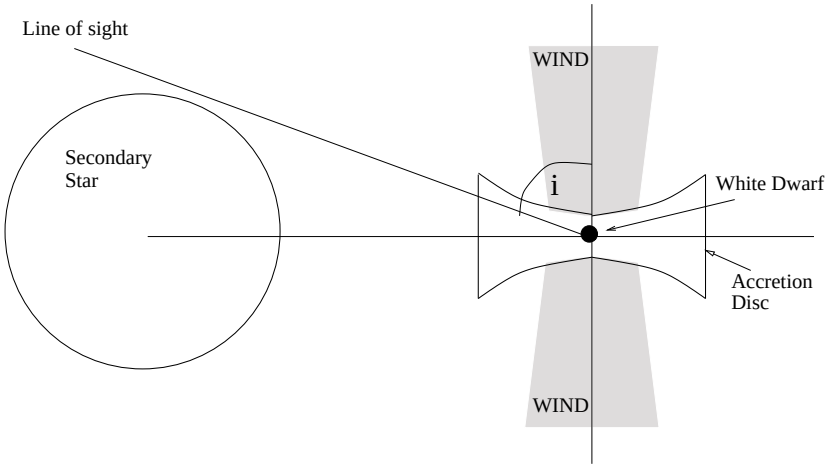

Figure 1.16: Accretion disc system with winds. i is the inclination angle of the system.

P Cygni line profiles are seen in low inclination CVs with emission in the red wing, and absorption in the blue wing of the line (Córdova & Mason 1982, St.Louis et al. 1993, Hartley et al. 2002). These profiles are not seen in higher inclination systems, but the asymmetry of emission lines further suggests a wind origin, in addition to the presence of these lines during eclipse (see Chapter 2, Section 2.1.2 for observational evidence).

1.2.3 The Classification of CV Systems

There are a number of sub-classes of CV system which were originally classified by the brightness variation of the system from long-term light curve observations. Many of these systems go through an 'outburst' phase, where the system increases in brightness. The CV sub-class system is also dependent on the magnetic field of the white dwarf, among other properties.

Here is a brief description of the sub-classes of CVs (see Warner 1995 for review).

1) Classical nova (CN) - These systems only have one observed outburst. The brightness of the system increases by up to 19 magnitudes during the outburst phase. These outbursts are due to the *thermonuclear runaway* effect from accretion on to the primary star.

2) Dwarf nova (DN) - These systems have re-occurring outbursts, in which the brightness of the system increases by up to 8 magnitudes. The outbursts in these systems are understood as an increased rate of mass accretion through the disc causing a release of *gravitational* energy. OY Car is a DN system; a further discussion on DNs can be seen in Section 1.4.

3) Magnetic CVs - These systems have a primary star with a magnetic field strong enough to partially or totally disrupt the accretion disc in the system. This restricts the flow of material to the magnetic poles of the white dwarf rather than a boundary layer. There are two sub-classes of magnetic CV, *polars* which have strong magnetic fields ($10 - 230$MG), and *intermediate polars* (IPs), which have weaker fields ($1 - 10$MG). Figure 1.17 illustrates how the magnetic field of the primary star disrupts the accretion process in an IP system.

4) Nova-like variables (NL) - These systems include all *non-eruptive* CVs. They appear to be in a state of permanent outburst, equivalent to a DN outburst state. RW Tri is a NL system; a discussion on NLs can be seen in Section 1.3.

5) Recurrent nova (RN) - These systems are classical nova systems that repeat their outbursts. During outburst a shell is ejected at high velocities, unlike DN

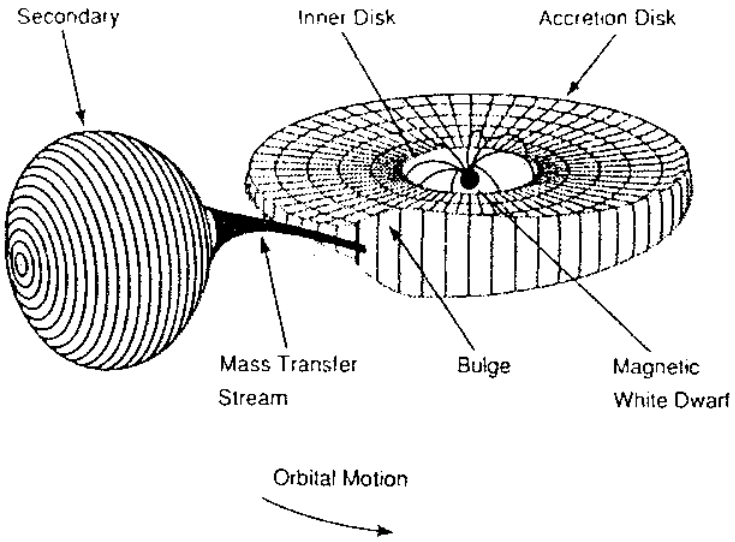

Figure 1.17: An illustration of the effects of a primary star magnetic field in an IP system, from Mason et al. (1988a).

where no shell is lost.

CV systems undergo a wide variety of *flickering*. Flickering is a random variability in the light curve, which does not recur with any periodic cycle. RW Tri shows low amplitude activity in the optical on time scales of 5 to 20 minutes (Warner 1995), other systems show rapid fluctuations lasting ∼seconds, and larger flares and dips lasting ∼hours. The longer lasting fluctuations have larger amplitudes.

RW Tri and OY Car are two very interesting systems to examine because of their eclipsing nature. The key parameters of these two systems can be seen in Table 1.1.

1.3 Nova-Like Variables

One of the objects studied in Chapters 2, 3 and 4, is the NL system RW Tri. Most NL CVs are non-eruptive systems that may have low-states in which their magnitude decreases by $\sim$ 1 mag. In general NLs are brighter than DN in quiescence but there is a sub-class, VY Scl stars, that undergo low states in which their brightness decreases by $2-6$ mag, leading to quiescent DN magnitudes (Hellier 2001, Warner

	RW Tri	OY Car	References
CV Type	Nova-Like	Dwarf Nova	1,2
Orbital Period (P_{orb})	5h 34 mins	1h 31 mins	2,3,4
Inclination (i)	$70^o - 82^o$	$82.6^o - 83.3^o$	5,6,7,8,9
Distance (D)	205pc - 341pc	86pc - 121pc	10,11,12,13
Visual Magnitude (m_V)	$13.5 - 12.5$	$15.2 - 12.4$	5,13,14
Primary Mass (M_1)	$0.45M_\odot - 0.58M_\odot$	$0.3M_\odot - 1.26M_\odot$	5,15,16,17
Secondary Mass (M_2)	$0.44M_\odot - 0.70M_\odot$	$0.07M_\odot - 0.15M_\odot$	7,8,18,19
Secondary Spectral Type	K5 - M0	M5 - M6	13,19,20

Table 1.1: General information about RW Tri and OY Car. References : 1. Africano et al. (1978), 2. Vogt (1979a), 3. Protitch (1956), 4. Protitch (1958), 5. Smak (1995), 6. Shafter (1983), 7. Kaitchuck et al. (1983), 8. Wood & Horne (1990), 9. Wood et al. (1989), 10. Dhillon et al. (2000), 11. McArther et al. (1999), 12. Bruch et al. (1996), 13. Sherrington et al. (1982), 14. Berriman (1984), 15. Frank & King (1981), 16. Ritter (1980b), 17. Cook (1985), 18. Longmore et al. (1981), 19. Vogt et al. (1981), 20. Echevarría (1983).

1995). It has been shown that NLs have luminosities similar to DN at maximum (Patterson 1984). NLs generally do not have prominent orbital humps like those seen in some quiescent DN (Section 1.4), which indicates that the bright spot is less significant in NL systems. NL accretion discs are highly luminous and optically thick, therefore making it hard to observe the secondary star spectra, even for high inclination systems.

All NLs have long-term variations about an average magnitude. The brightness of some NLs appear to vary quasi-periodically on time scales of years. These variations may by secondary stars with magnetic cycles similar to that of the Sun (Warner 1995). The variations in the internal magnetic pressure could produce changes in the radius of the secondary star, affecting the mass transfer of material from the

secondary star to the accretion disc. Increasing mass transfer rates affect the luminosity and hence radius of the accretion disc, as well as the thickness of the outer edge of the disc. This in turn produces variability in the brightness of the system.

1.3.1 RW Tri

RW Tri was discovered as a short period (P_{orb} = 20040s) close binary system with a deep varying eclipse by Protitch (1956, 1958), and later recognised as a nova-like system (Africano et al. 1978).

RW Tri is a high inclination NL system. The accretion disc in RW Tri shows evidence of radial stratification, where He II emission is confined to the inner disc while He I and H emission are found further away from the white dwarf (Kaitchuck et al. 1983). The relative strengths of the optical emission lines in these stars increase with inclination angle (Warner 1995, Table 4.4), and the ultraviolet emission lines are also very sensitive to inclination. The ultraviolet continuum is deeply eclipsed, but the ultraviolet emission lines are only mildly eclipsed which suggests that they originate from winds emanating from the system. These ultraviolet emission lines are also very asymmetric, indicating that they originate from wind emission (Section 1.2.2).

Eclipse timings of RW Tri undertaken by Africano et al. (1978), Longmore et al. (1981), and Robinson et al. (1991) show some evidence of a cyclic variation of the eclipse timings about a linear ephemeris. There are three possible mechanisms that may cause this residual cyclic behaviour, 1. motion of a third body around the binary system (Nather & Robinson 1974), 2. apsidal motion (Africano & Wilson 1976), and 3. magnetic cycles in the secondary star (Warner 1988). Still et al. (1995) produced timings from spectral measurements. They combined their results with timings from Africano et al. (1978), Robinson et al. (1991), Horne & Stiening (1985) and Rutten et al. (1992a), to show that the cyclic variations proposed by Africano et al. (1978) and Robinson et al. (1991) did not convincingly fit the data.

Optical light from the system comes primarily from the accretion disc in RW Tri (Africano et al. 1978). Eclipse mapping of the accretion disc at optical wavelengths shows an optically thick accretion disc with temperatures ranging from 10 000 K in the outer parts of the disc, to 40 000 K in the inner parts of the disc (Kaitchuck et al. 1983, Horne & Stiening 1985, Rutten et al. 1992a). The radial temperature profile of the accretion disc is consistent with the expected steady state accretion law of $T \propto R^{-3/4}$, where T is the temperature of the accretion disc and R is radial distance from the centre of the primary star (Horne & Stiening 1985).

Another interesting phenomenon of RW Tri is the variation of low amplitude orbital humps seen in the light curves of the system, showing the dynamic nature of the accretion disc. These low amplitude humps are often pre-eclipse, starting at $\phi \sim 0.75$ and peaking at $\phi \sim 0.90$; in other observations post-eclipse humps are seen, peaking at $\phi \sim 0.12$, but in general no humps are observed at all (Walker 1963, Africano et al. 1978, Frank & King 1981, Horne & Stiening 1985, Rutten et al. 1992a, and Mason et al. 1997). The range of orbital humps is larger at shorter wavelengths and may be due to continuum absorption by material above the plane of the accretion disc (Horne & Stiening 1985).

Recent observations of RW Tri have found orbital modulations in the ultraviolet (Mason et al. 1997). A large 'dip' is seen in the ultraviolet data a quarter of an orbital cycle before eclipse. This dip may by cooler vertical structure toward the outside of the disc, obscuring the hot inner disc regions (Mason et al. 1997).

RW Tri in the Ultraviolet

RW Tri was suggested to be a wind emitting system by Córdova & Mason (1985a). They observed emission lines in the ultraviolet that were not eclipsed to the same degree as the ultraviolet continuum, providing evidence that the emission lines were forming in an extended region above and below the disc. Evidence of asymmetry in the emission lines, their velocities and eclipse behaviour, indicated that the lines were being formed by an accelerated wind. Drew & Verbunt (1985) tried to fit

a spherically symmetric radiatively driven wind model to the ultraviolet data of Córdova & Mason (1985a). Drew & Verbunt (1985) found that the emission lines of RW Tri could not be formed from a single volume centred on the white dwarf, because their model could not be fitted to the data. Further modelling of these ultraviolet data, using an accretion disc wind flowing model, was carried out by Drew (1987). Drew (1987) showed that the emission line profiles of RW Tri were consistent with a bipolar wind, and proposed that only an accretion disc could produce this wind geometry. Wind model calculations carried out by Vitello & Shlosman (1993) also showed that a disc wind was preferable to a spherical wind produced from the primary star in the case of RW Tri, confirming the results of Drew (1987). The ultraviolet observations of Mason et al. (1997) also show asymmetric emission line profiles (Section 1.2.2) that do not significantly decrease in intensity during eclipse. This provided more evidence of large scale winds emanating from the binary system, and confirmed the observations of Córdova & Mason (1985a).

One of the driving forces behind CV winds is thought to be radiation pressure[4] in the ultraviolet emission lines (Drew & Verbunt 1985, Drew 1987, Vitello & Shlosman 1988). The radiation pressure drives the gas away from the radiation source. Figure 1.18 shows how the CV winds can be formed by radiation pressure.

The ultraviolet data of RW Tri observed by Córdova & Mason (1985a) not only provided evidence for winds in the system, but also evidence of absorption features at the wavelengths of λ1302Å and λ1260Å. Closer inspection of these, and other absorption features in the data of Mason et al. (1997), has shown that these features are narrow, and seen in emission during eclipse. These emission features are slightly broader than their non-eclipsed absorption counterparts (Chapter 2).

[4]The pressure exerted on a surface by electromagnetic radiation. As radiation carries momentum as well as energy, it exerts a force when it meets a surface, i.e. the photons transfer momentum when they strike the surface.

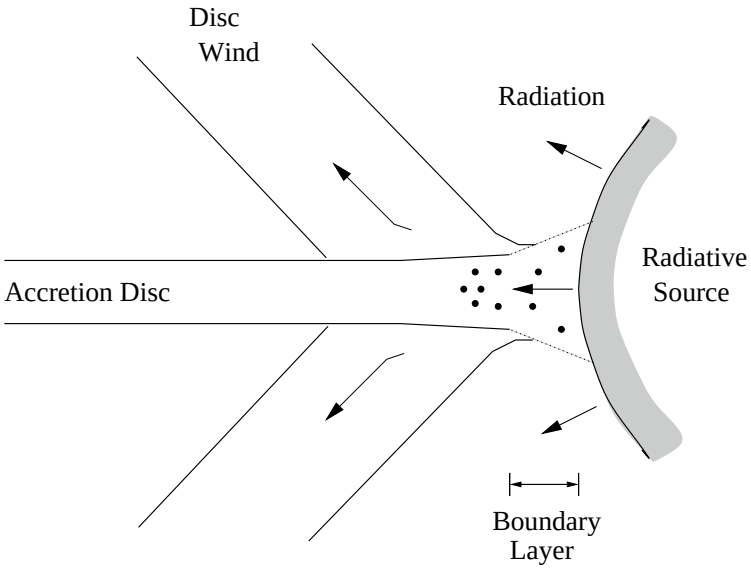

Figure 1.18: An illustration of the formation of CV winds by radiation pressure. Radiation produces a force on the material in the boundary layer, causing material to accelerate outwards to form a wind region.

RW Tri in the Far Red and the Near Infrared

The secondary star in a nova-like system is difficult to observe at optical wavelengths because of the brightness of the accretion disc. Secondary star features are more likely to be observed at longer wavelengths in the far red and near infrared. The secondary star in close binary systems is expected to be a low mass late-type main sequence star of spectral type K-M. From observations of single K-M type stars, absorption features characteristic to these spectral types can be identified in the far red and near infrared.

In the far red the Na I absorption doublet (λ8183.3Å, λ8194.8Å) has been identified in a number of CV systems as a secondary star absorption feature (Friend et al. 1988). This Na I doublet was later used to measure radial velocities in five dwarf nova systems (Friend et al. 1990). The radial velocity curve of RW Tri could not be directly measured from the Na I absorption doublet because the doublet was too

weak (Friend et al. 1988). Smith et al. (1993) measured the radial velocity amplitude of the secondary star of RW Tri indirectly, using the method of skew-mapping. Their results gave a velocity of ~ 250km/s.

A recent spectroscopic study in the near infrared has shown that secondary star features can be seen directly in the spectrum of RW Tri (Dhillon et al. 2000). In particular they observed the Na I absorption doublet (22062Å and 22090Å), and the Ca I absorption triplet (22614Å, 22631Å and 22657Å) as broad absorption features, consistent with an M0V type secondary star contributing 65% of the observed K-band out-of-eclipse flux.

Previous Mass Calculations for RW Tri

In 1981, Frank & King calculated the primary and secondary star masses of RW Tri as $1.3M_{\odot}$ and $0.47M_{\odot}$ respectively. They used near infrared and optical light curves, and fitted them with a standard CV model of a red dwarf secondary star eclipsing an optically thick steady state accretion disc. Frank & King (1981) found a large range in primary star masses of $0.6 - 1.4M_{\odot}$, due to uncertainties.

Kaitchuck et al. (1983) calculated the component masses of RW Tri using the radial velocity amplitude of the primary star. They used the radial velocity obtained from He and H accretion disc emission features. The results obtained by these authors were $0.46 - 0.74M_{\odot}$ and $0.68 - 0.77M_{\odot}$ for the masses of the primary and secondary star respectively. These results need to be treated with caution as the H and He lines used may be contaminated by the secondary star and bright spot, affecting the resultant velocity.

Smak (1995) analysed accretion disc and bright spot eclipses from optical light curves, and combined them with the secondary star radial velocity amplitude found by Kaitchuck et al. (1983) to produce primary and secondary star masses of $0.45 \pm 0.15M_{\odot}$ and $0.63 \pm 0.1M_{\odot}$ respectively. The long-term variations in RW Tri are attributed to variations in the mass transfer from the secondary to the accretion disc, and the accretion rate on to the primary (Smak 1995). If mass transfer is

varying, then the accretion disc and bright spot will also vary, so using these features to calculate the masses of the component stars may not give a true picture of the system.

The Picture of RW Tri so Far

RW Tri is a nova-like CV with an optically thick accretion disc (Kaitchuck et al. 1983, Horne & Stiening 1985, Rutten et al. 1992a) and a large vertically extended structure probably situated in the outermost regions of the accretion disc (Mason et al. 1997). In the ultraviolet, narrow ultraviolet absorption lines are observed in emission during eclipse, as well as bi-polar like winds protruding above and below the disc throughout the orbital cycle (Drew 1987, Vitello & Shlosman 1993).

To improve the picture of RW Tri I have undertaken the following in this thesis:-

- In Chapter 2 I have modelled the location of the material producing the narrow UV absorption features. I fit my model to the *Hubble Space Telescope* data of Mason et al. (1997).

- In Chapter 3 I calculate the velocity of the secondary star in two ways. 1. Re-analysing the far red data of Smith et al. (1993) using the skew-mapping technique and a rigorous Monte Carlo error analysis. 2. Obtaining time resolved spectroscopy using the *United Kingdom Infra-Red Telescope* to measure spectral features of the secondary star, and a cross-correlation technique to calculate the velocity.

- Also in Chapter 3, I calculate the rotational velocity of the secondary star using the *United Kingdom Infra-Red Telescope* observational data.

- In Chapter 4 I calculate the masses of the component stars in RW Tri using the radial velocity values of the component stars, and the rotational velocity of the secondary star.

1.4 Dwarf Nova Systems

DN systems have outbursts increasing their brightness by typically 2 to 5 mag. The duration of these outbursts is typically 2 to 20 days, and the time between subsequent outbursts are weeks to years (Warner 1995). In quiescence orbital humps are seen in light curves, due to the bright spot on the outer edge of the disc, where material from the secondary star is impacting with the accretion disc.

No two DN outbursts in a given system are alike. This makes it difficult to predict outburst phases and understand the origin of the outburst. In outburst orbital humps are observed at their quiescent amplitude (OY Car: Rutten et al. 1992b, CN Ori: Mantel et al. 1988, SS Cyg: Honey et al. 1989), therefore showing no evidence of an increase of the mass transfer from the secondary prior to, or during the rise to outburst maximum. Together with evidence that the accretion disc radius of a DN increases during outburst (U Gem: Smak 1984), this supports geometry where DN outbursts are centred on the accretion disc and primary star.

The favoured model for DN outburst is the disc instability model (DIM), first suggested by Osaki (1974). During quiescence, the mass transferred from the secondary star is stored in the disc until a critical mass is reached; the disc then becomes unstable due to viscous interactions, which greatly increases the mass transfer on to the white dwarf, producing an outburst. The mass transfer rate from the secondary star is assumed to be constant in the DIM.

During DN outburst variations in the light curves are seen on a variety of time scales. The most rapid variations are coherent dwarf nova oscillations (DNOs) lasting typically between 10s and 30s. Quasi-periodic oscillations (QPOs) are less coherent than DNOs, and last for time scales typically between 1 to 30 mins. Orbital modulations and flickering also occur.

OY Car is a member of the SU UMa star sub-class of DN, and undergoes superoutburst states. Superoutbursts are less frequent than normal outburst. The number of normal outbursts that can occur between each superoutburst can vary

widely for any given system. Superoutbursts are brighter than normal outbursts by 0.7 mag, and occur on time scales between 5 to 10 times longer than normal outbursts in the same system. The process that causes this prolonged outburst is not yet understood. One possibility is irradiation-induced mass overflow, where the secondary star is heated during normal outburst, leading to an enhancement of the mass transfer (Osaki 1985). A second possibility is tidal-thermal instability, where thermal instabilities produce normal outbursts, but an insufficient removal of disc angular momentum during normal outbursts produces a tidal instability and a superoutburst (Buat-Ménard & Hameury 2002).

1.4.1 Dwarf Nova Oscillations

Dwarf nova oscillations (DNOs) are low amplitude periodic brightness modulations typically lasting between 10 and 30s; they are seen at optical wavelengths, and occur during DN outburst. Most DNOs appear during the rise of an outburst, occur through outburst maximum, and disappear during the decline in outburst. Not all DN show DNOs during outburst.

DNO periods can vary over an outburst by up to $\sim 25\%$ (Hellier 2001); the white dwarf can not change period over such short time scales because of its large inertia. However, the increased accretion torque can spin the boundary layer and outer layers of the white dwarf up during outburst, setting up a phase-dependent instability because the boundary layer and the inner accretion disc have different angular velocities, causing interactions between them to set up a periodic oscillation. This can only occur in the case of a weak magnetic field, as a strong magnetic field will anchor the outer layers of the white dwarf to its core preventing differential rotation.

DNOs are not seen in quiescence so the weak magnetic field must be generated during outburst. The increase in mass transfer on to the primary during outburst may cause shearing effects between the differentially rotating layers of the white

dwarf. This shearing effect may create a dynamo producing a magnetic field.

X-ray DNOs have been observed, and associated with optical DNOs (Córdova & Mason 1984). These X-ray oscillations are consistent with emission from the hot inner regions of the accretion disc close to the surface of the primary star.

1.4.2 Quasi-Periodic Oscillations

Quasi-periodic oscillations (QPOs) are brightness oscillations that differ from DNOs. QPOs are observed during outburst, and generally have periods 2 to 3 times greater than DNOs. The longer periods of QPOs suggest that they are produced further out in the accretion disc, unlike DNOs that are produced in the regions near to the inner edge of the disc. The longest QPOs observed are comparable with the rotation period at the outer edge of the accretion disc.

The origin of QPOs is probably due to vertical or radial perturbations in the accretion disc, setting up oscillations at local Keplerian velocities (Kato 1978, Van Horn, Wesemael & Winget 1980, Cox 1981). Longer period QPOs coming from the outer edge of the accretion disc may be produced by inhomogeneities ('blobs') that orbit a few times at a local Keplerian velocity, before merging with the accretion disc. These 'blobs' could be created when the accretion stream impacts the accretion disc, or by tidal resonance with the secondary star.

1.4.3 OY Car

Vogt (1979a) discovered OY Car as a very short period ($P_{orb} = 5460$s) dwarf nova system. It was later sub-classified as an SU UMa type dwarf nova, due to its superoutburst nature (Vogt 1983). Normal outbursts in OY Car occur on time scales of 25 to 50 days with amplitudes of 3 mag and durations of about 3 days (Naylor et al. 1987). Superoutbursts in OY Car only occur about every 300 days, with amplitudes of 4 mag and durations of longer than 2 weeks (Naylor et al. 1987).

OY Car is a particularly interesting object in the X-rays where the boundary

layer of the system can be observed; previous observations of OY Car show that the X-ray flux changes during outburst phases (Naylor et al. 1988 and Pratt et al. 1999a). Observations have not yet been able to reveal the exact extent of the boundary layer in OY Car, as in the case of HT Cas, where the X-ray source has been constrained to $< 1.15R_1$ (Mukai et al. 1997).

The Boundary Layer of OY Car

In quiescence the boundary layer in a DN is thought to be an optically thin gas emitting hard X-rays (Section 1.1.5). Observations of OY Car in quiescence show that the X-ray emission is eclipsed (Pratt et al. 1999a, Pratt et al. 1999b). The X-ray eclipse width shows that the source of the X-ray emission is comparable to the size of the white dwarf and comes from a source close to the primary star, the boundary layer. By assuming that the X-ray flux was coming from the boundary layer, Pratt et al. (1999b) found that the X-ray luminosity of OY Car ($L_X \sim 10^{30}$erg/s) was an order of magnitude less than typical CV X-ray luminosities of 10^{31}erg/s quoted by Córdova & Mason (1984). Possible reasons for this are; 1. a rapidly rotating white dwarf, 2. a low rate of mass transfer through the boundary layer, or 3. absorption from either an interstellar or a local[5] medium.

During outburst the boundary layer in a DN is thought to be an optically thick gas emitting softer X-rays (Section 1.1.5). During the May 1985 superoutburst no X-ray eclipse was seen (Billington et al. 1996, Naylor et al. 1988, and Naylor et al. 1987). Ultraviolet spectra of OY Car during this superoutburst show asymmetric line emission, providing evidence of a wind-forming region (Naylor et al. 1988). Naylor et al. (1988) suggested that the X-ray source was an optically thin corona comparable to the size of the primary star Roche lobe, and not a direct observation of the white dwarf or boundary layer. These authors suggested that the X-ray region may be distributed through the ultraviolet winds in the system (as in radiatively

[5]This may be material in the outer edge of the accretion disc that is not connected with outburst.

driven shocks), as the X-ray emitting region (10^{6-7}K) and the ultraviolet emitting wind (2×10^4K) are very different, therefore creating physically distinct regions.

Periodic Oscillations in OY Car

Schoembs (1986) observed dwarf nova oscillations (DNOs) during the decline of the 1980 superoutburst of OY Car. These DNOs had periods between 19.44 and 27.99s decreasing in conjunction with a period luminosity relationship. These DNOs appeared during the deep descent from superoutburst with varying amplitude throughout the observation, typical of these types of oscillations. The eclipses of the DNO were delayed compared to the primary eclipse, implying that the source of the oscillations was near to the quiescent position of the bright spot.

Marsh & Horne (1998) observed a double-frequency DNO towards the end of a superoutburst in OY Car. The periods of both these oscillations are close to 18s, but are separated by 57.7 ± 0.5 cycles/day. The results of Marsh & Horne provide evidence that the region creating DNOs in OY Car is capable of creating two distinct oscillations at the same time. DNOs are thought to be formed in or near the white dwarf (Section 1.4.1); Marsh & Horne (1998) suggest that the frequency of a DNO can represent the orbital frequency of the inner accretion disc (Mauche 1996) indicating that the additional DNO may represent the rotation of the white dwarf.

Previous Mass Calculations for OY Car

Ritter (1980b) calculated the masses of the primary and secondary star in OY Car as $0.30 \pm 0.05 M_\odot$ and $0.12 \pm 0.02 M_\odot$ respectively using the optical photometric and spectroscopic observations of Vogt (1979b), with the assumption that the secondary is a main sequence Roche lobe filling star. By investigating the eclipse geometry of OY Car in quiescence and outburst, Vogt et al. (1981) calculated the masses of the primary and secondary star to be $0.95 \pm 0.15 M_\odot$ and $0.14 \pm 0.04 M_\odot$ respectively. The results of both authors are very different; this is due to the radial velocity of

the primary used by Ritter (1980b).

Cook (1985) used high-speed photometry of OY Car in quiescence to measure the mean eclipse light curves, and hence obtained the primary star mass. Cook (1985) found the lower limit for the mass of the primary to be $0.6 \pm 0.1 M_{\odot}$ in OY Car. Wood et al. (1989) also used high-speed photometry of OY Car to obtain a primary star mass of $0.685 \pm 0.011 M_{\odot}$, agreeing with the lower limit mass of Cook (1985). Wood et al. (1989) also found a secondary star mass of $0.070 \pm 0.002 M_{\odot}$.

An alternative result may be obtained using the ultraviolet or X-ray light curves to observe the eclipse of the white dwarf and material very close to the white dwarf.

The Picture of OY Car so Far

OY Car is a dwarf nova that undergoes outburst and superoutburst (Vogt 1983), with dwarf novae oscillations of 18 to 28s occurring during the decline of superoutburst (Schoembs 1986). In quiescence the X-ray source lies close to the primary star and is associated with the boundary layer (Pratt et al. 1999a, Pratt et al. 1999b), but in superoutburst the X-ray source becomes an optically thin extended corona (Billington et al. 1996, Naylor et al. 1988, Naylor et al. 1987).

To improve the picture of OY Car I have undertaken the following in this thesis:-

- In Chapter 5 I have used high quality light curves from *XMM-Newton* to pinpoint the source of X-ray emission and confine the boundary layer in quiescence.

- Also in Chapter 5 I used the eclipse timings of the *XMM-Newton* data to confine the mass of the component stars in OY Car.

Chapter 2

RW Tri in the Ultraviolet

The spectra of RW Tri in the ultraviolet (UV) has been studied since 1985. Observations of broad emission lines (Córdova & Mason, 1985a) have been modelled, showing that the emission line profiles are consistent with extended bipolar winds emanating from the accretion disc (Drew 1987, Vitello & Shlosman 1993). Narrow absorption lines have also been observed by Córdova & Mason (1985a) and Mason et al. (1997). To date, there have been no quantitative investigations to pinpoint where in the binary system these narrow absorption features are being produced.

Using the UV HST data of Mason et al. (1997), I investigate the possible position of the material producing these narrow absorption features. The observational data indicates that the absorbing material must be located at a distance from the white dwarf, which is less than the outer radius of the accretion disc. The absorbing region is also constrained by the width of the observed absorption features. By considering the inclination angle of the system, the physical nature of the UV continuum, and a cylindrical structure for the absorption material, I produce a model to simulate an absorption profile and fit this to the observed data. The position of this cylindrical structure is constrained by the effective extent of the UV continuum and the outer radius of the accretion disc; its front half is projected against the UV continuum, thereby producing a narrow line because the major component of its velocity is transverse to the line of sight of the observer.

2.1 Hubble Space Telescope Observations

RW Tri was observed by the *Goddard High Resolution Spectrograph* (GHRS) on the *Hubble Space Telescope* (HST) in January 1997 (see Table 2.1 for details). The RAPID (rapid readout) mode was used to take a continuous sequence of spectra with a 5s integration time. The G140L grating on 'Side A' of the GHRS was used to provided an optimal combination of wavelength coverage, signal to noise, and spectral resolution ($\Delta\lambda \sim 0.6$Å). [G160M, the grating on 'Side B' would have offered a better spectral resolution ($\Delta\lambda \sim 0.07$Å) but with reduced wavelength coverage and signal to noise].

Observational Date	UT start	Phase Coverage	Exposure Time (s)	Wavelength Range (Å)
22/01/97	16:44:40	0.811-0.850	760	1149-1435
22/01/97	17:47:58	1.001-1.134	2675	1149-1435
22/01/97	07:12:44	1.409-1.448	770	1149-1435
23/01/97	08:16:02	0.599-0.733	2685	1149-1435
23/01/97	09:52:26	0.888-1.022	2690	1149-1435
23/01/97	11:28:56	1.177-1.311	2690	1149-1435
25/01/97	17:05:56	0.806-0.844	760	1377-1663
25/01/97	18:09:14	0.996-1.129	2675	1377-1663
26/01/97	07:34:02	1.404-1.443	770	1377-1663
26/01/97	08:37:14	0.594-0.728	2690	1377-1663
26/01/97	10:13:44	0.882-1.520	2690	1377-1663
26/01/97	11:50:14	1.172-1.300	2690	1377-1663

Table 2.1: RW Tri observations in the UV.

Two specific wave bands were observed which I term the SHORT wavelength

band from 1149Å to 1435Å, and the LONG wavelength band from 1377Å to 1663Å. The light curves of the LONG and SHORT wavelength bands can be seen in Figure 2.1. This provided an overall combined wavelength range of 1149Å to 1663Å. The overlap, which covered $\sim$ 60Å, included the Si IV emission line doublet. Mason et al. (1997) calibrated the flux and wavelength using the standard Space Telescope Science Institute procedures.

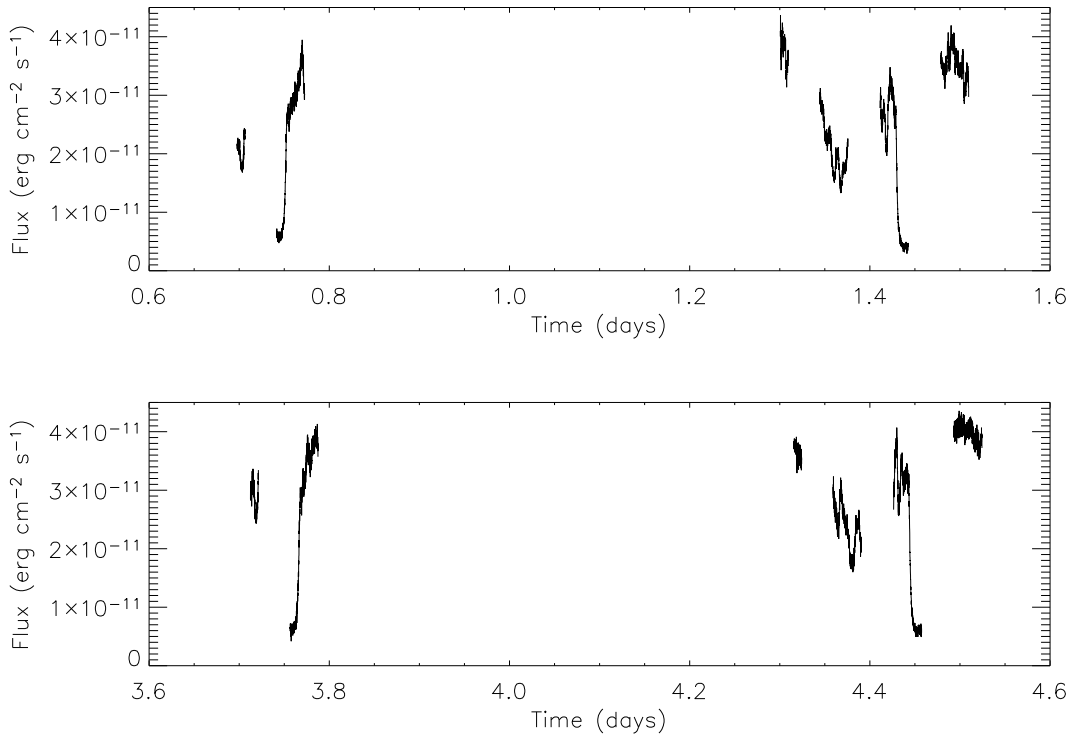

Figure 2.1: Light curves of the HST data. Top: SHORT wavelength band light curve (1149Å - 1435Å). Bottom: LONG wavelength band light curve (1377Å - 1663Å).

2.1.1 Ultraviolet Light Curve

Figure 2.2 shows the folded light curves of RW Tri, defining phase 0.0 at mid eclipse. The eclipse FWHM, $\Delta\Phi$, was measured to be 0.077 ± 0.022 orbital phase from this data. This agrees with the values of Frank et al. (1987) (0.078 ± 0.002 orbital phase) and Córdova & Mason (1985a) ($\sim$ 0.08 orbital phase). The SHORT wavelength band

light curve lags the LONG wavelength band by 0.001 orbital phase, but this lag is not significant within the ephemeris error of 0.022. The flux at eclipse minimum does vary, especially in the SHORT wavelength region. This can be attributed to changes in the overall flux of the system from cycle-to-cycle, noting that variations are possible between cycles of the system. In this case the ingress and egress of the eclipse profile are observed over two different cycles because of the disruptions of the HST visibility interval over each Earth orbit.

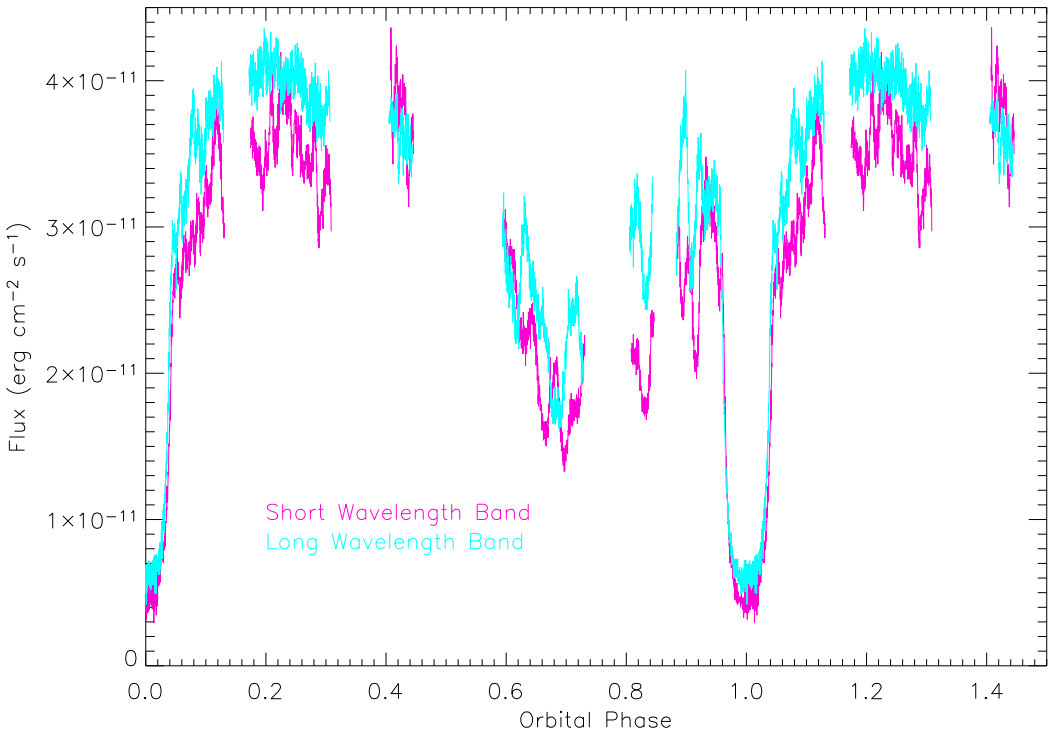

Figure 2.2: The folded light curves of the LONG (cyan) and SHORT (magenta) wavelength bands, showing a grazing eclipse (Chapter 1, Section 1.2.1).

A dip in the light curve can be seen with a minimum at phase ~ 0.7 of the orbital cycle (Figure 2.2). This was reported by Mason et al. (1997) who suggested that it was caused by cooler vertically extended material in the outer regions of the accretion disc, eclipsing the hot inner regions and the UV continuum. The dip has also been observed in some low mass X-ray binary systems (LMXBs) (e.g. Smale

et al. 1988). Mason et al. (1995) observed a similar dip in the light curves of UX UMa.

2.1.2 Ultraviolet Spectra

The average spectrum of RW Tri for all of the UV observations can be seen in Figure 2.3. The emission and absorption features labelled in Figure 2.3 are summarised in Table 2.2. Column 1 and 2 list the observed wavelength and line species, column 3 indicates whether the line is observed in emission or absorption, column 4 indicates the region of RW Tri in which the lines may be produced, and column 5 lists references.

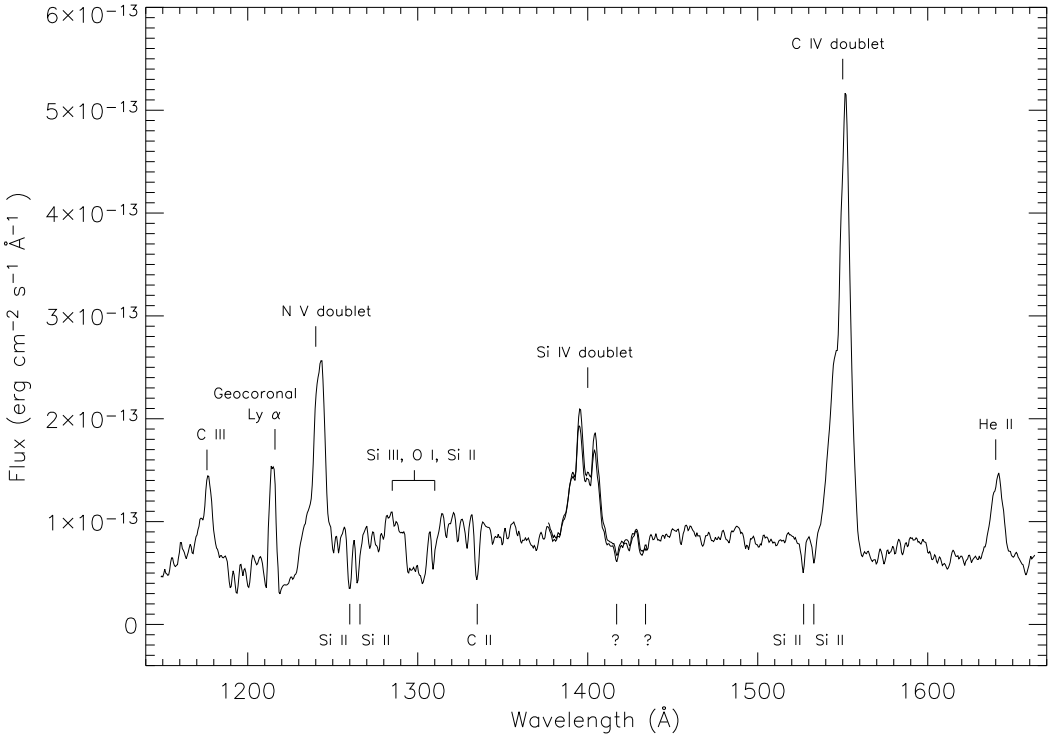

Figure 2.3: Plot of the average UV spectrum of RW Tri using HST observations.

Saturated Geocoronal Ly α is observed at λ1216Å. This line varies throughout

Wavelength (Å)	Line Species	Absorption (A)/ Emission (E)	Binary Region	Reference
1176	C III	E throughout	Extended wind	1, 3, 6
1216	Ly α	E throughout	Geocoronal	1
1239, 1243	N V doublet	E throughout	Extended wind	1, 3, 6
1260	Si II	A out-of-eclipse	Accretion disc ?	1, 2, 3, 6
1260	Si II	E in eclipse	Chromosphere ?	1, 2, 3, 6
1265	Si II	A out-of-eclipse	Accretion disc ?	2, 3, 6
1265	Si II	E in eclipse	Chromosphere ?	2, 3, 6
1300	Si III, O I, SiII	A out-of-eclipse	Accretion disc ?	2, 3, 6
1300	Si III, O I, SiII	E in eclipse	Chromosphere ?	2, 3, 6
1335	C II	A out-of-eclipse	Accretion disc ?	3, 4, 6
1335	C II	E in eclipse	Chromosphere ?	3, 4, 6
1394, 1403	Si IV doublet	E throughout	Extended wind	1, 2, 3, 6
1417	?	A out-of-eclipse	Accretion disc ?	-
1434	?	A out-of-eclipse	Accretion disc ?	-
1527	Si II	A out-of-eclipse	Accretion disc ?	3, 4, 5, 6
1527	Si II	E in eclipse	Chromosphere ?	3, 4, 5, 6
1533	Si II	A out-of-eclipse	Accretion disc ?	3, 6
1533	Si II	E in eclipse	Chromosphere ?	3, 6
1548, 1551	C IV doublet	E throughout	Extended wind	1, 2, 3, 6
1640	He II	E throughout	Extended wind	1, 2, 3, 6

Table 2.2: Spectral features of RW Tri in the UV. References: 1. Córdova & Mason 1985a, 2. Mason et al. 1997, 3. van Hoof 2003, 4. St-Louis et al. 1993, 5. Griesmann & Kling et al. 2000, 6. Pagano et al. 2000.

the observations due to the different solar illumination conditions at different observation times. The broad emission features C III, N V, Si IV, C IV and He II are observed throughout the orbital cycle of RW Tri, and are produced in extended wind regions (Córdova & Mason 1985a). These features have been extensively modelled (Chapter 1, Section 1.3.1) showing that the emission line profiles are consistent with bipolar winds emanating from the accretion disc (Drew 1997, Vitello & Shlosman 1993).

The narrow absorption features labelled in Figure 2.3 are observed throughout the orbital cycle except during eclipse. During eclipse these features are either observed in emission, or not at all in the case of lines 1417Å and 1434Å. There is also a broad absorption feature at λ1300Å due to a combination of Si III at λ1301Å, O I at λ1302Å, and SI II at λ1303Å; this feature is also observed in emission during eclipse. This can be more clearly seen in Figure 2.4 which plots eclipse and out-of-eclipse data for the SHORT wavelength band.

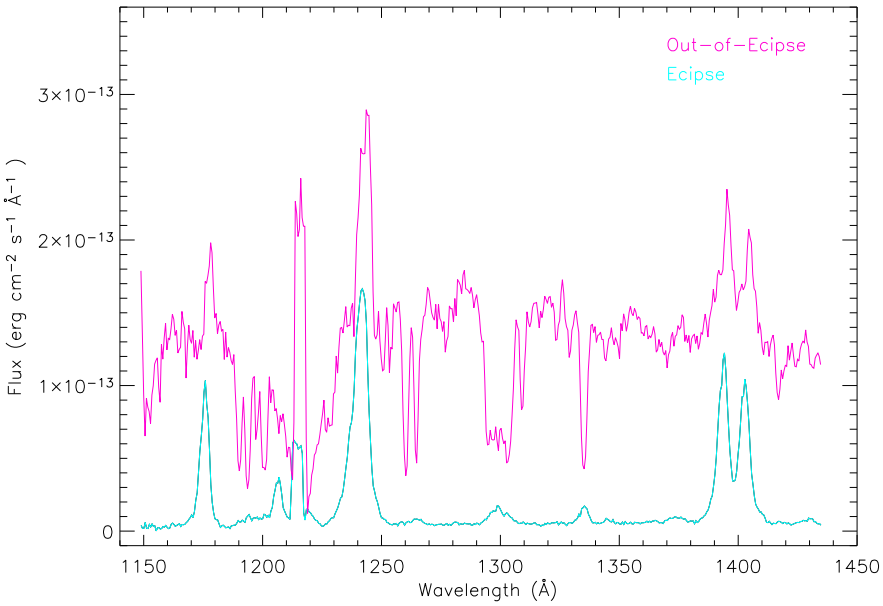

Figure 2.4: Narrow absorption/emission features in the SHORT wavelength band. Note the geocoronal Lyα line has different strengths in the out-of-eclipse and eclipse spectra due to the different solar illumination conditions at different observation times.

Figure 2.5 compares the full width half maximum (FWHM) of the eclipse and out-of-eclipse feature observed at λ1335Å. Both features have had the average continuum subtracted using values of $1.4 \pm 0.12 \times 10^{-13}$ erg cm^{-2} s^{-1} Å^{-1} and $5.2 \pm 1.4 \times 10^{-15}$ erg cm^{-2} s^{-1} Å^{-1} (Figure 2.3), for the absorption and emission features respectively. The spectra have also been normalised and the absorption feature (out-of-eclipse data) has been inverted so that a clear comparison can be seen. The FWHM of the absorption and emission features at λ1335Å were measured as 2.9 ± 0.2Å and 4.2 ± 0.2Å respectively. Note that the emission and absorption features appear to have the same width blueward of the line centre at 1335Å; this is due to a dip in the emission feature at 1334Å that may be due to absorption. Figure 2.5 shows that the emission feature is broader than the absorption feature, indicating that the emission feature is emanating from a region with a larger velocity spread than the absorption feature.

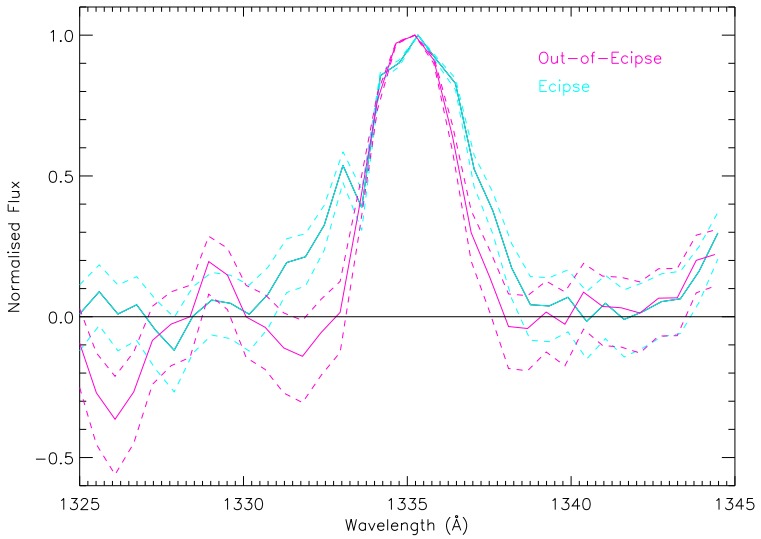

Figure 2.5: Comparison of the absorption/emission feature at 1335Å. The solid magenta line represents the inverted normalised absorption feature with a subtracted continuum of 1.4×10^{-13} erg cm^{-2} s^{-1} Å^{-1}; the dashed magenta lines represent subtracted continua of $1.4 \pm 0.12 \times 10^{-13}$ erg cm^{-2} s^{-1} Å^{-1}. The solid cyan line represents the normalised emission feature with a subtracted continuum of 5.2×10^{-15} erg cm^{-2} s^{-1} Å^{-1}; the dashed cyan lines represent subtracted continua of $5.2 \pm 1.4 \times 10^{-15}$ erg cm^{-2} s^{-1} Å^{-1}.

It is clear from Figure 2.4 that the absorption source is much stronger than the emission source, therefore the emission source is only observed when the absorption source is occulted by the secondary star. This means that the material producing the narrow emission lines either has some height above the orbital plane of the system, or is situated in the outer regions of the system. This material could therefore be part of an accretion disc chromosphere (as suggested in Table 2.2), or part of the wind forming region.

Also, the narrow absorption features are not present at orbital phase 0.7, where the minimum of the dip in the light curve occurs (Section 2.1.1). This can be more clearly seen in Figure 2.6, where spectra taken at orbital phase 0.4 and 0.7 are compared. The spectrum at orbital phase 0.4 shows the presence of the narrow absorption features, but at orbital phase 0.7 where the hot inner parts of the accretion disc are occulted and hence the UV continuum level of the spectrum is reduced, the narrow absorption features are not observed. The vertically extended material in the outer regions of the accretion disc must therefore be occulting the material producing the narrow absorption features as well as the UV continuum.

Mason (1999) showed that the narrow absorption features in the UV spectrum follow the expected orbital motions of the primary star, and hence may define the radial velocity amplitude (K_1) of the primary. Mason (1999) performed cross-correlation on the out-of-eclipse spectra to calculate K_1. The wavelength region 1250Å - 1355Å was used due to the presence of strong absorption features and the lack of wind emission lines. A template of the absorption features was created using a Gaussian profile and a flat continuum. The template was then cross-correlated with the spectrum producing a preliminary radial velocity curve. This velocity was then used to subtract orbital variations from all the spectra to produce a mean spectrum, which was used as a second template. The second template was then cross-correlated with the original data. The measured radial velocity amplitude was 296 ± 5km/s (used in Chapter 4).

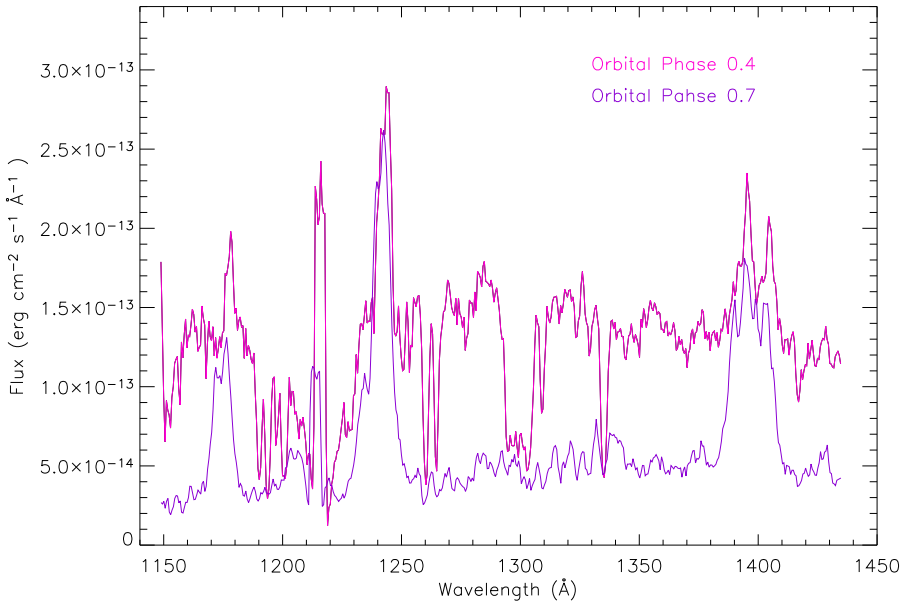

Figure 2.6: Short wavelength band at orbital phases 0.4 and 0.7. The narrow absorption features present in the spectra at orbital phase 0.4, are occulted by the vertically extended outer edge of the accretion disc (Mason et al. 1997) at orbital phase 0.7.

The material producing the narrow absorption features is occulted by the vertically extended outer regions of the disc and is therefore confined by the radius of the accretion disc. The absorbing region must also lie between the secondary star and the UV continuum along the observers' line of sight because it absorbs the UV continuum radiation.

2.2 The Ultraviolet Continuum

To investigate the size of the region emitting the UV continuum, a continuum light curve was extracted from the line-free wavelength region 1340 - 1380Å (Figure 2.7). This light curve exhibits a very steep and deep UV eclipse, decreasing to zero flux at eclipse minimum. The rounded eclipse profile suggests the presence of a steady-state ($T \sim R^{-3/4}$) accretion disc in the UV. Therefore, a model eclipse profile was fitted to the observed data using a primary star and steady state accretion disc. The

following sections describe the equations used to model a steady state accretion disc and primary star, and the model fitting to the data.

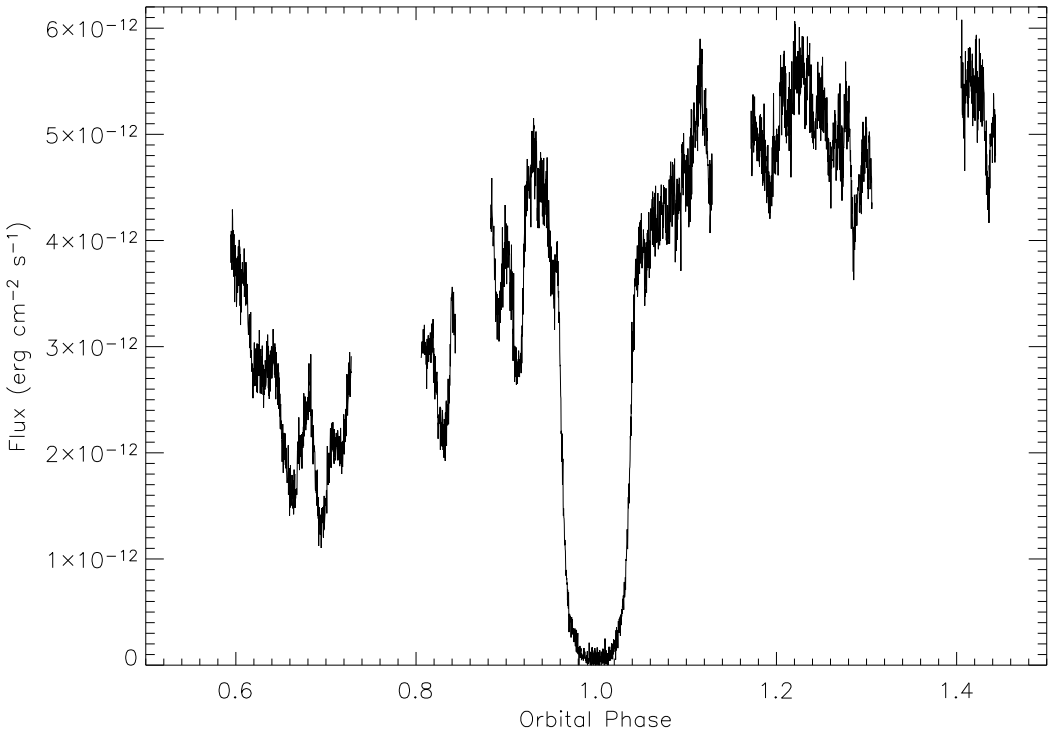

Figure 2.7: Observed continuum light curve in the line-free wavelength region 1340 - 1380Å.

2.2.1 Steady State Accretion Disc

A steady-state accretion disc is described by the equation

$$T(R) = \left\{ \frac{3GM_1\dot{M}}{8\pi\sigma R^3} \left[1 - \left(\frac{R_1}{R} \right)^{1/2} \right] \right\}^{1/4}, \tag{2.1}$$

where $T(R)$ is the temperature of the disc at disc radius R, G is the gravitational constant (6.673×10^{-11} Nm^{2}kg^{-2}), M_1 is the mass of the primary star, $\dot{M}$ is the accretion rate, σ is Stefan's constant (5.670×10^{-8} Wm^{-2}K^4), and R_1 is the radius of the primary star (Frank, King & Raine 1992).

For an observer at a distance, D, and inclination angle, i, from the system, the flux at wavelength λ is

$$F_\lambda = \frac{2\pi \cos i}{D^2} \int_{R_1}^{R_{out}} B_\lambda[T(R)] R dR, \tag{2.2}$$

where R_{out} is the outer radius of the accretion disc and $B_\lambda[T(R)]$ is the Planck function for black body radiation given by

$$B_\lambda[T(R)] = \frac{2hc^2}{\lambda^5} \frac{1}{e^{\left(\frac{hc}{k\lambda T(R)}\right)} - 1}, \tag{2.3}$$

where h is Planck's constant (6.626×10^{-34}J.s), c is the speed of light (2.99×10^8m.s^{-1}) , and k is Boltzmann's constant (1.381×10^{-23}JK^{-1}) (Frank, King and Raine 1992).

2.2.2 Primary Star

The primary star will also contribute to the total continuum UV flux. The surface flux of the star F_{surf} is given by

$$F_{surf} = \frac{L}{4\pi R_1^2} = f_{obs} \left(\frac{D}{R_1}\right)^2, \tag{2.4}$$

where the total luminosity of the star ($L = f_{obs} 4\pi D^2$) is given by the observed flux (f_{obs}) multiplied by the surface area of a sphere of radius D, where D is the distance of the star from the observer. Assuming the primary star is a blackbody, then

$$F_{surf} = \sigma T_1^2, \tag{2.5}$$

where T_1 is the temperature of the primary star. Therefore the observed flux of the primary star is

$$f_{obs} = \sigma T_1^4 \left(\frac{R_1}{D}\right)^2. \tag{2.6}$$

2.2.3 Ultraviolet Continuum Model Fits

I have simulated the binary system in IDL using the inclination angle (i), primary and secondary star radius (R_1 and R_2 respectively), and binary separation (a); these parameters were derived from

- FWHM of eclipse ($\Delta\Phi$ - Section 2.1.1)
- Relationship between eclipse width ($\Delta\Phi$), inclination angle (i) and mass ratio (q) (Chapter 4, Section 4.1.1)
- Best measured results of radial velocity amplitude (K_2) and the equatorial velocity ($V_{rot} \sin i$) of the secondary star (Chapter 3, Section 3.3)

and

$$\frac{R_2}{a} = \left((\pi\Delta\Phi)^2 + \cos^2 i\right)^{1/2} \tag{2.7}$$

Ritter (1980a). The calculations for the component star radii and separation are summarized in Table 2.3, along with other parameters required to calculate the UV continuum model.

The simulation followed the binary system through phase 0.9 to 1.1, producing a light curve of a single temperature accretion disc annulus. The simulation was run for 100 disc annuli with radii between R_1 and R_{out} (Table 2.3). The simulation was also run to obtain a primary star eclipsing light curve. FORTRAN code was then used to calculate the flux at each accretion disc annulus using Equations 2.1 and 2.2. The annuli fluxes were used to scale the corresponding light curves. These light curves, along with the primary star light curve, were then summed to produce the total UV continuum light curve.

To fit the model light curve to the observed light curve, the UV continuum level was set. The light curve in Figure 2.7 exhibits a broad dip in the UV continuum centred on orbital phase ~ 0.7, where the outer regions of the accretion disk eclipse the inner regions of the disc (Section 2.1.1, Mason et al. 1997). Between orbital phases 0.955 and 1.045 the outer parts of the accretion disc that are eclipsed by the extended material are also largely eclipsed by the secondary star as seen in

Parameter	Symbol	Value	Reference
Orbital period (s)	P_{orb}	20040	Table 1.1
Radial velocity amplitude of the secondary star (km/s)	K_2	221	Chapter 3
Equatorial rotational velocity of the secondary star (km/s)	$V_{rot} \sin i$	120	Chapter 3
Eclipse FWHM (orbital phase)	$\Delta\Phi$	0.077	Section 2.1.1
Inclination angle (^{o})	i	76.86	Figure 4.3 and Equation 2.7
Mass ratio	q	0.64	Figure 4.3
Primary star mass ($M_\odot$)	M_1	0.75	Equation 1.19
Secondary star mass ($M_\odot$)	M_2	0.48	Equation 1.15
Binary separation ($R_\odot$)	a	1.701	Equation 1.1
Primary star radius ($R_\odot$)	R_1	0.011	Equation 5.9
Secondary star radius ($R_\odot$)	R_2	0.565	Equation 2.7
Accretion disc outer radius ($R_\odot$)	R_{out}	0.402	Smak (1995)
Distance to binary system (pc)	D	341	McArthur et al. (1999)
Primary star temperature(K)	T_1	20800	Sion (1999)
Accretion rate ($M_\odot \mathrm{yr}^{-1}$)	$\dot{M}$	4×10^{-8}	Best-Fit

Table 2.3: All the parameters needed to produce the model continuum fit.

Figure 2.8. Therefore the eclipse profile between these phases has an equivalent 'uneclipsed' level equal to the maximum flux in the light curve i.e. the effect of the outer disc occultation can be ignored. Hence, the model eclipse profile was fitted to the observed data between the orbital phases of 0.955 and 1.045 assuming a

maximum UV continuum flux of $5.6 \pm 0.3 \times 10^{-12}$erg cm^{-2} s^{-}1 taken from Figure 2.7.

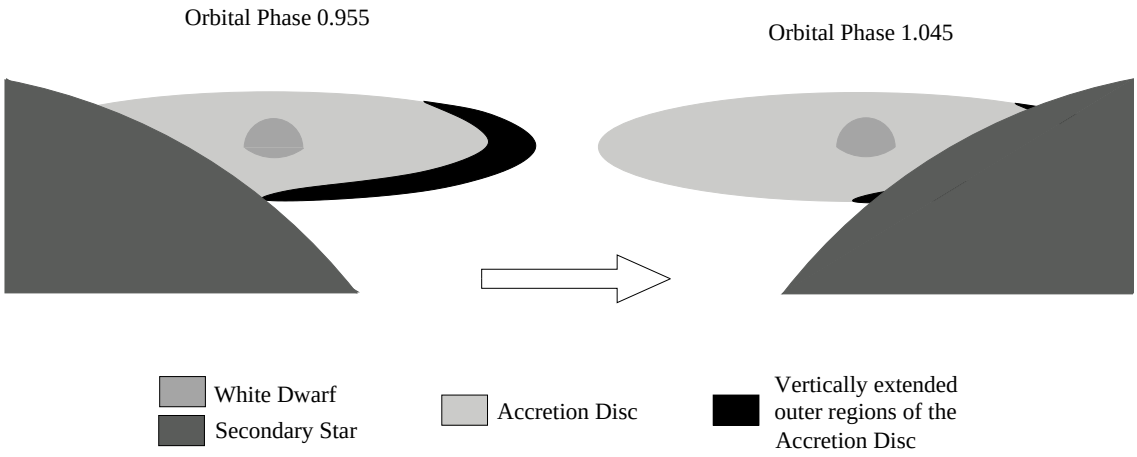

Figure 2.8: Sketch to show the eclipse profile between orbital phases 0.955 and 1.045 is mostly due to the hotter inner UV emitting disc regions and the primary star.

Figure 2.9 shows the final fit of the model steady-state blackbody accretion disc light curve (solid red line) to the observed light curve (∗). The solid blue line represents the eclipse of the primary star alone. Figure 2.9 shows that the eclipse profile between orbital phases 0.955 and 1.045 is not significantly affected by uncertainties in the UV continuum flux with range $5.6 \pm 0.3 \times 10^{-12}$ erg cm^{-2} s^{-1} (dotted red lines).

The $\dot{M}$ that produced the best-fit continuum light curve was $4 \times 10^{-8} M_{\odot}$yr^{-1}. This high accretion rate agrees with previous observations of Horne & Stiening (1985), who obtained a mass accretion rate of $\dot{M} = 10^{-7.9 \pm 0.4} M_{\odot}$yr^{-1} using eclipse mapping. These authors also demonstrated that the radial temperature dependence of the accretion disc was consistent with steady-state accretion.

Figure 2.9 shows that the UV RW Tri data can be fitted by a steady-state blackbody accretion disc. The model also provides an indication of where the ingress and egress of eclipse starts and ends; leading to $\Delta w_d = 0.060 \pm 0.002$ orbital phase for the time taken for the primary star to be fully eclipsed (Chapter 1, Section 1.2.1).

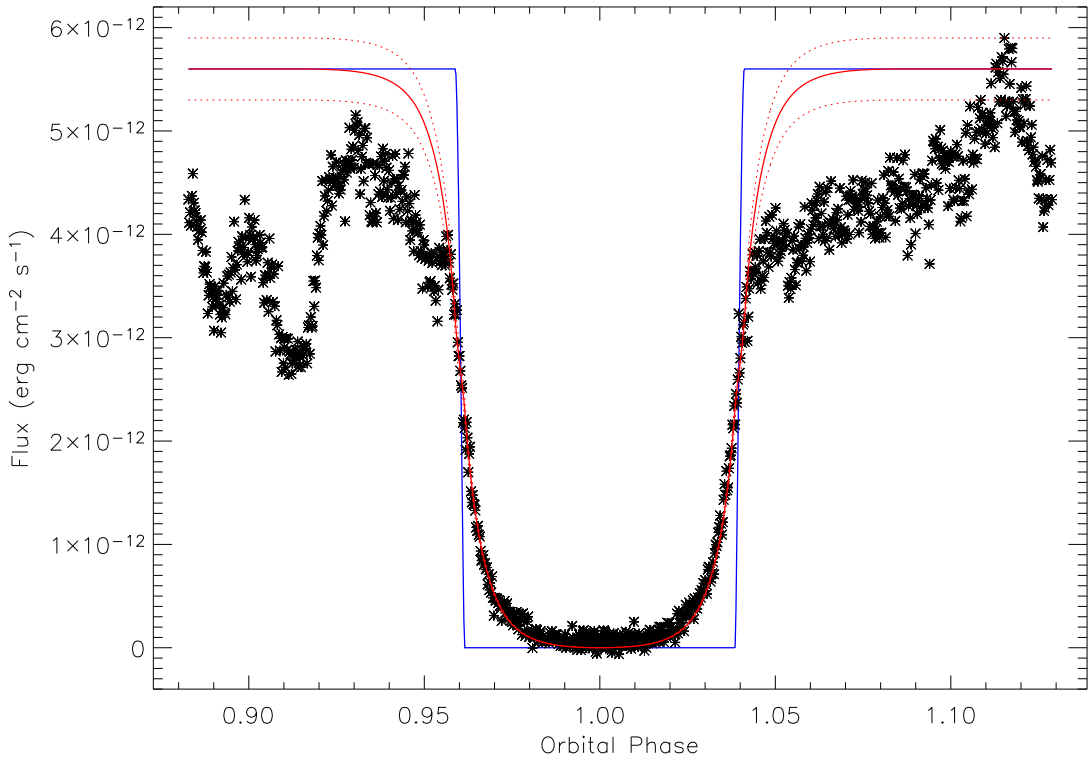

Figure 2.9: Observed continuum light curve (∗) fitted with a model steady-state blackbody accretion disc light curve (solid red line) in the line-free wavelength region 1340 - 1380Å. The dotted red lines represent a fit to the continuum of $5.6 \pm 0.3 \times 10^{-12}$ erg cm^{-2} s^{-1}. The solid blue line represents the eclipse of the primary star only.

The effective extent of the UV continuum (1360Å) was then calculated using Equation 2.7 and

$$\frac{R_{UV}}{a} = \pi^2 \Delta\Phi \Delta w_d \left(\frac{a}{R_2}\right) = 0.137. \tag{2.8}$$

(Ritter 1980a). Substituting $a = 1.701 R_\odot$ into Equation 2.8 lead to a $R_{UV} = 0.234 R_\odot$, which is $\sim$ 60% of the accretion disc (if R_{out} is $0.402 R_\odot$). Using the steady-state disc model (Equation 2.1), the temperature at radius R_{UV} is 18100K. Re-running the simulation with $R_{out} = 0.234 R_\odot$ and an $\dot{M}$ of $4 \times 10^{-8} M_\odot \mathrm{yr}^{-1}$, lead to the same results as seen in Figure 2.9.

2.3 Model Set-Up and Assumptions

Observations of RW Tri (Mason et al. 1997) show that the material producing the absorption features lies within the extent of the accretion disc (Section 2.1.2), but the absorption lines are narrow. A possible origin for the absorbing material is a ring-like structure around the UV continuum that lies within the outer radius of the accretion disc as seen in Figure 2.10. In this geometric set up, the absorption region is situated in the front half of the ring-like structure where the material is projected against the UV continuum. This absorption region has the major component of its velocity transverse to the observers' line of sight, which should therefore lead to a relatively narrow absorption line.

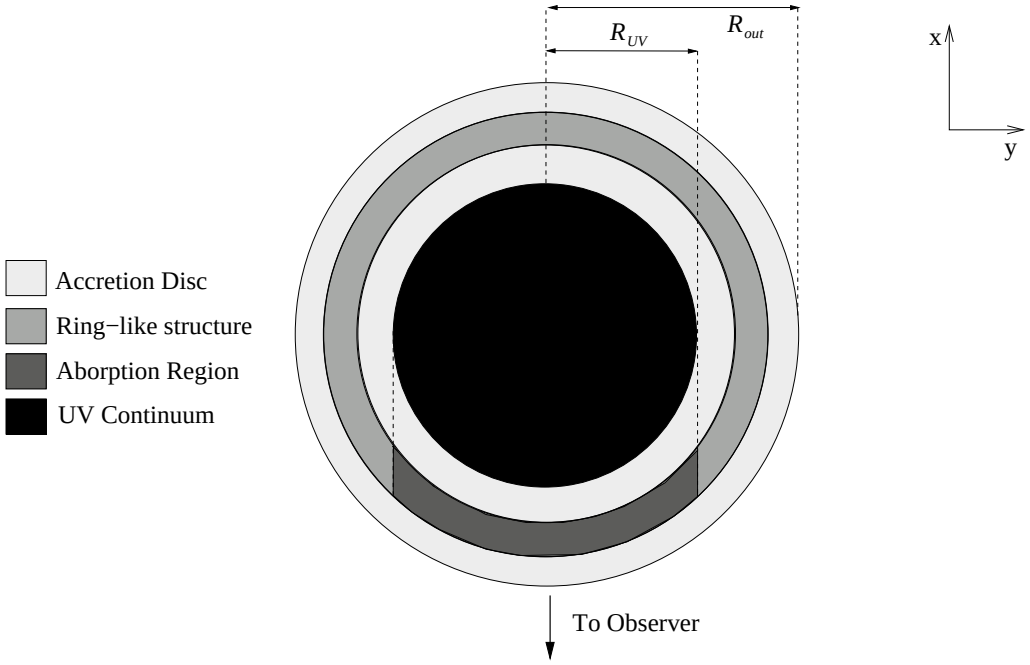

Figure 2.10: Sketch of the position of the absorbing region within the coordinate system of Figure 2.11, in the x-y plane. R_{UV} is the effective radial extent of the UV continuum, and R_{out} is the outer radius of the accretion disc. The ring-like structure producing the absorption regions lies between R_{UV} and R_{out}.

A simulation of the UV continuum and absorbing material in RW Tri was produced to model the observed absorption feature at λ1335Å (C II - Figure 2.3). The

λ1335Å feature was chosen because it was the least complicated feature observed. An orbital phase of close to 0.5 was considered, therefore eliminating the added complication of the eclipse of the UV continuum and absorbing material due to the secondary star (modelling the observed line profiles at different orbital phases is discussed further in Section 2.8).

In the following sections I define the coordinate system of the model, the assumptions made in the model, the set-up of the model, and the equations used to produce the model.

2.3.1 System Geometry

Figure 2.11 illustrates the coordinate system of the model. The primary and secondary stars rotate around the centre of mass of the binary system.

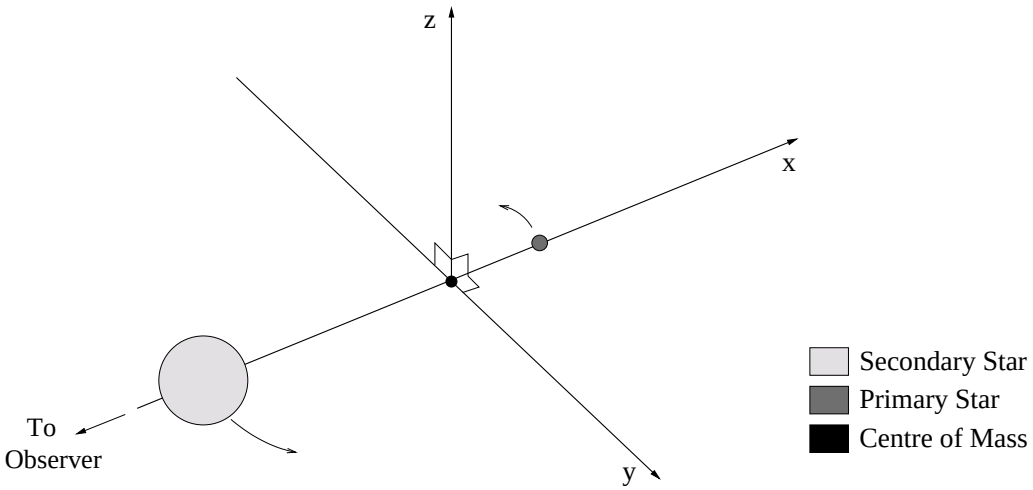

Figure 2.11: Coordinate system of the model.

2.3.2 Assumptions Made in the Model

Why Consider Only the Absorption Feature?

The emission feature has a low intensity and can only be seen when the UV continuum is eclipsed (Section 2.1.2). From Figure 2.4 the emission feature at λ1335Å has a line flux of $4.8 \pm 0.66 \times 10^{-14}$ erg cm^{-2}s^{-1}Å^{-1} which is small compared to the absorption feature line flux of $2.6 \pm 0.63 \times 10^{-13}$ erg cm^{-2}s^{-1}Å^{-1}. Therefore the emission feature is not considered in this simple absorption model.

The UV Continuum

The UV continuum is produced from the primary star and the accretion disc (Section 2.2), therefore the UV continuum is assumed to be flat, and lies in the orbital plane (x-y plane - Figure 2.11) of the system (Chapter 1, Section 1.1.4). The temperature of the accretion disc in RW Tri varies radially (Equation 2.1), therefore the intensity of the UV continuum will vary with radius from R_1 to R_{UV}; where the effective extent of the UV continuum was calculated to be $0.234R_\odot$ in Section 2.2.3.

The Absorbing Material

The absorption material lies within the orbit of the secondary star, inside the outer radius of the accretion disc. This is because the observed absorption features are not seen at orbital phases around 0.0 and 0.7 (Figures 2.4 and 2.6) as they are eclipsed by the secondary star and the vertically extended outer regions of the accretion disc. To produce a narrow feature the absorption material must also lie outside the radius of the UV continuum, so that the major component of the velocity in the absorbing region is transverse to the observers' line of sight (Figure 2.10).

The absorbing material is assumed to lie in a ring-like structure centered on the primary star (similarly to the accretion disc), and will therefore have Keplerian motion due to the mechanics of the binary system (Chapter 1, Sections 1.1.1 and 1.1.4) as sketched in Figure 2.12.

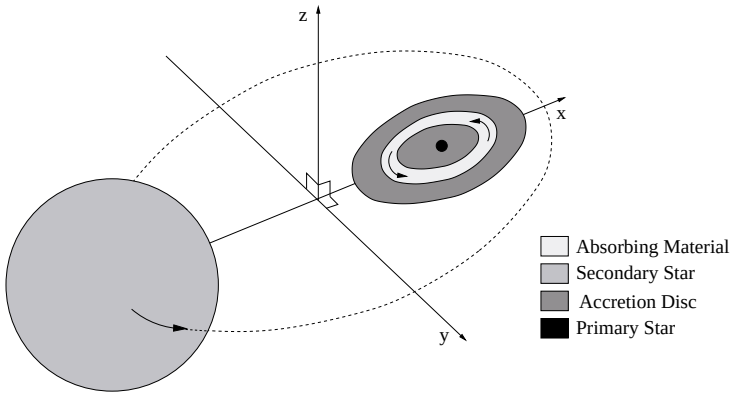

Figure 2.12: Sketch of the Keplerian motion of the absorbing material within the coordinate system of Figure 2.11. The absorbing material is centred on the primary star, and lies within the orbit of the secondary star.

RW Tri has an inclination angle of 76.86^o, so for a ring-like structure of material to absorb radiation form the UV continuum, it must have some height above the orbital plane (Figure 2.13 - top). Therefore the absorbing material has a cylindrical structure centred on the primary star (Figure 2.13 - bottom right). The modelled absorbing material was assumed to have sufficient height above the orbital plane for all light sourced inside or behind the absorbing material, to pass through the full radial extent of the absorbing material. A small "arc" of the cylinder was actually modelled, because the system was considered at only one orbital phase.

Main Assumptions

The main assumptions made in order to model the effects of the absorbing material on the UV continuum are as follows.

1. The UV continuum is a combination of the primary star and accretion disc with a effective radial extent of $R_{UV} = 0.234 R_{\odot}$.
2. The UV continuum temperature and therefore intensity varies radially.
3. The absorbing material lies within the orbit of the secondary star inside the

outer radius of the accretion disc (R_{out}).

4. The absorbing material lies outside the effective radial extent of the UV continuum (R_{UV}).
5. The absorbing material has Keplerian motion centred on the primary star.
6. The absorbing material has a height above the orbital plane, and therefore a cylindrical structure (although an "arc" of the cylinder is considered for only one phase).

Illustration of the Model

Figure 2.13 illustrates the layout of the UV continuum, accretion disc and absorbing material. The top illustration shows a 'side-on' view of the system marking View A and View B, which are a 'birds-eye' view and an 'observers' view of the system respectively. These two views are seen at the bottom left and right of Figure 2.13. The UV continuum has a radius R_{UV}, the accretion disc has an outer radius R_{out}, and the absorbing material has an inner radius of R and a radial thickness of T. T_1 and T_2 indicate the variation in temperature of the UV continuum.

2.3.3 Set-Up of the Model

The flat two-dimensional UV continuum was split up into annuli of equal thickness (δr), each annulus was then split up into segments of equal length (δl) (Section 2.4.1). The light path of each segment was traced from the segment position in the UV continuum through the absorbing material along the observers' line of sight at an inclination angle (i) to the orbital plane of the system. As the light path from each segment passed through the cylindrical absorbing material, it was split up into equally sized elements (δs) (Section 2.4.4). The wavelength contribution (λ_e), and the intensity leaving each element (I_e) is calculated, and summed to produce a model of the observed absorption profile.

The wavelength of each element (λ_e) was calculated using the radial distance of

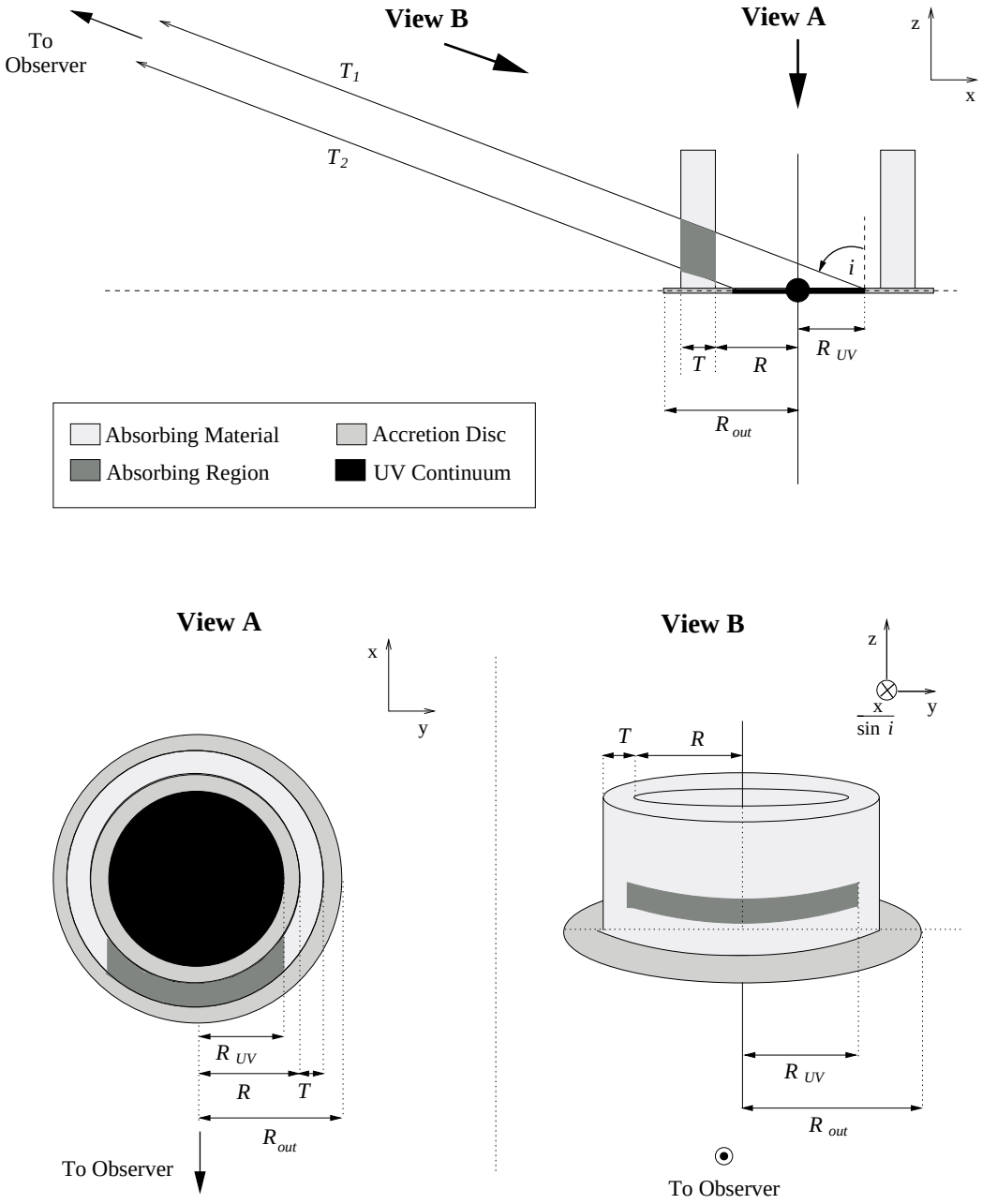

Figure 2.13: Three sketches illustrating the layout of the UV continuum, accretion disc and absorbing material in different planes defined by Figure 2.11. Top: A view in the z-x plane, where the height of the absorption material can be seen. View A and B are also marked on this view, and are illustrated in the bottom left and right panels of this figure respectively. Bottom left: View A - a view in the x-y plane, where the ring-like structure of the absorbing material can be seen. Bottom right: View B - a view in the z-y plane looking at the system along the inclination angle, i, where the cylindrical structure of the absorbing material can be seen.

the element in the orbital plane (r_e), and the Keplerian velocity and Doppler shift equation (Section 2.4.5). The relative intensity of each element (I_e) was calculated by considering the intensity of the segment producing the light path (I_s), and the path length of light from the UV continuum through the absorbing material in the direction of the observer (S) (Section 2.4.6). The intensity of the segment was calculated using the accretion disc temperature-radius relationship (Equation 2.1) and the wavelength contribution of the segment (λ) (Section 2.4.2 and Section 2.4.3).

2.4 Mathematics of the Model

2.4.1 Splitting the UV Continuum into Segments

The UV continuum is split up into n annuli, and each annulus is split up into N segments of equal length, δl. The radial distance between the centre of the UV continuum and each segment (r) is given by

$$r = (m - 0.5)\delta r = (m - 0.5)\frac{R_{UV}}{n}, \tag{2.9}$$

where m is $1 \rightarrow n$, δr is the thickness of a segment, R_{UV} is the radial extent of the UV continuum, and 0.5 is used to calculate r to the centre of the annulus. The UV continuum is taken form the centre of the primary star (where R_1 is the radius of the primary star), to R_{UV} as in Section 2.2.3.

The position of each segment in the UV continuum is defined by the angle θ between the line of sight of the observer and the radial distance r, and is given by

$$\theta = \frac{2\pi(j - 0.5)}{N} = \frac{(j - 0.5)\delta l}{r}, \tag{2.10}$$

where 0.5 is used to calculate θ from the centre of the segment, and j is $1 \rightarrow N$, where N is given by

$$N = \frac{2\pi r}{\delta l}. \tag{2.11}$$

These dimensions can be more clearly seen in Figure 2.14.

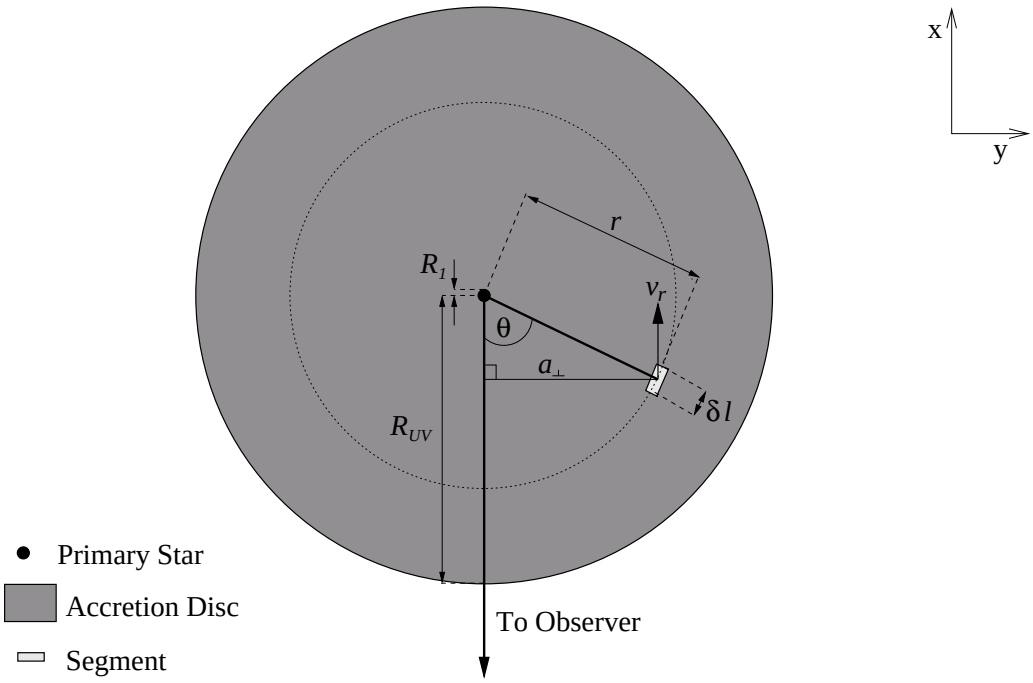

Figure 2.14: Definition of the dimensions within the UV continuum, where v_r is the radial velocity of the segment.

Note that $a_\perp$ is the perpendicular distance from the line of sight of the observer to the segment, and is given by

$$a_\perp = r \sin\theta. \tag{2.12}$$

2.4.2 Intensity Calculation of a Continuum Segment

Each segment in the UV continuum has a specific temperature dependent on the radial distance from the centre of the primary star, r, as seen in Figure 2.15.

If $r \leq R_1$, the temperature is constant and defined by the primary star. The surface intensity of the primary star (I_1) is given by

$$I_1 = \frac{f_{obs}}{\pi} = \frac{\sigma T_1^4}{\pi} \left(\frac{R_1}{D}\right)^2 \tag{2.13}$$

(Weisstein 2003) using Equation 2.6, where σ is Stefan's constant (5.670×10^{-8} $\mathrm{Wm^{-2}K^4}$), and T_1 is the temperature of the primary star (20800K, Sion 1999).

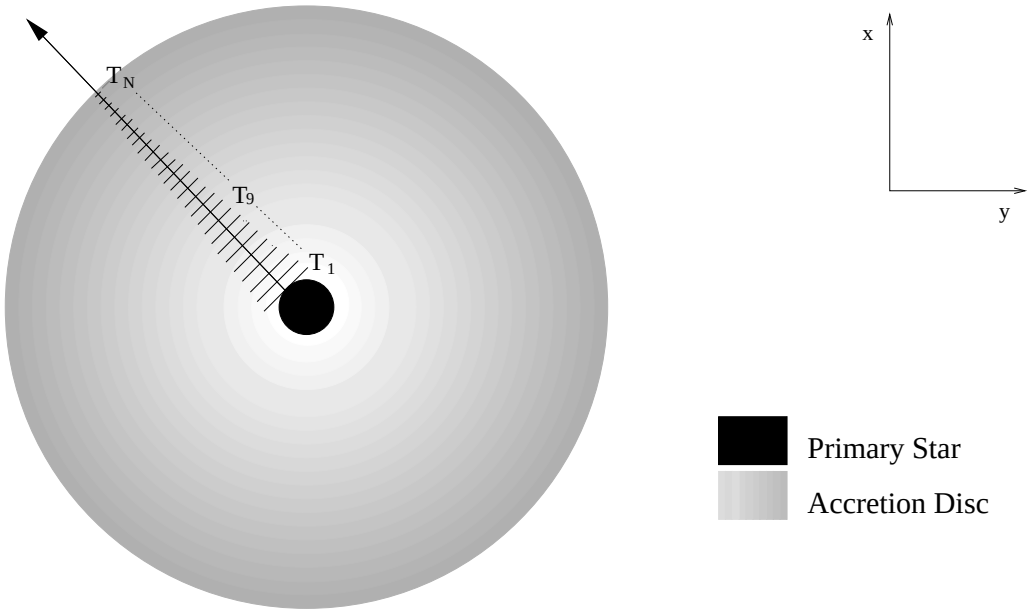

Figure 2.15: Temperature dependence of the UV continuum. The temperature decreases with increasing radial distance.

For $R_1 < r \leq R_{UV}$, the temperature of the UV continuum (T_r) is governed by the accretion disc and therefore Equation 2.1. The intensity of the accretion disc (I_r) is then given by

$$I_r = \frac{2c^2h}{\lambda^5} \frac{1}{e^{\left(\frac{hc}{k\lambda T_r}\right)} - 1} \tag{2.14}$$

(Frank, King and Raine 1992), where h is Planck's constant (6.626×10^{-34}J.s), c is the speed of light (2.99×10^5km/s), k is Boltzmann's constant (1.381×10^{-23}JK^{-1}), and λ is the wavelength of the segment calculated in the next section. So the intensity of a segment (I_s) is given by,

- $I_s = I_1$ - Equation 2.13 for $0 < r \leq R_1$,

- $I_s = I_r$ - Equation 2.14 for $R_1 < r \leq R_{UV}$.

2.4.3 Wavelength Calculation of an Accretion Disc Segment

Considering an accretion disc edge on (i.e $i = 90^o$), the radial velocity (v_r) of any segment within the disc can be calculated using the equation

$$\frac{v_r}{c} = \frac{\Delta\lambda}{\lambda_o} = \frac{\lambda - \lambda_o}{\lambda_o}, \tag{2.15}$$

where λ_o is the emitted wavelength, and λ is the observed wavelength of the segment due to the motion of the material within the accretion disc (Chapter 1, Section 1.1.1).

The accretion disc is assumed to be rotating with Keplerian velocity (v_k) around the primary star, hence

$$v_r = v_k \sin\theta = \left(\frac{GM_1}{r}\right)^{1/2} \sin\theta, \tag{2.16}$$

where G is the gravitational constant (6.673×10^{-11} $\mathrm{Nm^2kg^{-2}}$), M_1 is the mass of the primary star, and r is the radial distance from the centre of the primary star to the accretion disc segment, as shown in Figure 2.16.

In an inclined system ($i < 90^o$) such as RW Tri, Equation 2.16 must be modified to include the inclination angle (i). Therefore the observed velocity (v_i) is given by

$$v_i = v_r \sin i = v_k \sin\theta \sin i, \tag{2.17}$$

$$v_i = \left(\frac{GM_1}{r}\right)^{1/2} \sin\theta \sin i, \tag{2.18}$$

using Figures 2.17 and 2.18.

Substituting Equation 2.18 into Equation 2.15, and rearranging gives a segment wavelength of

$$\lambda = \lambda_o + \frac{\lambda_o}{c}\left(\frac{GM_1}{r}\right)^{1/2} \sin\theta \sin i. \tag{2.19}$$

2.4.4 Absorption Region: Tracing the Light Path from a UV Continuum Segment to the Observer

The cylindrical structure of the absorbing material lies outside the radius of the UV continuum (Section 2.3), therefore the absorbing region within this material is dependent on the size of the UV continuum (Figure 2.10). The height of the absorbing

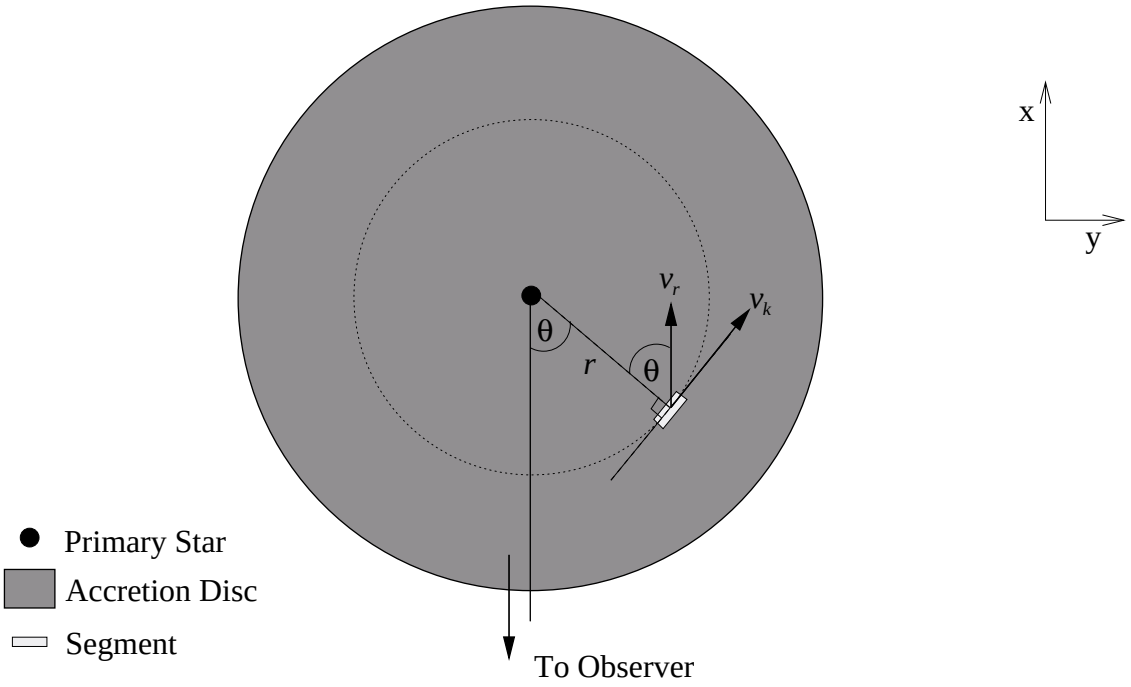

Figure 2.16: Radial velocity of a segment in the accretion disc.

material is assumed to be sufficiently high that all UV continuum segments (Section 2.4.1) are absorbed through the full radial thickness of the absorbing material (Section 2.3.2). Therefore the light path from each UV continuum segment through the absorbing material will only be constrained by the radial distance of the inner (R) and outer ($R+T$) edge of the absorbing material. Note that R and T are two of the three free parameters that the program tests.

Consider the light path from a UV continuum segment through the absorbing material as seen in Figures 2.19 and 2.20. As the light path from the segment passes through the absorbing material, it is split up into E elements of equal length δs, where E is given by

$$E = \frac{S}{\delta s} = \frac{B}{\delta s \sin i} \tag{2.20}$$

where S is the total path length through the absorption region along the observers' line of sight, and B is the total path length through the absorption region in the

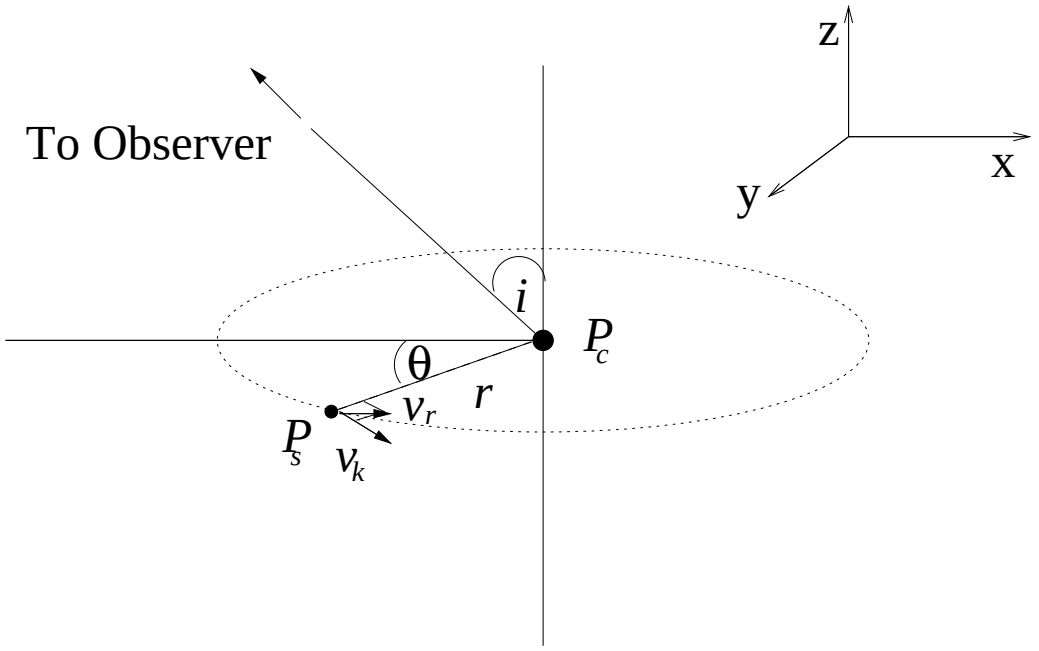

Figure 2.17: Inclination angle effect. P_c is the position of the primary star, and P_s is the position of a segment.

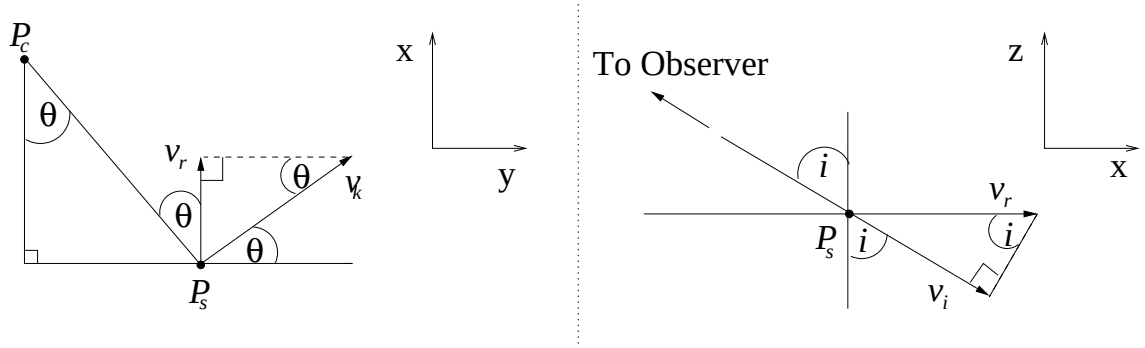

Figure 2.18: Angles used to calculate the radial velocity of the system.

orbital plane ($B = S \sin i$) (Figure 2.20).

From Figure 2.19, B can be calculated as

$$B = x_2 - x_1, \tag{2.21}$$

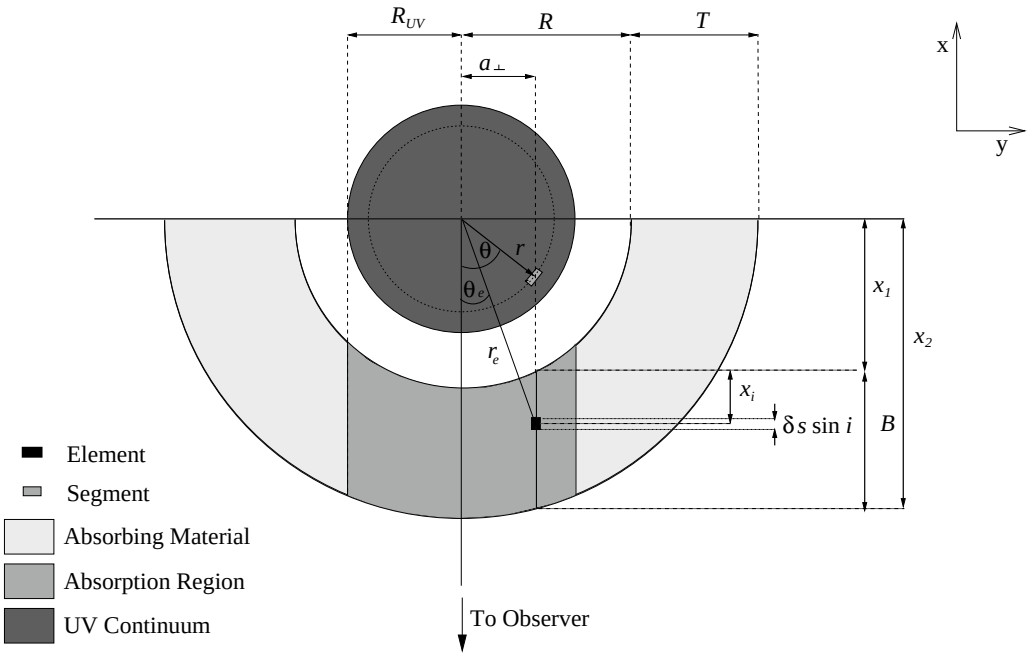

Figure 2.19: Absorption region governed by the effective extent of the UV continuum.

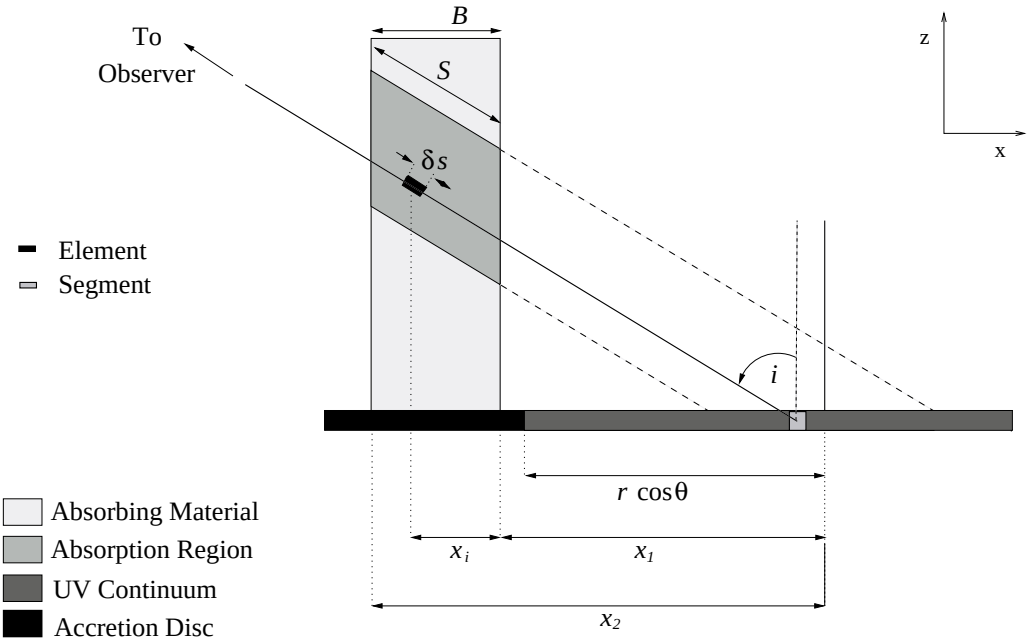

Figure 2.20: Absorption region governed by the effective extent of the UV continuum.

where

$$x_1 = \left(R^2 - a_\perp^2\right)^{1/2}, \tag{2.22}$$

and

$$x_2 = \left([R+T]^2 - a_\perp^2\right)^{1/2}, \tag{2.23}$$

using Pythagoras' Theorem, where $a_\perp$ is defined in Section 2.4.1. Substituting Equations 2.22 and 2.23 into Equation 2.21 leads to

$$B = \left([R+T]^2 - a_\perp^2\right)^{1/2} - \left(R^2 - a_\perp^2\right)^{1/2}. \tag{2.24}$$

The radial distance of the element in the absorbing material in the orbital plane, r_e, (used in element wavelength calculations - Section 2.4.5) is given by

$$r_e^2 = a_\perp^2 + [x_1 + x_i]^2, \tag{2.25}$$

using Pythagoras' Theorem in Figure 2.19. x_i is the distance to each element through the absorbing material parallel to the orbital plane (Figure 2.20), and is given by

$$x_i = (p - 0.5)\delta s \sin i, \tag{2.26}$$

where p is $1 \rightarrow E$ and 0.5 is used to calculate the mid-point of the element. Substituting Equations 2.22 and 2.26 into Equation 2.25, leads to

$$re = \left(a_\perp^2 + \left[\left(R^2 - a_\perp^2\right)^{1/2} + (p - 0.5)\delta s \sin i\right]^2\right)^{1/2}. \tag{2.27}$$

2.4.5 Wavelength Calculation of an Element in the Absorbing Material

The wavelength of each element (λ_e) in the path length is calculated in the same way as the accretion disc segment wavelength (λ - Section 2.4.3). Therefore the wavelength contribution of an element is given by

$$\lambda_e = \lambda_o + \frac{\lambda_o}{c}\left(\frac{GM_1}{r_e}\right)^{1/2} \sin\theta_e \sin i, \tag{2.28}$$

where r_e is the radial distance from the centre of the primary star to the current element calculated in Section 2.4.4, and θ_e is the angle subtended for the observers' line of sight to the current element as seen in Figure 2.19, and is given by

$$\theta_e = \sin^{-1}\left(\frac{a_\perp}{r_e}\right). \tag{2.29}$$

2.4.6 Intensity Calculation of an Element in the Absorbing Material

The intensity of each UV continuum segment (I_s - Section 2.4.2) is affected by the properties of the absorbing material. By considering the radiative transfer equation the absorption properties of the material can be taken into account.

The change in intensity of radiation from the UV continuum as it travels through the absorbing material is given by

$$dI_\lambda = -\kappa_\lambda \rho I_\lambda dS, \tag{2.30}$$

where dI_λ is the change in intensity, κ_λ is the absorption coefficient of the material, ρ is density of the absorbing material, I_λ is the intensity at λ, and dS is change in optical path of radiation from the UV continuum through the absorbing material (Carroll & Ostlie, 1996). As radiation propagates through the absorbing material, the absorbing material removes photons from the UV continuum, changing I_λ. This leads to a solution of

$$I_\lambda(\tau_\lambda) = I(0)e^{-\tau_\lambda} = I_s e^{-\tau_\lambda}, \tag{2.31}$$

where $I_\lambda(\tau_\lambda)$ is the intensity at an optical depth τ_λ in the absorbing material, and $I(0)$ is the intensity of the UV continuum segment ($I(0) = I_s$). A full derivation of the radiative transfer equation can be found in Appendix A.

The optical depth (τ_λ) is a measure of how opaque a medium is to radiation passing through it. If $\tau_\lambda >> 1$ the medium is *optically thick* and opaque, if $\tau_\lambda << 1$ the medium is *optically thin* and transparent. Optical depth is defined as

$$\tau_\lambda = \kappa_\lambda \rho S = \sigma_\lambda n_d S = HS, \tag{2.32}$$

where σ_λ is the cross sectional area of the absorbing particles producing the scattering, n_d is the number distribution of the absorbing material, and S is the path length of radiation from a segment through the disc material. H $(= \kappa_\lambda \rho = \sigma_\lambda n_d)$ is one of the three unknown free parameters that the program tests.

The light from each UV continuum segment will be absorbed along the path length S. To consider the intensity of the UV continuum along S through the absorbing material, S is split up into elements of equal length δs, where the number of elements E along the path S is given by Equation 2.20, as seen in Figure 2.21.

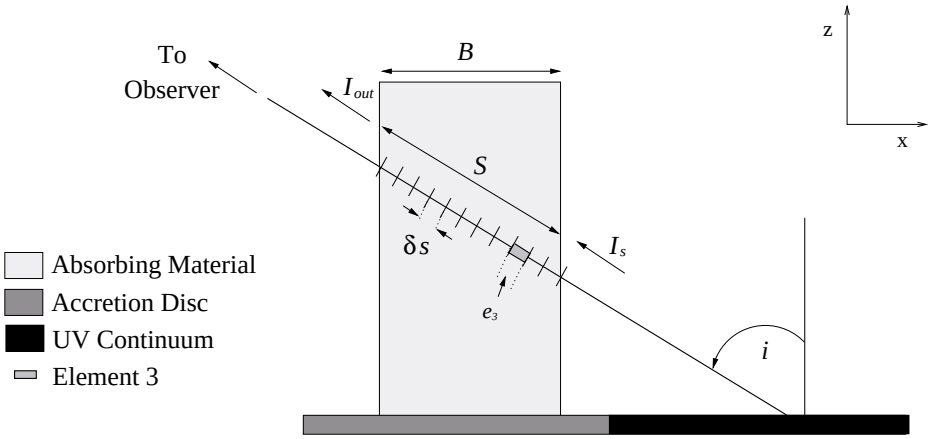

Figure 2.21: Intensity of an element (e_3), along a path length (S).

To calculate the intensity absorbed by each element, assume that each element is independent of its neighbours (i.e. the element only knows about its initial and final intensity, it does not know about other elements and therefore does not know about the total path length S). Considering element 3 (e_3) from Figure 2.21

$$I_3 = I_2 e^{-H\delta s} = I_1 e^{-H\delta s} e^{-H\delta s} = I_s e^{-H\delta s} e^{-H\delta s} e^{-H\delta s}, \tag{2.33}$$

$$I_3 = I_s e^{-3H\delta s}. \tag{2.34}$$

So the intensity absorbed by any element in the absorbing material (I_e) is given by

$$I_e = I_s e^{-pH\delta s}, \tag{2.35}$$

where I_s is the intensity from the UV continuum segment, and p is $1 \rightarrow E$.

The wavelength of the absorbing material along S will change due to the motion of the material in the absorbing cylinder (Section 2.3.2). Therefore, to produce a spectral profile the wavelength contribution from each element in the absorbing material (λ_e) is calculated using Equation 2.28 (Section 2.4.5), then the intensity of each element can be binned into discrete wavelength bins. The $I_e - \lambda_e$ distribution can then be summed over all elements for all UV continuum segments, producing a final absorption profile.

2.5 The Model Program

The model was produced by calculating the wavelength and intensity of each element, and then summing the intensities and binning into discrete wavelength bins to form a spectral line, as described in Section 2.4.6.

The model data was fitted to the observed feature at 1335Å in the HST data (Figure 2.3). This feature was observed close to orbital phase 0.5, there is no eclipse of the UV continuum and absorbing material due to the secondary star (Section 2.3). Figure 2.22 shows a plot of the observed 1335Å absorption feature after continuum flux was removed. The model data was normalised to the observed data (seen in Figure 2.22), enabling the model data to be fitted to the observed data.

The goodness of fit of the model data was tested by varying the input parameters R, T and H and calculating the minimum reduced chi-squared (Appendix B). The standard deviation of the UV continuum level of $\pm 1.2 \times 10^{-14}$ erg cm^{-2}s^{-1}Å^{-1} (marked as an error bar in Figure 2.22), was considered in the reduced chi-squared calculation.

The FORTRAN program written to produce the disc model can be seen in Appendix C. The following section discusses the input and output values of the program.

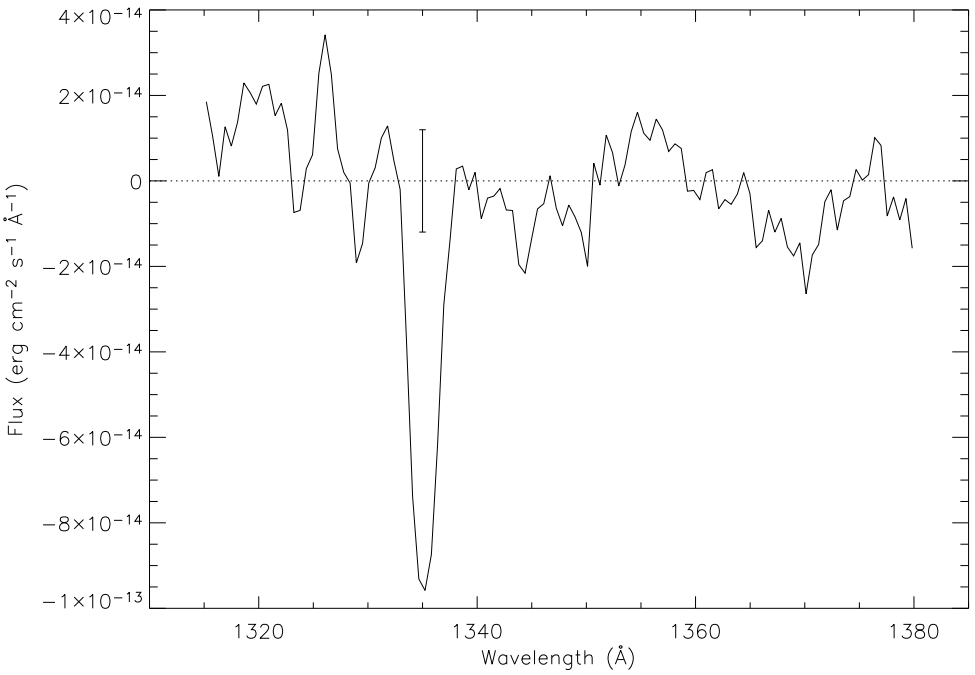

Figure 2.22: 1335Å absorption feature observed at an orbital phase close to 0.5, with the UV continuum removed. The error bar is the standard deviation of the UV continuum in the regions 1314Å - 1331Å and 1339Å - 1379Å. This data was used in the FORTRAN program.

2.5.1 Input Values for the Model

A list of constant program input parameters is given below. The bold text represents the names of the parameters in the FORTRAN program (Appendix C).

- Mass of primary star ($M_1 = 0.75 M_\odot$) - **MASS**
  - Table 2.3, Section 2.2.3.
- Inclination angle ($i = 76.86^o$) - **INC**
  - Table 2.3, Section 2.2.3.
- Radius of the primary star ($R_1 = 0.011 R_\odot$) - **RADWD**
  - Table 2.3, Section 2.2.3.
- Radius of the UV continuum ($R_{UV} = 0.234 R_\odot$) - **RADUV**
  - Section 2.2.3.
- Accretion rate ($\dot{M} = 4 \times 10^{-8} M_\odot \mathrm{yr}^{-}1$) - **MDOT**

- Section 2.2.3.

- Temperature of the primary star ($T_1 = 20800$K) - **TEMPWD**
  - Table 2.3, Section 2.2.3.
- Length of a UV continuum segment ($\delta l = 2.0 \times 10^7$cm) - **SEGL**
  - chosen to give a smooth profile
- Length of absorption material element ($\delta s = 2.0 \times 10^7$cm) - **ELES**
  - chosen to give a smooth profile
- Number of a UV continuum annulus ($n = 815$) - **NUM**
  - chosen to give a smooth profile, so that $\delta r = \delta l = \delta s$
- Emitted wavelength of central peak ($\lambda_o = 1335$Å) - **WAVEO**
- Size of wavelength bin (0.59Å) - **BIN**
  - from the spectral resolution of the HST data
- Start wavelength for the first wavelength bin ($\lambda_1 = 1318.445$Å) - **WAVE1**
  - from the HST observational data
- Number of free parameters (3) - **PAR**
  - see the list of these free parameters below

The following is a list of free parameters that the user inputs into the program. The bold text represents the names of these parameters in the FORTRAN program (Appendix C).

- Distance from the centre of the UV continuum to the inner annulus of the cylinder (R in cm) - **INR**
- Radial thickness of the cylinder (T in cm) - **RTHICK**
- Optical depth constant (H in cm^{-1}) - **CONST**

2.6 Model Fits

The model program was run for a range of input values. The best results for the minimum reduced chi-squared (Appendix B) value of 1.1 ± 0.3 are,

- $R = 0.3 \pm 0.1 R_{\odot}$
- $T = 0.01 \pm 0.005 R_{\odot}$
- $H = 7.0 \times 10^{3} \pm 3.4 \times 10^{3} R_{\odot}^{-1}$

The errors on these values were calculated by minimising the reduced chi-squared of the best-fit, and considering the 68.3% (1σ) confidence level. The best-fit profile can be seen in Figure 2.23 (red line).

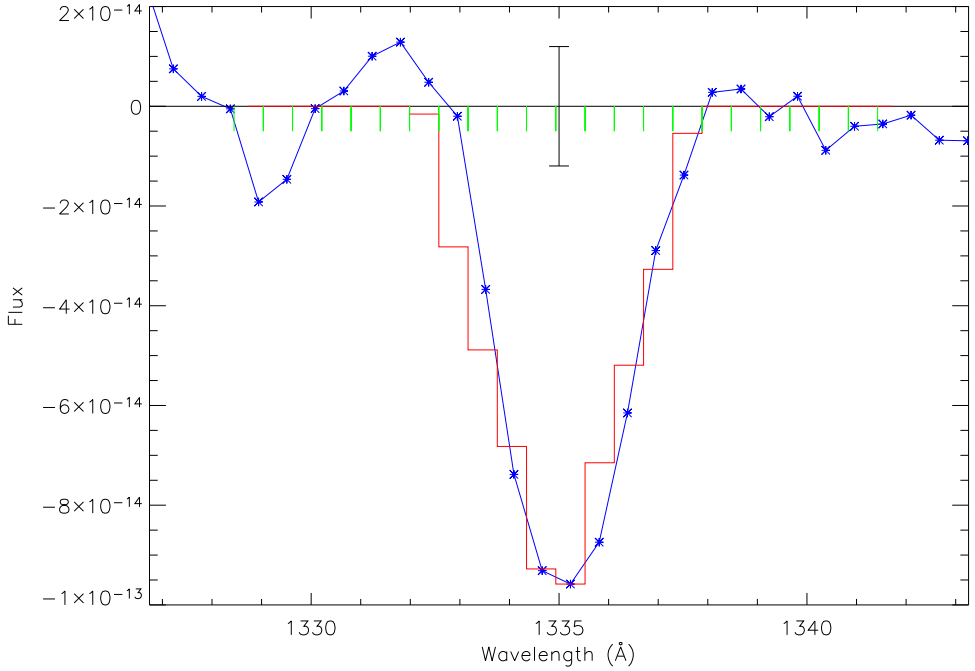

Figure 2.23: Best-fit model (red) plotted with the observed out-of-eclipse profile with continuum removed (blue). The green lines represent the wavelength bins used in the model. The error bar is the standard deviation of the UV continuum from Figure 2.22.

2.6.1 Is the Value of H as Expected?

The value of H obtained from my simple geometric model was $7.0\times10^3\pm3.4\times10^3 R_\odot^{-1}$. The absorption feature used to fit the simple geometric model, observed at 1335Å, was due to C II (Section 2.1.2). The optical depth (τ_λ) of the absorbing material is defined as

$$\tau_\lambda = \sigma_\lambda N_i, \tag{2.36}$$

where σ_λ is the cross sectional area of the absorbing particles, and N_i is the column density of the absorbing material (Weisstein, 2003). A value of H can therefore be estimated using

$$H = \frac{\sigma_\lambda N_i}{S}, \tag{2.37}$$

from Equations 2.32 and 2.36.

The cross sectional area of the carbon atoms producing the absorption at the central wavelength (λ_o) is given by

$$\sigma_{\lambda_o} = 1.16157 \times 10^{-14} f_{ik} \lambda_o \left(\frac{A}{T_a}\right)^{1/2}, \tag{2.38}$$

where f_{ik} is the oscillator strength or f-value for the transition between states i and k, A is the atomic weight of the atoms in the absorbing material, and T_a is the temperature of the absorbing material (Rybicki & Lightman, 1985). The atomic weight of carbon is 12.011 amu (Helman 2002), and f_{ik} and λ_o are summarised in Table 2.4. The temperature of the absorbing material is calculated using Equation 2.1 (Section 2.2.1) where the radial extent of the material is $R + T = 0.31 \pm 0.1 R_\odot$, leading to a temperature of 15363 ± 4714K. Substituting these values into Equation 2.38 leads to a σ_{λ_o} of $5.5 \times 10^{-14} \pm 0.8 \times 10^{-14}$ cm^2.

The column density (N_i) can be calculated from the equivalent width[1] (W_i) of the observed absorption line at 1335Å by considering the theoretical curve of growth[2]

[1]The equivalent width is the measure of the intensity of a spectral line when normalised to the continuum level (Zeilik, Gregory, & Smith, 1992).

[2]The curve of growth is a logarithmic graph of the equivalent width, W_i, as a function of the number of absorbing atoms, N_i (Carroll & Ostlie, 1996).

for C II. The equivalent width of a spectral line is the width of a box (in Å) reaching to the continuum that has the same area as the spectral line; it is calculated using

$$W_i = \int \frac{F_c - F_\lambda}{F_c} d\lambda, \tag{2.39}$$

where F_c is the flux from the continuous spectrum outside the spectral line (i.e. the continuum flux level), and F_λ is the flux of the spectral line as a function of wavelength (λ) (Carroll & Ostlie, 1996). Considering a continuum flux level of $1.4 \pm 0.12 \times 10^{-13}$ erg cm^{-2}s^{-1}Å^{-1} (Figure 2.4, Section 2.2.1), a W_i of 2.12 ± 0.34Å was calculated.

The theoretical curve of growth for a range of velocities from 25-800 km/s was produced using the program EW_COLUMN_VOIGT written by Mat Page (Figure 2.24). The input parameters for the program can be seen in Table 2.4. The dashed line in Figure 2.24 represents the W_i of the observed absorption line at λ1335Å, calculated using Equation 2.39.

Parameter	Symbol	Value	Reference
Equivalent width (Å)	W_i	2.12 ± 0.34	Figure 2.22, Section 2.5
Wavelength (Å)	λ_o	1335.3130	Verner, Verner & Ferland 1996
Oscillator strength	f_{ik}	0.127	Verner, Verner & Ferland 1996
Natural width (s^{-1})	A_{ki}	2.85×10^8	Verner, Verner & Ferland 1996

Table 2.4: Input parameters for EW_COLUMN_VOIGT.

EW_COLUMN_VOIGT also produced an N_i - V plot for the given W_i range. This can be seen in Figures 2.25 where the black lines represent $W_i = 2.12 \pm 0.32$Å, and the magenta lines represent $V = 650 \pm 44$km/s calculated from the FWHM of the absorption feature at 1335Å (Figure 2.5, Section 2.1.2). From Figure 2.25 an N_i of $1.19 \times 10^{15} \pm 0.22 \times 10^{15}$ cm^{-2} was obtained.

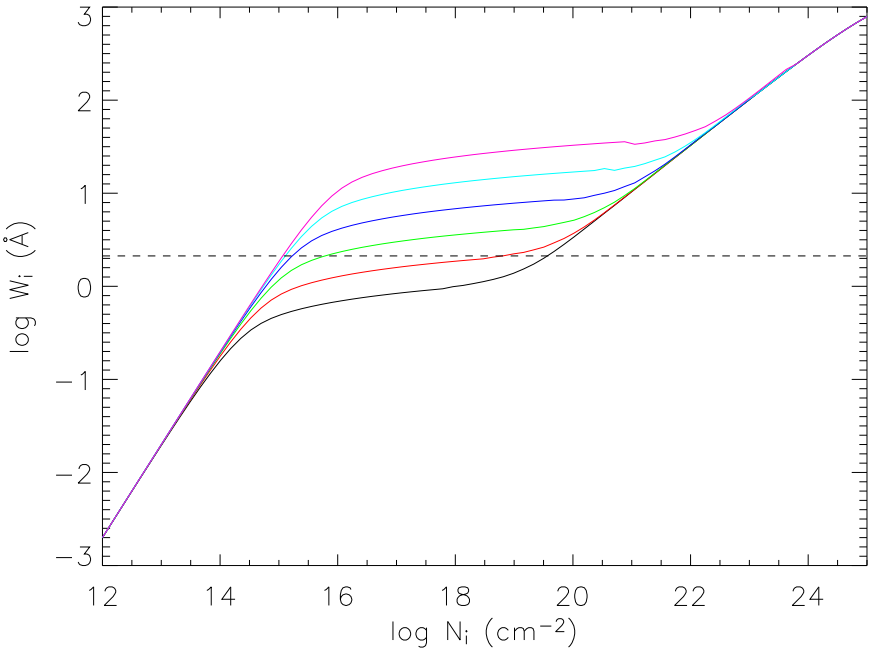

Figure 2.24: Theoretical curve of growth for C II. The curve of growth has been calculated for velocities of 25km/s (black), 50km/s (red), 100km/s (green), 200km/s (blue), 400km/s (cyan), and 800km/s (magenta). The dashed black line represents the equivalent width (2.12Å) of the observed absorption feature at 1335Å.

The path length, S, along the central wavelength is given by

$$S = \frac{T}{\sin i} = 0.01 \pm 0.005 R_{\odot} \tag{2.40}$$

from Figure 2.21, where T is the thickness of the absorbing material ($0.01 \pm 0.005 R_{\odot}$), and i is the inclination angle of the system (Table 2.3, Section 2.2.3). Therefore using Equation 2.37, the final calculated value of H was $1.1 \times 10^{-7} \pm 0.7 \times 10^{-7}$ cm^{-1} (or $7.5 \times 10^{3} \pm 4.9 \times 10^{3} R_{\odot}^{-1}$). Within error this agrees with the simulated value of $7.0 \times 10^{3} \pm 3.4 \times 10^{3} R_{\odot}^{-1}$ obtained from the simple absorption model.

2.7 Implications of the Model Results

There are several possible origins for the narrow absorption line region. These possibilities are:-

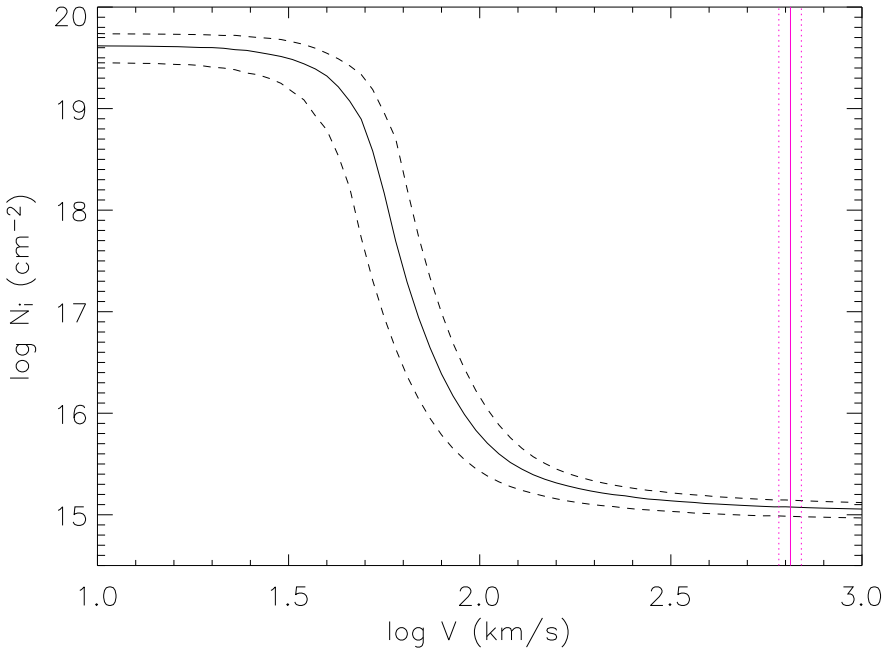

Figure 2.25: Column density (N_i) versus velocity (V) for the equivalent width of the observed absorption profile at 1335Å. The solid black line represents the equivalent width of 2.12Å, and the dashed black lines represent equivalent widths of 2.12 ± 0.34Å. The solid magenta line represents $V = 650$ km/s, and the dotted magenta lines represent $V = 650 \pm 44$ km/s.

1) Material from the disc that has not reached the wind.

Material in an accretion disc corona that acts as a reservoir for the UV wind could produce a ring-like feature above (and below assuming symmetry) the accretion disc.

2) In-fall from wind.

Wind material can lose the momentum gained by the initial force exerted on it by radiation pressure. A disc structure will form due to the capture of this material by the gravitational field of the primary stars, in the same way as material from the secondary star is captured to form an accretion disc (Chapter 1, Section 1.1.4).

3) Material build-up due to flow from the secondary star.

The region producing the absorption features could be related to the 'dip' seen in the UV light curve in Figure 2.2. If this observed dip is equivalent to the proposed model of Frank et al. (1987) for LMXB dips, then the absorption region may originate from stream overflow material. Considering the circularisation radius (r_{cir} - Chapter 1,

Section 1.1.4)

$$r_{cir} = 0.6 P_{day}^{2/3} R_{\odot} \quad \text{for } q > 0.5 \tag{2.41}$$

(Frank, King & Raine, 1992), where P_{day} is the orbital period of the system in days (0.2319 days), produces $r_{cir} = 0.23 R_{\odot}$. The radius of the cylindrical absorption material (0.3 ± 0.1) calculated in Section 2.6, is in agreement with r_{cir} within error.

Figure 2.26 shows a scale 'birds eye' view of the system at orbital phase 0.5 using the results from this model. The separation of the component stars is $a = 1.701 R_{\odot}$ (from Section 2.2.3). The distance from the inner Lagrangian point (Chapter 1, Section 1.1.2) to the centre of the white dwarf (l_1) is given by

$$l_1 = a(0.500 - 0.227 \log q) = 0.93 R_{\odot} \tag{2.42}$$

Plavec & Kratochvil (1964), where $a = 1.701 R_{\odot}$ and $q = 0.64$ (Section 2.2.3). From Table 2.3, $R_2 = 0.57 R_{\odot}$. The radius of the UV continuum is $0.234 R_{\odot}$ from Section 2.2.3. The radius of the accretion disc (R_{out}) was calculated to be $0.402 R_{\odot}$ by Smak (1995).

A 'theoretical double-peaked accretion disc profile' is not seen in the narrow emission features (Figure 2.23). Using $R = 0.3 R_{\odot}$, with $M_1 = 0.75 M_{\odot}$, the orbital velocity (v) of the material in the inner radius of the cylinder is

$$v = \left(\frac{G M_1}{R}\right)^{1/2} \sim 710 \text{km/s}, \tag{2.43}$$

which corresponds to a wavelength shift ($\Delta\lambda$) of

$$\Delta\lambda = \frac{v}{c} \lambda_o \sim 3\text{Å} \tag{2.44}$$

(Chapter 1, Section 1.1.1, Equation 1.3), where $\lambda_o = 1335$Å is the rest wavelength of the emission feature. This wavelength shift suggests a double peak feature, but the results show that the ring of material is optically thick ($HT = 70 \rightarrow \tau_{\lambda} > 1$ from Equation 2.32), which will effectively boost the core of the line producing a single absorption line.

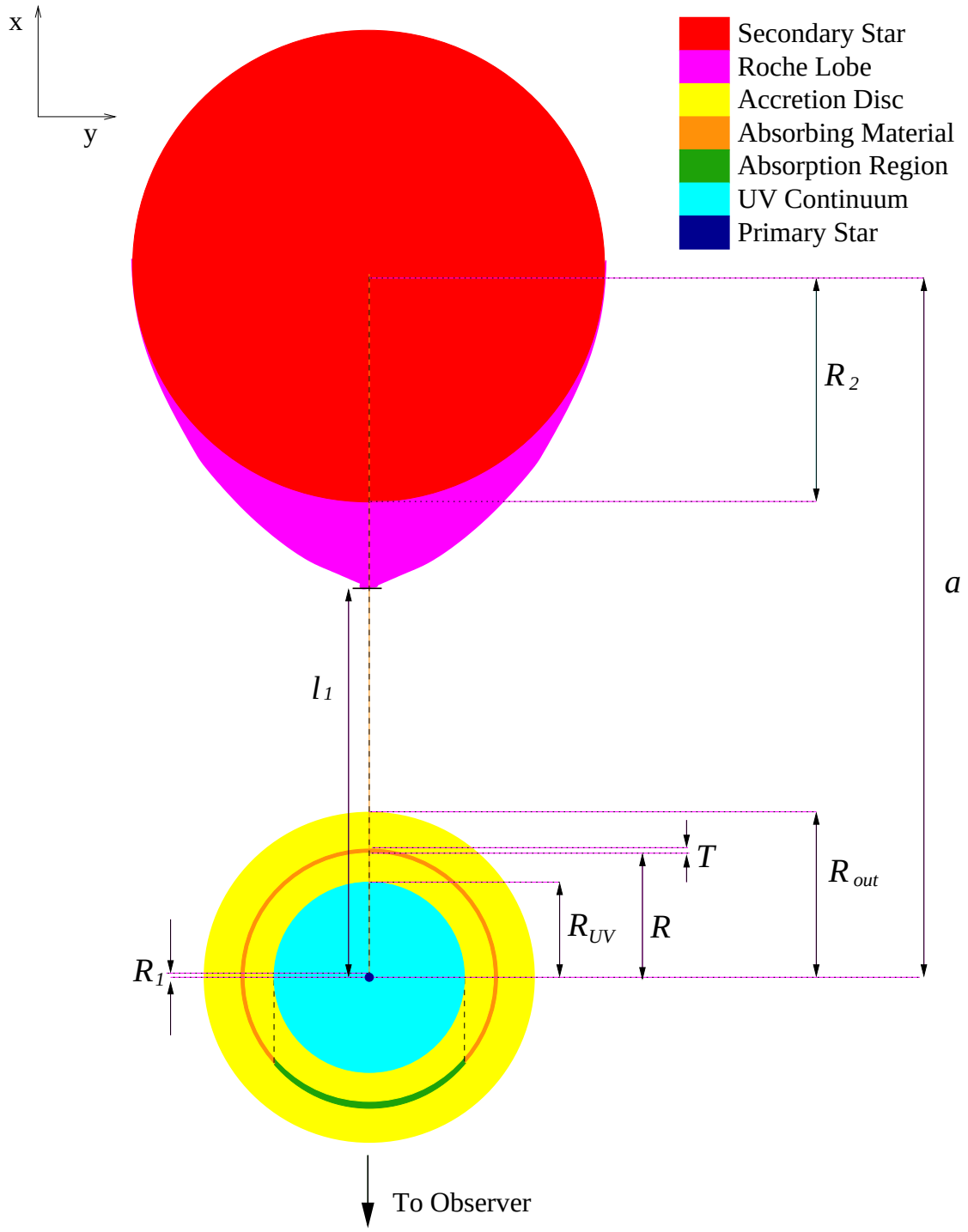

Figure 2.26: Scale diagram of the system at orbital phase 0.5 in the x-y plane from the results found using the disc model; a 'birds eye' view.

2.8 Further Development of the Model

These results show that the material producing the absorption features in the HST UV observations of Mason et al. (1997), could lie on an arc defined by a thin cylindrical structure very close to the primary star. The inclination angle of the system and the physical properties of the UV continuum are considered in the model, but the model is only fitted to the absorption feature at 1335Å close to orbital phase 0.5. To improve the model other absorption features and other orbital phases should be simulated. This would lead to a better understanding of the shape, position and extend of the absorbing material.

Spiral shocks have been seen in the nova-like system V347 Pup (Still et al. 1998). A correctly orientated spiral shock could mimic the modeled absorption 'arc'. This could be tested by modeling the system at different orbital phases; if the 'arc' changes radius with orbital phase the absorption could be due to spiral shocks.

The observations of the HST UV data during eclipse show the presence of a weak emission feature (Figure 2.4 and 2.5). This underlying emission feature was ignored to simplify the model, but will affect the profile of the absorption features. The emission profile can be included in the model by assuming that it is produced from the accretion disc chromosphere.

2.9 Conclusions

From the *Hubble Space Telescope* observations of Mason et al. (1997), I have modelled the unusual narrow absorption lines seen as emission lines in eclipse. From the nature and profile of the feature seen at 1335Å, I produced a simple absorption model with the geometry shown in Figure 2.26. My model is consistent with the HST observations close to orbital phase 0.5, and confines the region producing the absorption lines to within $0.3 \pm 0.1 R_{\odot}$ of the white dwarf. I have also discussed future improvements that can be added to the model to make it more viable.

Chapter 3

The Secondary Star of RW Tri

The secondary star of RW Tri is expected to be of late spectral-type, and is observable at far red (FR) and near infrared (NIR) wavelengths. The secondary star only contributes ∼10% of the out-of-eclipse flux in the FR, compared to ∼65% in the NIR (Dhillon et al. 2000), therefore the secondary star will be seen more strongly at longer wavelengths.

Measurements of the secondary star velocity are hampered by the large contrast in brightness with the accretion disc. Weak secondary star absorption features were detected in the FR spectrum of RW Tri by Friend et al. (1988), and later used by Smith et al. (1993) to roughly estimate the secondary star velocity as $\sim$ 250km/s using the method of 'skew-mapping'. Skew-mapping is a back projection technique similar to Doppler tomography (Marsh & Horne 1988), which allows the mapping of velocity from emission features in the binary system. Dhillon et al. (2000) have detected secondary star features in low-resolution K-band spectra of RW Tri.

In this Chapter I report on the time-resolved spectral observations of RW Tri in the NIR that I took in November 2000, using the *United Kingdom Infrared Telescope* (UKIRT). I use these observations to determine the radial velocity of the secondary star in RW Tri. I also re-analyse the original reduced FR *Isaac Newton Telescope* (INT) observations of Smith et al. (1993) to calculate the secondary star velocity. Finally I compare the secondary star velocities at these different wavelengths.

3.1 The Far Red Data

The far red data of Robert Smith was too noisy to use conventional cross-correlation techniques, so the method of skew-mapping is used to calculate the velocity of the secondary star. To interpret a skew map it is important to understand how the map is constructed using the technique of cross-correlation. In the next sections the skew-mapping method is expanded, tested, and a Monte Carlo simulation method for calculating the error on the skew map is discussed. These sections are followed by a brief description of the observing run undertaken by Robert Smith, following which I go on to discuss the analysis and data results.

3.1.1 Construction of the Skew Map

The motion of the secondary star around the centre of mass of the binary system results in a sinusoidal motion of secondary star absorption features over the orbital period (P_{orb}) of the system (Chapter 1, Section 1.1.1). When the secondary star absorption features are too weak to use conventional cross-correlation methods to map this motion, the technique of skew-mapping can be used. The method of skew-mapping considers all possible velocity amplitudes (A) and zero-crossing phases (Φ_o - inferior junction of the secondary star). The resultant skew map produces a peak indicating the best sinusoidal fit to the correlation distribution, and hence the velocity of the secondary star.

Assuming that the secondary star rotates around the system's centre of mass (c.m.) with circular motion as in Figure 3.1, the radial velocity of the secondary star (V) can be expressed as

$$V = A \sin[2\pi(\Phi - \Phi_o)], \tag{3.1}$$

where $0 \leq A \leq 1000$ km/s, $0 \leq \Phi_0 \leq 1$, and Φ is phase.

The values of A and Φ_o that produce the best-fit model to the observed data are taken as the best solution. In practice this is done using a cross-correlation

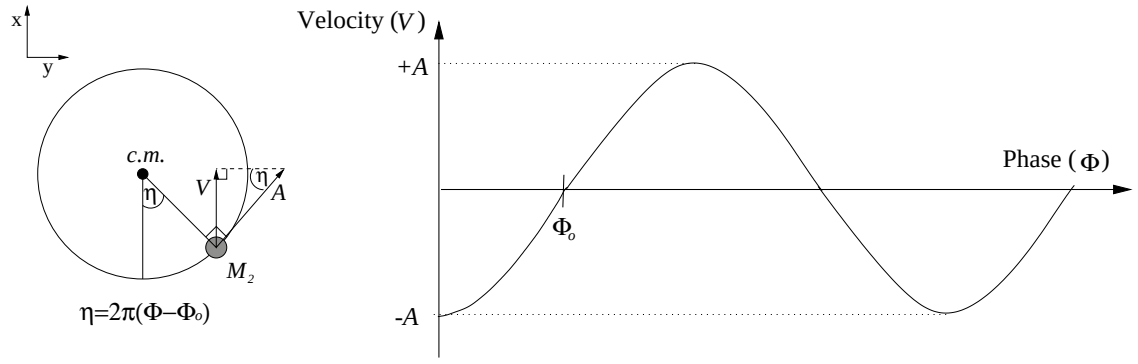

Figure 3.1: Motion of the secondary star. Left: Circular orbit of the secondary star in the coordinate system defined by Figure 1.2 (Chapter 1, Section 1.1). M_2 is the mass of the secondary star, and c.m. is the centre of mass of the system. A is the velocity amplitude of the secondary star. Right: The sinusoidal motion of the secondary star absorption features.

technique to optimise the secondary star features.

Observations of the system need to be obtained over an orbital period of the system. The wavelength of each spectrum is then corrected to a linear velocity scale. This is done using

$$v = \frac{c\Delta\lambda}{\lambda_o}, \tag{3.2}$$

where c is the speed of light (2.99×10^5 km/s), λ_o is the wavelength of the line centre, and $\Delta\lambda$ is the wavelength dispersion. (See Appendix D for derivation).

The spectrum of a single red dwarf is used as a template to cross-correlate with the observed spectra. The Na I doublet (λ8183.3Å, λ8194.8Å) is used as the secondary star's distinguishing feature in the far red. This leads to a series of cross-correlation functions at different phases, where

$$V_{2ndary} = V_o + A\sin[2\pi(\Phi - \Phi_o)], \tag{3.3}$$

$$V_{template} = V_T, \tag{3.4}$$

V_{2ndary} and $V_{template}$ are the velocities of the secondary and template stars respectively, V_o and V_T are the systemic[1] velocities of the binary system and template star

[1]Centre of mass velocity of the system.

respectively.

With perfect correlation a sinusoidal or 's-wave' radial velocity curve is formed from the peaks of the cross-correlation functions (CCFs), where N is the number of observations. Each cross-correlation peak is positioned on the s-wave defined by

$$V_{ccp} = V_o - V_T + A\sin[2\pi(\Phi - \Phi_o)]. \tag{3.5}$$

This can be seen in Figure 3.2.

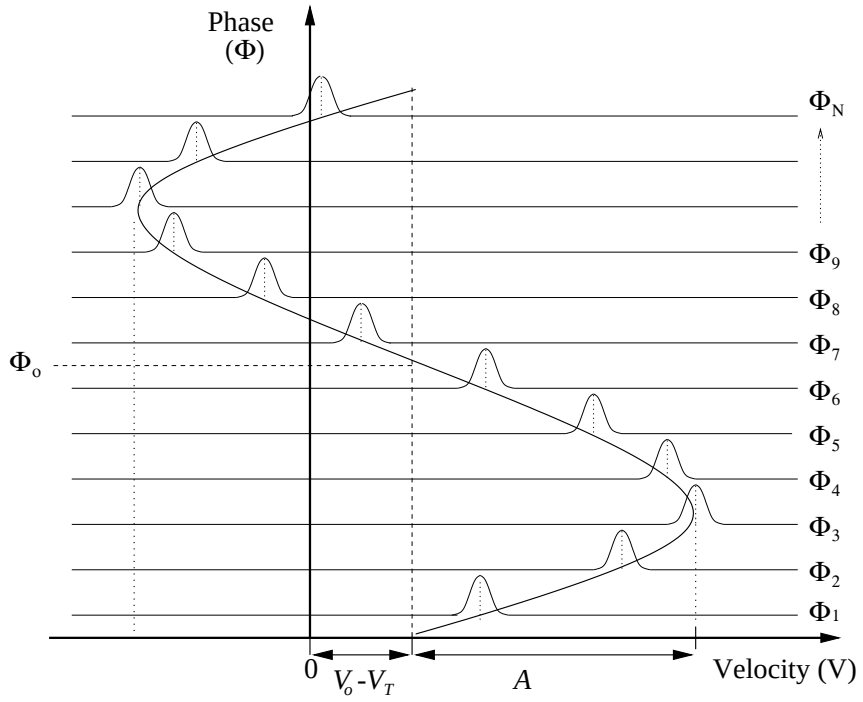

Figure 3.2: S-wave radial velocity curve formed from the cross-correlation peaks. N is the number of observations.

The s-wave defines a line integral[2], I_{nt}. Generally I_{nt} will be small, but if the s-wave equals the locus of the cross-correlation functions, then I_{nt} will be a strong maximum.

There are three unknowns, A, Φ_o, and $V_o - V_T$. The best estimate of these unknowns is the one that maximizes the line integral. A range of templates of

[2]Integral in time along a path through the cross-correlation function time series.

different spectral types is considered. Then, the line integral is evaluated along the sinusoidal path defined by (A,Φ_o) for each template.

The skew map is constructed by plotting all the line integral values in velocity space as seen in Figure 3.3. When $V_o - V_T = 0$, each pixel in the skew map corresponds to a sinusoid defined by A and Φ_o. This sinusoid is integrated through the data so that the line flux is summed along the sinusoid. There will be a point on the skew map, which corresponds to an s-wave that exactly follows the peaks of the cross-correlation functions of the data. This will be seen as a peak in the map.

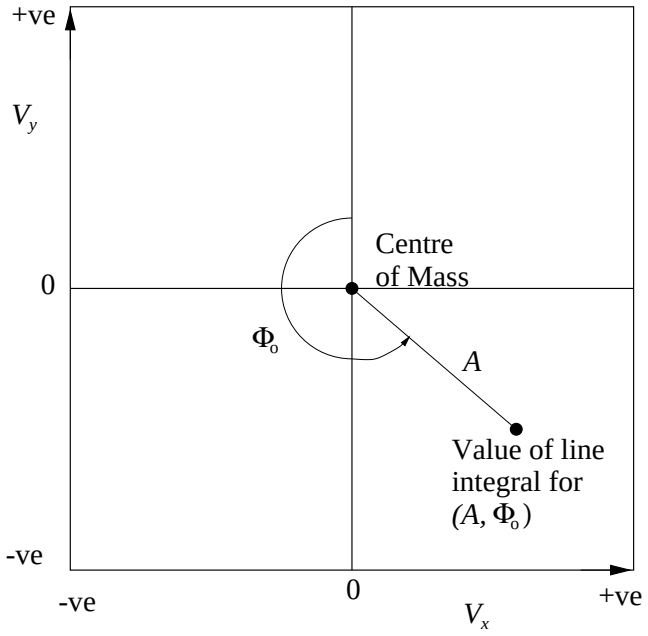

Figure 3.3: Skew map in velocity space.

For an eclipsing system the phase of each spectrum is known. The peak of the skew map will be located at $\Phi_o = 0$ and $A = K_2$, where K_2 is the velocity amplitude of the secondary star (Figure 3.4).

The difference in secondary and template systemic velocity ($V_o - V_T$) is expected to be small because systemic velocities of these systems are typically $\pm 10 - 20$km/s. Therefore $V_o - V_T$ will have very little effect on the position of the peak on the skew map. This is further discussed in Section 3.1.6.

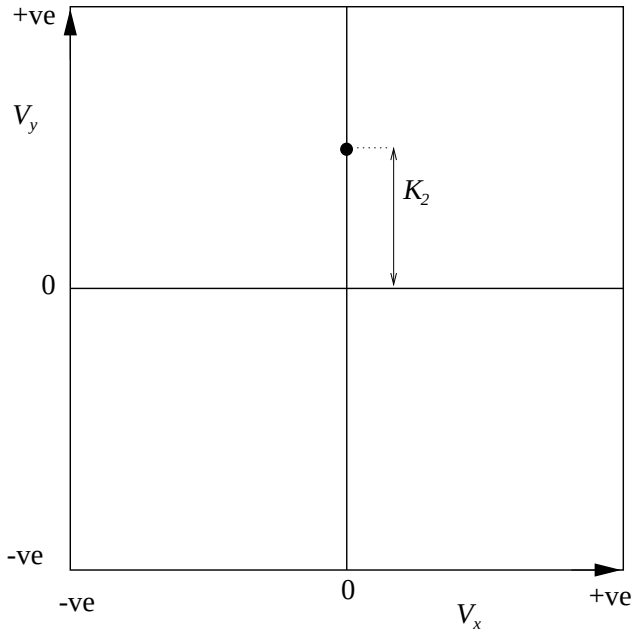

Figure 3.4: Position of the secondary star. The point-like peak on the skew map indicates the position of the secondary star.

3.1.2 Skew Map Testing

The skew-mapping method was tested using synthesised absorption features formed in IDL and the MOLLY code written by Tom Marsh. Two separate single peak absorption features were synthesised using a Gaussian profile. The first feature was wavelength shifted 20 times with a sinusoidal variation to mimic the effect of orbital motion in a binary system. The second feature represented the template star. These two features were then cross-correlated and back projected using the method described in Section 3.1.5. This was repeated with a double absorption feature.

Figure 3.5 shows the results of cross-correlating two single absorption features (left) and two double absorption features (right). For the single feature skew map, a central peak with 20 evenly spaced 'spokes' (e.g. Figure 3.5, cyan and magenta) are clearly visible. For the double feature skew map a main peak and ring of lower intensity (Figure 3.5, red) centred on the main peak are seen. Also 20 sets of three 'spokes' centred on the main peak and the ring respectively can be seen. These sets

of spokes are equally incremented as in the single feature case. Considering one set of three spokes, the 'secondary' outer two spokes are less intense than the 'primary' inner spoke.

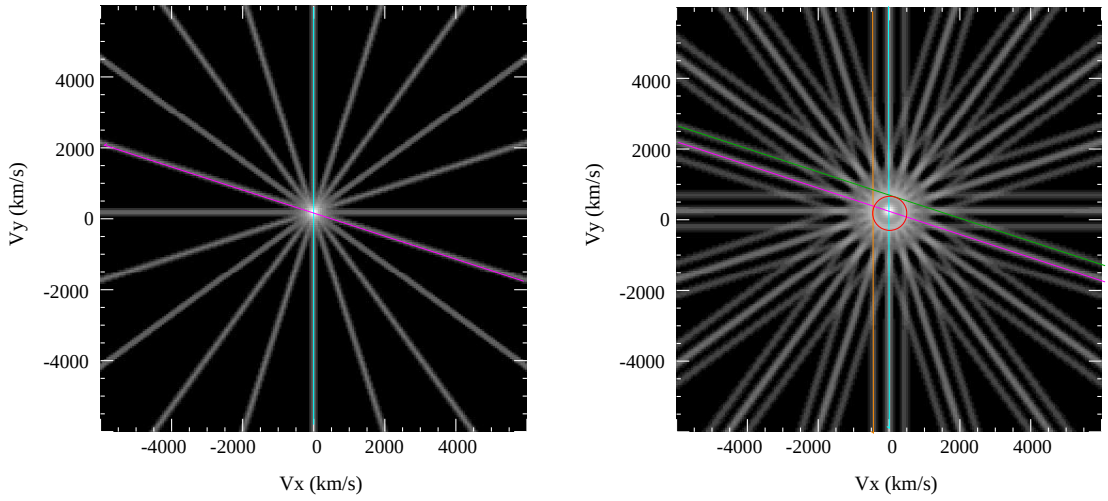

Figure 3.5: Skew map results of synthesised absorption lines. Left: A single absorption line cross-correlated with a single absorption line. Two different 'spokes' are highlighted with solid cyan and magenta lines. Right: A double absorption line cross-correlated with a double absorption line. Two 'secondary spokes' are highlighted with solid orange and green lines. Two 'primary spokes' are highlighted with solid cyan and magenta lines, and are equivalent to the spokes on the single absorption line map (left). The peak ring is highlighted by solid red circle.

To understand what causes the primary spokes on the skew map consider the simple case where only single features have been cross-correlated. In Figure 3.6 each cyan and magenta s-wave represents a point along the cyan and magenta lines on the skew map in Figure 3.5 (left) respectively. These s-waves each have their own amplitude (A) and phase (Φ_o) as in Figure 3.3 (Section 3.1.1), but all pass through two cross-correlation peaks. By transferring points on the skew map into s-waves and plotting (Figure 3.6), the formation of the spokes can be pictorially built up.

The s-wave of the peak point (black s-wave in Figure 3.6) defines a central coherency sine wave. Only along this central coherency sine wave do all the cross-correlation peaks contribute to one point on the map. The 20 spokes are formed by sets of sine waves focused on the peak of each individual CCF ('$*$'s in Figure 3.6).

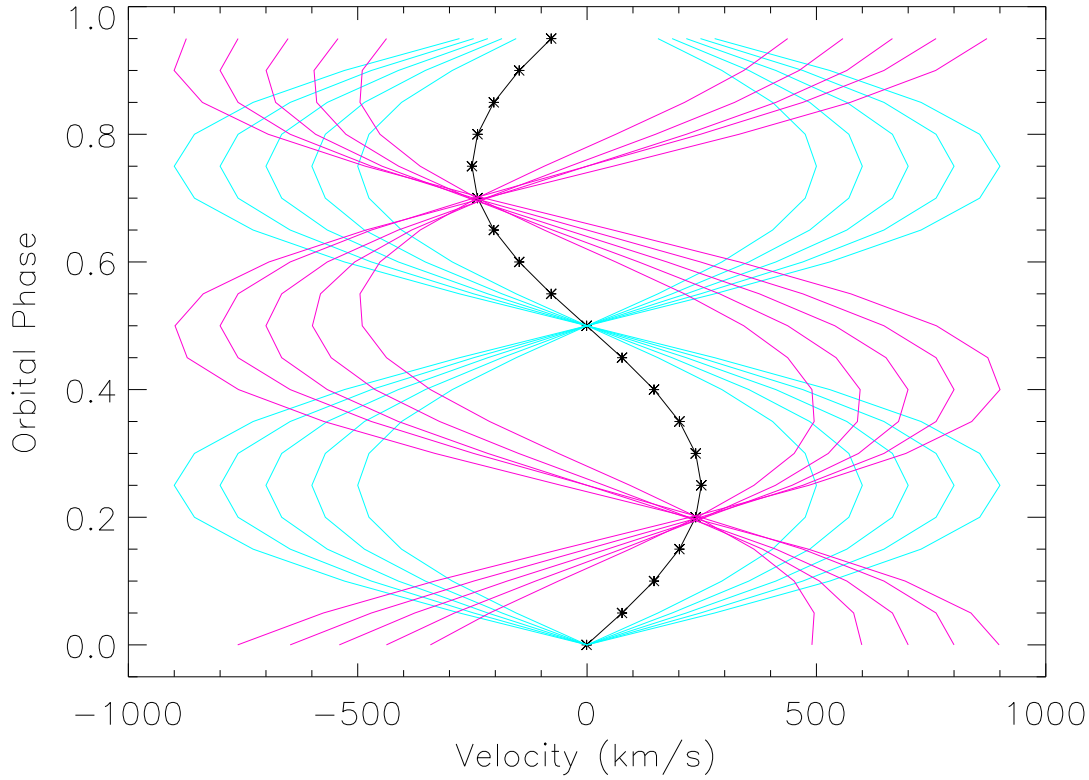

Figure 3.6: Explanation of how 'primary' spokes are formed. Cyan and magenta s-waves correspond to points on the cyan and magenta spokes of the skew map in Figure 3.5 (left). The thick black line corresponds to the peak point on the skew map in Figure 3.5 (left). The '$*$'s represent the peaks of the 20 CCFs.

The sets of sine waves will always pass through two points on the central coherency sine wave which are 180^o out of phase. The cyan spoke is constructed from s-waves passing through CCFs at phase 0.0 and 0.5, and the magenta spoke constructed from s-waves passing through the CCFs at phase 0.2 and 0.7. Hence,

- there are 20 spokes corresponding to the 20 CCFs,
- the amplitude along each of these spokes is $\sim 1/10$th of the peak point intensity as the set of sine waves along these spokes all pass through two CCF peaks on the central coherency sine wave.

  i.e. If the amplitude of the central peak is C and there are 20 CCFs, the peak of each CCF is $C/20$. The sine wave of each spoke passes through the central

coherency sine wave twice hence the intensity of each spoke is,

$$\frac{2C}{20} = \frac{C}{10}. \tag{3.6}$$

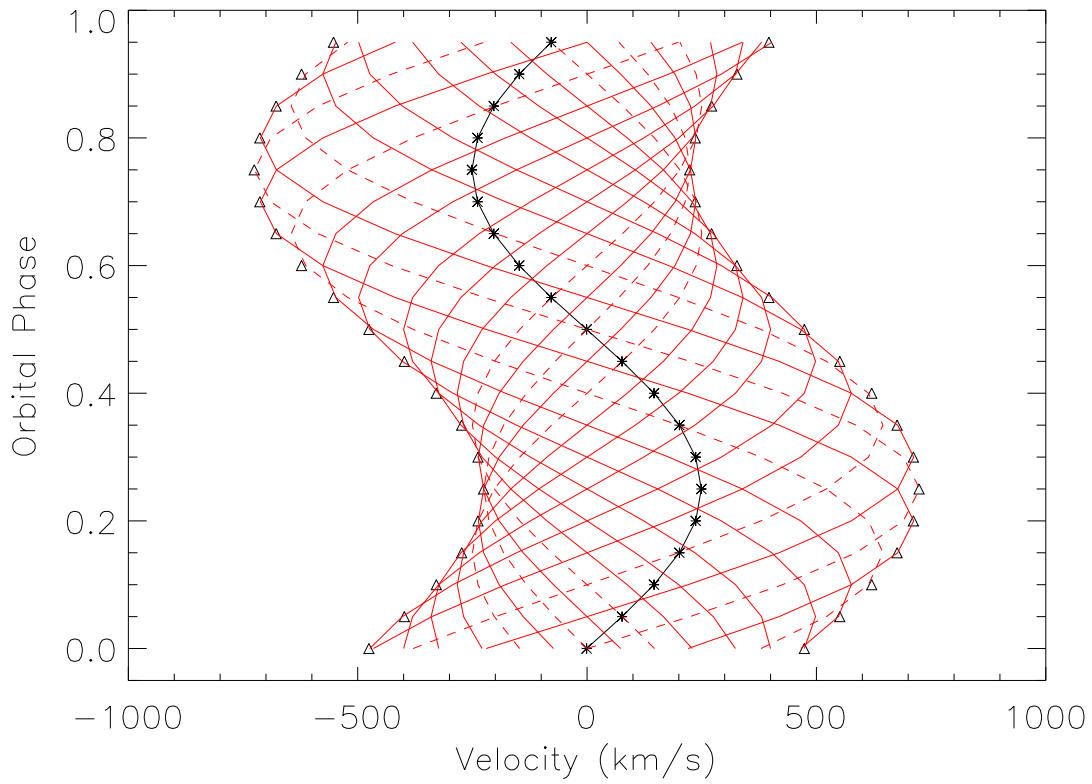

Figure 3.7: Explanation of how the ring is formed. Red s-waves correspond to points on the red ring of the skew map in Figure 3.5 (right). The thick black line corresponds to the peak point on the skew map in Figure 3.5 (right). The '$*$'s represent the peaks of the 20 CCFs. The 'Δ's represent the secondary peaks of the 20 CCFs that lie on either side of the main peak. Dashed lines represent the special case where a point on a secondary spoke passes through two primary CCF peaks as well as secondary CCF peaks.

To understand what causes the ring on the skew map in Figure 3.5 (right), consider the more complex case where double features have been cross-correlated. As in Figure 3.6, each red s-wave in Figure 3.7 represents a point on the red circle in the skew map in Figure 3.5 (right) defined by A and Φ_o. Figure 3.7 shows that the ring represents a set of sine waves which produces a 'thick' s-curve shape centred on the main peak s-wave. The ring is produced from constructive interference from all

the spokes centred on the secondary CCF peaks ('△'s Figure 3.7), and the special case where a point on the secondary spoke also passes through two primary CCF peaks (dashed lines in Figure 3.6).

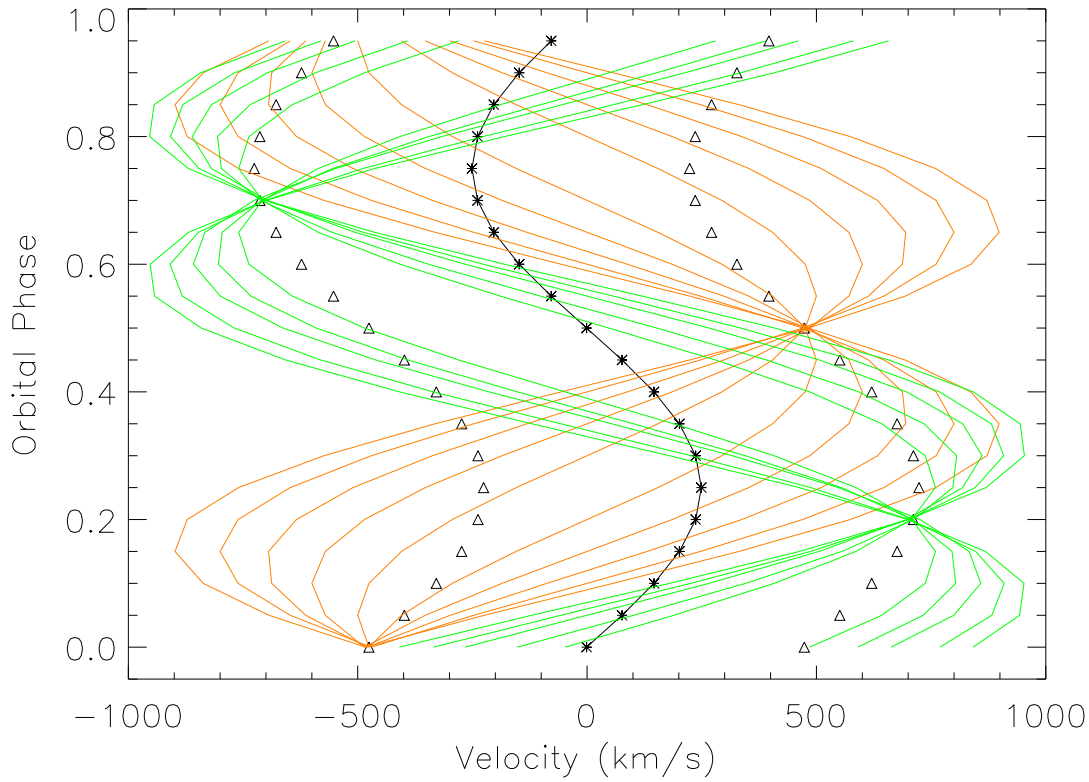

Figure 3.8: Explanation of how 'secondary' spokes are formed. Orange and green s-waves correspond to points on the orange and green spokes of the skew map in Figure 3.5 (right). The thick black line corresponds to the peak point on the skew map in Figure 3.5 (right). The '∗'s represent the peaks of the 20 CCFs. The '△'s represent the secondary peaks of the 20 CCFs that lie on either side of the main peak.

To understand what causes the secondary spokes on the skew map in Figure 3.5 (right), again consider the more complex case where double features have been cross-correlated. As in Figure 3.6 and 3.7, each orange and green s-wave in Figure 3.8 represents a point on the orange and green spokes in Figure 3.5 (right). These secondary spokes are formed in the same way as the primary spokes (in Figure 3.6), but instead of crossing the main CCF peaks twice, they cross each of the two secondary CCF peaks once. This is illustrated in Figure 3.8 where the orange spoke is

constructed from s-waves passing through secondary CCFs at phase 0.0 and 0.5, and the green spoke is constructed from s-waves passing through the secondary CCFs at phase 0.2 and 0.7. The secondary spokes are less intense than the primary spokes because they are centred on the secondary CCF peaks.

3.1.3 Monte Carlo Simulation

A Monte Carlo simulation was used to calculate the error of the skew map. The noise level on the normalised RW Tri spectra was used as a seed to generate normally distributed random numbers. This could be done because the calculated standard error (σ) is related to the full width half maximum (Γ) of a normal distribution using

$$\sigma = \frac{\Gamma}{2.354}. \tag{3.7}$$

The random numbers were added to the RW Tri spectra and a skew map was produced using the method in Section 3.1.5. In this way 150 skew maps were produced, and the distribution of peak velocity values was measured to derive an error. Each trial was weighted with the line integral intensity of its respective map, and used to compute a weighted standard deviation (σ_w) of the resulting distribution. σ_w is defined by

$$\sigma_w^2 = \frac{\sum_{i=1}^{N}(X_i - \bar{X}_w)^2 W_i}{\sum_{i=1}^{N} W_i}, \tag{3.8}$$

where X_i is velocity, W_i is the peak weighting, N is the number of values, and $\bar{X}_w$ is the weighted mean defined by

$$\bar{X}_w = \frac{\sum_{i=1}^{N} W_i X_i}{\sum_{i=1}^{N} W_i}. \tag{3.9}$$

NOTE - This method adds noise to the original data, therefore resulting errors will be overestimated.

3.1.4 Isaac Newton Telescope Observations

The FR spectra of RW Tri were obtained by R. C. Smith using the *Isaac Newton Telescope* (INT) and the 831R grating, giving a wavelength coverage of 7700Å - 8300Å (I-band). This range includes the Na I absorption feature (λ8183.3Å λ8194.8Å) that is expected in the spectrum of a late-type star. The INT has a 2.54m diameter primary mirror and belongs to the Isaac Newton Group of telescopes located in La Palma. A total of 27 time resolved spectra were taken over two nights spanning the full orbital cycle: 19 spectra were taken on the 2nd September 1985, and 8 spectra were taken on 3rd September 1985. The ephemeris of Robinson et al. (1991) was used to phase the spectra. A range of 7 template stars of spectral type K5 to M1.5 were taken from Martin (1988), the details of which are given in Table 3.1.

Name	Colour Index (J-I)	Spectral Type	Radial Velocity (km/s)
Gl 653	0.49	K5	23.0 ± 6
Gl 717	0.54	K7	-
Gl 673	0.60	K7	-28.3
Gl 488	0.67	M0$^-$	2.9 ± 1
Gl 383	0.70	M0	8.0 ± 15
Gl 281	0.71	M0	17.0 ± 6
Gl 908	0.87	M1.5	-71.2 ± 1

Table 3.1: Template stars from Martin (1988).

3.1.5 Skew-Mapping Method

Skew-mapping of spectra in the FR produces a radial velocity amplitude for the secondary star. The method used to obtain the skew maps was similar to the method used by Smith et al. (1998).

Template stars with different spectral types were normalised by dividing each spectrum by a low order spline fit of the respective continuum. The continuum of the template star was then set to zero by subtracting a higher order fit to the continuum. The 27 RW Tri spectra were also normalised using the same method and then cross-correlated with each template. A mask between 7760Å and 7800Å was used to remove the accretion disc absorption feature of neutral oxygen at 7774Å (Friend et al. 1988). The CCFs were then back projected to produce skew maps using MOLLY, a software package written by Tom Marsh. The systemic velocity was assumed to be zero. The skew map that gives the highest line integral value (the strongest peak) is the most accurate map (Section 3.1.1). The Monte Carlo simulation (Section 3.1.3) was then applied to produce an error for the best-fit skew map.

3.1.6 Skew-Mapping Results

Figure 3.9 shows the normalised template spectra for the FR in order of spectral type. The Na I absorption doublet can be clearly seen in Figure 3.9.

Figure 3.10 shows the average spectrum of RW Tri in the FR with and without the secondary star velocity removed. Figure 3.10 also show the best-fit template Gl 281. The 7774Å neutral oxygen triplet, and to a lesser extent the sodium doublet, can be seen as broad absorption features in the average FR spectra.

Plots of the skew maps can be seen in Appendix E, Figures 6.1 to 6.7. From these figures a large dispersion of radial velocity amplitudes can be seen, but the peaks of the maps are clear and lie on or just left of the $V_x = 0$ plane. The observed data were very noisy so absorption features could not be resolved very well (Figure 3.10),

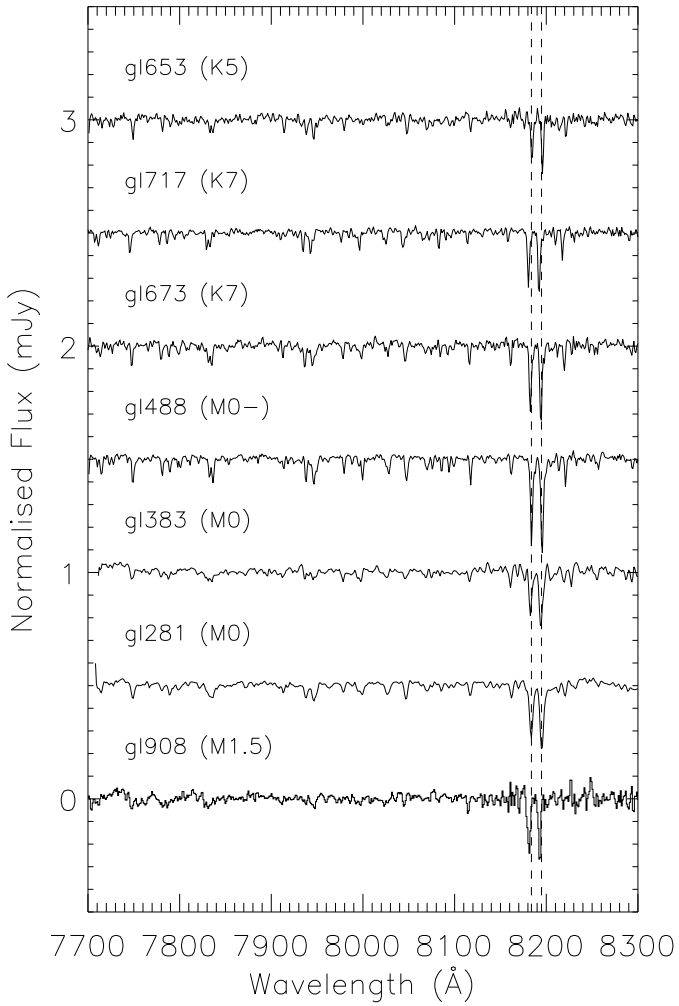

Figure 3.9: The normalised template spectra of the FR. The double dashed lines represent the rest wavelength of the Na I doublet λ8183.3Å and λ8194.8Å. The spectra are offset vertically by 0.5 normalised flux (mJy).

and therefore the peaks of the maps were not point like.

The velocity amplitude was found using the display package GAIA (version 2.5-3 written by Peter W. Draper & Norman Gray, and derived from Sky Cat version 2.4) enabling the peak to be magnified. Results can be seen in Table 3.2. Columns 1 and 2 list the name and spectral type of the template, column 3 lists the maximum peak strength and columns 4 and 5 list the corresponding V_y and V_x values. Template stars with the same spectral type have subtle differences in their spectrum (Figure 3.9), and therefore produce different skew maps with varying line integrals (Table 3.2,

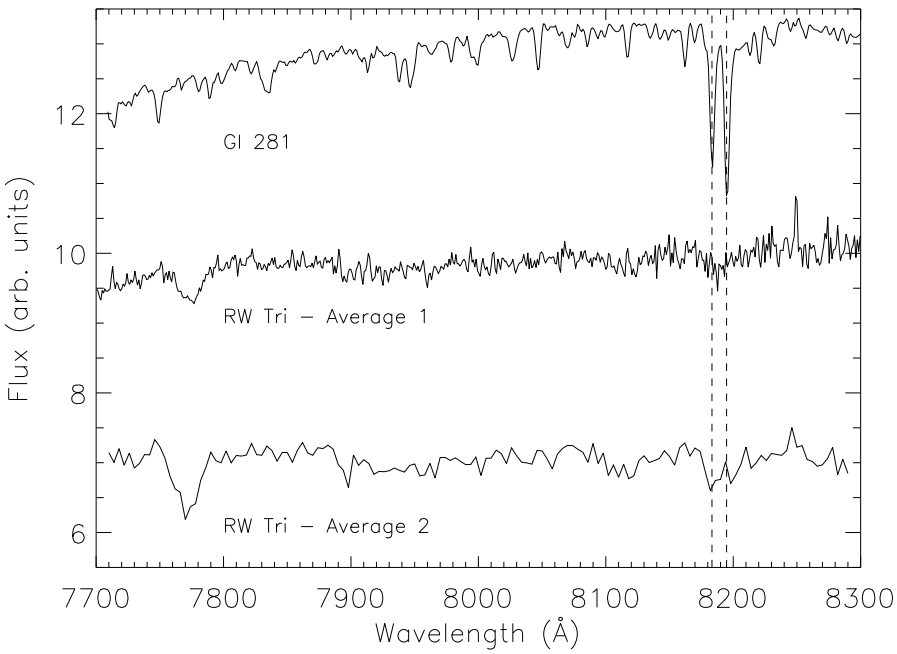

Figure 3.10: Average 1 is the average RW Tri spectra in the FR. Average 2 is the average RW Tri spectra in the FR with the secondary star velocity removed, the NaI doublet can be seen more clearly in this average plot. The best-fit template Gl 281 is flux scaled by a factor 1/34000 and offset by 5mJy. As in Figure 3.9 the dotted lines represent the rest wavelengths of Na I doublet.

Column 3).

The skew map with the strongest peak was found with the M0 template Gl 281. Patterson (1984) estimated the secondary star of RW Tri to be of spectral type M0, based on the empirical zero-age main-sequence (ZAMS) mass-radius relation. The result is also consistent with the statistical prediction of $K9 \pm 3$ by Smith & Dhillon (1998).

The best-fit skew map (Figure 3.11) has,

- $K_2 = 235 \pm 47$ km/s
- $V_x = 55 \pm 40$ km/s
- $I_{nt} = 107 \pm 62$

The peak value of the skew map is represented by •, and the '+'s represent the Monte Carlo simulated data peaks. The large blue cross hair represents $\bar{X}_w \pm \sigma_w$.

Template Name	Spectral Type	Line Integral (I_{nt})	V_y (km/s)	V_x (km/s)
Gl 653	K5	18.0	291.5	-29.5
Gl 717	K7	19.9	117.5	25.5
Gl 673	K7	35.1	246.5	19.5
Gl 488	M0$^-$	56.3	231.5	67.5
Gl 383	M0	78.2	255.5	42.5
Gl 281	M0	106.6	234.5	54.5
Gl 908	M1.5	44.1	69.5	42.5

Table 3.2: Skew map results of RW Tri in the FR, showing V_x and V_y for different template stars. The higher the value of I_{nt}, the better the match between the peak s-wave and the cross-correlation peaks of the data.

My result agrees within error with the value of $\sim$ 250km/s from Smith et al. (1993). Figure 3.10 plots the average RW Tri spectrum (Average 2) in the FR where the secondary star velocity has been removed using the best-fit skew map results. This plot shows that the Na I doublet can be resolved.

From the simulated data in Section 3.1.2, two things are expected. Firstly, the skew map should have spokes centred on the peak of the map corresponding to the number of cross-correlation functions (CCFs). Secondly, a point peak along $V_x = 0$ with a ring surrounding it should be seen. In this map 27 spokes are seen in an enhanced image (Figure 3.12) due to the 27 spectra producing the skew map. These spokes have different intensities due to the different fluxes of the spectra at different orbital phases. This is unlike the simulated data (Section 3.1.2), which had constant intensity throughout the orbital phase. The spokes in Figure 3.12 are not evenly distributed around the orbital cycle because the observations were not taken at equal increments in time. There are two strong spokes observed in the skew map,

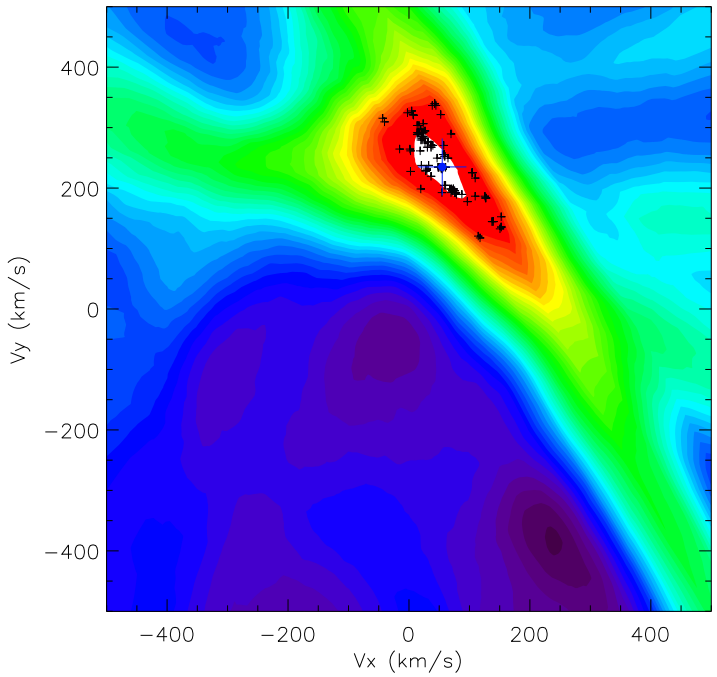

Figure 3.11: Best-fit skew map of RW Tri in the FR, resulting in $K_2 = 235 \pm 47$ km/s, over-plotted with Monte Carlo simulation data represented by '+'s. The peak of the skew map is represented by •. $\bar{X}_w \pm \sigma_w$ is represented by the large blue cross hair.

they are plotted as the 'main' spoke (magenta) and 'secondary' spoke (orange) in Figure 3.12.

The main spoke (magenta line in Figure 3.12) corresponds to a set of s-waves with varying amplitude. This set of s-waves crosses the s-wave which defines the peak value of the skew map at the phases of 0.07 and 0.57, corresponding to 24^o and 206^o in Figure 3.12.

The left arm (green line in Figure 3.12) corresponds to a strong CCF peak that lies very close to the main s-wave defining the peak value of the skew map. The left arm lies at the same phase as the point where the set of s-waves defining the secondary spoke (orange line in Figure 3.12) crosses the s-wave which defines the peak value of the skew map. This arm feature is not mirrored to the right of the main peak on the skew map because there are no CCF peaks occurring around this phase. A point-like peak surrounded by a ring as expected from the simulated data

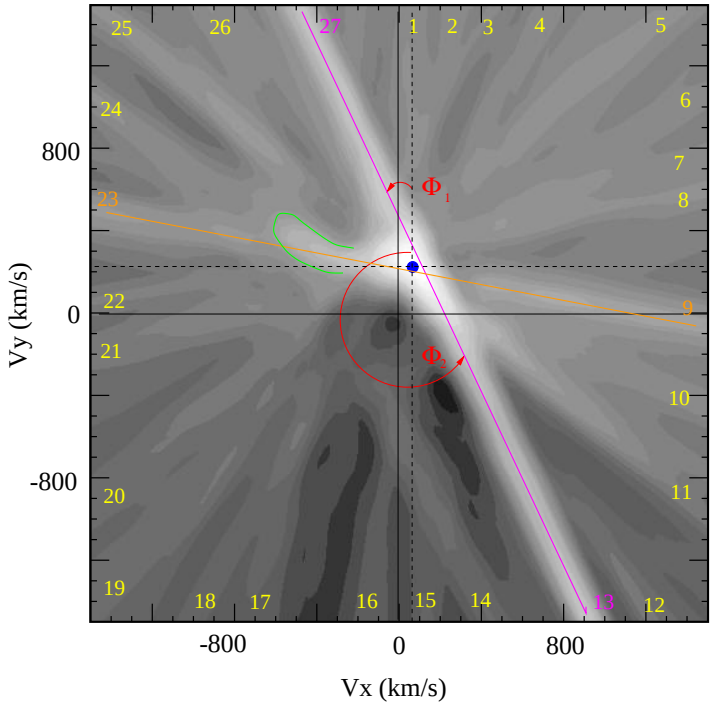

Figure 3.12: Enhanced best-fit skew map showing 27 spokes. Each spoke is numbered. The solid lines define the main spoke (magenta), secondary spoke (orange) and left arm feature (green). The two angles $\Phi_1 = 24^o$ and $\Phi_2 = 206^o$ correspond to the phases at which the set of main peak s-waves cross the s-wave defining the peak value of the skew map. • represents the peak of the skew map.

(Section 3.1.2) is not seen in the skew map because the RW Tri INT data are very noisy.

The peak of the data is expected to lie along $V_x = 0$ (Section 3.1.1), but my results show the peak of the map is at $V_x = 55 \pm 40$km/s. To test if this V_x value is due to the systemic velocities of RW Tri or the template star I input a range of $V_o - V_T$ values from -20km/s to 20km/s into the skew-mapping method and measure the peaks of the different maps produced. Figure 3.13 shows the results of this testing, where V_y is represented by $*$, and V_x is represent by $\triangle$. The solid and dotted lines represent skew map results of $V_y = 235$km/s and $V_x = 55$km/s respectively. Figure 3.13 shows within the skew map errors of ± 47km/s and ± 40km/s for V_y and V_x respectively, the systemic velocity does not greatly effect the position of the peak, therefore the V_x offset of the peak is due to the noise in the data. Figure 3.13 also shows that V_y is relatively insensitive to the systemic velocity, as shown by Smith

et al. (1998).

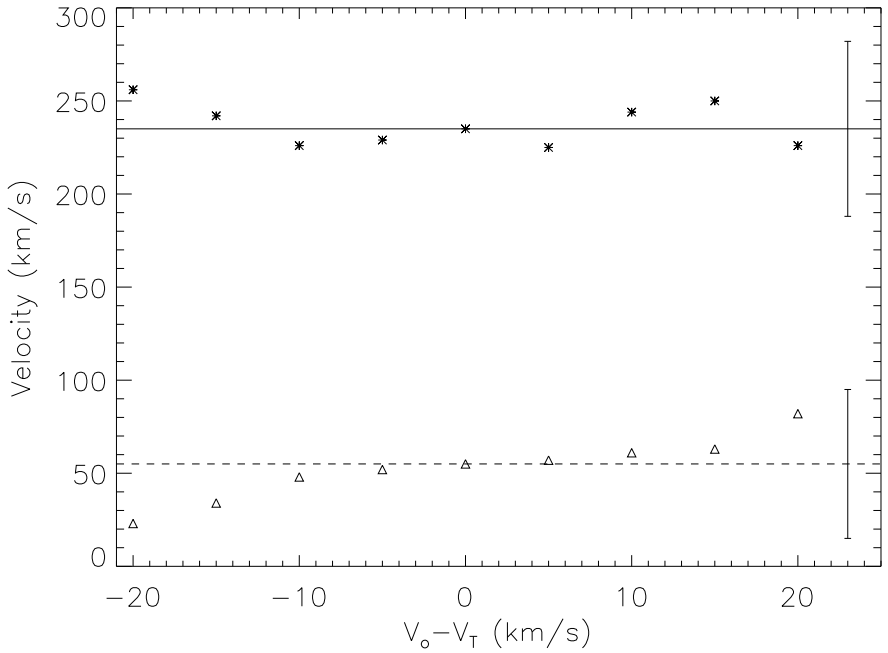

Figure 3.13: Test to see if systemic velocity is the cause of $V_x = 55 \pm 40$km/s in the skew map results. V_y ($*$) and V_x ($\triangle$) peak coordinates for a set of skew maps (y-axes) are plotted against the $V_o - V_T$ values (x-axes) used to produce the maps. The solid line represents $V_y = 235$km/s with an error bar of ± 47km/s. The dotted line represents $V_x = 55$km/s with an error bar of ± 40km/s.

Results using the same set of FR RW Tri data, but a different set of templates ranging from K5 to M4.5e have been obtained by Vande Putte et al. (2003). They find a best-fit skew map using the M1 template Gl 514 with $K_2 = 263 \pm 30$ km/s, and use a more sophisticated technique to obtain the systemic velocity of -11 ± 15 km/s involving an iterative process. Extrapolating V_x to zero from Figure 3.13, the systemic velocity appears to be between -20 and -30 km/s which is not dissimilar to the results of Vande Putte et al. (2003). The differences between their value of K_2 and those presented here (which are within the respective errors), are due to the different set of templates used.

3.2 Near Infrared Data

In the following sections I describe my UKIRT observations and data reduction, and then the results using this data.

3.2.1 United Kingdom Infra-Red Telescope Observations

The *United Kingdom Infra-Red Telescope* (UKIRT), located on the summit of Mauna Kea, Hawaii, is operated by the Joint Astronomy Centre (JAC) on behalf of the U.K. Particle Physics and Astronomy Research Council (PPARC). The telescope is a 3.8m classical Cassegrain Telescope with a thin primary mirror.

Data on RW Tri from 6th to 7th August 2000 were taken in the NIR K-band using the Cooled Grating Spectrometer 4 (CGS4) on UKIRT. CGS4 is a $1-5\mu$m multi-purpose 2D grating spectrometer containing a 256×256 InSb array, installed in a cryostat which is cooled by liquid nitrogen and closed cycle coolers (Hirst 2001). The instrument has a calibration unit containing a blackbody source for flat-field measurements, and argon, krypton, and xenon arc lamps for wavelength calibration.

I obtained observations using the 150 line/mm grating. This gave a spectral resolution of 100 km/s at 2.2μm using the 150 mm camera, and wavelength coverage of 0.075μm allowing different secondary star absorption features to be observed. The telescope was also nodded up and down the slit taking spectra at different detector positions to facilitate the removal of night sky spectrum.

The majority of each night was taken up observing RW Tri in order to cover the orbital period of the system; observational data of RW Tri can be seen in Table 3.3. During the first night there was a very fine cloud coverage around 10:15 UT that had dissipated by 10.25 UT. At 8.15 UT on the second night a software crash halted observations for $\sim$40mins. A total of 35 spectra were taken of RW Tri over the two nights: 15 spectra on the first night, and 20 spectra on the second. Summing the data from the telescope nodding positions gave a total exposure time of 600s for each RW Tri spectrum. This exposure time is equivalent to 0.03 orbital cycles,

which is short enough to prevent any significant smearing due to orbital effects. The instrumental smearing [3] (v_{res}) is

$$v_{res} = \frac{2\pi K_2 t_{exp}}{P_{orb}} = 44 \pm 8 \text{ km/s} \tag{3.10}$$

(Watson & Dhillon 2001), where K_2 is taken from the skew-mapping results (Section 3.1.6), t_{exp} is the exposure time (600s), and P_{orb} is the orbital period of the system (20040s). The instrumental smearing is half the instrumental resolution of 100 km/s, therefore the secondary star radial velocity (235 km/s from Section 3.1.6) is clearly measurable.

Name	Observational date (UT)	UT start	UT end	Exposure Time (s)	Central Wavelength (μm)
RW Tri	6/9/00	05:35:31	06:32:52	150	2.290
RW Tri	6/9/00	07:38:09	14:03:39	150	2.235
RW Tri	7/9/00	05:16:01	08:15:18	150	2.235
RW Tri	7/9/00	08:52:37	13:57:07	150	2.235

Table 3.3: RW Tri observations in the NIR.

Towards the end of each night after RW Tri had set, template stars in the spectral range K5 to M2 were observed (Table 3.4). A total of ten template stars were observed over the two nights.

In order to observe the secondary star of RW Tri, the 150 line/mm grating was used to cover a wavelength range 2.255μm - 2.330μm to include the Ca I and ^{12}CO absorption features observed in RW Tri by Dhillon et al. (2000). On inspecting the real time reduced data using ORAC-DR the Ca I absorption triplet was weakly seen, and the ^{12}CO absorption band features were not present. Hence the observed

[3] Instrumental smearing is the smearing due to the use of a finite exposure time.

Name	Spectral type	Observational date (UT)	UT start	UT end	Exposure Time (s)	Radial Velocity (km/s)
Gl 397	K5	7/9/00	15:33:32	15:36:19	5	21
Gl 334	K7	6/9/00	15:28:58	15:32:49	10	32.2
Gl 3478	K7	7/9/00	14:43:44	14:49:04	20	-
Gl 182	M0	6/9/00	14:32:27	14:38:34	20	39
Gl 281	M0	7/9/00	14:23:49	12:28:01	12	18.5
Gl 383	M0	7/9/00	15:53:09	15:57:53	14	8.0
Gl 212	M0.5	6/9/00	15:02:06	15:05:52	10	-3.0
Gl 390	M1	7/9/00	15:18:53	15:22:40	10	25.0
Gl 382	M1.5	7/9/00	15:04:15	15:07:19	7	12.2
Gl 393	M2	7/9/00	15:12:32	15:15:32	7	12.7

Table 3.4: Template stars observed in the NIR. The radial velocity values were obtained from Simbad (2004).

wavelength range was altered to cover 2.200μm - 2.275μm. This wavelength range covered the Na I and Ca I absorption lines recorded by Dhillon et al. (2000), and both features were present in the real time data reduction spectra.

A-type standard stars were observed to flux calibrate the RW Tri and template spectra and to remove telluric lines. The RW Tri standard star was observed at the beginning of each night, and then three more times during each night. On the first night the RW Tri standard star was observed at 7:22 UT, after the cloud coverage at 11:15 UT, and again at 13:07 UT. On the second night the RW Tri standard star was observed at 7:00 UT, 9:41 UT, and 12:02 UT. The template standard stars were observed before each template star observation.

Arc and flat field spectra were also observed through both nights before standard

A-star observations. The Xenon arc lamp was used because it contained the most features in the observed wavelength range. Arc and flat field spectra are used for wavelength calibration and the removal of pixel-to-pixel array variations respectively.

To calculate the secondary star velocity in RW Tri normalised spectra are used, hence an absolute flux scale is not needed, therefore I do not correct for atmospheric extinction. However, for completeness, I note that the range in the airmass of RW Tri was 1.10-1.79 on the first night and 1.01-2.04 on the second night, with the standard stars reaching air masses of 2.07 and 1.98 respectively. The relatively low extinction for the standard stars (0.096 mag/airmass in the K band) has no appreciable effect on their brightness. The range in airmass of the template stars and their standard stars were 1.09-1.44 on the first night and 1.01-1.85 on the second night.

3.2.2 UKIRT Data Reduction

The initial steps of the data reduction were undertaken at the telescope using the ORAC-DR data reduction package developed at the Joint Astronomy Centre by Frossie Economou and Tim Jenness in collaboration with the UK Astronomy Technology Centre as part of the ORAC project. These initial steps were;

- applying a bad pixel mask to remove bad pixels,
- bias frame subtraction,
- flat field division to remove pixel-to-pixel variations across the array,
- interlacing and co-adding the source spectrum obtained at different detector positions as a result of nodding the telescope along the slit, to accurately remove night sky spectrum.

Bad pixels were found close to the Na I doublet feature at 22063Å and 22101Å on night 1, and 22078Å and 22116Å on night 2. The difference between the apparent wavelengths of the bad pixels between the nights is due to a slight shift in the grating

angle. These bad pixels were removed from the ORAC-DR images by interpolation, before the spectra were extracted.

Further data reduction was carried out using the FIGARO general data reduction package version 5.4.0 developed by Keith Shortridge. Spectra were extracted, and wavelength calibrated using the arc spectrum, and telluric lines were removed using standard A-stars. RW Tri and template spectra were then flux calibrated using the appropriate standard A-stars. The resulting RW Tri and template spectra were smoothed and rebinned on to a linear wavelength scale. The ephemeris of Robinson et al. (1991) was used to phase the data. The midpoint of each 600s exposure was used as the observation time.

3.2.3 Near Infrared Results

Figure 3.14 shows the normalised template spectra for the NIR in order of spectral type. The Na I doublet and Ca I triplet absorption features in the NIR can clearly be seen. There are no large differences in the depths of the Ca I and Na I lines in the different spectral types, making it hard to distinguish between the different spectral types in this wavelength band.

Figure 3.15 shows the average spectrum of RW Tri in the NIR with the M0 template Gl 281. Figure 3.16 shows the individual spectra of RW Tri distributed in orbital phase. The Na I and Ca I absorption features appear to shift from spectrum to spectrum on both nights.

The Secondary Star Velocity

The velocity of the secondary star in RW Tri was investigated by cross-correlating the spectra of RW Tri with the template spectra. The RW Tri and template spectra were normalised in the same way as described for the FR data (Section 3.1.5), and rebinned on to the same wavelength scale. Each RW Tri spectrum is cross-correlated with each template spectrum in turn. The position of the correlation peak was then

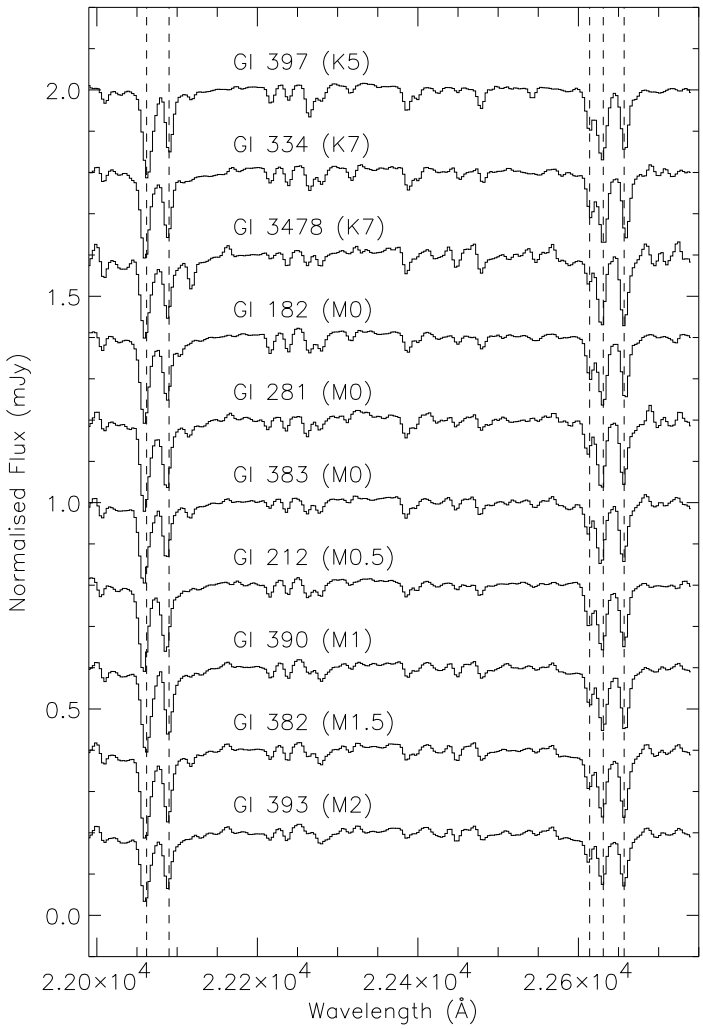

Figure 3.14: The normalised template spectra of the NIR data. The double dashed lines on the left of the plot represent the rest wavelengths of the Na I doublet λ22062Å λ22090Å, and the triple lines on the right indicate the wavelengths of the Ca I triplet λ22614Å, λ22631Å, λ22657Å. The spectra are offset vertically by 0.2 normalised flux (mJy).

plotted against orbital phase to produce the velocity curve of the secondary star. The method of skew-mapping was not used for this data set, because the position of the cross-correlation peaks could be clearly defined. As in skew-mapping (Section 3.1.5), the spectral template that yields the strongest cross-correlation peak is the best-fit to the data. All the cross-correlation results gave similar values, which is what I expect as there is little variation in the relative strengths of the Na I and Ca I lines from Figure 3.14; therefore I consider the average of all the templates.

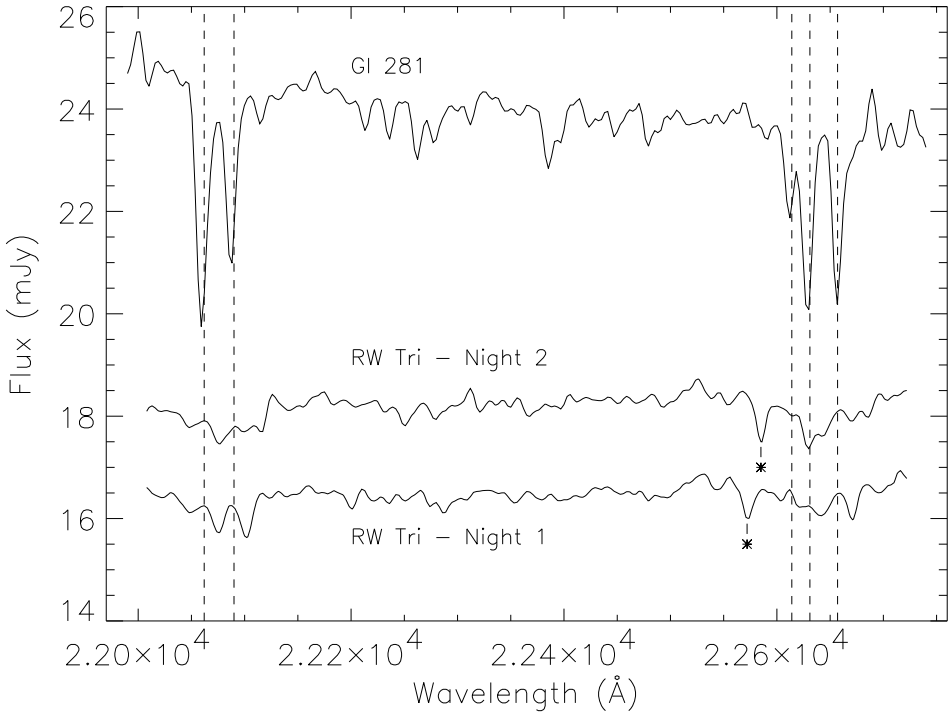

Figure 3.15: Average RW Tri spectra of each night in the NIR. The M0 template Gl 281 is flux scaled by a factor 1/170 and offset by 1.5mJy, and the average night 2 data is offset by 1.2mJy. The absorption feature marked by $*$ is due to bad pixels. As in Figure 3.14 the dotted lines represent the rest wavelength of Na I doublet (left), and the Ca I triplet (right).

The radial velocity of the templates was not taken into account when averaging, because these velocities are smaller than the resolution of the data (Section 3.2.1). The best-fit radial velocity curve of the average cross-correlation lags using all the template data is illustrated in Figure 3.17.

This velocity curve can be interpreted as

$$V = \gamma + K_2 \sin(2\pi(\Phi - \Phi_o)), \tag{3.11}$$

where V is the radial velocity, γ is the systemic velocity, K_2 is the radial velocity amplitude, Φ is the binary orbital phase defined by the ephemeris of Robinson et al. (1991), and Φ_o is the orbital phase of blue to red zero crossing (inferior conjunction of the secondary). A sinusoidal curve was fitted to the velocity data

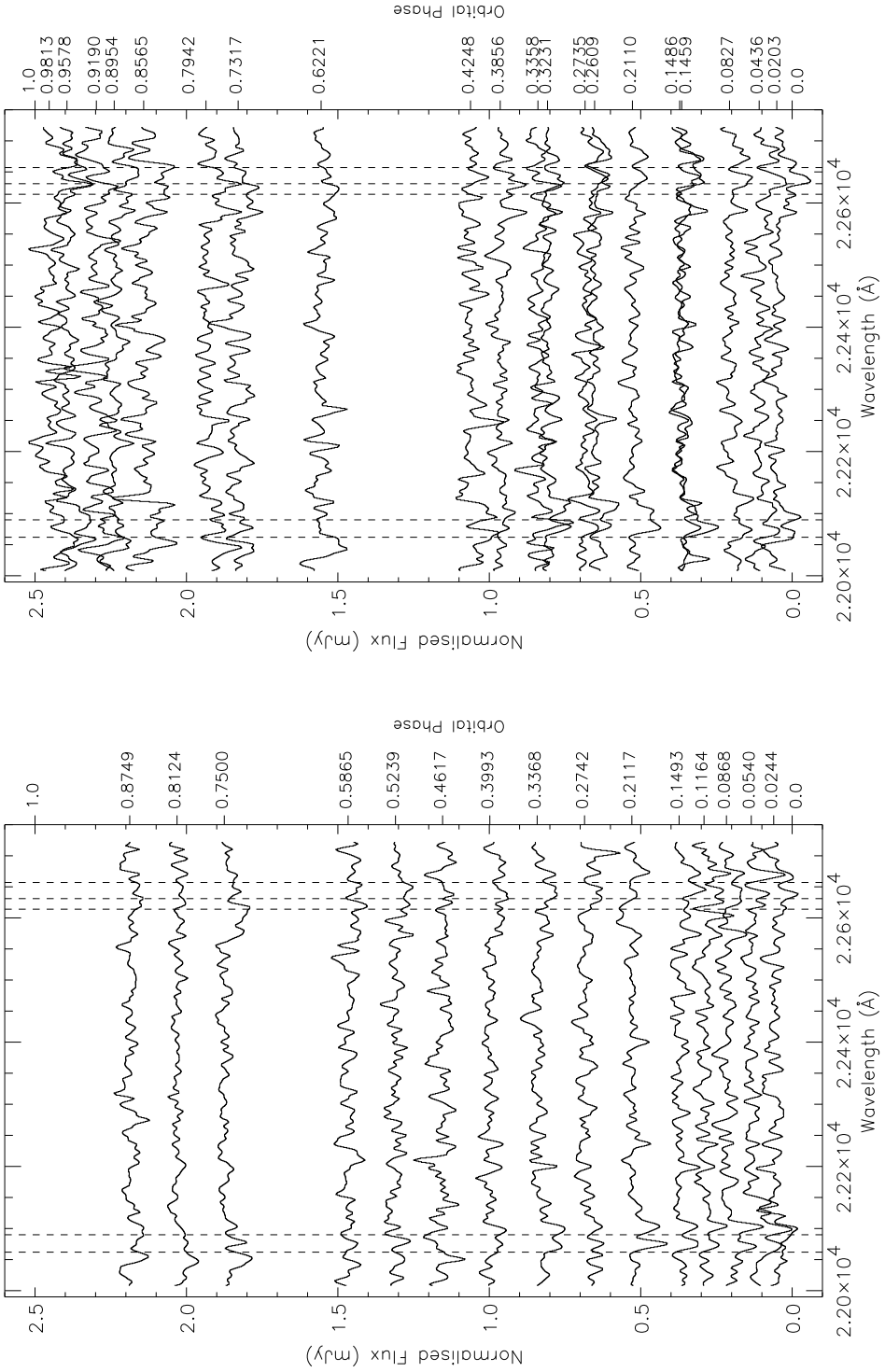

Figure 3.16: Normalised RW Tri spectra. Bottom: The normalised RW Tri spectra of the first night plotted in orbital phase. Top: The normalised RW Tri spectra of the second night plotted in orbital phase. In both plots the dotted lines represent the rest wavelength of Na I doublet (left) and Ca I triplet (right) as in Figure 3.14. Each spectrum is vertically offset by 2.5 times its orbital phase.

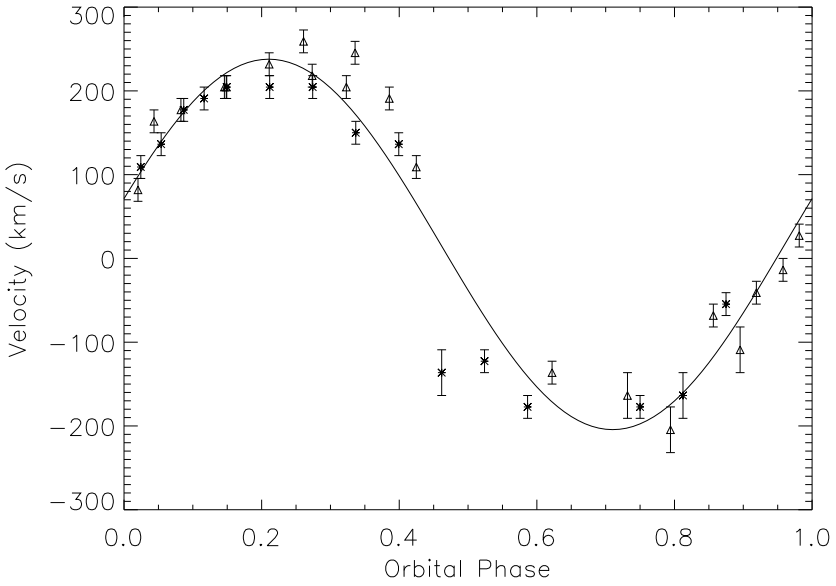

Figure 3.17: The best-fit radial velocity curve of the two nights combined. The symbols $*$ and $\triangle$ represent the data points from night 1 and 2 respectively. Each point is the mean of the lags derived from various stellar templates used (Table 3.4) and the error bars are the standard deviation of the results from the different templates, and therefore express the systematic error on the data due to template choice. The sinusoidal line represents the best-fit velocity curve.

using the Levenberg-Marquardt algorithm in IDL; by minimising the reduced chi-squared (Appendix B) and considering the 68.3 % (1σ) confidence level, a best-fit velocity and error was calculated. This results in,

- $K_2 = 221 \pm 29$ km/s
- $\gamma = 17 \pm 20$ km/s
- $\Phi_o = -0.040 \pm 0.020$ orbital phase ($= 0.002 \pm 0.001$ days)

Figure 3.18 shows the O-C diagram for the ephemeris of Robinson et al. (1991) for RW Tri using eclipse minimum data spanning from 1937 to my NIR data (Mandel 1965, Africano et al. 1978, Longmore et al. 1981, Robinson et al. 1991, Horne & Stiening 1985, Still et al. 1995, Rutten et al. 1992, and Mason et al. 1997). The large error on the NIR data in Figure 3.18 is caused by the eclipse time which is inferred from spectral data fitted with a sinusoid rather than being measured directly

using an eclipse profile.

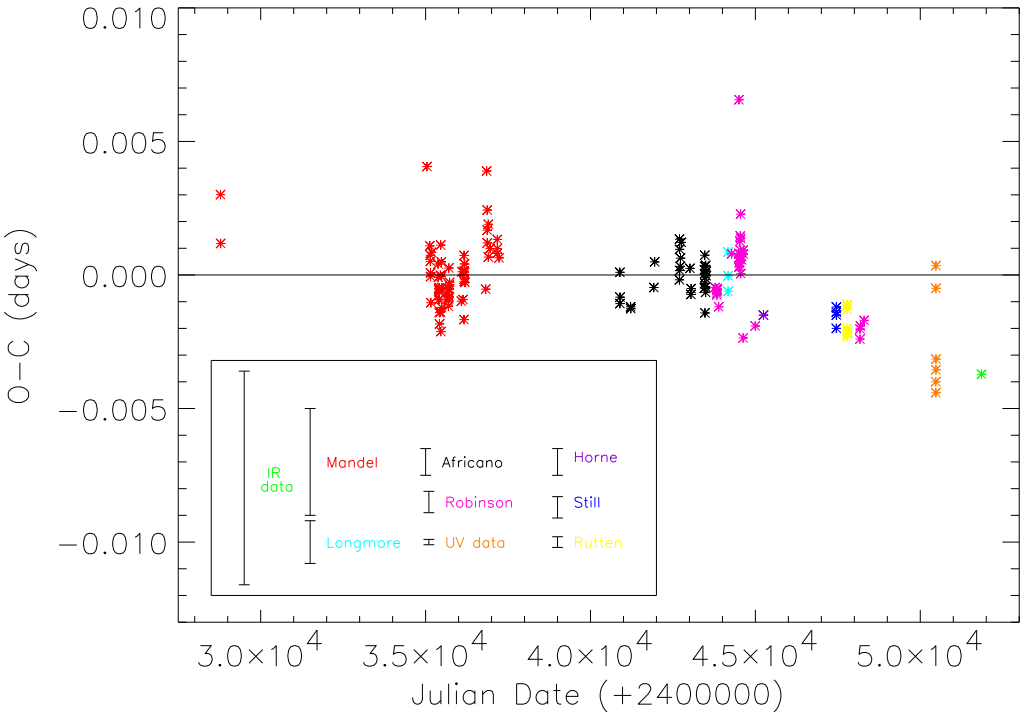

Figure 3.18: O-C diagram for the ephemeris given by Robinson et al. (1991). Data points are obtained from Mandel (1965 - red), Africano et al. (1978 - black), Longmore et al. (1981 - cyan), Robinson et al. (1991 - magenta), Horne & Stiening (1985 - purple), Still et al. (1995 - blue), Rutten et al. (1992 - yellow), ultraviolet data from Chapter 2 (orange), and NIR data from this Chapter (green). The error bars for each data set are shown at the bottom of the plot using the same colour key.

Only the inner accretion disc and white dwarf emit in the ultraviolet, therefore the continuum is relatively small in size and is likely to give a more accurate measurement of the primary star eclipse. However, there is no previous ultraviolet eclipse minimum to compare the HST data points to, therefore NIR and optical data from previous authors must be used to formulate the ephemeris. The data points in Figure 3.18 have a dispersion about the mean of up to 0.007 days. There is no convincing cyclic variation with time in the O-C diagram; a linear fit to these data is adequate (see Chapter 1 Section 1.3.1 for discussion).

In Figure 3.19 the individual spectra of RW Tri are plotted as a function of

orbital phase, as in Figure 3.16, but with the best-fit absorption velocity shift taken out (221 ± 29 km/s) and the orbital phase corrected (-0.040 ± 0.020 orbital phase). Figure 3.20 shows the velocity corrected average spectrum of RW Tri for each night, and the scaled M0 template Gl 281. The Na I doublet and Ca I triplet are clearly seen in both nights (Figures 3.19 and 3.20).

Secondary Star Absorption Features

To determine whether the absorption features in RW Tri vary in strength through the orbital cycle, I compare the depth of the strongest features in the velocity corrected spectrum of RW Tri with the values observed in the template star spectrum. I use the Gl 281 template because it gave the best match to RW Tri in the I-band (Section 3.1.6). The combined regions around the Na I absorption feature (22010Å - 22140Å) and the Ca I absorption feature (22570Å to 22700Å) are considered, masking out the rest of the spectrum. Figure 3.21 shows a plot of the ratio of RW Tri versus template star absorption feature deficit through the orbital cycle. There is some evidence that the secondary features are strongest near phase 0.0 and weaker near phase 0.5. This suggests that the centroid of the secondary features is shifted to the hemisphere of the secondary that faces away from the disc. To a first approximation the best sinusoidal fit to the data has an amplitude of 0.27 ± 0.18 (solid line in Figure 3.21). This sinusoidal fit implies that the secondary star contributes $\sim 39\%$ of the NIR flux at phase 0.0, while at phase 0.5 this percentage is reduced to $\sim 15\%$. Hence, the absorption in the hemisphere of the secondary star nearest to the primary star is ~ 0.4 times the strength of the absorption in the back hemisphere. If part of the modulation in Figure 3.21 is due to the primary star and accretion disc eclipsing the secondary star, the sinusoid will overestimate the degree of heating. In Chapter 4 I consider the strength of absorption in the front hemisphere of the secondary star (hemisphere closest to the primary star) to be between 0 and 0.4 times the strength of absorption in the back hemisphere derived from the sinusoidal fit (Chapter 4, Section 4.3.3).

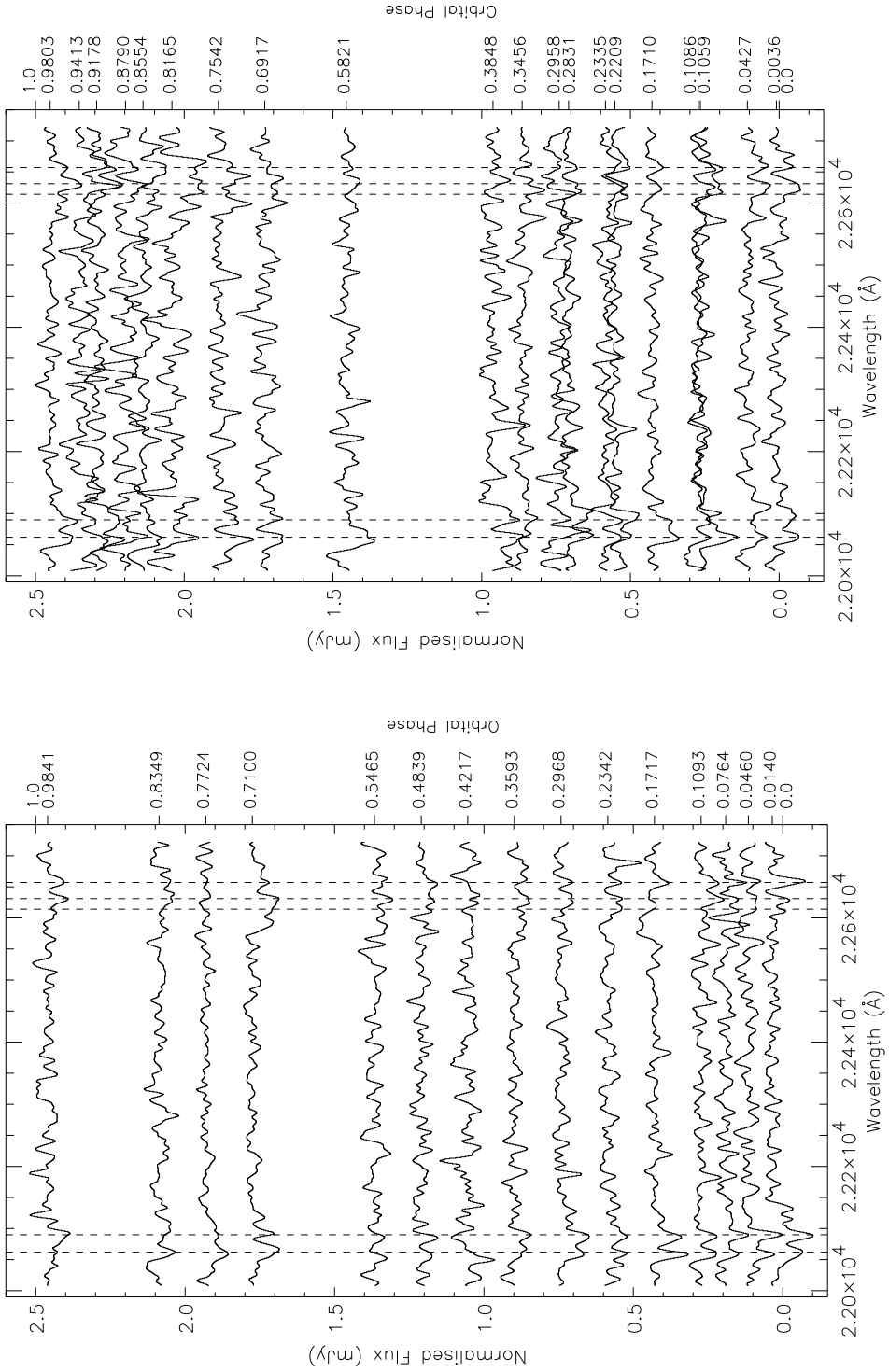

Figure 3.19: Normalised RW Tri spectra with the secondary star velocity removed and corrected orbit phase. Bottom: The normalised RW Tri spectra of the first night plotted in orbital phase with the secondary star velocity removed. Top: The normalised RW Tri spectra of the second night plotted in orbital phase with the secondary star velocity removed. In both plots the dotted lines represent the rest wavelength of the Na I doublet (left) and Ca I triplet (right) as in Figure 3.14. Each spectrum is vertically offset by 2.5 times its orbital phase.

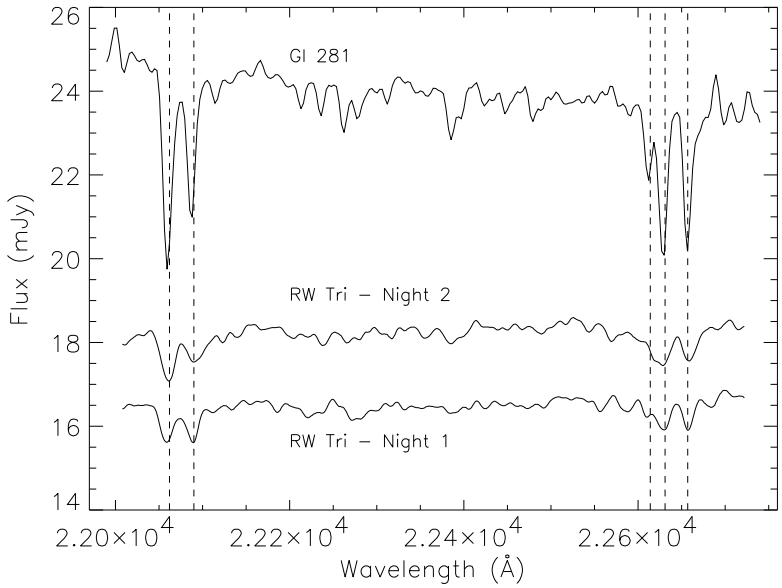

Figure 3.20: Average NIR RW Tri spectra of each night with the secondary star velocity removed. The best-fit template Gl 281 is flux scaled by a factor 1/170 and offset by 1.5mJy, and the average night2 data is offset by 1.2mJy. As in Figure 3.14 the dotted lines represent the rest wavelengths of Na I doublet (left), and the Ca I triplet (right).

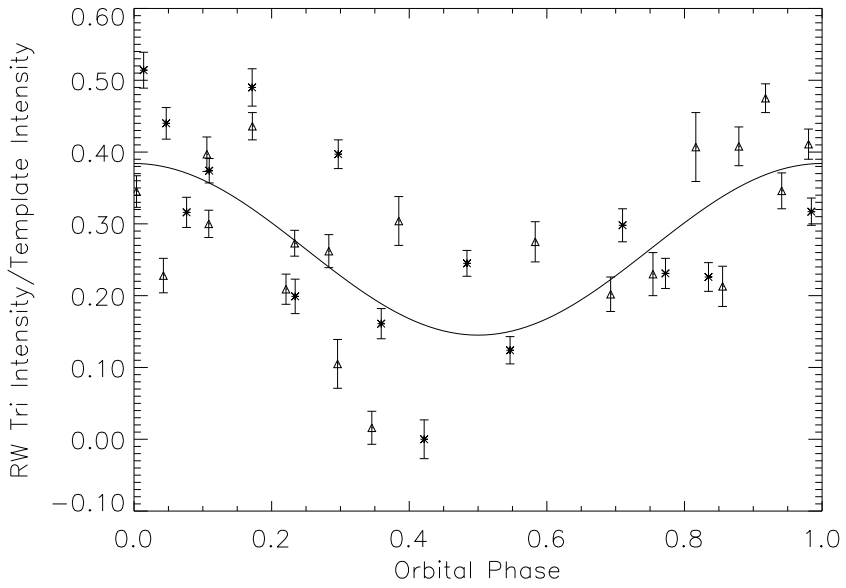

Figure 3.21: The total flux deficit in the Na I and Ca I RW Tri secondary star absorption features, expressed as an equivalent width (EW), divided by the corresponding equivalent width in the template star Gl 281. Each spectrum was corrected for secondary star velocity shift and orbital phase. Night 1 is represent by $*$, and night 2 is represented by $\triangle$. The solid line represents the best sinusoidal fit to the data.

Averaging over orbital phase the results suggest that the secondary star contributes on average $29 \pm 13\%$ of the K-band flux. This is considerably different from the $65 \pm 5\%$ out-of-eclipse flux estimated by Dhillon et al. (2000). The AAVSO quick look light curves of RW Tri at the time of my UKIRT observations show that RW Tri was at a magnitude of $m_1 \sim 13$, but during the observations of Dhillon et al. (2000) RW Tri appeared to be in a low state with a magnitude of $m_2 \sim 13.8$. Thus using

$$m_2 - m_1 = 2.5 \log \left(\frac{f_{m1}}{f_{m2}} \right), \tag{3.12}$$

where f_{m1} and f_{m2} are the fluxes relating to the magnitudes m_1 and m_2 respectively. RW Tri was approximately a factor of 2 brighter during my observations than when observed by Dhillon et al. (2000), accounting for the different estimates of the secondary star contribution. Assuming that the flux of the secondary star is constant, the accretion disc and stream increased by a factor of ~ 4.1 in brightness between the two observations (using Equation 3.12).

Secondary Star Rotational Velocity

The equatorial rotational velocity of the secondary star is defined as

$$V_{rot} = \frac{2\pi R_2}{P_{orb}}, \tag{3.13}$$

assuming that the secondary star is locked to the binary orbit due to tidal interactions (Friend et al. 1990). Dividing Equation 1.9 (Chapter 1, Section 1.1.1) by Equation 3.13, and substituting in Equations 1.12, 1.15 and $M = M_1 + M_2$ (Chapter 1, Section 1.1.1) leads to

$$\frac{K_2}{V_{rot} \sin i} = \left[(1+q) \left(\frac{R_2}{a} \right) \right]^{-1}, \tag{3.14}$$

where $q = M_2/M_1$ is the mass ratio of the system, R_2 is the radius of the secondary star, a is the binary separation, and $V_{rot} \sin i$ is the projected rotational velocity as determined from the spectral broadening of the secondary star lines.

The radial velocity of the secondary star can be calculated in the NIR by artificially broadening the template star spectra which are assumed to have low $V_{rot} \sin i$, and fitting it to the RW Tri spectra. The method used to obtain the rotational velocity of the secondary star was similar to that described by North et al. (2000).

At orbital phases other than 0 the absorption features are altered by irradiation, so I considered the velocity corrected NIR RW Tri spectra close to phase 0 (0.9−1.1), along with each template spectrum. The continuum was removed from the RW Tri and template spectra using a low order polynomial after masking out strong absorption features. Each template spectrum was then artificially broadened in the velocity range $V_{rot} \sin i = 10 - 200$km/s in steps of 10km/s, assuming a range of limb darkening coefficients from $0.0 - 1.0$ using MOLLY. The template and RW Tri spectra were rebinned onto the same wavelength scale and cross-correlated, then the broadened template spectra were shifted by the cross-correlation lag results. Residual spectra were produced by subtracting a constant that was multiplied by the shifted broadened template with each RW Tri spectrum; the constant was adjusted to minimise the scatter on each residual spectrum. A boxcar average smoothing was applied to the residual spectrum to eliminate any large-scale structure. The reduced chi-squared (χ^2_ν - Appendix B) was calculated between each residual and smoothed spectrum in the wavelength regions containing the Na I feature (22040Å to 22108Å) and the Ca I feature (22570Å to 22700Å).

All template stars gave the same order of χ^2_ν values around the phases $0.9 - 1.1$, confirming that data is not template sensitive in this wavelength band. The minimum χ^2_ν values for given templates lead to a range of $V_{rot} \sin i$. Table 3.5 shows the range in $V_{rot} \sin i$ when the average data of nights 1 and 2 for the Na I and Ca I absorption features are considered, along with all template stars and limb darkening coefficients of $0.0 - 1.0$. These results show that the limb darkening coefficient does not greatly effect the final results, although a value of 0.0 generally produces a lower limit to $V_{rot} \sin i$ while 1.0 leads to an upper limit.

Figure 3.22 shows the minimum χ^2_ν values produced for the M0 template Gl

Limb darkening coefficient	Na I feature (km/s)	Ca I feature (km/s)
0.0	120 - 150	90 - 100
0.5	130 - 160	90 - 100
1.0	140 - 170	100 - 110

Table 3.5: $V_{rot} \sin i$ results for different limb darkening coefficients, corresponding to a range of template stars. The results for each feature contain the average for nights 1 and 2.

281. The black, cyan and magenta lines indicate the average Na I and Ca I results for the limb darkening coefficients of 0.0, 0.5 and 1.0 respectively; the dashed line represents the average data of all the templates. Figure 3.22 shows how a change in the limb darkening coefficient produces a lower and upper limit for $V_{rot} \sin i$. Based on the χ^2_ν distribution in Figure 3.22 and Table 3.5, I estimate a best guess $V_{rot} \sin i = 120 \pm 20$km/s. I checked that the $V_{rot} \sin i$ of each template was $\sim$ 0km/s, by cross-correlating the templates against each other.

When using $V_{rot} \sin i = 120$km/s to broaden the template stars and reproduce the skew maps in the FR and the velocity curve in NIR, the velocity results were not affected. This is because rotational broadening affects the profile of the absorption lines, but not the position of the line centroids, which govern the cross-correlation peak positions.

3.3 Conclusions

I have calculated the radial velocity amplitude of the secondary star in RW Tri using the methods of skew-mapping in the FR and cross-correlation in the NIR. It is the first time that the NIR has been used to measure the secondary star velocity using a direct cross-correlation technique. The results of 235 ± 47 km/s (in FR) and 221 ± 29

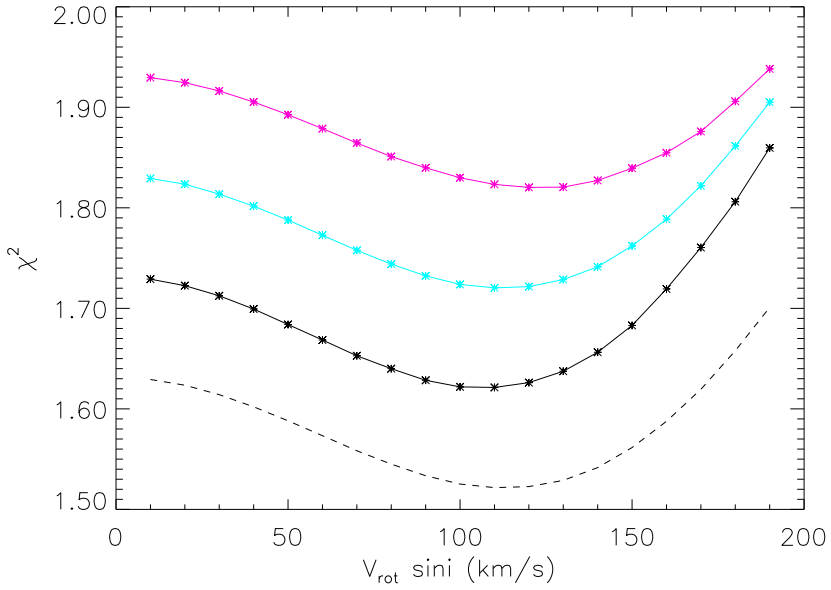

Figure 3.22: Plot of χ^2_ν obtained when the NIR M0 template GL 281 was artificially broadened by $V_{rot} \sin i$ in the range $10 - 200$km/s. This shows the minimum χ^2_ν for limb darkening coefficients 0.0 (black - offset by $0.1\chi^2_\nu$), 0.5 (cyan - offset by $0.2\chi^2_\nu$) and 1.0 (magenta - offset by $0.3\chi^2_\nu$), where the Na I and Ca I results have been averaged. The average data of all the templates is represented by the dashed line.

km/s (in NIR) agree within the errors. The spectral type for the secondary star is found to be M0 in the FR, but there is little variation in the relative strengths of the absorption features in the NIR, making the data insensitive to spectral type.

Using the NIR data I find a $V_{rot} \sin i = 120 \pm 20$km/s using the Na I and Ca I secondary star features, and a range of limb darkening coefficients.

Chapter 4

The Component star masses of RW Tri

Since first being observed as an eclipsing variable (Protitch 1937) multi-wavelength studies of RW Tri have provided much insight into the system but have yet to yield an accurate measurement of the masses of the two component stars. By observing the velocity of the component stars, their masses can be calculated using Kepler's third law (Chapter 1, Section 1.1).

In this Chapter I use the radial velocity amplitudes of 235 km/s in the far red and 221 km/s in the near infrared found in Chapter 3. I use these velocities with $V_{rot} \sin i$ results of Chapter 3 and proposed white dwarf velocities found by other authors (Kaitchuck et al. 1983, Still et al. 1995 and Mason 1999), to calculate the mass ratio and individual masses of the component stars within RW Tri.

4.1 Calculating the Mass

To calculate the masses of the two component stars in the system, the mass ratio (q) is used

$$q = \frac{K_1}{K_2} = \frac{M_2}{M_1}, \tag{4.1}$$

where K_1 and K_2 are the radial velocity amplitudes of the primary and secondary stars respectively, and M_1 and M_2 are the primary and secondary star masses respectively.

The inclination angle (i) of the system also needs to be determined. RW Tri is an eclipsing system, therefore the eclipse width leads to an estimate of the inclination angle.

4.1.1 Eclipse Width

The geometry of an eclipsing binary system is controlled by the inclination angle (i) and the mass ratio (q). Since the mass ratio defines the size and shape of the Roche lobe (Chapter 1 Section 1.1.2). Chanan et al. (1976) numerically calculated the white dwarf eclipse half width ($\phi_{1/2}$) as a function of the inclination angle and mass ratio using Roche lobe geometry. Their results are shown graphically in Figure 4.1, where curves of $\phi_{1/2}$ are plotted as a function of inclination angle for various values of mass ratio.

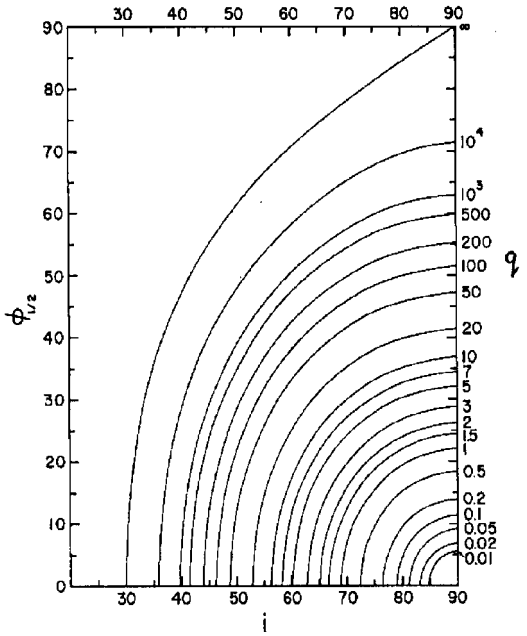

Figure 4.1: A plot of eclipse half angle ($\phi_{1/2}$) versus orbital inclination (i) for 21 fixed values of mass ratio (q) for a point-mass-Roche-lobe-filling binary, from Chanan et al. (1976).

Three assumptions were made by Chanan et al. (1976) to obtain this relationship; 1. the gravitational potential of the component stars are point mass potentials, 2. the binary system rotates as a rigid body around its centre of mass, and 3. the secondary star fills its Roche lobe.

Horne (1993) produced a relationship between mass ratio and inclination angle for different values of the white dwarf eclipse duration ($\Delta\Phi$); this can be seen in Figure 4.2.

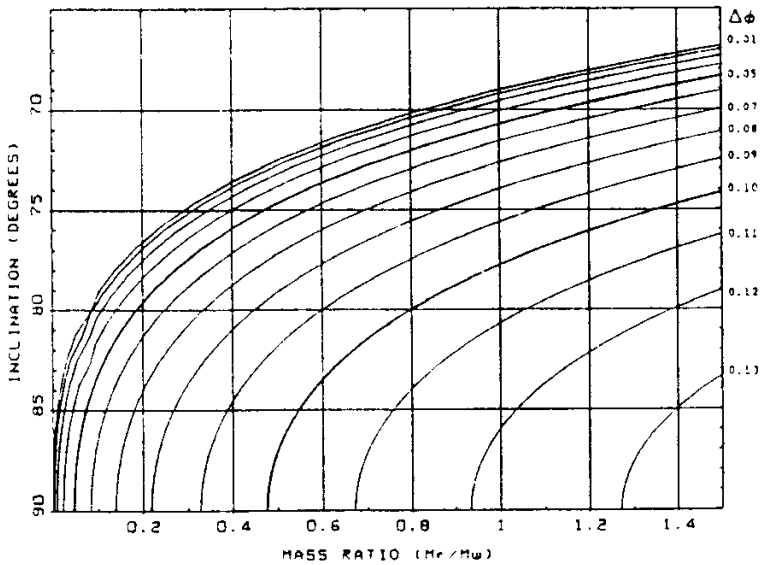

Figure 4.2: Relationship between mass ratio (q) and inclination angle (i) for different eclipse phase widths ($\Delta\Phi$), from Horne (1993).

The main difference between Figures 4.1 and 4.2 is the parameterisation of the eclipse width. Chanan et al. (1976) considered the white dwarf half width in units of degrees ($\phi_{1/2}$), whereas Horne (1993) considered the full duration of white dwarf eclipse in units of orbital phase ($\Delta\Phi$). Therefore

$$\Delta\Phi = \frac{2\phi_{1/2}}{360}. \tag{4.2}$$

Both authors obtain the eclipse width in the same way using Roche lobe geometry to calculate where the observers' line of sight just touches the limb of the secondary star.

For binary systems with orbital period $P_{orb} > 0.13$ days, the optical light from the system is normally dominated by the accretion disc (Bailey 1990), but there are exceptions where the optical light is dominated by the secondary star (e.g. AE Aqr - van Paradijs 1989). To reduce contamination from the accretion disc, Bailey (1990) used the eclipse width at half-light as a good approximation of the white dwarf eclipse duration. In the ultraviolet only the hot inner parts of the accretion disc are seen, therefore the ultraviolet eclipse width at half light is a better approximation of the white dwarf eclipse duration.

For RW Tri the width of eclipse at half-light in the ultraviolet (the FWHM) is $\Delta\Phi = 0.077 \pm 0.022$ orbital phase (Chapter 2, Section 2.1.1). A curve for $\Delta\Phi = 0.077$ can be calculated in terms of the inclination angle (i) and the mass ratio (q) using

$$\frac{R_2}{a} = \frac{0.49q^{2/3}}{0.6q^{2/3} + \ln\left(1 + q^{1/3}\right)}, \tag{4.3}$$

and

$$\left(\frac{R_2}{a}\right)^2 = \sin^2 \pi\Delta\Phi + \cos^2 \pi\Delta\Phi \cos^2 i. \tag{4.4}$$

Equation 4.3 defines the volume-equivalent radius of the Roche lobe which is close to the equatorial radius of the secondary star as seen during eclipse (Eggleton 1983). Equation 4.4 as given by, for example Smith et al. (1998) using simple geometry. This curve can be seen in Figure 4.3.

4.1.2 Masses

The mass function of the component stars can be derived by considering the circular motion of the component stars around the centre of mass of the binary system and Kepler's third law (Chapter 1, Section 1.1.1). Using the mass functions (Equations 1.13 and 1.14, Chapter 1) and Equation 4.1 the masses of the primary and secondary stars can be calculated using

$$M_1 \sin^3 i = \frac{P_{orb} K_2}{2\pi G}(K_1 + K_2)^2, \tag{4.5}$$

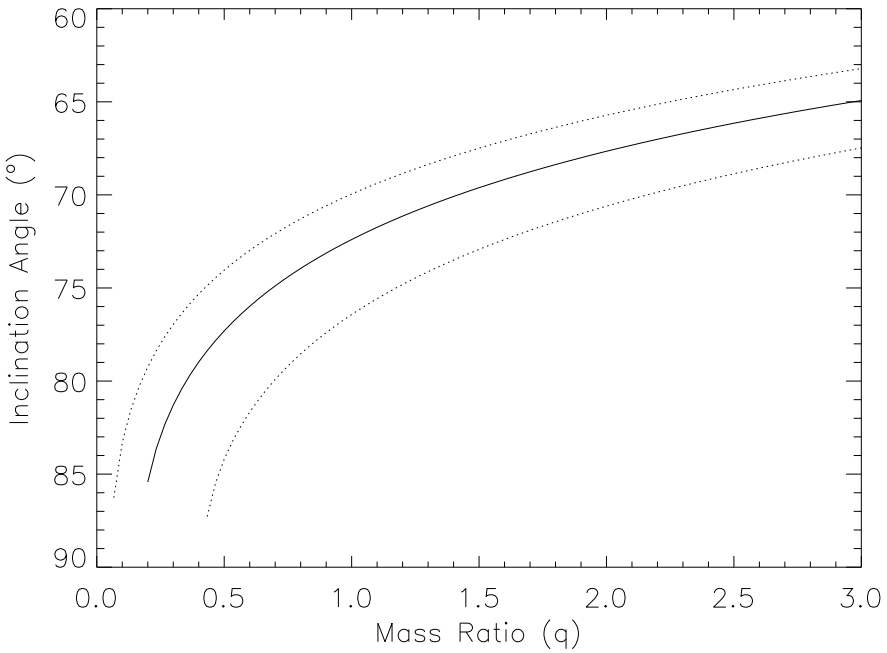

Figure 4.3: Relationship between mass ratio (q) and inclination angle (i) for $\Delta\Phi = 0.077 \pm 0.022$ using Equations 4.3 and 4.4. The solid line represents the curve of $\Delta\Phi = 0.077$, the dotted lines represent the curves of $\Delta\Phi = 0.077 \pm 0.022$ orbital phase.

and

$$M_2 \sin^3 i = \frac{P_{orb} K_1}{2\pi G}(K_1 + K_2)^2, \tag{4.6}$$

where P_{orb} is the orbital period of the system, and G is the gravitational constant (6.673×10^{-11} Nm^{2}kg^{-2}).

4.2 Primary Star Velocity Measurements

There have been a number of different estimates of K_1 which have produced a range of values for K_1. Hydrogen and Helium accretion disc emission lines are produced from regions surrounding the white dwarf, these lines should reflect its orbital motion. The centroids of these emission lines are likely to be contaminated by the secondary star, the accretion stream, and the bright spot; the wings of these features represent the gas closest to the white dwarf and hence should map its motion

most precisely. Doppler maps of RW Tri (Kaitchuck et al. 1983) show that the He II λ4686Å emission arises from the inner accretion disc region. He I λ4471Å emission is found further out in the accretion disc, and Hβ and Hγ emission originates from the outer regions of the accretion disc and the inner face of the secondary star.

Still et al. (1995) obtained K_1 values of 208 ± 8 km/s from Hβ, 223 ± 11 km/s from Hα, and 216 ± 9 km/s from He II (λ4686Å) using Doppler maps. The He II measurement of Still et al. (1995) is consistent with the 197 ± 20 km/s measurement of Kaitchuck et al. (1983), who also found a K_1 velocity of $\sim 170 \pm 20$ km/s for He I. Still et al. (1995) also used the convolution technique of Schneider & Young (1980) to measure the wings of Hβ, Hγ and He II emission lines. When comparing these velocities to Doppler maps of RW Tri, their measured values were not consistent with the likely white dwarf velocity coordinates. These inconsistencies were probably due to absorption affecting the wings of the accretion disc emission lines.

Recently HST data has been used to measure the velocity of narrow absorption features in the ultraviolet (UV). Mason et al. (1997) detected velocity shifts in the UV absorption lines and found they had the same orbital phase as that expected for the white dwarf. The simple disc model I produce in Chapter 2 using this data suggests that these absorption features are coming from a region within the accretion disc and may therefore mirror the white dwarf motion. By cross-correlating each series with the average spectrum through the orbital cycle, Mason (1999) found $K_1 = 296 \pm 5$ km/s (Chapter 2, Section 2.1.2).

4.3 Secondary Star Velocity Measurements

4.3.1 Far red Data

The tomographic technique of skew-mapping (Chapter 3, Section 3.1.1) was used to analyse far red data provided by Robert Smith. A velocity of 235 ± 47 km/s was obtained from these data (Chapter 3, Section 3.1.6).

4.3.2 Near Infrared Data

Time resolved spectroscopy of RW Tri was obtained using the *United Kingdom Infra-Red Telescope* and analysed using the method of cross-correlation. These observations produced a velocity of 221 ± 29 km/s (Chapter 3, Section 3.2.3).

4.3.3 Factors affecting Secondary Star Velocity

The value of K_2 may be affected by heating, line quenching, and line contamination (Friend et al. 1990). *Heating* of the secondary star occurs due to hard photons from the accretion disc. Roche and doppler tomography of Na I lines shows the non-uniform appearance of the secondary star, which can be attributed to heating (Watson et al. 2003 and Catalán et al. 1999). *Line quenching* occurs due to the ionisation of the atoms by flux from the disc and has been attributed to the decrease in Na I line flux observed by Wade & Horne (1988). Both irradiation and line quenching can deplete the absorption line strength on the surface of the secondary star that faces the accretion disc and would therefore shift the apparent centroid of the absorption line region to the hemisphere facing away from the disc. This would lead to an over-estimate of the K_2 value. The magnitude of this effect may be reduced if the accretion disc has a thick rim, which shields the secondary star. This appears to be the case in RW Tri (Mason et al. 1997). *Line contamination* may occur due to weak accretion disc features. This could also lead to variations in the strengths of the absorption lines through the orbit. This has been suggested by Mukai & Charles (1987) and Catalán et al. (1999).

Wade & Horne (1988) produced a rough estimate for the likely correction required for the radial velocity amplitude of the secondary star. This 'K-correction' is given by

$$\Delta K = \frac{\Delta R}{a_2} K_2 = \frac{f R_2}{a_2} K_2, \tag{4.7}$$

where ΔR is the displacement between the effective centre and the centre of mass of the secondary star, R_2 is the secondary star radius, $|f| < 1$ is a weighting factor

representing the strength of the absorption feature, and a_2 is the distance of the centre of mass of the secondary star from the centre of mass of the system given by

$$a_2 = \frac{a}{1+q}, \tag{4.8}$$

where a is the separation of the component stars and q is the mass ratio ($q = M_2/M_1$). A full derivation of the 'K-correction' can be seen in Appendix F.

To estimate the rough magnitude and uncertainty of the correction I use $f = \frac{4}{5\pi} \sim 0.25$, where the front hemisphere of the secondary star has ~ 0.4 of the absorption of the back hemisphere. This is based on the measured change in the amplitude of the absorption features with orbital phase from Chapter 3 (Section 3.2.3). A full derivation of $f = \frac{4}{5\pi}$ is given in Appendix G. Each hemisphere is assumed to have uniform absorption, and R_2/a is related to the mass ratio using Equation 4.3.

4.4 Calculating the Mass Ratio

The mass ratio of RW Tri is calculated using the various component star radial velocity amplitudes. When combined with my best estimate of the secondary star velocity (221 ± 29km/s), the primary star velocity amplitudes discussed in Section 4.2 lead to a range of mass ratios seen in Table 4.1 (Column 4).

The K_1 velocity values that most likely reflect the motion of the white dwarf are the UV absorption lines of Mason (1999) (Section 4.2) and the He II emission lines of Still et al. (1995) that originate in a region close to the white dwarf. These velocities therefore give a 'most likely' mass ratio in the range $1.0 - 1.3$. To consider the effects of the 'K-correction' on this most likely mass ratio range, Equation 4.7, 4.3 and $f \sim 0.25$ are used. This results in a ΔK range of $\sim 19\%$ to $\sim 24\%$. Thus the worst-case minimum value of K_2 in RW Tri is ~ 178km/s, implying a revised mass ratio (q) in the range $1.2 - 1.7$ (Table 4.1, Column 5).

The rotational broadening of the secondary star can also be used to calculate

Features	K_1 (km/s)	K_2 (km/s)	q using K_2	q using $\Delta K \sim 24\%$
UV absorption	296 ± 5	221 ± 29	1.34 ± 0.18	1.66 ± 0.27
Hα emission	223 ± 11	221 ± 29	1.01 ± 0.14	1.25 ± 0.21
He II emission	216 ± 9	221 ± 29	0.98 ± 0.14	1.21 ± 0.20
Hβ emission	208 ± 8	221 ± 29	0.94 ± 0.13	1.17 ± 0.20
He I emission	170 ± 20	221 ± 29	0.77 ± 0.14	0.96 ± 0.19

Table 4.1: Mass ratio results for different combinations of K_1 and K_2.

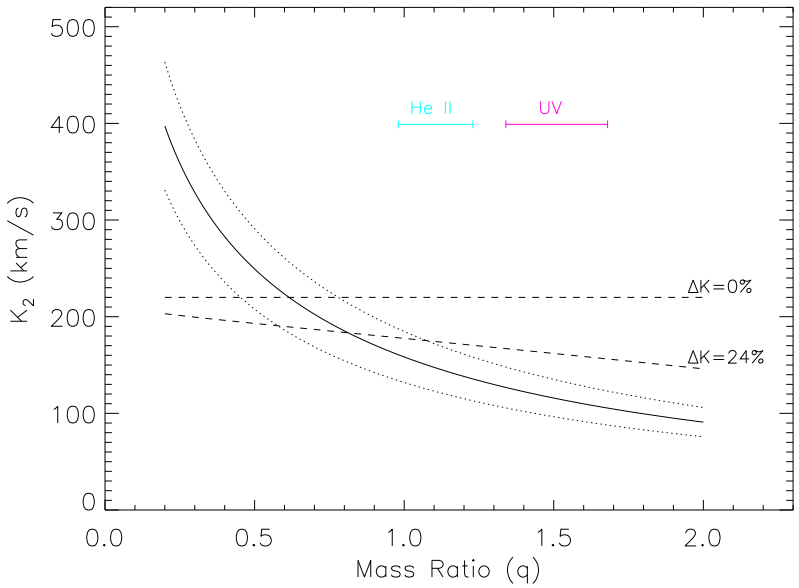

Figure 4.4: Radial velocity of the secondary star (K_2) versus a range of mass ratios ($q = K_1/K_2$). The solid black curved line represents K_2 calculated using $V_{rot} \sin i = 120$km/s, and Equations 4.3 and 3.14 (Chapter 3, Section 3.2.3). The dotted curved lines represent K_2 using $V_{rot} \sin i = 120 \pm 20$km/s. The dashed straight lines represent the variation of K-corrected $K_2 = 221$km/s (Section 4.3.3) as a function of mass ratio, when $\Delta K = 0\%$ and $\Delta K = 24\%$. The thick cyan and magenta lines represent the mass ratio range of He II and UV respectively, using $\Delta K = 0\%$ and $\Delta K = 24\%$ from Table 4.1.

the mass ratio ranges using Equation 3.14 where R_2/a is found using Equation 4.3. The results are shown in Figure 4.4 where the solid and dotted lines represent $V_{rot} \sin i = 120 \pm 20$km/s (from Chapter 3, Section 3.2.3) as a function of mass ratio between $q = 0.2$ and $q = 2.0$. The dashed lines in Figure 4.4 represent the variation of K-corrected $K_2 = 221$km/s as a function of the mass ratio when $\Delta K = 0\%$ and $\Delta K = 24\%$. From Figure 4.4, I find a value of q in the range $0.5 - 0.8$ when no correction for possible heating effects is applied ($\Delta K = 0\%$). This is not consistent with either of the He II or UV mass ratio ranges (cyan and magenta lines in Figure 4.4 respectively). When $\Delta K = 24\%$, I find a mass ratio range of $q = 0.6 - 1.1$ (Figure 4.4) which again does not overlap the He II or UV range.

This can be more clearly seen in Figure 4.5 where the derived values of q are expressed as a function of ΔK. The solid and dotted black lines in Figure 4.5 represent the mass ratio range where the K_2 value implied by $V_{rot} \sin i = 120 \pm 20$km/s coincides with the K-corrected $K_2 = 221$km/s as a function of ΔK, and the cyan and magenta lines represent the mass ratio derived from the He II and UV line estimates of K_1 as a function of ΔK. For $V_{rot} \sin i$ to be consistent with the He II mass ratio range, $\Delta K > 34\%$. This strongly suggests that the velocities found using the UV absorption and He II emission lines may contain a non-orbital component.

If I assume that the K_1 velocities using the UV and He II features are correct, I can predict the expected $V_{rot} \sin i$ for given K_2 values. This is shown in Figure 4.6 where the solid curved black lines represent $V_{rot} \sin i$ using $K_1 = 295$km/s (UV data) and $K_1 = 216$km/s (He II data). Using a range of ΔK from 0% to 24%, $V_{rot} \sin i$ of $200 - 210$km/s and $155 - 165$km/s is found using $K_1 = 295$km/s and $K_1 = 216$km/s respectively. These ranges lie above the measured value of $V_{rot} \sin i = 120 \pm 20$km/s found in Chapter 3 (section 3.2.3). The calculated $V_{rot} \sin i$ ranges all have larger values due to K_1, so reducing K_1 will reduce $V_{rot} \sin i$. These results show that K_1 calculated from the UV and He II lines are overestimates, assuming my measured value of $V_{rot} \sin i = 120$km/s is correct.

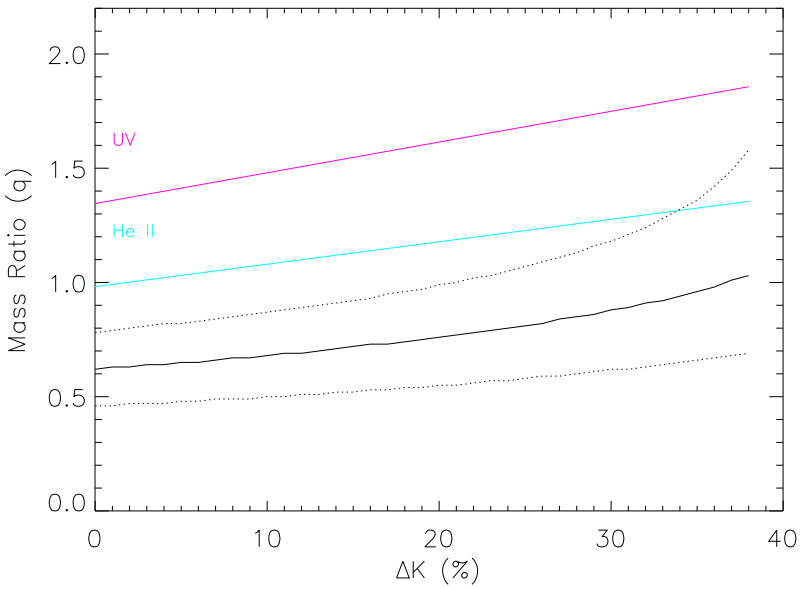

Figure 4.5: The possible mass ratio ranges of RW Tri ($q = M_2/M_1$) as a function of the 'K-correction' of the secondary star (ΔK) due to heating effects. The solid black curved line represents the mass ratio (q) found when a K_2 using $V_{rot} \sin i = 120$km/s (solid back cured line in Figure 4.4) coincides with a K-corrected $K_2 = 221$km/s (dashed lines in Figure 4.4), as a function of ΔK. The dotted curved lines represent the mass ratio as a function of ΔK using $V_{rot} \sin i = 120 \pm 20$km/s. The magenta and cyan lines represent the mass ratio range of He II and UV respectively, as a function of ΔK using Equation 4.7.

4.5 The Mass Results for the Component Stars in RW Tri

To calculate the masses using Equations 4.5 and 4.6, the inclination angle (i) needs to be calculated. Using the relationship between i, q and the eclipse duration ($\Delta\Phi$), a set of inclination angles can be calculated using Figure 4.3. The inclination angle ranges from 68^o to 72^o for the mass ratio range $1.1 - 2.0$.

The results derived using UV and He II K_1 velocities are shown in Figure 4.7. Using the UV measurement, both the uncorrected and K-corrected mass ratios lie above the critical value (q_{crit}) of 4/3 (Chapter 1 Section 1.1.3) in the region of the diagram where mass transfer is unstable. The upper mass of the primary star

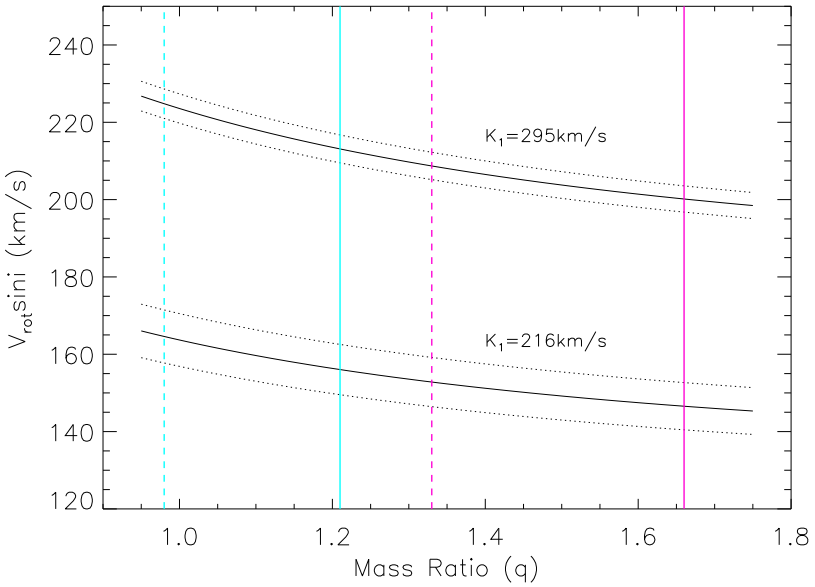

Figure 4.6: $V_{rot} \sin i$ of the secondary star versus a range of mass ratios ($q = K_1/K_2$). The solid curved black lines represent $V_{rot} \sin i$ calculated using $K_1 = 295$km/s (top) and $K_1 = 216$km/s (bottom). The dotted curved black lines represent $V_{rot} \sin i$ calculated using $K_1 = 295 \pm 5$km/s (top) and $K_1 = 216 \pm 9$km/s (bottom). The vertical magenta lines represent q calculated using $K_1 = 295$km/s combined with $K_2 = 221$km/s ($\Delta K = 0\%$ - dashed line) and $K_2 = 178$km/s ($\Delta K = 24\%$ - solid line). The vertical cyan lines represent q calculated using $K_1 = 216$km/s combined with $K_2 = 221$km/s ($\Delta K = 0\%$ - dashed line) and $K_2 = 178$km/s ($\Delta K = 24\%$ - solid line).

exceeds the Chandrasekhar mass limit of $1.44 M_{\odot}$, and the secondary star mass is also very large and inconsistent with that of a main-sequence star. This reinforces my suspicions that the UV velocities contain a non-orbital component. A reduction of K_2 below the K-corrected value of 178km/s would decrease the secondary mass but further increase the mass ratio.

Adopting instead the K_1 measurements derived from He II data, I find values of q that broadly lie between $q_{crit} = 4/3$ and $q_{ad,rc} = 1$ (Figure 4.7). The masses of the primary and secondary stars lie in the range of $0.8 - 1.1 M_{\odot}$ and $0.9 - 1.1 M_{\odot}$ respectively. The white dwarf mass is well within the Chandrasekhar mass limit of $1.44 M_{\odot}$ and includes the mean primary mass of $0.8 M_{\odot}$ for CV systems with $P_{orb} > 3$

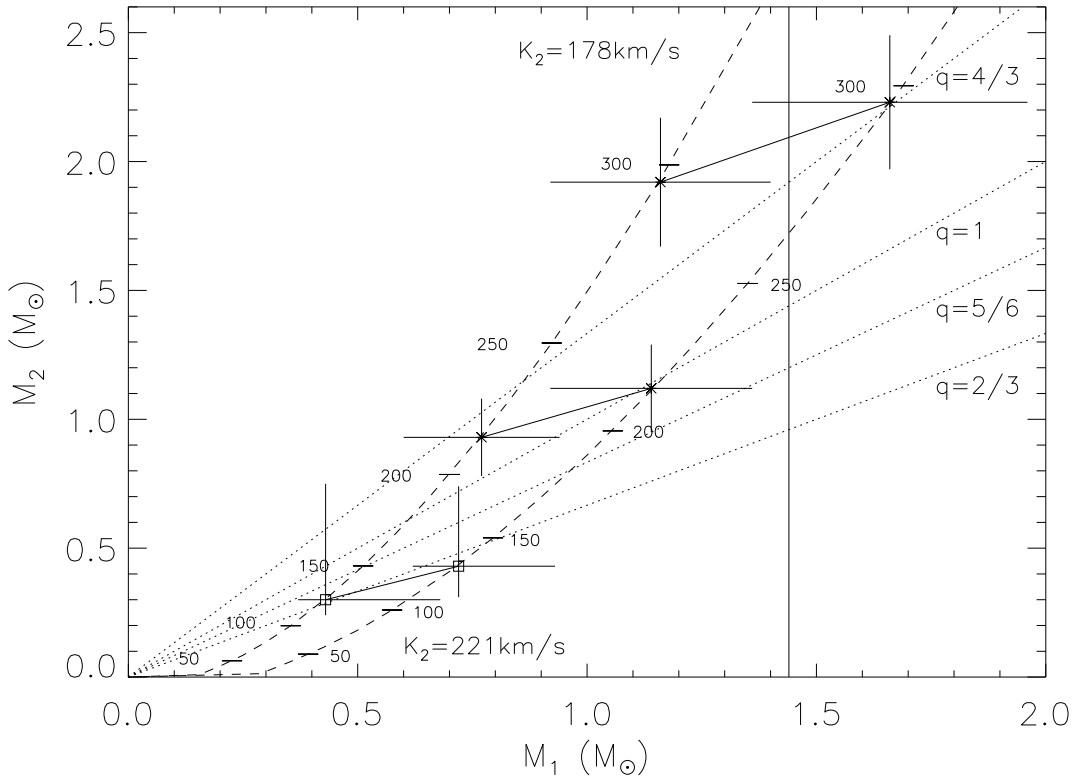

Figure 4.7: The mass of the component stars in RW Tri is derived by combining the measurement of K_2 with different estimates of K_1 (represented by $*$) and $V_{rot}\sin i$ (represented by $\Box$). In each case I show values corrected for the effects of heating of the secondary star using $\Delta K \approx 24\%$ ($K_2 = 178$km/s - Section 4.4) as well as values with no correction for heating (221 ± 29km/s - Chapter 3, Section 3.2.3). A straight line links these values. The upper set of results are obtained using the UV absorption $K_1 = 296 \pm 5$ km/s velocity (Mason 1999), and the middle set of results are obtained using the He II accretion disc emission $K_1 = 216 \pm 9$ velocity (Still et al. 1995). The error bars combine the uncertainties in K_1 and K_2. The lower set of results show the mass values derived from the K_2 measurement combined with $V_{rot}\sin i = 120 \pm 20$km/s. The error bars are calculated using the ± 20km/s uncertainty on $V_{rot}\sin i$. The vertical solid line represents the $1.44M_{\odot}$ Chandrasekhar mass limit for white dwarf stars. The two dashed lines represent the locus of masses calculated when $K_2 = 178$km/s and $K = 221$km/s respectively with varying K_1 values; the tick marks on the two dashed lines mark K_1 velocity values of 50km/s, 100km/s, 200km/s, 250km/s and 300km/s. The four dotted lines represents the $q_{crit} = 4/3$ thermal mass transfer limit, $q_{ad,rc} = 1$ adiabatic response with a radiative core, $q = 5/6$ and $q_{ad,fc} = 2/3$ fully convective adiabatic response limit respectively (Chapter 1, Section 1.1.3).

hrs (Smith & Dhillon 1998). The lower limit for the secondary star, however, exceeds the predicted mass of $0.52M_{\odot}$ based on the main-sequence mass-radius relation for an orbital period of 5.25 h (Smith & Dhillon 1998).

Given the evidence for a non-orbital component in the UV absorption line velocities, other optical emission line velocities may also be similarly affected. Forcing the secondary star to its equivalent main sequence value $0.55M_{\odot}$ predicts a primary star velocity of $152-169$km/s for $K_2 = 221-178$km/s. This is closer to the K_1 value of 170 ± 20km/s derived by Kaitchuck et al. (1983) from the He I emission line. The implied mass ratio for a K_1 velocity of 170km/s lies in the range 0.8 ($\Delta K = 0\%$) to 1.0 ($\Delta K = 24\%$) and is consistent with the results obtained using rotational velocity of the secondary.

Alternately, I can obtain mass values using the combination of $V_{rot} \sin i$ and K_2 without any assumption about K_1, which is preferable due to the uncertainty of K_1 (Smith & Dhillon 1998). Using the mass ratio values of $0.6-1.1$ for the $\Delta K = 24\%$, and $0.5-0.8$ for $\Delta K = 0\%$ from Section 4.4, and assuming K_2 values of 178 and 221 km/s respectively, the stellar masses can be calculated using Equations 4.1, 4.5 and 4.6. Figure 4.7 shows the results. The most likely masses of the primary and secondary stars lie in the ranges $0.4-0.7M_{\odot}$ and $0.3-0.4M_{\odot}$ respectively for the range of $\Delta K = 24-0\%$ and better agree with the expected masses for the component stars in a CV. The expected value of K_1 based on these results is in the range $120-130$ km/s with an upper limit of approximately 190 km/s.

The mass of the secondary star can also be estimated from $V_{rot} \sin i$ directly using

$$\left(\frac{M_2}{M_{\odot}}\right) = 0.043 \left(\frac{V_{rot} \sin i}{100\text{km/s}}\right)^3 P_{hrs} \tag{4.9}$$

(Smith & Dhillon 1998), where P_{hrs} is the orbital period of the system in hours. Equation 4.9 results in an M_2 of $0.41 \pm 0.12M_{\odot}$, which lies within the calculated range of secondary star masses.

4.5.1 Secondary Star Mass

My results using the UV absorption feature and He II emission feature (Figure 4.7) suggest that the secondary star in RW Tri is more massive than the MS predictions of $M_2 = 0.55M_{\odot}$ (Echevarría 1983). The observed spectral type is also later than

the MS predictions of spectral type K6 (Echevarría 1983). This difference is puzzling because over-massive secondary stars in a CV are expected to be smaller and hence hotter than a main-sequence star of the same mass. This paradox was also found in studies of U Gem (Friend et al. 1990 and references therein). This scenario could occur due to the evolutionary effects on the binary system. For example, during the 'propeller phase' of CV evolution (Chapter 1, Section 1.1.6), the outer atmosphere of an originally more massive secondary star may be stripped off, leaving a more dense, less luminous secondary star core.

4.6 Conclusions

I combine the secondary star rotational velocity of 120 ± 20km/s found in Chapter 3, with the secondary star radial velocity corrected for non-uniform heating (178 ± 29km/s) derived from the variation in the absorption line strengths. I find a mass ratio range of $0.6 - 1.1$ which contains the lower adiabatic response limit ($q_{ad,fc} = 2/3$).

Considering the radial velocity amplitudes of the secondary star with the best candidate radial velocities of the primary found using He II emission (Still et al. 1995) and UV narrow absorption (Mason et al. 1997), I obtain a range of mass ratios of $1.0 - 1.3$ and $1.2 - 1.7$ respectively when considering a range of possible heating effects ($\Delta K = 0{-}24\%$). The UV mass ratio range lies above the critical mass ratio ($q_{crit} = 4/3$); this range is also inconsistent with the rotational velocity results, suggesting that the UV velocity may contain a non-orbital component. The He II mass ratio range broadly lies below $q_{crit} = 4/3$ but is inconsistent with rotational velocity results; its mass ratio range lies above $q_{ad,fc} = 2/3$.

The results obtained using the combination of $V_{rot} \sin i$ and K_2 are more reliable because they make no assumption about K_1. Using the rotational broadening I find primary and secondary mass ranges of $0.4 - 0.7 M_{\odot}$ and $0.3 - 0.4 M_{\odot}$ respectively for a range of possible heating effects.

Chapter 5

OY Car in X-rays

In Chapter 2 ultraviolet wavelengths were used to detect features in the accretion disc. In this Chapter I use X-ray wavelengths to probe deeper into the hotter boundary layer[1] region. The dwarf nova OY Car is an eclipsing system and is therefore ideal for investigating the boundary layer. By studying the eclipse profile, the X-ray emitting boundary layer can be located.

Dwarf novae have relatively low flux levels; therefore a large collecting area is needed to obtain eclipse profiles with good time resolution and high signal-to-noise. *XMM-Newton* (Jansen et al. 2001) provides a large collecting area allowing eclipse profiles of dwarf novae to be investigated in detail. OY Car was observed as part of the performance verification phase of *XMM-Newton*. Two papers on the initial results have been published. 1. Initial analysis of the optical and X-ray light curves (Ramsay, Poole et al. 2001a). 2. Initial analysis of the spectral data (Ramsay et al. 2001b). This Chapter is devoted to the X-ray timing studies which I undertook using the *XMM-Newton* observations of OY Car. I re-analysed the originally reduced data published in the paper by Ramsay, Poole et al. (2001a) to further investigate eclipse profiles and periodic variations.

[1]Where the accretion disc is decelerated and merges with the white dwarf (Chapter 1, Section 1.1.5).

5.1 XMM-Newton

The effective collecting area of each nest of 58 coaxial confocal mirrors (Aschenbach et al. 1987) in *XMM-Newton* is far larger than any previous mission. Figure 5.1 compares the effective areas of the *XMM-Newton* EPIC instruments that I use with those of previous X-ray satellites ROSAT and ASCA. Another new feature of *XMM-Newton* is the *Optical Monitor* telescope, which enables the observer to obtain simultaneous ultraviolet/optical observations.

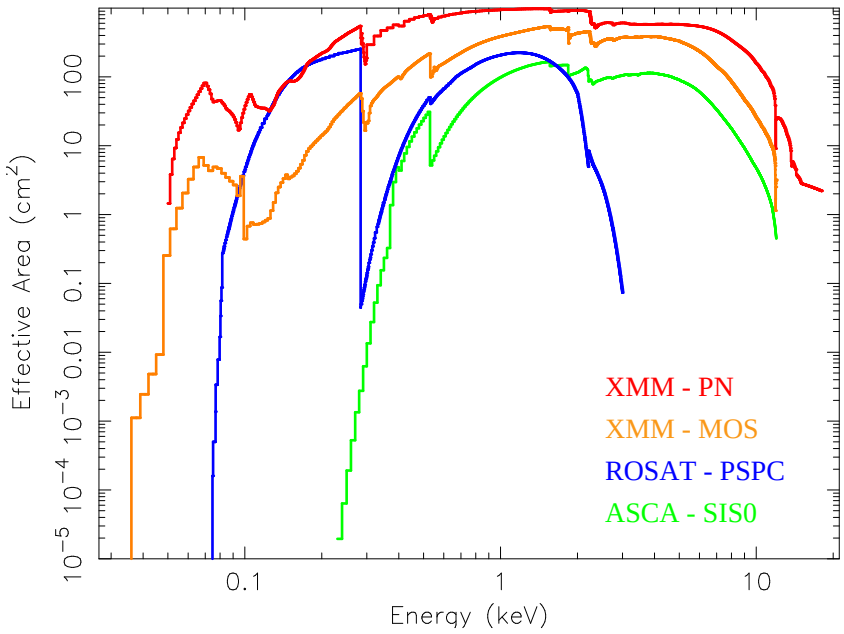

Figure 5.1: The effective area of *XMM-Newton* EPIC PN and MOS cameras (red and orange respectively), with the missions of ROSAT (blue) and ASCA (green).

XMM-Newton carries three X-ray telescopes and an optical/ultraviolet telescope. There are three types of scientific instrument on *XMM-Newton*. 1. European Photon Imaging Camera (EPIC - 0.1 – 12.0keV), consisting of three cameras of 2 different types; 1 pn chip array camera (PN) and 2 Metal Oxide Semi-conductor chip array cameras (MOS), for X-ray imaging and moderate resolution spectroscopy (Strüder et al. 2001, Turner et al. 2001 respectively). 2. Reflection Grating Spectrometer

(RGS - $0.35 - 2.5$keV), consisting of two spectrometers for high resolution X-ray spectroscopy (den Herder et al. 2001). 3. Optical Monitor (OM - $170 - 650$nm), a microchannel-plate pre-amplified CCD detector for optical/ultraviolet imaging and grism spectroscopy (Mason et al. 2001). The six instruments can be operated independently and in different modes of data acquisition.

This Chapter discusses the *XMM-Newton* EPIC detector observations. The next section looks at the two different EPIC cameras in more detail.

5.1.1 European Photon Imaging Camera

The three EPIC cameras can perform extremely sensitive imaging observations over a field of view of 30 arcmin and the energy range $0.1 - 12.0$keV, with moderate spectral resolution ($E/\Delta E \sim 20 - 50$) and angular resolution (FWHM$\sim$ 6arcsec, HEW[2]$\sim$ 15arcsec). Figure 5.2 shows the focal plane organisation of the MOS and PN chip arrays.

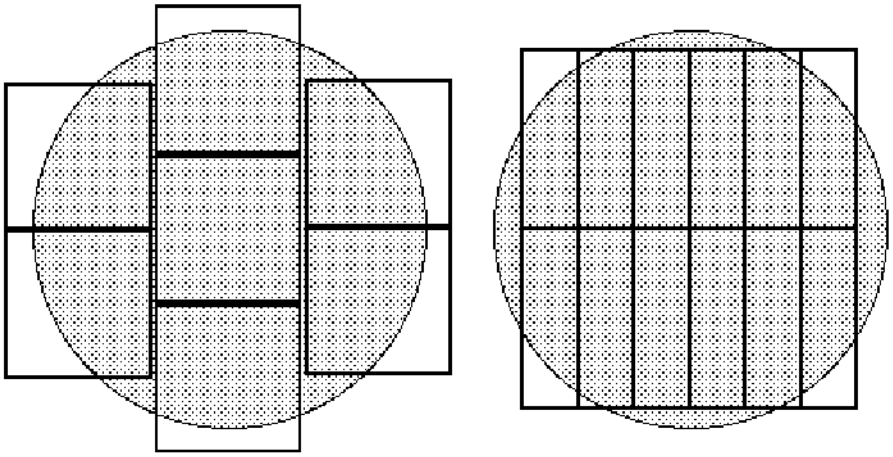

Figure 5.2: The layout of the CCDs of EPIC PN and MOS. Left: EPIC MOS - 7 CCDs each 10.9×10.9 arcmin. Right: EPIC PN - 12 CCDs each 13.6×4.4 arcmin adapted from Figure 15 in Ehle et al. (2001). The shaded circle depicts the 30 arcmin diameter field of view.

[2]HEW=Half Energy Width

Each MOS consists of an array of 7 CCD chips, each chip with 600×600 pixels. The chips are built and wired individually and then arranged into the pattern seen in Figure 5.2 (left). The MOS chips physically overlap one another; the central chip being located slightly behind the 6 chips forming the outer ring (Figure 5.2, left) to allow more of the CCDs to be in focus. The dead space between the MOS chips are not gaps, they are unusable areas at the edges of the detectors (Ehle et al. 2001).

The PN CCDs are new technology X-ray CCDs consisting of an array of 12 chips, each chip with 64×200 pixels. The 12 chips are produced on a single wafer (Figure 5.2, right), and not assembled later as in the case of each MOS. The PN chip array is slightly offset with respect to the axis of its X-ray telescope so that the nominal on-axis observing position does not fall on the central chip boundary. This ensures that an on-axis point is observed on one PN chip only.

The two main differences between the MOS and PN chip arrays are the readout time and illumination of the chips. Each pixel column in the PN has its own readout mode, enabling time resolution of 73.3ms in full window mode, where the readout speed of a MOS CCD is 2.6s in the same mode. MOS chips are front-illuminated and PN chips are back-illuminated which affects the detector quantum efficiencies (QE). The QE of the MOS limits the energy bandpass at high energies (QE drops off around $5 - 6$keV) whereas the PN detects photons with high efficiency up to 12keV. Figure 5.1 shows that PN has the greater effective area of the two types of camera.

5.1.2 Science Analysis System

The Science Analysis System (SAS) is the software package used to reduce and analyse *XMM-Newton* science data (Gondoin 2000). The SAS contains reduction pipelines and a set of file manipulation tools. The reduction pipelines produce calibrated event lists for the X-ray cameras, and flat-fielded OM sky images. The SAS tools allow the observer to generate appropriate instrument response matrices,

and extract spectra, light curves, images and source lists from the X-ray event lists.

5.2 Observations

OY Car was observed using *XMM-Newton* on 29th-30th June 2000 and the 7th August 2000, as part of the performance verification phase of the mission. OY Car was an ideal target because of its short binary period of $P_{orb} = 1.51$hrs. An optical outburst was observed by the AAVSO (Mattei 2000a) on 24th-25th June reaching $\sim$ 12 mag, and fading below $\sim$ 15 mag by June 27th, prior to the first *XMM-Newton* observation. OM Observations of OY Car on June 29th (Ramsay, Poole et al. 2001a) show V$\sim 16.0 - 16.2$ mag, indicating a rapid decline in brightness after outburst. Further OM observations show that OY Car was at a similar optical brightness during the August 7th observations (Ramsay, Poole et al. 2001a). The AAVSO observations (Mattei 2000b) of OY Car, show that there is typically 180 days between outbursts of duration > 7 days (Ramsay, Poole et al. 2001a). This suggests that it was unlikely that there were any outbursts between the two *XMM-Newton* observations.

Observations were made with each EPIC camera (PN, MOS1 and MOS2), and the exposures were taken in the full window mode using the medium filter (used to prevent optical contamination from point sources brighter than $m_V \approx 8 - 10$). Towards the end of the EPIC exposures a significant particle background was seen and removed before analysis. Figure 5.3 shows the EPIC MOS1 and EPIC PN images after removing the high particle background.

The raw data were processed using the SAS released on 12th June 2000, and then light curves were extracted from the EPIC cameras. Table 5.1 shows the duration of the resultant EPIC observations, along with the mean background subtracted count rates. OY Car faded by a factor of ~ 2 between the two X-ray observations (Table 5.1). In total 11 eclipses were observed in the EPIC PN camera (9 in June and 2 in August), and 12 eclipses were observed in the EPIC MOS cameras (9 in

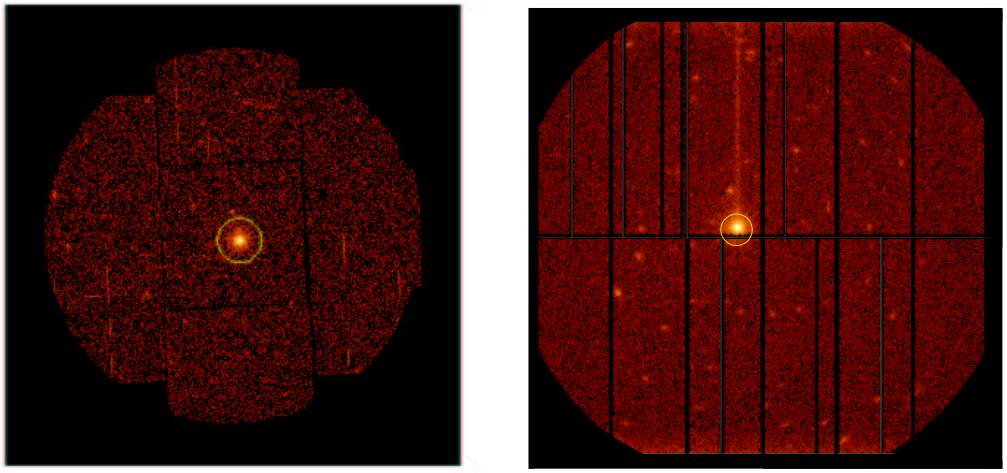

Figure 5.3: EPIC MOS1 and PN images of OY Car. Left: EPIC MOS1 image of OY Car. Right: EPIC PN image of OY Car. The bright vertical line in the PN image is due to out of source events, and the black vertical lines are due to chip edges and bad columns in the chips. Both images had time intervals in which the particle background was high and therefore removed. The yellow circles outline the position of OY Car.

June and 3 in August).

5.2.1 Extracting the Light Curves

The light curves of OY Car were extracted from the three EPIC cameras using XMMSELECT (Gondoin 2000). The light curves were extracted using an aperture radius of $\sim$ 30 arcsec centred on OY Car. This encompassed $\sim$ 90% of the integrated PSF (Aschenbach et al. 2000). Background light curves were extracted using aperture radii of $\sim$ 96 arcsec for PN and $\sim$ 112 arcsec for MOS1 and MOS2 from a source free region of the same CCD on which OY Car was detected. Background light curves were then scaled and subtracted from the light curves centred on OY Car.

There were timing discrepancies between the three EPIC camera light curves, and a time gap in the PN light curve where no counts were recorded. These timing discrepancies were caused by an error in the SAS reduction tools and were corrected

	29th/30th June 2000 orbit 102	7th August 2000 orbit 121
PN	48 ks, 1.09 counts/s	7 ks, 0.56 counts/s
MOS1	51 ks, 0.43 counts/s	14 ks, 0.20 counts/s
MOS2	51 ks, 0.41 counts/s	14 ks, 0.22 counts/s

Table 5.1: The duration of the EPIC observations, and the mean background subtracted count rates.

at a later stage in the mission. The time gap was removed from the PN data. Cross-correlating the three light curves and using the lag timings to align the eclipse ingress and egress removed time discrepancies. The three light curves were then added together to increase the signal-to-noise. The summed light curve was phased on the orbital period, and aligned so that phase 0.0 occurred at the centre of the eclipse profile.

5.3 Results

Figure 5.4 shows the summed EPIC light curves of the first *XMM-Newton* observation split into 0.1−1.0keV and 1.0−4.0keV energy bands, and the 0.1−1.0keV/1.0−4.0keV hardness ratio. In the soft band (0.1 − 1.0keV) there is a significant variation in the light curve from cycle-to-cycle, but there is little variation in the hard band (1.0 − 4.0keV) apart from the eclipses. The variation in the soft X-ray band is manifested in the hardness ratio. The 4.0 − 12.0keV energy band is not included in Figure 5.4 because of the low signal-to-noise of the light curve in this band.

The signal-to-noise in the second observation was not sufficient to examine the light curve in the energy bands of Figure 5.4 in detail. However, Figure 5.5 shows the light curve of the second observation in the full 0.1−12.0keV EPIC energy range,

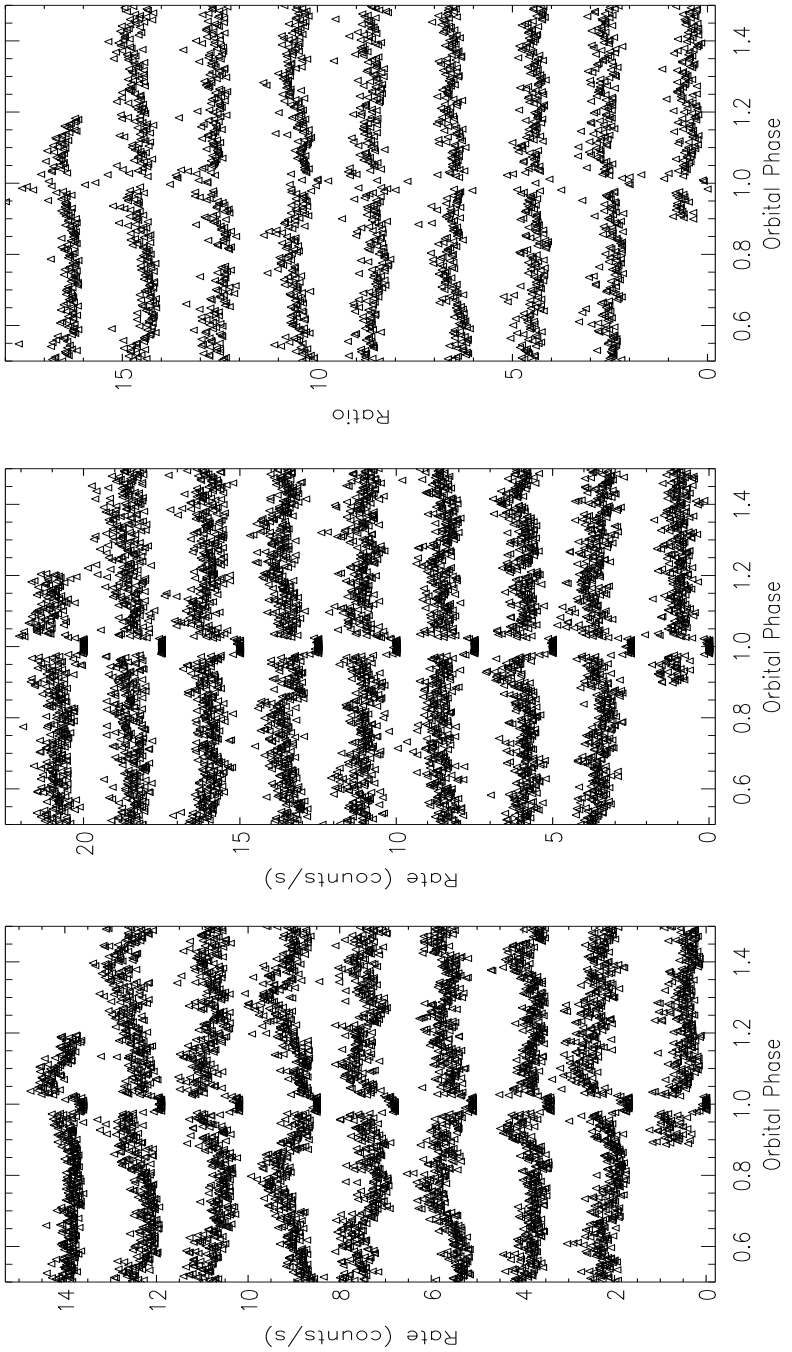

Figure 5.4: The summed EPIC light curves of the first *XMM-Newton* observation. Bottom: 0.1 – 1.0keV soft energy band, binned into 10s bins and offset vertically by 1.7 counts/s. Middle: 1.0 – 4.0keV hard energy band, binned into 10s bins and offset vertically by 2.5 counts/s. Top: Hardness ratio of 0.1 – 1.0keV/1.0 – 4.0keV, binned into 10s and offset vertically by 2.0 counts/s.

illustrating a variation similar to that seen in Figure 5.4.

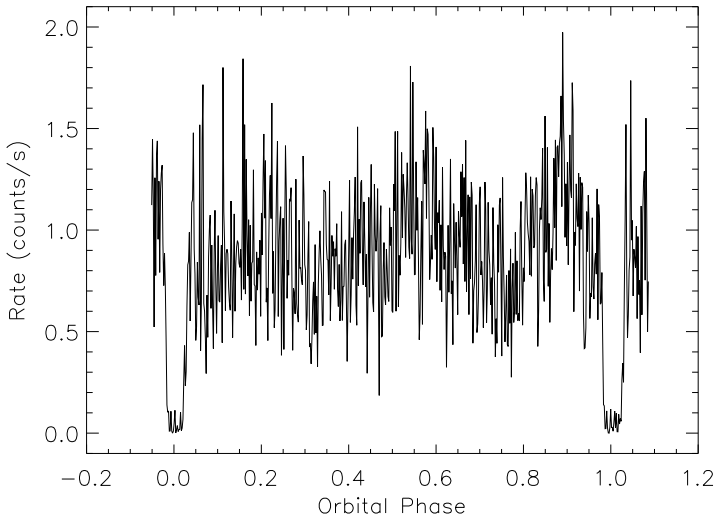

Figure 5.5: The summed EPIC light curves of the second *XMM-Newton* observation in the full energy band (0.1 – 12.0keV) binned into 10s.

5.3.1 Periodic Variations

The Periodogram

To understand the origin of the modulations seen in the discrete EPIC data, time series analysis was undertaken using the discrete Fourier transforms (DFT) defined by

$$FT_X(w) = \sum_{j=1}^{N_0} X(t_j) \exp(-i\omega t_j), \tag{5.1}$$

for an arbitrary sampled data set $\{X(t_j), j = 1, 2, ...N_o\}$, where t_j is the set of observations times, N_0 is the number of points in the data set, and ω is the period. The periodogram is then conventionally defined as

$$P_X(\omega) = \frac{1}{N_0}|FT_X(\omega)|^2 = \frac{1}{N_0}\left[\left(\sum_{j=1}^{N_0} X(t_j)\cos\omega t_j\right)^2 + \left(\sum_{j=1}^{N_0} X(t_j)\sin\omega t_j\right)^2\right], \tag{5.2}$$

(Schuster 1898, Thompson 1971, Deeming 1975, Scargle 1982).

The classical periodogram (Equation 5.2) is exactly equivalent to the least squares fitting of sine waves of various periods to the data. Therefore a power level, z_0, can be defined, such that peaks in the periodogram above z_0 are significant. Scargle (1982) defined z_0 using the *false alarm probability* (p_0) as

$$z_0 = -\ln\left[1 - (1 - p_0)^{1/N}\right], \tag{5.3}$$

where N is the number of frequencies searched ($= N_0/2$). For a 90% confidence level $p_0 = 0.1$.

The periodograms in Figure 5.6 were produced using EAGLE written by Darragh O'Donoghue. Only the first six eclipse profiles in the first *XMM-Newton* observation were used due to the time gap in the PN data. The data were normalised by dividing the original data by the mean. This was done to reduce red noise resulting from sampling at low frequencies. The DFT was then calculated. The first plot in Figure 5.6 (top of top panel) shows the results in the energy range $0.1 - 12.0$keV, and indicates contamination from the harmonics of the orbital period, P_{orb} (marked by the red ticks in the plot). Harmonics are seen due to the nature of the eclipse profile. The eclipse profile is a box function, so to fit this function the program uses a number of sine waves (Equation 5.2) with different amplitudes and harmonic frequencies. This results in peaks at the fundamental (P_{orb}) and the harmonics of the fundamental. The window function can be seen in the fourth plot of Figure 5.6 (top of bottom panel).

To investigate the nature of these harmonics I simulated a light curve with six consecutive eclipses using the average eclipse profile with a fixed out-of-eclipse level. I also used two sinusoids representing the highest peaks of the observed data periodogram positioned at frequencies of 0.31mHz (3266s) and 0.45mHz (2233s) from Figure 5.6 (top of top panel). A periodogram of this light curve was produced using the same method as above. The result can be seen in the third plot of Figure 5.7 (top of bottom panel). The first harmonic of the orbital period gave the highest amplitude followed by the fundamental, then the second, third, and fourth harmonics

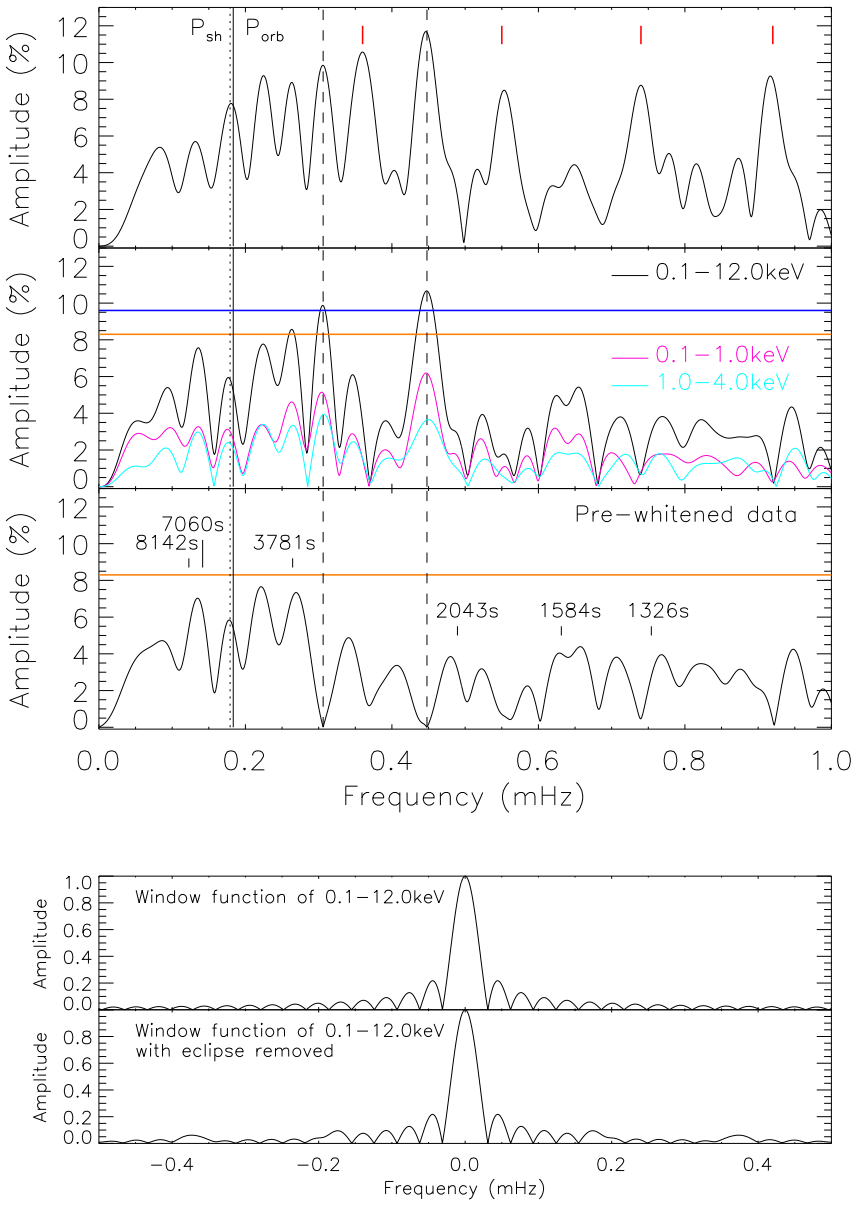

Figure 5.6: Periodograms of OY Car. Top of top panel: $0.1-12.0$keV of first *XMM-Newton* observation. The red tick marks indicate the harmonic frequencies of the orbital period. Middle of top panel: $0.1-1.0$keV (magenta), $1.0-4.0$keV (cyan) and $0.1-12.0$keV (black) of first *XMM-Newton* observation with orbital period harmonics removed. The horizontal lines represents z_0 at the 90% (blue) and 68% (orange) confidence limit. Bottom of top panel: Pre-whitened spectrum with the periods 2233s and 3266s. Periods marked and labelled are those discussed in Section 5.4.1. Top panel: The solid vertical line represents P_{orb}, the orbital period of 5453.65s. The dotted vertical line represents P_{sh}, the super-hump period of 5584.12s found by Krzeminski & Vogt (1985). The dashed vertical lines represent P_{2233}, the 2233s period, and P_{3266}, the 3266s period. Top of Bottom panel: The window function of $0.1-12.0$keV. Bottom of bottom panel: The window function of $0.1-12.0$keV with eclipse profile removed.

having similar values. The observed data (Figure 5.6 top of top panel) have the first harmonic with the highest amplitude and the second, third, and fourth harmonics all with similar amplitudes like the simulated data, but the fundamental in the real data has a significantly reduced amplitude unlike the simulated data. A closer look at the light curve of OY Car folded on the orbital period (Figure 5.8) reveals that there is a dip around 0.5 orbital phase. This dip will add power to the first harmonic causing the respective peak amplitude in the periodogram to increase. The 0.5 phase dip in the folded light curve was added to the simulated data (Figure 5.7 bottom of top panel) using a box function, and the resulting periodogram can be seen in the fourth plot of Figure 5.7 (bottom of bottom panel). This periodogram shows that the peak amplitude of the first harmonic does increase due to the dip in the folded light curve; this dip also reduced the fundamental and affects the higher harmonics. There are other dips seen in the folded light curve of Figure 5.8 (noticeably at 0.9 phase) which will correspond to higher harmonics, resulting in increases in the respective peak amplitudes of the periodogram.

The P_{orb} harmonics were removed by subtracting the averaged eclipse profile from the 10s binned light curves before normalisation. The DFT was then calculated. The second plot in Figure 5.6 (middle of top panel), shows the results of the energy ranges $0.1-1.0$keV, $1.0-4.0$keV, and $0.1-12.0$keV, with the eclipse profile removed. Two peaks lie above the z_0 90% confidence limit (blue vertical line) and correspond to frequencies of 2233 ± 10s and 3266 ± 10s. The error on the peaks was calculated using the Cash statistic (Cash, 1979) adapted to EAGLE by Mark Cropper. These peaks are more prominent in the soft band. The data were split into two halves and the resulting periodograms show the 2233s and 3266s signals. The window function can be seen in the fifth plot of Figure 5.6 (bottom of bottom panel).

There is a third peak with a frequency of 3797s that lies above the 68% confidence

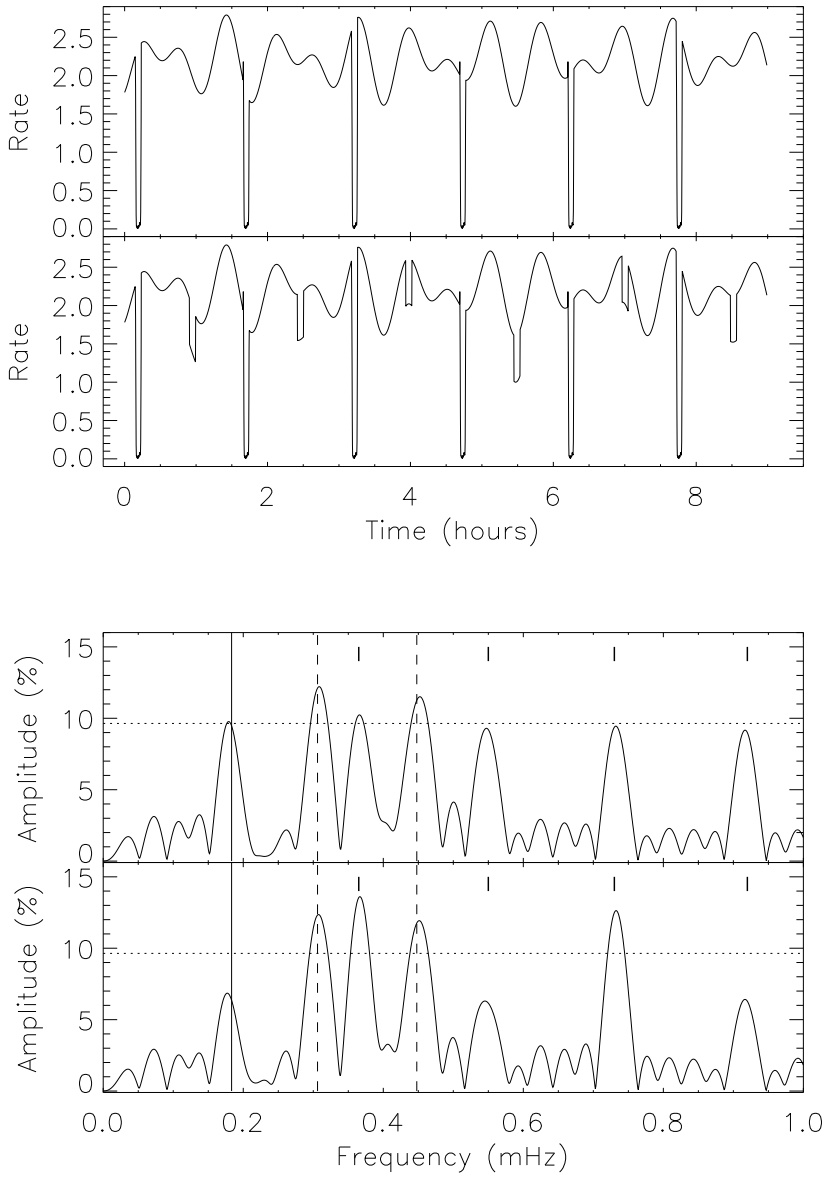

Figure 5.7: Simulated data of OY Car and resulting Periodograms. Top of top panel: Simulated light curve of OY Car using the average eclipse profile with a fixed continuum and two sinusoids relating to the frequencies at 0.31mHz (3266s) and 0.45mHz (2233s) seen in the observed data (Figure 5.6). Bottom of top panel: Simulated light curve of OY Car using the average eclipse profile with a fixed continuum, a box function for the dip at 0.5 orbital phase, and two sinusoids relating to the frequencies at 0.31mHz (3266s) and 0.45mHz (2233s) seen in the observed data (Figure 5.6). Top of bottom panel: Periodogram of simulated data in top of top panel. Bottom of bottom panel: Periodogram of simulated data in bottom of top panel. Bottom panel: The tick marks indicate the harmonic frequencies of the orbital period. The solid vertical line represents P_{orb}, the orbital period of 5453.65s. The vertical dotted line corresponds to the 90% confidence limit. The dashed vertical lines represent the frequencies at 0.31mHz (3266s) and 0.45mHz (2233s) seen in the observed data (Figure 5.6).

limit (orange line) in the second plot (Figure 5.6, middle of top panel). After pre-whitening[3] the data on the 2233s and 3266s periods (third plot in Figure 5.6, bottom of top panel), the 3797s peak reduced to well below the 68% confidence limit, and is therefore no longer considered as a significant period.

The window functions (Figure 5.6 bottom panel) show the effects of spectral leakage. Leakage of power to nearby frequencies is due to the finite interval over which data is sampled, whereas leakage of power to distant frequencies is due to the finite size of intervals between samples. The window functions in Figure 5.6 (bottom panel) show a small amount of leakage to nearby frequencies, which is enough to reduce the peak near 3781s to below the 68% confidence line in the pre-whitened data (Figure 5.6 bottom of top panel). Humps are seen in the window function of the data with the average eclipse profile removed (Figure 5.6 bottom of bottom panel); these humps occur at 5454s and 2727s, and are due to the removal of the eclipse.

The amplitude spectrum of the second *XMM-Newton* observation did not show any significant periods because the exposure time was not long enough for many orbits to be observed. Significant periods of less than 100s, that may indicate the presence of dwarf nova oscillations (DNOs) were not found in either the first or second *XMM-Newton* observations.

Folded Light Curves

The summed EPIC light curve of the first *XMM-Newton* observation in the energy band $0.1 - 10.0$keV was folded on the orbital period (5454s). As well as the eclipse profile, Figure 5.8 shows that there is a noticeable dip in the folded light curve at 0.5 orbital phase; this may be due to X-ray absorption in accretion disc material with significant vertical height above the orbital plane. This dip may be related to light curve dips seen in dwarf nova U Gem (Mason et al. 1988b).

[3]Pre-whitened data has had a least one period and its harmonics removed from the periodogram.

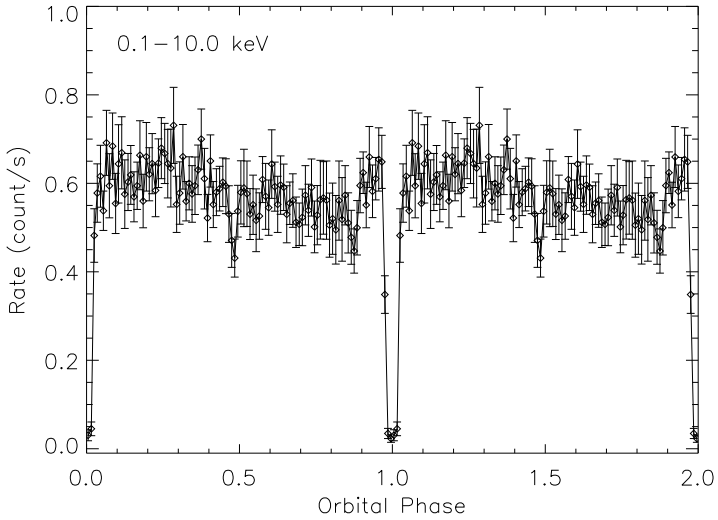

Figure 5.8: The summed EPIC light curve of the first *XMM-Newton* observations in the energy band $0.1 - 10.0$keV ($\diamond$), folded on the orbital period.

Eclipse profiles were removed from the summed EPIC light curves from the first *XMM-Newton* observation to reduce orbital period effects. These light curves were then folded on the 2233s and 3266s periods. Figure 5.9 shows the folded light curves in the energy bands $0.1 - 1.0$keV, $1.0 - 4.0$keV and $4.0 - 10.0$keV. Even though the $1.0 - 4.0$keV energy band has a higher count rate than the $0.1 - 1.0$keV energy band for both periods, it has a lower amplitude modulation[4] of $\sim$ 30% (2233s period) and $\sim$ 33% (3266s period) compared to $\sim$ 55% (2233s period) and $\sim$ 58% (3266s period) for the $0.1 - 1.0$keV energy band. The $4.0 - 10.0$keV light curve shows no significant modulation in both cases. This confirms the energy dependence of the amplitude spectra shown in Figure 5.6 (middle of top panel).

Stability of the Periodic Variations

To investigate the stability of the 2233s and 3266s modulation, the summed EPIC data for the first *XMM-Newton* observation was phased on these periods. Figure 5.10 shows the variation in the modulations. There are cycles in which there is virtually no variation and others where there is significant variation, showing that the

[4]The amplitude modulation is defined as, maximum-minimum/mean.

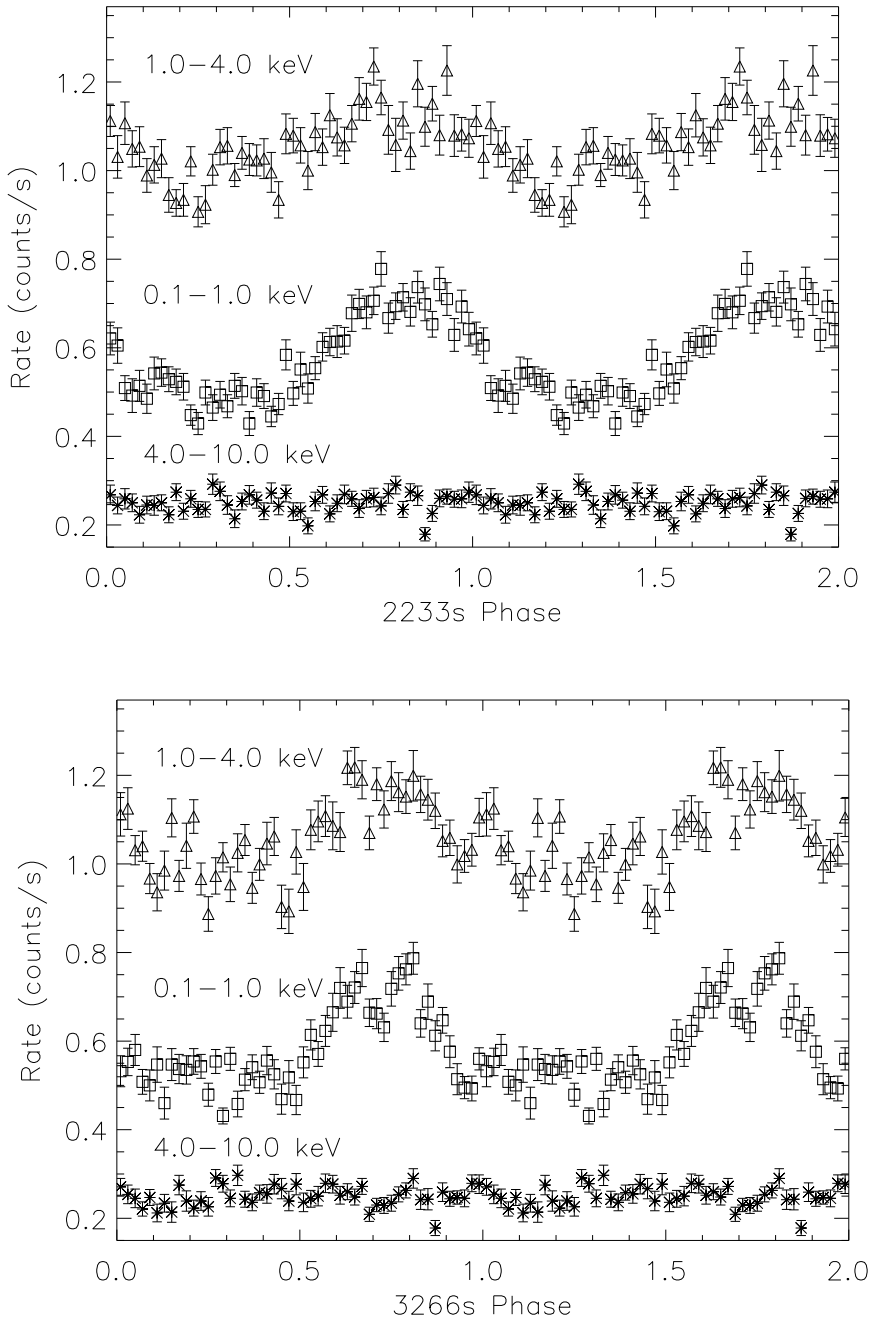

Figure 5.9: The folded light curves of the summed EPIC data with the eclipses removed, from the first *XMM-Newton* observation in the energy ranges $0.1 - 1.0$keV (□), $1.0 - 4.0$keV (△) and $4.0 - 10.0$keV (∗). Errors are 1σ. Top: Data folded on 2233s period. Bottom: Data folded on 3266s period.

amplitude and possible the shape of the oscillations are varying. All of the broad maxima for the 2233s period in Figure 5.10 appear to be centred on the phase range of $\phi_{2233} = 0.7 - 1.2$, whereas the maxima appear throughout the cycle for the 3266s period. The possible origins for these modulations are discussed further in Section 5.4.1.

5.3.2 Eclipse Profiles

When studying the mean eclipse profiles of different energy bands, only the first *XMM-Newton* observations were considered because the second *XMM-Newton* observations had a lower signal-to-noise.

Mean Eclipse Profile

The mean eclipse profile of the energy bands $0.1 - 1.0$keV and $1.0 - 4.0$keV can be seen in Figure 5.11. The eclipse duration is 295 ± 5s from first contact to fourth contact, the FWHM ($\Delta\Phi$) is 260 ± 5s, and the ingress and egress time is 30 ± 5s (Chapter 1, Section 1.2.1). These short duration eclipse times are discussed further in Section 5.4.2.

There are two differences between the mean soft and hard eclipse profiles seen in Figure 5.11. Firstly there is marginal evidence that the $0.1 - 1.0$keV energy band eclipse profile is eclipsed before the $1.0 - 4.0$keV energy band profile, but this is within one bin width. The FWHM of the $0.1 - 1.0$keV (0.047 ± 0.001) and the $1.0 - 4.0$keV (0.049 ± 0.001) eclipses agree within the errors. The second difference is the non-zero flux during the later part of the $0.1 - 1.0$keV energy band eclipse (phase $1.01 - 1.02$), which is discussed further in the next section.

Mid Eclipse Flux

During the first *XMM-Newton* observation eclipse times, the EPIC PN camera shows the presence of a faint source at the location of OY Car (Figure 5.12). The summed

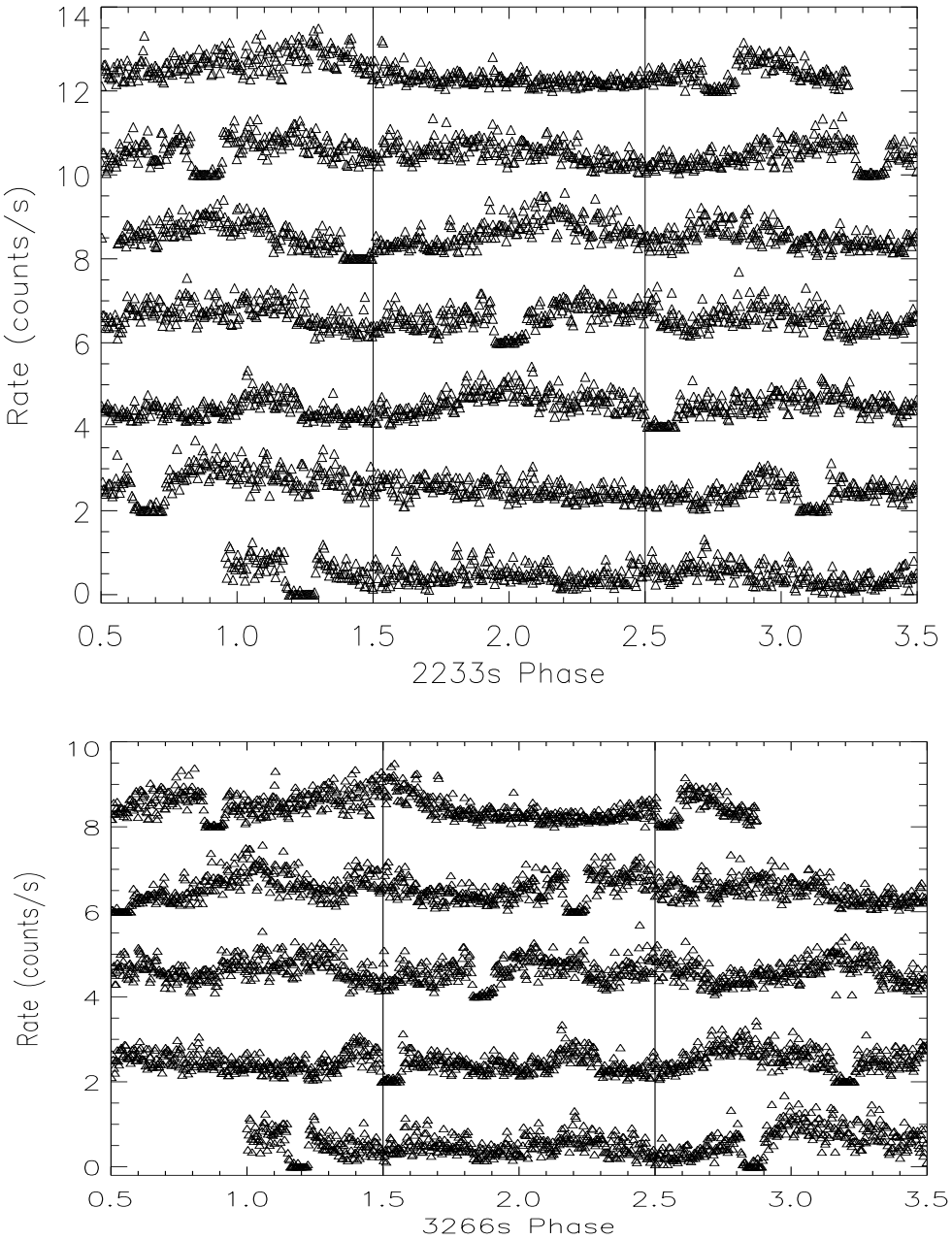

Figure 5.10: Top: The summed EPIC data from the first *XMM-Newton* observation in the energy band 0.1 – 1.0keV, phased on the 2233s period. Bottom: The summed EPIC data from the first *XMM-Newton* observation in the energy band 0.1 – 1.0keV, phased on the 3266s period. Time increases from left to right. Data have been binned into 10s, and offset vertically by 2.0 counts/s every three cycles.

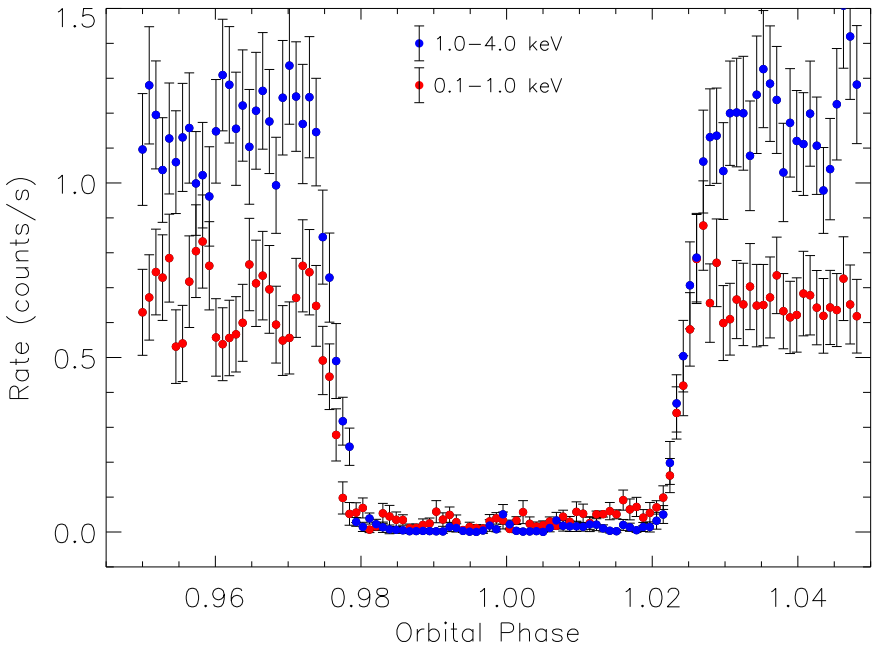

Figure 5.11: The eclipse profile obtained from the summed EPIC data in the energy ranges $0.1-1.0$keV and $1.0-4.0$keV. The data are binned in 5s bins.

EPIC background subtracted count rates of 0.006 ± 0.004 counts/s in the $1.0-12.0$keV band and 0.027 ± 0.004 counts/s in the $0.1-1.0$keV band, suggest that there is a residual low energy X-ray flux during the eclipse; confirming the non-zero flux seen in the eclipse of energy band $0.1-1.0$keV at phase $1.01-1.02$ in Figure 5.11.

To investigate this further, the source and background light curve of each eclipse in each of the detectors was examined. In the PN detector there was a very short ($\sim$ 30s) small increase (within 2σ) in the object flux during eclipse 2. This was not seen in either of the MOS detectors. A 3σ increase in flux was detected towards the end of eclipse 9 in MOS2 which was not seen in PN or MOS1. These observed values are statistically acceptable. These two eclipses were excluded and the background subtracted summed count rate during eclipse was recalculated as 0.003 ± 0.003 counts/s for the $1.0-12.0$keV energy band and 0.024 ± 0.004 counts/s for the $0.1-1.0$keV band. The count rate in the $0.1-1.0$keV band is significant at

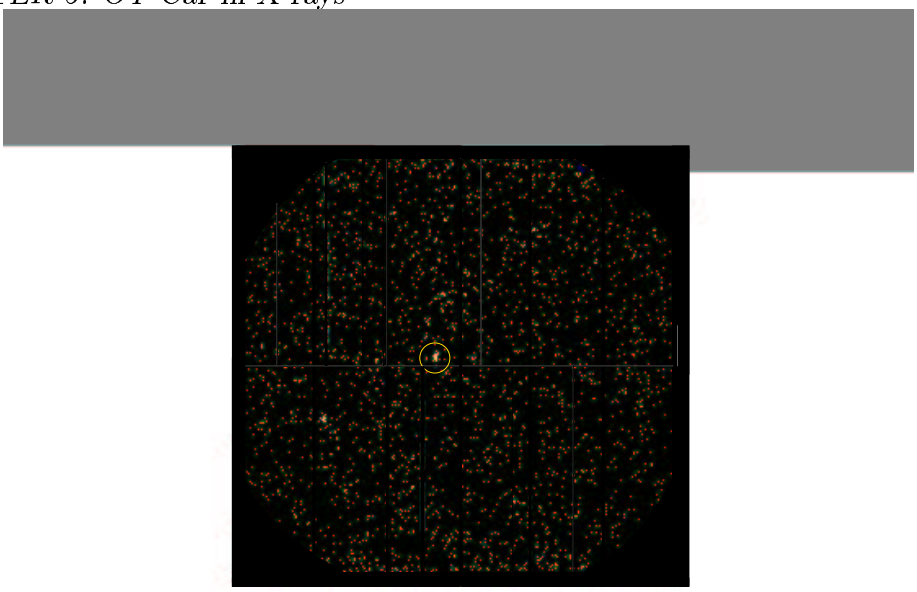

Figure 5.12: Eclipse image from the EPIC PN camera in the energy band $0.1 - 12.0$keV. The yellow circle outlines the position of OY Car.

the 6σ level. The origin of this non-zero flux is discussed further in Section 5.4.3.

There was no detection of an increase in the flux level in the $4.0-12.0$keV energy band. No significant flux was observed in the eclipse profiles of OY Car during the second *XMM-Newton* observation.

Individual Eclipse Profiles

In Ramsay, Poole et al. (2001a), only the mean eclipse profile and the mid eclipse flux were discussed. Here I investigate the individual eclipse profiles of each observation to search for unusual features.

Figure 5.13 shows the eclipse profiles of the first (top) and second (bottom) *XMM-Newton* observations increasing in ϕ_{2233} phase order ($\triangle$). Figure 5.14 shows the eclipse profiles of the first (top) and second (bottom) *XMM-Newton* observations increasing in ϕ_{3266} phase order ($\triangle$). The magenta '$*$'s in Figures 5.13 and 5.14 are eclipse profiles mirrored around phase 1.0, so that the ingress of an individual eclipse profile can be directly compared to the egress of that same eclipse profile. The

first *XMM-Newton* observation eclipse profiles are considered in the energy range $0.1-1.0$keV where the system is more variable (Figure 5.4), and the second *XMM-Newton* observation eclipse profiles are considered in the energy range $0.1-12.0$keV due to the reduced signal-to-noise in this observation.

Consider the first *XMM-Newton* observations (Figure 5.13 and 5.14, top) where nine eclipse profiles are observed through the 2233s cycle. Eclipses where the phase of the 2233s modulation (ϕ_{2233}) is 0.67 and 0.76 (ϕ_{3266}= 0.86 and 0.55) show a slight asymmetry in ingress and egress, with the egress being slightly steeper than the ingress in both cases. In contrast, eclipses with ϕ_{2233} = 0.56, 0.89, 1.01 and 1.45 (ϕ_{3266}=1.20, 1.21, 0.87 and 0.54) all have symmetric profiles. The most asymmetric profiles are those of eclipses with ϕ_{2233} = 1.12, 1.24 and 1.33 (ϕ_{3266}= 0.53, 1.19 and 0.88) which occur half a ϕ_{2233} cycle after the first asymmetry seen in eclipses 0.67 and 0.76 (ϕ_{3266}= 0.86 and 0.55). Eclipse 1.12 (ϕ_{3266}=0.53) shows the clearest asymmetry with a much steeper egress to ingress. Eclipse 1.33 (ϕ_{3266}=0.88) shows the reverse of eclipse 1.12 (ϕ_{3266}=0.53) where the ingress is steeper than the egress. The two eclipse profiles from the second *XMM-Newton* observations (Figure 5.13 and 5.14, bottom) show an eclipse of ϕ_{2233} = 0.59 (ϕ_{3266} = 0.94) with a symmetrical profile, and an eclipse of ϕ_{2233} = 1.15 (ϕ_{3266} = 1.44) with an asymmetrical profile; the shape of these profiles fits into the pattern that emerges in the first *XMM-Newton* observations folded on the 2233s period, but not the 3266s period. The ingress and egress of the eclipses are very rapid, ranging from 20s in eclipses ϕ_{2233} = 0.89 and 1.45 (ϕ_{3266}=1.21 and 0.54) to 50s in eclipse ϕ_{2233} = 0.67 (ϕ_{3266} = 0.86).

The asymmetries seen in Figures 5.13 and 5.14 could potentially be due to some sort of brightening within the X-ray boundary layer, comparable to the accretion regions seen on the surface of the white dwarf in IPs (Chapter 1, Section 1.2.1). The variations in the eclipse profile may alternatively be due to flickering. Generating a normally distributed set of random numbers to represent flickering, and adding them to the average eclipse profile tested this. The standard deviation of the mean 'out-of-eclipse' flux level was used to define the full width half maximum of the normally

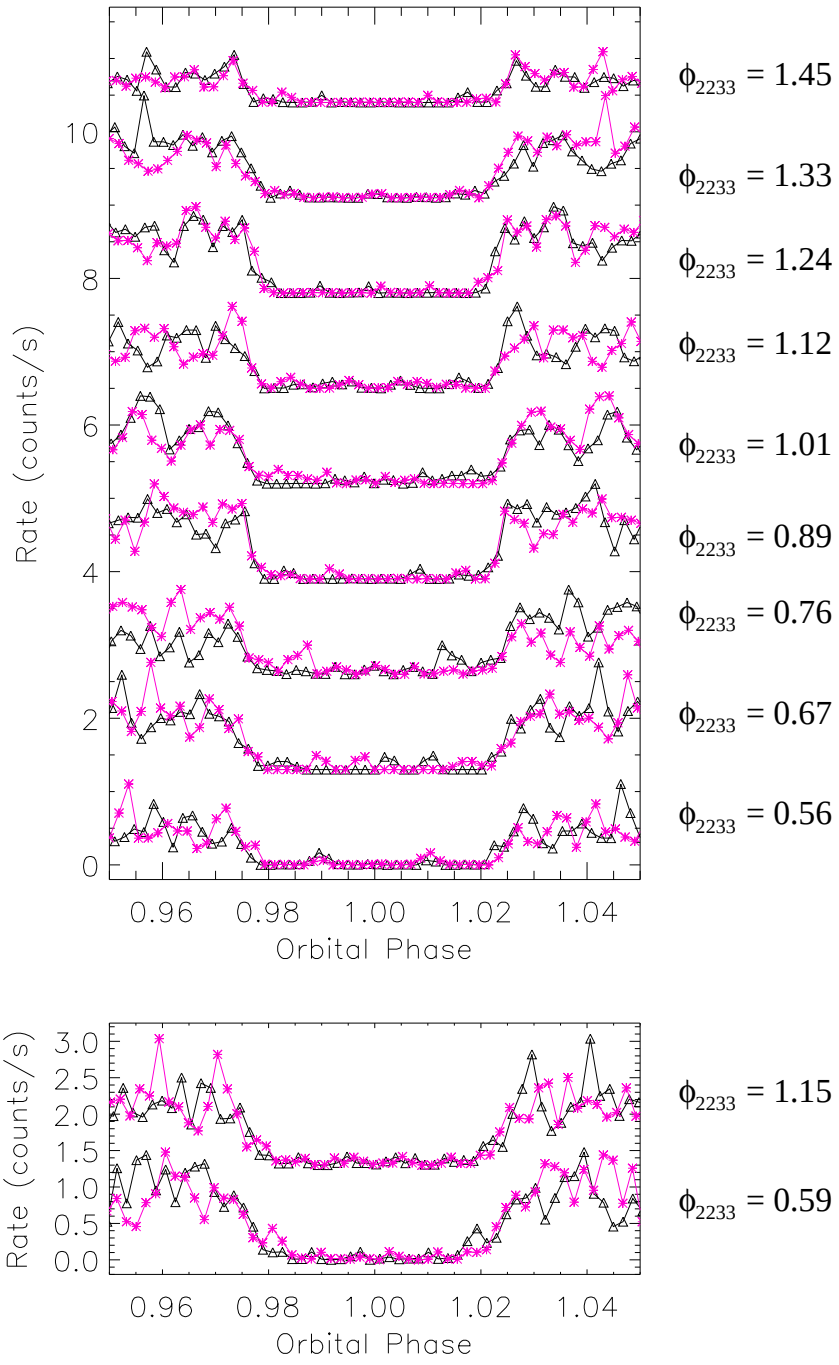

Figure 5.13: Summed EPIC eclipse profiles of OY Car in order of ϕ_{2233} phase. Top: The first *XMM-Newton* observations in the energy band 0.1 – 1.0keV. Bottom: The second *XMM-Newton* observations in the energy band 0.1 – 12.0keV. The magenta '$*$'s are mirrored eclipse profiles. The data is binned into 10s bins and is vertically offset by 1.3 counts/s.

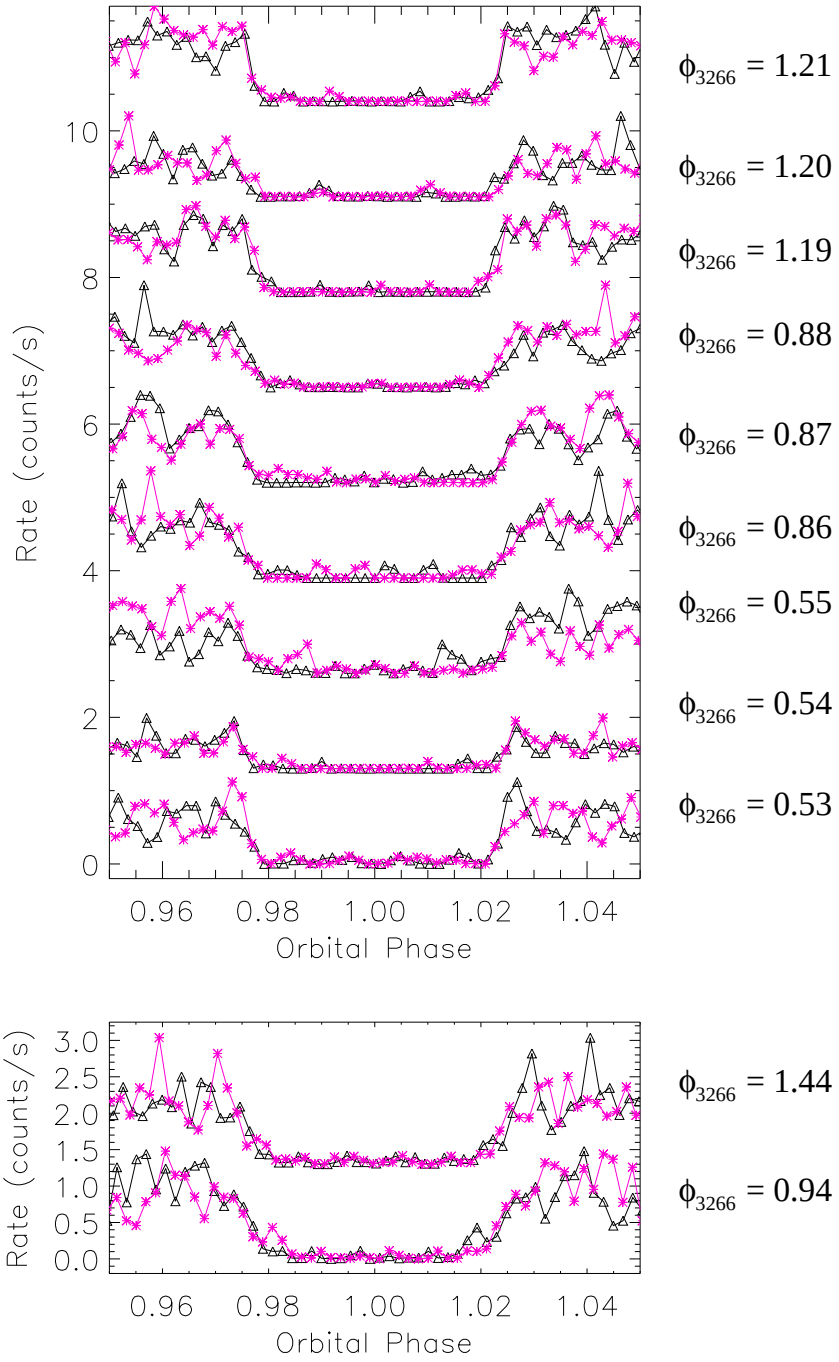

Figure 5.14: Summed EPIC eclipse profiles of OY Car in order of ϕ_{3266} phase. Top: The first *XMM-Newton* observations in the energy band $0.1 - 1.0$keV. Bottom: The second *XMM-Newton* observations in the energy band $0.1 - 12.0$keV. The magenta '$*$'s are mirrored eclipse profiles. The data is binned into 10s bins and is vertically offset by 1.3 counts/s.

distributed random numbers using Equation 3.7 (Chapter 3, Section 3.1.3). This was repeated 150 times producing a range of reduced chi-squared values of 0.4 to 1.3 for the eclipse profiles (Appendix B). These results do not greatly differ from the expected reduced chi-squared value of 1 ± 0.18, so the variations in the eclipse profile are probably due to flickering.

5.4 Discussion

Optical observations using the Optical Monitor (Ramsay, Poole et al. 2001a) show that OY Car was at the same optical brightness for both observations, but the *XMM-Newton* EPIC observations show that the X-ray flux had reduced by a factor ~ 2. The higher X-ray flux in the first observation may be due to the residual effects of the outburst prior to the first X-ray observation.

5.4.1 What is the Nature of the 2233s and 3266s Periods?

In Section 5.3.1 I showed evidence for 2233s and 3266s periods (cf. orbital period=5454s). It is possible, though unlikely, that these periods may have been due to an instrumental effect. To investigate this, EPIC observations of the source RX J0720-31 (in *XMM-Newton* orbit 78) that had similar exposure to OY Car were studied to search for similar periods/amplitudes (Ramsay, Poole et al. 2001a). We found no evidence for periods similar in time scale in the RX J0720-31 data, hence it is almost certain that the 2233s and 3266s periods are intrinsic to OY Car.

There are a number of possible origins for the 2233s and 3266s periods. These possibilities are:

1) Quasi-Periodic Oscillations (QPOs)

There are a number of periods seen in dwarf nova other than the binary period, including dwarf nova oscillations (DNOs), and quasi-periodic oscillations (QPOs).

DNOs are rapid ($10-30$s) coherent oscillations similar to oscillations seen in magnetic CV systems, whereas QPOs are thought to originate in the accretion disc or in magnetically-controlled accretion on time scales of $1-30$mins (Warner 1995). DNOs and QPOs produce a variation in luminosity that is observed as modulations in the light curve of a system. The 2233s and 3266s periods are too long to be associated with DNOs, but are the same order of magnitude as X-ray QPOs seen in the Intermediate Polar GK Persei of 3000s (Watson et al. 1985) and 5000s (Hellier & Livio 1994). Watson et al. (1985) postulate that these unusually long QPOs are the result of variation in the rate of accretion of material onto the white dwarf, but Hellier & Livio (1994) suggest that the QPOs are the result of the accretion stream from the secondary star overflowing the accretion disc, causing vertical structure where the stream collapses back onto the accretion disc at a radius which corresponds to a Keplerian orbital period of ≈ 5000s.

Both QPOs and DNOs are seen in the outburst phase of dwarf novae (although QPOs of ~ 600s have been observed in the dwarf nova VW Hyi at minimum light by Warner & Woudt 2001); the *XMM-Newton* observation of OY Car is seen in quiescence, and therefore the two oscillations that are observed are probably not due to the same phenomenon as the QPOs seen in the outburst of GK Persei.

2) Particle Resonance

An alternative explanation is a resonance in the outer parts of the accretion disc around the white dwarf. Tidal effects from the secondary star at the resonance radius affect the luminosity of the region, producing modulations in the light curve of the system. Disc particles will be trapped in a resonance orbital motion if

$$\frac{P_p}{P_{orb}} = \frac{(n-1)}{n}, \tag{5.4}$$

where P_p is the particle period and n is an integer (Vogt et al. 1980, Lin & Papaloizou 1979). For a particle period of 2233s my observations give a ratio of 2:5; this is not consistent with the resonance Equation 5.4 which gives ratios of 1:2, 2:3,

3:4 and 4:5 etc. For a particle period of 3266s my observations give a ratio of 3:5, which again is not consistent with Equation 5.4. Therefore I conclude that neither the 2233s or the 3266s periods arise from a particle resonance.

3) New class of Intermediate Polars (IPs)

A new class of Intermediate polars (IPs) below the period gap has been suggested by King & Wynn (1999). This new class includes EX Hya (P_{orb} = 5880s, P_{spin} = 4020s; Vogt et al. 1980). King & Wynn's calculations predict that EX Hya represents a new equilibrium spin state of

$$\frac{P_{spin}}{P_{orb}} \sim 0.53; \tag{5.5}$$

this is comparable with the observational value of 0.68 for EX Hya (Córdova et al. 1985b). The equilibrium spin state for a typical non-magnetic system below the period gap is ~ 0.07 (King & Wynn 1999 and references therein), making the results on EX Hya eight times greater than typically expected. Another possible candidate for this new class of IPs is RX J1238-38 (P_{orb} = 5077s, P_{spin} = 2147s; Buckley et al. 1998), with an equilibrium spin state of 0.42. Considering the 2233s/3266s periods as the spin period of the white dwarf, OY Car would have spin equilibrium states of 0.41 or 0.60 respectively; both of these values seem reasonable when considering the results of EX Hya and RX J1238-38 above. This would put OY Car into the new class of objects. The mechanism causing the modulations in an IP system is the change in visibility of the accretion regions on the surface of the white dwarf caused by occultation and absorption.

The best explanation for the origin for both the 2233s and 3266s period from these three possibilities is **3)**, to include OY Car in the new class of IPs with EX Hydrae and RX J1238-38. This would mean that the DNOs observed by Marsh & Horne (1998) (Chapter 1, Section 1.4.3) would not be due to the spin period of the white dwarf, as they suggest. An alternative source for the DNOs found by Marsh

& Horne (1998) may be a beat period between the outer layers of the white dwarf and the inner accretion disc.

If OY Car is indeed magnetic, the eclipse profiles should show accretion on to regions governed by the magnetic field of the white dwarf; this type of accretion implies asymmetry in the eclipse profiles due to the ever-changing nature of the accretion region (Chapter 1, Section 1.2.1). An asymmetry is seen in Figure 5.13 (Section 5.3.2), but the results suggest this is attributed to flickering. Non-magnetic systems are assumed to have symmetric eclipse profiles due to uniform accretion on to the white dwarf.

In the case of IPs, the accretion region on the white dwarf irradiates the disc. The disc-heated region rotates at a Keplerian velocity that is different from the accretion region velocity, setting up a beat period (P_{beat}). Using

$$\frac{1}{P_{beat}} = \frac{1}{P_{spin}} \pm \frac{1}{P_{orb}} \tag{5.6}$$

and an orbital period of 5454s for OY Car, beat periods of 3781s and 1584s ($P_{spin} =$ 2233s), or 8142s and 2043s ($P_{spin} = 3266$s) can be calculated. All these periods are close to peaks in the periodogram of Figure 5.6 (Bottom of top panel). Periods close to both the 1584s and 2043s are weak in comparison to the orbital, 2233s and 3266s periods, but the 3781s and 8142s periods lie close to the second and third highest peaks in the pre-whitened data respectively.

The beat period values, along with the equilibrium state calculation, imply that the 2233s period may be the spin period of OY Car. The variation in the profiles of the 2233s modulation from cycle-to-cycle (Figure 5.10) could be due to the accretion disc obscuring at least part of the X-ray emission region from time to time. Obscuration could be due to vertical structure on the outer edge of the disc caused by stream overflow, or the bright spot. The 3266s modulation also shows variations in its profile form cycle-to-cycle, further implying obscuration.

I attribute the 3266s period to a new oscillation, which may be produced by perturbations in the accretion disc (Chapter 1, Section 1.4.2). This oscillation may

also be obscured in the same way as the spin period, and may beat with the spin period. Substituting 2233s and 3266s in Equation 5.6 produces beat periods of 1326s and 7060s. The 1326s period does not lie close to any peaks in the periodogram (Figure 5.6), but the 7060s period lies close to the third highest peak in the pre-whitened data.

The question remains - do other dwarf novae show similar X-ray periods when observed with *XMM-Newton*, or is OY Car an unusual magnetic dwarf nova system? This can only be answered by further investigations of similar systems.

5.4.2 Origin of the X-ray Emission

The ingress/egress times of the X-ray eclipses in OY Car are typically $20 - 40$s (Figure 5.11 and Figure 5.13), suggesting that the X-ray emission originates from the white dwarf. These ingress/egress times are unlike the X-ray ingress times of less than 10s seen in magnetic CVs (e.g. Steiman-Cameron & Imamura 1999). Therefore the X-ray emission in OY Car is not coming from small accretion regions on the white dwarf, but more likely originates from an equatorial boundary layer with small ($<< R_1$) height above the surface of the white dwarf as illustrated in Figure 5.15.

To determine the extent of the X-ray emitting region in the orbital plane (R_x), consider Equations 2.7 and 2.8 (Chapter 2, Section 2.2.3). OY Car is a fully eclipsed system, so by assuming $\cos^2 i \sim 0$ these two equations can be simplified to

$$\frac{R_x}{a} \approx \frac{\pi t_e}{P_{orb}} = 0.017 \pm 0.006, \tag{5.7}$$

where a is the binary separation, $P_{orb} = 5454$s is the orbital period, and $t_e = 30 \pm 10$s is the ingress/egress X-ray time. Considering a white dwarf mass of $0.83 M_\odot$ and a mass ratio of 0.1 (results from Section 5.5), leads to a secondary star mass of $0.083 M_\odot$ using the mass ratio, and a white dwarf radius of $R_1 = 0.0097 R_\odot$ using the mass radius relation of Nauenberg (1972). The masses of the component stars can then be substituted into Kepler's third law, Equation 1.1 (Section 1.1, Chapter

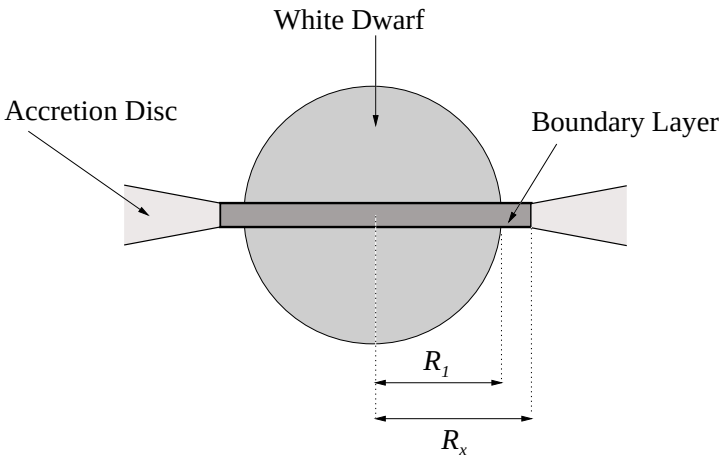

Figure 5.15: Illustration of the equatorial boundary layer. The extent of the boundary layer in the orbital plane from the centre of the white dwarf is given by R_x, and the radius of the white dwarf is R_1. The 'height' of the boundary layer above the surface of the white dwarf is given by $R_x - R_1$, and is exaggerated in this illustration.

1) resulting in $a = 0.647R_\odot$. Using the results of Equation 5.7 and $a = 0.647R_\odot$ leads to $R_x = 0.011 \pm 0.004R_\odot$. Therefore the maximum extent of the X-ray emitting material is $1.13 \pm 0.21R_1$; the height of the boundary layer above the surface of the white dwarf is $13\% \pm 21\%$ of the radius of the white dwarf, so the boundary layer could have a negligible height above the white dwarf considering the error. OY Car has an inclination angle of less than 90^o, so the height of the boundary layer above the white dwarf will decrease. Setting the inclination angle to 83^o (Wood et al. 1989, Wood & Horne 1990) leads to a boundary layer with negligible height above the surface of the white dwarf.

5.4.3 Origin of the Non-Zero X-ray Flux during Eclipse

A non-zero X-ray flux in the soft energy band was observed in the eclipse profiles of OY Car during the first *XMM-Newton* observation, but was not evident in the second observation (Section 5.3.2). There are several possibilities for the origin of this excess of emission.

1) The secondary star.

The secondary star in OY Car is assumed to be a low mass late type main sequence star (Ritter 1980b). This type of secondary star is expected to have a luminosity of $L_x < 4 \times 10^{27}$ ergs/s using the L_x/L_{bol} saturation of 1×10^{-3} (Randich et al. 1996), and the mass-luminosity relationship

$$\log\left(\frac{L_{bol}}{L_\odot}\right) = -2.961 \tag{5.8}$$

(Malkov, Piskunov & Shpil'Kina 1997) for $M_2 = 0.1 M_\odot$ (Section 5.5), where L_{bol} is the bolometric luminosity of the secondary star and $L_\odot$ is the luminosity of the Sun. In Ramsay, Poole et al. (2001a) we calculated the in-eclipse luminosity of OY Car as 4.5×10^{28} ergs/s by assuming that the secondary star has a softer spectrum than the integrated spectrum of OY Car by a factor of ~ 2. The observed luminosity of OY Car (4.5×10^{28}erg/s) thus exceeds the expected luminosity of the secondary star ($< 4 \times 10^{27}$erg/s), therefore it is unlikely this excess X-ray flux can be attributed to the secondary star. Also, if this excess X-ray flux is from the secondary star, it should have also been present in the second *XMM-Newton* observation, and throughout primary eclipse. The excess X-ray flux is not seen in the second *XMM-Newton* observation, or throughout primary eclipse, therefore is most probably not due to the secondary star.

2) The weak remnant of a large corona.

During a previous outburst of OY Car, a large (Roche lobe sized) X-ray corona was observed by Naylor et al. (1988). These authors found that any optically thin X-ray emitting region must have temperatures of the order 10^{6-7}K, which agrees with the observed energy band of $0.1 - 1.0$keV. The excess X-ray flux seen in eclipse during the first *XMM-Newton* observation may be due to a weak remnant of the OY Car outburst occurring 4 days before, but this scenario does not explain the asymmetry of the non-zero flux observed during eclipse.

3) An X-ray region fixed in the binary frame.

The non-zero flux may be produced from an asymmetric X-ray emission region close to the white dwarf, at a fixed position in the binary frame offset from the line of

centres. The mechanism generating this flux is not clear, but two possibilities are stream overflow or magnetically controlled accretion. If the accretion stream from the secondary star overflows the outer edge of the accretion disc, it can impact the accretion disc closer to the white dwarf. The mechanism producing the soft X-ray emission in this case would be the conversion of the stream's kinetic energy as it passes through the shock generated at the impact point. Alternatively, if the magnetic field of the white dwarf is strong enough (Chapter 1, Section 1.2.3) it will channel the accreting material onto the surface of the star via columns or curtains. In this case lower energy radiation is absorbed by the photosphere of the white dwarf, thermalised and then re-emitted as soft X-rays (Warner 1995). If the white dwarf in OY Car is weakly magnetic it would asynchronously rotate, and therefore the position of the X-ray region would slip slightly from cycle-to-cycle; this may be observed in Figure 5.13 where a small excess flux does shift slightly during the eclipse minimum at ϕ_{2233} of 0.67, 0.76, 1.01 and 1.45, but this could also be attributed to flickering (Section 5.3.2).

5.5 Calculating the Mass of the Component Stars in OY Car

Although the inclination angle (i) of OY Car is widely accepted as 83^o (Wood et al. 1989, and Wood & Horne 1990), there is a large variation in the reported masses of the primary star of $0.30 - 1.26 M_{\odot}$ (Ritter 1980b and Cook 1985), and the secondary star of $0.07 - 0.15 M_{\odot}$ (Wood et al. 1989 and Vogt et al. 1981); for a more detailed discussion see Chapter 1, Section 1.4.3. However, the mass ratio of OY Car has recently been better constrained to $0.10 - 0.11$ (Wood et al. 1989). Using the eclipse timings from Section 5.3.2, some of the physical parameters of OY Car can be constrained.

Using Figures 4.1 and 4.2 (Chapter 4, Section 4.1.1), $i = 83^o$, and $\Delta\Phi = 0.048 \pm$

0.001 orbital phase (or $\phi_{1/2} = 8.6 \pm 0.2^o$) from FWHM of the mean eclipse profile (Section 5.3.2), a mass ratio of $q = 0.1$ is found; this value is in good agreement with the previous results of $0.10 - 0.11$ (Wood et al. 1989). The results of Section 5.4.2 show that the boundary layer could have a negligible height above the white dwarf considering the error. Assuming the shape of the boundary layer is a flat disc of radius R_1, and using the full X-ray eclipse duration of 295 ± 5s ($= 0.055 \pm 0.001$ orbital phase) from Section 5.3.2, an R_1/a of 0.0173 ± 0.0029 can be calculated by tracing the Roche lobe of the secondary through the binary system. The volume-equivalent radius of the Roche lobe has been approximated by Smith & Dhillon (1998) as

$$\frac{R_2}{a} = 0.47 \left(\frac{q}{1+q} \right)^3, \tag{5.9}$$

and is accurate to less than 3% for CVs with $0.01 < q < 1.0$. From the R_1/a value and Equation 5.9 ($R_2/a = 0.2113$ for $q = 0.1$), a ratio of the component stars can be calculated as

$$\frac{R_2}{R_1} = 12.4 \pm 2.0. \tag{5.10}$$

assuming the secondary star fills the Roche lobe.

To find the set of R_1 and R_2 values that satisfy Equation 5.10, a range of primary (M_1) and secondary (M_2) star masses were considered. M_1 values from 0.70 to 1.00 were used, providing a range of M_2 values from 0.070 to 0.100 using $q = 0.1$. R_1 and R_2 were then calculated using the following mass-radius relationships. R_1 was calculated using

$$R_1 = 0.779 \left(\left[\frac{M_1}{M_{ch}} \right]^{-2/3} - \left[\frac{M_1}{M_{ch}} \right]^{2/3} \right)^{1/2} \times 10^9 \text{cm} \tag{5.11}$$

(Nauenberg 1972), where M_{ch} is the Chandrasekhar mass of $1.44 M_\odot$. R_2 was calculated using

$$R_2 = M_2^{0.867} \tag{5.12}$$

for $0.08 M_\odot < M_2 < 1.0 M_\odot$ (Warner 1995) assuming the secondary star is a main sequence star.

Figure 5.16 shows a plot of R_1 vs R_2. The area between the two dashed lines in Figure 5.16 represents the acceptable results of Equation 5.10, leading to the mass ranges of $M_1 = 0.85 \pm 0.07 M_\odot$ and $M_2 = 0.085 \pm 0.007 M_\odot$. If the boundary layer has a non-negligible height, then the primary star radius will be smaller, increasing the primary mass.

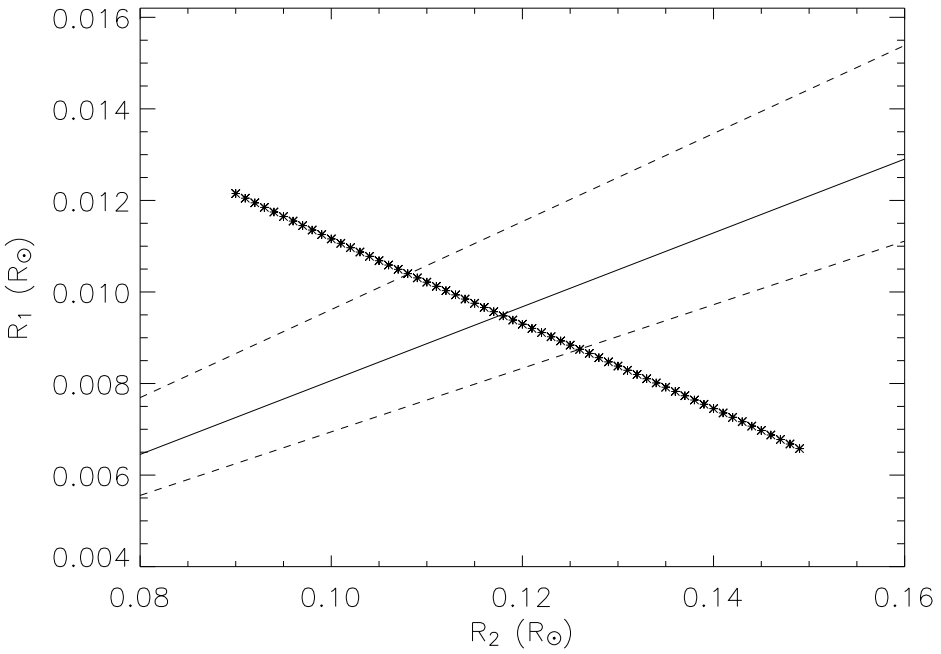

Figure 5.16: Plot of R_2 vs R_1 ($*$). The solid black line represents the $R_2/R_1 = 12.4$ gradient (Equation 5.10), and the dashed lines represent the ± 2.0 error on that gradient. Any radius combination that lies inside the dashed lines is an acceptable result.

Previous optical observations of OY Car in quiescence have led to white dwarf eclipse times of 0.0562 ± 0.0010 orbital phase (Vogt et al. 1981), 0.0577 ± 0.0010 orbital phase (Cook 1985), and 0.0580 ± 0.0004 orbital phase (Wood et al. 1989); measured as the full duration of the eclipse. These optical eclipse times are larger than the X-ray eclipse time (0.055 ± 0.001 orbital phase), which is what is expected if the X-ray continuum is being produced by an equatorial boundary layer rather than the primary star as I suggest. Using the average of these three optical eclipse widths (0.0573 ± 0.0007 orbital phase) and $i = 83^o$, leads to $R_1/a = 0.0200 \pm 0.0017$,

and hence a radius ratio of $R_2/R_1 = 10.6 \pm 0.9$ using Equation 5.9 with $q = 0.1$. From Figure 5.16, a decrease in R_2/R_1 leads to a decrease in R_2 and an increase in R_1, and hence a decrease in the masses of the component stars. Using the optical data I calculate a range of primary and secondary star masses of $0.78 \pm 0.04 M_\odot$ and $0.078 \pm 0.004 M_\odot$ respectively, which overlap with the X-ray results within error.

Comparing the X-ray and optical eclipse widths, the optical eclipse is $6\% \pm 3\%$ larger than the X-ray eclipse. This is consistent with the X-ray eclipse resulting from the occultation of an equatorial boundary layer with very little height $(R_x - R_1)$ above the surface of the white dwarf. Therefore the mass results obtained using the optical eclipse widths are more accurate because the primary star eclipse is directly observed, unlike the X-ray observations where a boundary layer is eclipsed.

5.6 Conclusions

I have presented *XMM-Newton* X-ray timing studies of OY Car, which have allowed me to investigate the X-ray eclipse profile of this dwarf nova system in more detail. The most important result to come from this study is the short ingress/egress times of the eclipse profiles that suggest that the boundary layer has a very small extent above the white dwarf.

The total eclipse duration of 295 ± 5s was found using the average eclipse profile of OY Car, and was used to constrain the mass of the component stars within the system. Roche lobe geometry was used to constrain the radii of the component stars, hence producing mass ranges using mass-radius relationships. The masses of the primary and secondary stars using the X-ray data, are confined to the ranges of $M_1 = 0.78 - 0.92 M_\odot$ and $M_2 = 0.078 - 0.092 M_\odot$ assuming an empirical mass radius relationship. Considering the previous optical observations of Vogt et al. 1981, Cook 1985, and Wood et al. 1989, leads to a range of primary and secondary masses of $0.74 - 0.82 M_\odot$ and $0.074 - 0.082 M_\odot$ respectively.

The average eclipse profile of OY Car in the soft energy band showed a non-zero

flux. X-rays from the secondary star are ruled out as a possible solution due to the high level of this flux. An extended X-ray corona produced in a previous outburst of OY Car is also ruled out due to the asymmetric nature of the non-zero flux. A more plausible solution is an X-ray emission region resulting from either stream overflow or a magnetic white dwarf, which is fixed in the binary frame.

Another important result obtained from this study is the detection of oscillations with underlying periods of 2233s and 3266s. The 2233s modulation is most probably due to the spin period of the white dwarf, therefore suggesting that OY Car may belong to the new class of IPs below the period gap (King & Wynn 1999). The question remains whether OY Car is an unusual dwarf nova system, or if other dwarf nova systems show evidence of magnetism. This is discussed further in Chapter 6.

Chapter 6

Conclusions

6.1 RW Tri

The eclipsing nova-like system RW Tri is very interesting to study because of its many different observable features. In particular, RW Tri is very active in the ultraviolet; with spectra showing broad emission features attributed to extended collimated winds, and unusual narrow absorption features that appear in emission during eclipse. In Chapter 2 I produce a simple absorption model, including the physical nature of the UV continuum and the inclination angle of the system. This model was used to fit an absorption line profile to a narrow feature observed at λ1335Å in the ultraviolet *Hubble Space Telescope* observations of Mason et al. (1997). The results of this model confirm that at an orbital phase close to 0.5, the material producing the absorption feature is confined to an arc, that has a height above the orbital plane with an inner radius at a distance of $0.3R_{\odot}$ from the centre of the white dwarf, and an azimuthal thickness of $0.01R_{\odot}$. Although this does not tell us how these narrow absorption features are produced, it goes a long way in pinpointing the position of the material creating the absorption features within the system. To further investigate the geometry of this absorbing material a more complex model was discussed to include the effects of the underlying emission features observed

during eclipse, and multiple orbital phase analysis to predict the behaviour of the features during eclipse.

The UV continuum of the *Hubble Space Telescope* observations of Mason et al. (1997) was also modelled in Chapter 2. A radial velocity line-free continuum light curve was extracted from the observations and then fitted using a steady-state blackbody accretion disc model. This lead to a blackbody UV continuum with an effective extent of $0.234 R_{\odot}$ which is 20 times larger than the white dwarf radius and over half the accretion disc radius.

At longer wavelengths, the effects of the secondary star of RW Tri can be observed. The velocity of the secondary star plays a key role in calculating the mass of the component stars within the system, and is therefore an important value to constrain in any CV. In Chapter 3, I calculate the radial velocity amplitude of the secondary star in RW Tri using time resolved spectroscopy and a range of late-type spectral template stars. The method of skew-mapping is used on the far red data of Smith et al. (1993), due to the low signal-to-noise of the data. The method of cross-correlation is used on the near infrared data I obtained using the *United Kingdom Infra-Red Telescope*. The final results of 235 ± 47 km/s (in the far red) and 221 ± 29 km/s (in the near infrared) agree within the errors. The spectral type for the secondary star of M0 in the far red agrees with the statistical prediction of K9$\pm$3 (Smith & Dhillon, 1998), but in the near infrared the spectral type of the secondary is indistinguishable. Using the near infrared data I find a $V_{rot} \sin i = 120 \pm 20$km/s for the projected rotational velocity of the secondary star.

To understand the accretion processes and geometry of RW Tri, it is vital to constrain the masses of the system. The masses of the component stars in RW Tri have been poorly constrained, but with component star velocities, their masses can be calculated using Kepler's third law. In Chapter 4 I combine the secondary star velocity of RW Tri from the near infrared results in Chapter 3, with the white dwarf velocities of other authors (ultraviolet features - Mason 1999, H and He emission - Still et al. 1995, H and He emission - Kaitchuck et al. 1983). I find a range of

mass ratio values of 0.8 to 1.3. Using the He II emission (Still et al. 1995) which originates in a region close to the white dwarf, primary and secondary star masses of $0.8-1.1M_{\odot}$ and $0.9-1.1M_{\odot}$ are found respectively. The 'K-correction' of Wade & Horne (1988), based on the absorption feature results of Chapter 3, is also considered in the mass calculation.

Difficulties in calculating the velocity of the primary star contribute to the large range of masses I find. The main problem with calculating the primary star velocity is finding a feature that represents the velocity of the white dwarf. Up until now, H and He disc emission features have been used to estimate this velocity, producing a large range of values from 223km/s for Hγ (Still et al. 1995) to 170km/s for He I (Kaitchuck et al. 1983). The main difficulty with using these features is that they originate from accretion disc and secondary star regions, and therefore their velocities are affected by the motions of the secondary star, stream material, bright spot and accretion disc. The wings of these emission lines will represent gas closest to the white dwarf, but velocity measurements using the wings of these lines in RW Tri were not consistent with Doppler maps (Still et al. 1995). Recently Mason (1999) found that ultraviolet narrow absorption features mirrored the orbital phase of the white dwarf, but the resulting mass ratio is too high to produce a stable mass accreting system, therefore these features probably do not reflect the white dwarf velocity.

The rotational velocity of the secondary star found in Chapter 3 is also used to calculate the masses of the component stars. This method does not consider the velocity of the primary star, and therefore produces more reliable results. Using $V_{rot} = 120 \pm 20$km/s and secondary star velocities of 178km/s and 221km/s leads to primary and secondary masses of $0.4-0.7M_{\odot}$ and $0.3-0.4M_{\odot}$ respectively. These results better agree with the expected masses of component stars within CVs.

The secondary star velocity is well constrained from my infrared data, but will vary depending upon the region over which the secondary star is being irradiated by the accretion disc; my results show evidence that the secondary star absorption

features are stronger when observing the hemisphere that faces away from the accretion disc. This phenomenon has been taken into consideration when calculating the mass ratio range for RW Tri using the 'K-correction' of Marsh & Horne (1988).

6.2 OY Car

In Chapter 5 I use X-ray observations to probe the extent of the boundary layer in OY Car. Using *XMM-Newton* I have been able to study the X-ray eclipse profile of the system in detail, allowing me to resolve the boundary layer. The eclipsing dwarf nova system OY Car is an ideal system to study this phenomenon due to its short period and total eclipse. The short ingress/egress times of the eclipse profiles and the full eclipse width time, suggest a boundary layer with a very small extent, which is extended in azimuth around the white dwarf.

For the first time, the X-ray light curves of OY Car also show energy dependent quasi-sinusoidal variability's. These variability's have underlying periods of 2233s and 3266s, which may be due to the spin period of the white dwarf. This suggests that OY Car may belong to a new class of intermediate polars below the period gap (King & Wynn 1999).

As in RW Tri, it is important to be able to constrain the masses of the component stars within OY Car. At X-ray wavelengths the duration of eclipse provides vital information about the size of the component stars. The total eclipse duration of 295 ± 5s for OY Car was used to confine the secondary and primary star masses to ranges of $M_2 = 0.078 - 0.092 M_\odot$ and $M_1 = 0.78 - 0.92 M_\odot$ respectively. Considering the previous optical observations of Vogt et al. 1981, Cook 1985, and Wood et al. 1989 leads to a range of primary and secondary masses of $0.72 - 0.80 M_\odot$ and $0.072 - 0.080 M_\odot$ respectively.

6.3 Future Work

This work carried out on RW Tri and OY Car provides a strong foundation for constraining the masses of the component stars within each system. It also provides the first steps to understanding specific features seen within each system. These foundations can be built up to provide a more accurate knowledge of nova-like and dwarf nova systems, as well as fine tuning the methods of confining the component star masses within CV systems.

6.3.1 RW Tri (and UX UMa)

The nova-like CV UX UMa is very similar in nature to RW Tri. Narrow absorption features in ultraviolet *Hubble Space Telescope* data of UX UMa have a velocity of $\sim$ 100km/s, which is smaller than the same ultraviolet features seen in RW Tri (Mason 1999). UX UMa was observed in the far red by Vande Putte et al. (2003). It would be very interesting to observe UX UMa in the near infrared to further investigate the radial velocity amplitude of the secondary star. This data, along with the results from Vande Putte et al. (2003) could then be used to check the ultraviolet results, limit the masses of the component stars to see how they differ from RW Tri, and build on the knowledge already gained about these systems.

The Narrow Ultraviolet Absorption Features in RW Tri

The simple absorption model I produce in Chapter 2 was only used to fit the single narrow absorption feature seen at 1335Å and orbital phase close to 0.5. The model should also be tested more rigorously using other orbital phases and other features. The model results could also be improved by considering the effects of the underlying emission feature observed at eclipse.

The possible origin of the narrow absorption line region is discussed in Chapter 2, Section 2.7. Further investigation of these ideas should be undertaken to try to understand how and why these features come about.

Further Constraining the Masses in RW Tri

Currently, the best method for determining the mass of the component stars in an eclipsing CV system is by using a combination of the radial and rotational velocity of the secondary star. These parameters only depend upon the assumption that the secondary star fills its Roche lobe, and can be easily obtained if the secondary star is observable.

The main problem with using the primary star velocity to calculate the mass ratio of the system is the difficulty in identifying white dwarf line features (as discussed in Section 6.1). Better measurements of the white dwarf velocity are needed. Still et al. (1995) had problems measuring the wings of H and He features due to absorption features. If it is possible to mask these line features out using a modelled template, a more accurate velocity may be found using the wings of emission lines.

Another approach to confine the masses of RW Tri is the method I use in Chapter 5, using the X-ray eclipse duration to confine the size of the white dwarf. To date, RW Tri has been observed to have a ROSAT PSPC count rate of 0.007 ± 0.003 counts/s in the energy range 0.1-2.4keV (Van Teeseling et al. 1996). With the larger collecting area and energy range of *XMM-Newton* better observations of RW Tri will be possible in the X-ray regime.

6.3.2 OY Car

Is OY Car a Magnetic System?

In Chapter 5 I have shown evidence that OY Car may be a magnetic system, but further investigation is needed to confirm this finding. Magnetic fields are observed at optical wavelengths in CV systems in three ways (see Hellier 2001 for review). 1. Cyclotron humps. 2. Polarisation. 3. Zeeman splitting.

There have been no observations to date that provide evidence for these phenomena in OY Car, but a thorough investigation of previous observations may uncover evidence that has previously been overlooked.

Source	Orbital Period	Visible Magnitude	Right Ascension	Declination	References
OY Car	1.5149	15.6 - 12.4	10 06 22.43	70 14 04.9	1, 2, 3, 4
Z Cha	1.788	16.0 - 12.4	08 07 28.2	-76 32 01	1, 5, 6, 7, 8
WX Hyi	1.796	14.7 - 12.5	02 09 50.65	63 18 39.9	1, 9, 10, 11
CU Vel	1.855	15.5 - 11.1	08 58 32.87	-41 47 50.8	1, 12, 13, 14
YZ Cnc	2.086	14.4 - 11.9	08 10 56.62	20 08 33.6	1, 15, 16

Table 6.1: Eclipsing dwarf novae with similar properties to OY Car. References: 1. Downes et al. 1997, 2. Vogt 1979a, 3. Bruch et al. 1996, 4. Berriman 1984, 5. Mumford 1969, 6. Mumford 1971, 7. Harlaftis et al. 1992, 8. Rayne & Whelan 1981, 9. Schoembs & Vogt 1981, 10. Bateson 1988, 11. Kuulkers et al. 1991, 12. Bateson 1977, 13. Ritter 1990, 14. Downes & Shara 1993, 15. Elsworth & Jameson 1986, 16. Shafter & Hessman 1988. The orbital period in column 2, is measured in days.

Is OY Car Unique?

The question remains - "Is OY Car a unique system, or are there other dwarf novae below the period gap that show quasi-periodic variations on the same time scales as OY Car?" A further study of other eclipsing dwarf nova systems below the period gap can be undertaken using *XMM-Newton*. Possible sources are listed in Table 6.1, and are all observable by *XMM-Newton*.

6.4 In Conclusion

The masses of the component stars in the nova-like system RW Tri and the dwarf nova system OY Car have been further constrained. The mass ratio and masses of RW Tri were calculated using the rotational velocity and the radial velocity amplitude of the secondary star from near infrared observations. The mass ratio and

masses of OY Car were calculated using X-ray and optical eclipse timings.

In addition to constraining the masses of these two systems, I have investigated specific features within RW Tri and OY Car. A simple absorption model was fitted to ultraviolet spectroscopic observations of RW Tri, to show that narrow absorption features may be found in an arc, defined by a cylindrical region centred on the white dwarf. From X-ray observations of OY Car, I have been able to limit the boundary layer of the system to a region very close to the white dwarf.

Acknowledgments

First of all I would like to thank my family for putting up with my mood swings throughout the three years of my PhD., especially my husband Gordon; without his constant love and support I would never have got through the bad patches.

I would like to thank members of the Astrophysics group for their valuable discussion and encouragement. To Mark Cropper, thank you for the use of your Roche lobe tracing program, and your support when the going got tough. To Gavin Ramsay, thanks for making me feel like a valuable member of the team, and to Mat Page for use of your curve-of-growth program. I would also like to thank my fellow students for keeping me going, especially Lucie Green and Cynthia James.

Thanks go to Robert Smith for allowing me to use *Isaac Newton Telescope* RW Tri spectra and related template stars for analysis. I also thank Robert Smith and Dave Vande Putte for valuable discussion on the analysis of this data.

I thank Paul Hurst for help with CGS4 data reduction, and the Joint Astronomy Centre who run the *United Kingdom Infrared Telescope* on behalf of the U.K. Particle Physics and Astronomy Research Council. I would like to thank Tom Marsh for help with MOLLY, and Janet Drew for valuable input into proposal and paper writing.

In this research, I have used, and acknowledge with thanks, data from the AAVSO International Database, based on observations submitted to the AAVSO by variable star observers worldwide.

I would finally like to thank my supervisors Keith Mason and Liz Puchnarewicz for their ongoing supervision; and PPARC for my funding, without which I would not have been able to produce this work.

References

Africano, J. L., Nather, R. E., Patterson, J., & Robinson, E. L., 1978, *Publs astr. Soc. Pacif.,* **90**, 568

Africano, J., & Wilson, J., 1976, *Publs astr. Soc. Pacif.,* **88**, 8

Aschenbach, B., Briel, U., Haberl, F., Brüninger, H., Burket, W., Oppitz, A., Gondoin, P., Lumb, D., 2000, SPIE, 4012, Paper 86, [astro-ph/0007256]

Aschenbach, B., Citterio, O., & Ellwood, J., 1987, The High-Throughput Spectroscopic Mission, Report of the Telescope Working Group, Proc., ESA SP-1084

Bailey, J., 1990, *Mon. Not. R. astr. Soc.,* **243**, 57

Bateson, E. M., 1988, *Pub. Var. Star Sec. RAS NZ*, **14**, 1

Bateson, E. M., 1977, *Pup. Var. Star Sec. RAS NZ*, **5**, 1

Berriman, G., 1984, *Mon. Not. R. astr. Soc.,* **210**, 223

Beiser, A., 1987, Concepts of Modern Physics, McGraw-Hill Book Company

Bevington, P., R., & Robinson, D., K., 1992, Data Reduction and Error Analysis for the Physical Sciences, McGraw-Hill, Inc.

Billington, I., Marsh, T. R., Horne, K., Cheng, F. H., Thomas, G., Bruch, A., O'Donoghue, D., Eracleous, M., 1996, *Mon. Not. R. astr. Soc.,* **279**, 1274

Bruch, A., Beele, D., & Baptista, R., 1996, *Astr. & Astrophys.,* **306**, 151

Buckley, D. A. H., Cropper, M., Ramsay, G., Wickramasinghe, D. T., 1998, *Mon. Not. R. astr. Soc.,* **299**, 83

Buat-Ménard, V., & Hameury J.-M., 2002, *Astr. & Astrophys.,* **386**, 891

Catalán, M. S., Schwope, A. D., & Smith, R. C., 1999, *Mon. Not. R. astr. Soc.,* **310**, 123

Carroll, B. W., & Ostlie, D. A., 1996, An Introduction to Modern Astrophysics, Addison-Wesley Publishing Company, Inc.

Cash, W., 1979, *Astrophys. J.,* **228**, 939

Chanan, G. A., Middleditch, J., & Nelson, J. E., 1976, *Astrophys. J.,* **208**, 512

Christy, R. W., & Pytte, A., 1965, The Structure of Matter, W. A¿ Benjamin, Inc.

Cook, M. C., 1985, *Mon. Not. R. astr. Soc.,* **215**, 211

Córdova, F. A., & Mason, K. O., 1985a, *Astrophys. J.,* **290**, 671

Córdova, F. A., Mason, K. O., & Kahn, S. M., 1985b, *Mon. Not. R. astr. Soc.,* **212**, 447

Córdova, F. A., & Mason, K. O., 1984, *Mon. Not. R. astr. Soc.,* **206**, 879

Córdova, F. A. & Mason, K. O., 1982, *Astrophys. J.,* **260**, 716

Cox, J. P., 1981, *Astrophys. J.,* **247**, 1070

Deeming, T. J.,1975, *Ap. Space Sci.,* **36**, 137

den Herder, J. W., Brinkman, A. C., Kahn, S. M., Branduardi-Raymont, G., & Thomsen, K., 2001, *Astr. & Astrophys.,* **365**, L7

Dhillon, V. S., Littlefair, S. P., Howell, S. B., Ciardi, D. R., Harrop-Allin, M. K., & Marsh, T. R., 2000, *Mon. Not. R. astr. Soc.,* **314**, 826

Downes, R., Webbink, R. F., Shara, M. M., 1997, *Publs astr. Soc. Pacif.,* **109**, 345

Downes, R. A., & Shara, M. M., 1993, *Publs astr. Soc. Pacif.,* , **105**, 127

Drew, J. E., 1987, *Mon. Not. R. astr. Soc.,* **224**, 595

Drew, J. E. & Verbunt, F., 1985, *Mon. Not. R. astr. Soc.,* **213**, 191

Echevarría, J., 1983, *Rev. Mexicana Astron. Astrof.,* **8**, 109

Eggleton P. P., 1983, *Astrophys. J.,* **268**, 368

Ehle, M., Breitfellner, M., Dahlem, M., Guainazzi, M., Rodriguez, P., Santos-Lleo, M., Schartel, N., & Tomas L., 2001, XMM-Newton Users' Handbook, V-2.0

Elsworth, Y., & Janseon, J. F., 1986, *Mon. Not. R. astr. Soc.,* **220**, 895

Frank, J., King, A., & Raine, D., 1992, Accretion Power in Astrophysics, Cambidge University Press

Frank, J., King, A. R. & Lasota, J.-P., 1987, *Astr. & Astrophys.,* **178**, 137

Frank, J. & King, A. R., 1981, *Mon. Not. R. astr. Soc.,* **195**, 227

Friend, M. T., Martin, J. S., Smith, R. C., & Jones, D. H. P., 1990, *Mon. Not. R. astr. Soc.,* **246**, 637

Friend, M. T., Martin, J. S., Smith, R. C., & Jones, D. H. P., 1988, *Mon. Not. R. astr. Soc.,* **233**, 451

Gondoin, P., 2000, User's Guide of the XMM-Newton Science Analysis System

Griesmann, U., & Kling, R., 2000, *Astrophys. J.,* **536**, L113

Harlaftis, E. T., Naylor, T., Hassall, B. J. M., Charles, D. A., Sonnenborn, G., & Bailey J., 1992, *Mon. Not. R. astr. Soc.,* **259**, 593

Hartley, L. E., Drew, J. E., Long, K. S., Knigge, C. & Proga, D., 2002, *Mon. Not. R. astr. Soc.,* **332**, 127

Hellier, C., 2001, Cataclysmic Variable Stars: How and why they work, Springer

Hellier, C., & Livio, M., 1994, *Astrophys. J.,* **424**, L57

Hjellmung, M. S., & Taam, R. E., 1991, *Astrophys. J.,* **370**, 709

Hjellming, M. S, & Webbink, R. F., 1987, *Astrophys. J.,* **318**, 754

Helman, C., 2002, The Pictorial periodic Table,
http://chemlab.pc.maricopa.edu/periodic/periodic.html

Hirst, P., 2001,
http://www.jach.hawaii.edu/JACpublic/UKIRT/instruments/cgs4/cgs4.html

Honey, W. B., Bath, G. T., Charles, P. A., Whitehurst, R., Jones, D. H. P., Echevarría, J., Areval, O. M. J., Solheim J. -E, Tovmassian, G., & Takagishi, K., 1989, *Mon. Not. R. astr. Soc.,* **236**, 727

Horne, K., 1993, in Accretion Discs in Compact Stellar Systems, ed. C. Wheeler, World Sci. Pub. Co., 117

Horne, K., & Stiening, R. F., 1985, *Mon. Not. R. astr. Soc.,* **216**, 933

Hut, P., 1981, *Astr. & Astrophys.,* **99**, 126

Jansen, F., Lumb, D., Altieri, B., Clavel, J., Ehle, M., Erd, C., Gabriel, C., Guainazzi, M., Gondoin, P., Much, R., Munoz, R., Santos, M., Schartel, N., Texier, D., & Vacanti, G., 2001, *Astr. & Astrophys.,* **365**, L1

Kaitchuck, R. H., Honeycutt, R. K., & Schlegel, E. M., 1983, *Astrophys. J.,* **267**, 239

Kato, S., 1978, *Mon. Not. R. astr. Soc.,* **185**, 629

King, A.R., & Wynn G.A., 1999, *Mon. Not. R. astr. Soc.,* **310**, 203

Krzeminski, W., Vogt, H., 1985, *Astr. & Astrophys.,* **144**,124

Kuulkers, E., Hollander, A., Oosterbrock, T., & van Paradijs, J., 1991, *Astr. & Astrophys.,* **242**, 401

Lang, K. R., 1974, Astrophysical Formulae, Springer-Verlag.

Lin, D. N. C., & Papaloizou, J., 1979, *Mon. Not. R. astr. Soc.,* **186**, 799

Longmore, A. J., Lee, T. J., Allen, D. A., & Adams, D. J., 1981 *Mon. Not. R. astr.*

Soc., **195**, 825

Malkov, O. Yu., Piskunov, A. E., & Shpil'Kina, D. A., 1997, *Astr. & Astrophys.,* **320**, 79

Mandel, O., 1965, *Per. Zvesdy.*, **15**, 474

Mantel, K. H., Marschhaeusser, H., Schoembs, R., Haefner, R., & La Dous, C., 1988, *Astr. & Astrophys.,* **193**, 101

Marsh, T. R., & Horne, K., 1998, *Mon. Not. R. astr. Soc.,* **299**, 921

Marsh.,T. R., & Horne, K., 1988, *Mon. Not. R. astr. Soc.,* **235**, 269

Marsh., T. R., 1987, *Mon. Not. R. astr. Soc.,* **228**, 779

Martin, J. S., 1988, submitted D. Phil thesis, University of Southampton

Mason, K. O., Breeveld, A., Much, R., Carter, M., et al. 2001, *Astr. & Astrophys.,* **365**, L36

Mason,K.O., 1999, private communication

Mason, K. O., Drew, J. E., & Knigge, C., 1997, *Mon. Not. R. astr. Soc.,* **290**, L23

Mason, K. O. Drew, J. E., Córdova, F. A., Horne, K.,, Hilditch, R., Knigge, C., Lanz, T., Meylan, T., 1995, *Mon. Not. R. astr. Soc.,* **274**, 271

Mason, K. O., Rosen, S. R., & Hellier, C., 1988a, (COSPAR and IAU, Symposium on the Physics of Compact Objects, Sofia, Bulgaria, July 13-18, 1987) Advances in Space Research, Vol8, no. 2-3, p293

Mason, K. O., Córdova, F. A., Watsonm M. G., & King, A. R., 1988b, *Mon. Not. R. astr. Soc.,* **232**, 779

Mattei, J. A., 2000a, Observations from AAVSO online 'quick look' data file, http://www.aavso.org

Mattei, J. A., 2000b, Observations from AAVSO International database, http://www.aavso.org

Mauche, C. W., 1996, *Astrophys. J.,* **463**, 87

McArthur, B. E., Benedict, G. F., Lee, J., Lu, C.-L., van Altena, W. F., Deleyannis, C. P., Girard, t., Freduck, L. N., Nelan, e., Dunconbe, R. L., Hernenway, R. D., Jefferys, W. H., Shelus, P. J., franz, O. G., Wassermen, L. H., 1999, *Astrophys. J.,* **520**, L59

Meyer, F., 1999, Disk Instabilities in Close Binary Systems, eds Mineshige, S., & Wheeler J. C., 209

Meyer, F., & Meyer-Hofmeister, E., 1979, *Astr. & Astrophys.,* **78**, 167

Mukai, K., Wood, J. H., Naylor, T., Schlegel, E. M., Swank, J. H., 1997, *Astrophys. J.,* **475**, 812

Mukai, K. & Charles, P. A., 1987, *Mon. Not. R. astr. Soc.,* **226**, 209

Mumford, G. S., 1969, *Inf. Bull. Var. Star*, **337**, 1

Mumford, G. S., 1971, *Astrophys. J.,* **165**, 369

Nauenberg, M., 1972, *Astrophys. J.,* **175**, 417

Nather, R. E. & Robinson, E. L., 1974, *Astrophys. J.,* **190**, 637

Naylor, T., Bath, G. T., Charles, P. A., Hassal, B. J. M., Sonneborn, G., van der Woerd, H., van Paradijs, J., 1988, *Mon. Not. R. astr. Soc.,* **231**, 237

Naylor, T., Charles, P. A., Hassall, B. J. M., Bath, G. T., Berriman, G., Warner, B., Bailey, J., Reinsch, K., 1987, *Mon. Not. R. astr. Soc.,* **229**, 183

North, R. C., Marsh, T. R., Moran, C. K. J., Kolb, U., Smith, R. C., & Stehle, R., 2000, *Mon. Not. R. astr. Soc.,* **313**, 383

Osaki, Y., 1996, *Publs astr. Soc. Pacif.,* **108**, 39

Osaki, Y., 1985, *Astr. & Astrophys.,* **144**, 369

Osaki, Y., 1974, *Pub. astr. Soc. Japan*, **26**, 429

Ostriker, J. P., 1976, *In. Astr. Uni. Synop.*, **73**, 206

Paczynski, B., 1971, *Ann, Rev. Astr, Astrophys.*, **9**, 182

Paczynski, B., 1976, *In. Astr. Uni. Synop.*, **73**, 75

Pagano, I, Linsky, J. L., Carkner, L., Robinson, R. D., Woodgate, B., & Timothy, G., 2000, *Astrophys. J.,* **532**, 497

Patterson, J., 1984, *Astrophys. J. Suppl.,* **54**, 443

Plavec, M., & Kratochvil, P., 1964, *Bull. Astr. Czech.,* **15**, 165

Poole, T., Mason, K. O., Ramsay, G., Drew, J. E., & Smith, R. C., 2003, *Mon. Not. R. astr. Soc.,* **340**, 499

Poole, T., Mason, K., Ramsay, G., & Drew, J., 2002, ed. Gänsicke, B.T. Beuermann, K., & Reinsch, K., ASP Conference Series, The Physics of Catclysmic Variables and Related Objects, **261**, 67

Pratt, G. W., Hassall, B. J. M., Naylor, T., & Wood, J. H., 1999a, *Mon. Not. R. astr. Soc.,* **307**, 413

Pratt, G. W., Hassall, B. J. M., Naylor, T., Wood, J. H., & Patterson, J., 1999b, *Mon. Not. R. astr. Soc.,* **309**, 847

Protitich, M., 1958, *Peremennye Zvezdy*, **11**, 312

Protitich, M., 1956, *Astron. Circ. USSR*, **No. 174**, 15

Protitch, M., 1937, *Bull. Astr. Obs. Belgrade*, **38**, 9

Ramsay, G., Poole, T., Mason, K., Córdova, Priedhorsky, W., Breeveld, A., Much, R., Osborne, J., Pandel, D., Potter, S., West, J., Wheatley, P., 2001a, *Astr. & Astrophys.,* **365**, L288

Ramsay, G., Córdova, F., Cottam, J., Mason, K., Much, R., Osborne, J., Pandel, D., Poole, T., & Wheatley, P., 2001b, *Astr. & Astrophys.,* **365**, L294

Randich, S., Schmitt, J. H. M. M., Prosser. C. F., Stauffer, J. R., 1996, *Astr. & Astrophys.,* **305**, 785

Rasio, F. A., & Livio, M., 1996 *Astrophys. J.,* **471**, 366

Rayne, M. W., & Whelan J. A. J., 1981, *Mon. Not. R. astr. Soc.,* **196**, 73

Ritter, H., 1990, *Astr. & Astrophys. Supp.* **85**, 1179

Ritter, H., 1980a, *Astr. & Astrophys.,* **86**, 204

Ritter, H., 1980b, *Astr. & Astrophys.,* **85**, 362

Robinson, E. L., Shetrone, D., & Africano, J. L., 1991, *Astr. J.,* **102**, 1176

Rubenstein, E. P., & Patterson, J., 1991, *Publs astr. Soc. Pacif.,* **103**, 1258

Rutten, R. G. M., van Paradijs, J. & Tinbergen, J. 1992a, *Astr. & Astrophys.,* **260**, 213

Rutten, R. G. M., Kuulkers, E., Vogt, N., & van Paradijs, J., 1992b, *Astr. & Astrophys.,* **265**, 159

Rybicki, G. B., & Lightman, A. P., 1985, Radiative Processes in Astrophysics, Wiley-Inerscience

Scargle, J. D., 1982, *Astrophys. J.,* **263**, 835

Schneider, D. P., & Young, P. J., 1980, *Astrophys. J.,* **238**, 946

Schoembs, R., 1986, *Astr. & Astrophys.,* **158**, 233

Schoembs, R., & Vogt, N., 1981, *Astr. & Astrophys.,* **97**, 185

Schuster, A., 1898, *Terrestrial Magnetism* (now *J. G. R.*), **3**, 13

Shafter, A. W., & Hessman, F. V., 1988, *Astr. J.,* **95**, 178

Shafter, A. W., 1983, PhD Thesis, California Univ., Los Angeles

Sherrington, M. R., Jameson, R. F., Bailey, J., & Giles, A. B., 1982, *Mon. Not. R. astr. Soc.,* **200**, 861

Simbad, 2004, *http://simbad.u-strasbg.fr/sim-fid.pl*

Sion, E. M., 1995 *Publs astr. Soc. Pacif.,* **111**, 532.

Smak, J., 1995, *Acta Astro.,* **45**, 259

Smak, J., 1984, *Acta Astro.,* **34**, 93

Smale, A. P., Mason, K. O., White, N. E. & Gottwald, M, 1988, *Mon. Not. R. astr. Soc.,* **232**, 647

Smith, D. A., Dhillon, V. S., & Marsh T. R., 1998, *Mon. Not. R. astr. Soc.,* **296**, 465

Smith, D. A., & Dhillon, V. S., 1998, *Mon. Not. R. astr. Soc.,* **301**, 767

Smith, R.C., Cameron A., & Tucknott D. S., 1993, in Regev O., Shaviv G., eds, Cataclysmic Variables and Related Physics. Inst. Phys. Publ., Bristol, p. 70

Steiman-Cameron, T. Y., & Imamura, J. N., 1999, *Astrophys. J.,* **515** 404

Still, M. D., Buckley, D. A. H., & Garlick, M. A., 1998, *Mon. Not. R. astr. Soc.,* **299**, 545

Still, M. D., Dhillon, V. S., & Jones, D. H. P., 1995, *Mon. Not. R. astr. Soc.,* **273**, 849

St. -Louis, N., Willis, A. J., & Stevens, I. R., 1993, *Astrophys. J.,* **415**, 298

Strüder, L., Briel, U., Dennerl, K., Hartmann, R., Kendziorra, E., Meidinger, N., Pfeffermann, E., Reppin, C., et al. 2001, *Astr. & Astrophys.,* **365**, L18

Taam, R. E., & Bodenheiner, P., 1991, *Astrophys. J.,* **373**, 246

Thompson, R. O. R. Y., 1971, *IEEE Trans.*, **GE-9**, 107

Turner, M., Abbey, A., Arnaud, M., Balasini, M., Brbera, M., Belsole, E., Benniew, P. J., et al. 2001, *Astr. & Astrophys.,* **365**, L27

van Blerkom, D., 1970, *Mon. Not. R. astr. Soc.,* **149**, 53

Vande Putte, D., Smith, R. C., Hawlins, N. A., & Martin, J. S., 2003, *Mon. Not. R. astr. Soc.,* **342**, 151

van Hoof,P., 2003, Atomic Line List v2.04, www.pa.uky.edu/peter/atomic

van Horn, H. M., Wesemael, F., & Winget, D. E., 1980, *Astrophys. J.,* **235**, 143

van Paradijs, J., van Amerongen, S., & Kraakman, H., 1989, *Astr. & Astrophys., Suppl.,* **79**, 205

van Teeseling, A., Beuermann, K., & Verbunt, F., 1996, *Astr. & Astrophys.,* **315**, 467

Verner, D. A., Verner, E. M., & Ferland, G. J., 1996, Atomic Data Nucl. Data Tables, **64**, 1

Vitello, P. & Shlosman, I., 1993, *Astrophys. J.,* **410**, 815

Vitello, P. & Shlosman, I., 1988, *Astrophys. J.,* **327**, 680

Vogt, N., 1983, *Astr. & Astrophys.,* **128**, 29

Vogt, N., Schoembs, R., Krzeminski, W., & Pedersen, H., 1981, *Astr. & Astrophys.,* **94**, L29

Vogt, N., Krzeminski, W., & Sterken, C., 1980, *Astr. & Astrophys.,* **85**, 106

Vogt, N., 1979a, *IAU Circ.,* **3357**, 2

Vogt, N,. 1979b, ESO Messenger, **17**, 39

Wade, R. A., & Horne, K., 1988, *Astrophys. J.,* **324**, 411

Walker, M. F., 1963, *Astrophys. J.,* **137**, 485

Warner, B., & Woudt, P. A., 2001, ed. Gänsicke, B.T. Beuermann, K., & Reinsch, K., ASP Conference Series, The Physics of Catclysmic Variables and Related Objects

Warner, B., 1995, Cataclysmic Variable Stars, Cambridge Univ. Press

Warner, B., 1988, *Nature*, **336**, 129

Warson, C. A., Dhillon, V. S., Rutten, R. G. M., & Schwope, A. D., 2003, *Mon. Not. R. astr. Soc.,* **341**, 129

Watson, C. A., & Dhillon V. S., 2001, *Mon. Not. R. astr. Soc.,* **326**, 67

Watson, M. G., King, A. R., & Osborne, J., 1985, *Mon. Not. R. astr. Soc.,* **212**, 917

Weisstein, E. W, 2003, Eric Weisstein's Word of Physics, http://scienceworld.wolfram.com/physics/Intensity.html

Wood, J. H., & Honre, K., 1990, *Mon. Not. R. astr. Soc.,* **242**, 606

Wood, J. H., Horne, K., Berriman, G., & Wade, R. A., 1989, *Astrophys. J.,* **341**, 974

Zeilik, M., Gregory, S. A., & Smith, E. v.P., 1992, Introductory Astronomy & Astrophysics, Saunders College Pub.

Zombeck, M. V., 1990, HandBook of Space Astronomy & Astrophysics, Cambridge University Press.

Appendix A

The derivation for the equation of radiative transfer was taken from a selection of references,

- Carroll & Ostlie, 1996
- Lang, 1974
- Rybicki & Lightman, 1985
- Zeilik, Gregory & Smith, 1992

The change in intensity of a ray of light at wavelength, λ as it travels through a gas is a combination of the decrease in intensity due to absorption radiation ($-\kappa_\lambda \rho I_\lambda dS$) and the increase produced by emission ($j_\lambda \rho dS$), given by

$$dI_\lambda = -\kappa_\lambda \rho I_\lambda dS + j_\lambda \rho dS, \tag{6.1}$$

where dI_λ is the change in intensity, κ_λ is the absorption coefficient of the gas, ρ is density of the gas (kg m^{-3}), I_λ is the intensity at wavelength λ, dS is the change in optical path length through the gas, and j_λ is the emission coefficient ($\mathrm{cm.s^{-3}s.T^{-1}}$).

The change in optical depth ($d\tau_\lambda$) is defined from the absorption and density of the gas, and the change in optical path length through the gas, and is given by

$$d\tau_\lambda = \kappa_\lambda \rho dS. \tag{6.2}$$

The source function (S_λ) is defined by the ratio of emission to absorption coefficients,

$$S_\lambda = \frac{j_\lambda}{\kappa_\lambda} \qquad (\mathrm{erg.s^{-1}cm^{-3}Sr^{-1}}). \tag{6.3}$$

Dividing both sides of Equation 6.1 by $\kappa_\lambda \rho dS$ leads to

$$\frac{dI_\lambda}{\kappa_\lambda \rho dS} = -I_\lambda + \frac{j_\lambda}{\kappa_\lambda}, \tag{6.4}$$

and then substituting in Equations 6.2 and 6.3 gives

$$\frac{dI_\lambda}{d\tau_\lambda} = S_\lambda - I_\lambda. \tag{6.5}$$

Multiplying both sides of Equation 6.5 by e^{τ_λ} and rearranging leads to

$$\frac{dI_\lambda e^{\tau_\lambda}}{d\tau_\lambda} + I_\lambda e^{\tau_\lambda} = S_\lambda e^{\tau_\lambda}, \tag{6.6}$$

$$\frac{d}{d\tau_\lambda}[I_\lambda e^{\tau_\lambda}] = S_\lambda e^{\tau_\lambda}, \tag{6.7}$$

$$dI_\lambda e^{\tau_\lambda} = S_\lambda e^{\tau_\lambda} d\tau_\lambda. \tag{6.8}$$

Integrating both sides of Equation 6.8 gives

$$\int_{I(0)}^{I(\tau_\lambda)} e^{\tau_\lambda} dI_\lambda = S_\lambda \int_0^{\tau_\lambda} e^{\tau_\lambda} d\tau_\lambda, \tag{6.9}$$

$$[I_\lambda e^{\tau_\lambda}]_{I(0)}^{I(\tau_\lambda)} = S_\lambda [e^{\tau_\lambda}]_0^{\tau_\lambda}, \tag{6.10}$$

$$I_\lambda(\tau_\lambda) e^{\tau_\lambda} - I(0) = S_\lambda (e^{\tau_\lambda} - 1), \tag{6.11}$$

which leads to the solution,

$$I_\lambda(\tau_\lambda) = I(0) e^{-\tau_\lambda} + S_\lambda (1 - e^{-\tau_\lambda}). \tag{6.12}$$

Absorption Only

From Equation 6.1 absorption is given by,

$$dI_\lambda = -\kappa_\lambda \rho I_\lambda dS. \tag{6.13}$$

Dividing both sides of Equation 6.13 by $\kappa_\lambda \rho dS$ and substituting in Equation 6.2 gives

$$\frac{dI_\lambda}{\kappa_\lambda \rho dS} = -I_\lambda, \tag{6.14}$$

$$\frac{dI_\lambda}{d\tau_\lambda} = -I_\lambda. \tag{6.15}$$

Multiplying both sides of Equation 6.15 by e^{τ_λ} and rearranging leads to

$$\frac{dI_\lambda}{d\tau_\lambda} e^{\tau_\lambda} = -I_\lambda e^{\tau_\lambda}, \tag{6.16}$$

$$\frac{dI_\lambda}{d\tau_\lambda} e^{\tau_\lambda} + I_\lambda e^{\tau_\lambda} = 0, \tag{6.17}$$

$$\frac{d}{d\tau_\lambda}[I_\lambda e^{\tau_\lambda}] = 0. \tag{6.18}$$

Integrating both sides of Equation 6.18 gives

$$\int_{I(0)}^{I(\tau_\lambda)} e^{\tau_\lambda} dI_\lambda = 0, \tag{6.19}$$

$$[I_\lambda e^{\tau_\lambda}]_{I(0)}^{I(\tau_\lambda)} = 0, \tag{6.20}$$

$$I_\lambda(\tau_\lambda) e^{\tau_\lambda} - I(0) = 0, \tag{6.21}$$

which leads to the solution,

$$I_\lambda(\tau_\lambda) = I(0) e^{-\tau_\lambda}. \tag{6.22}$$

Appendix B

Chi-squared (χ^2), is the weighted mean of the square of the fractional difference between two frequency distributions. When considering this 'best-fit' method, a normal distribution of errors around the model is assumed. The chi-squared statistic is given by

$$\chi^2 = \sum_{n_e} \frac{(F_{obs}(n_e) - F_{mod}(n_e))^2}{E_{obs}}, \tag{6.23}$$

where n_e is the number of events, F_{obs} is the observed frequency distribution, F_{mod} is the model frequency distribution, and E_{obs} is the variance on each value in the observed frequency distribution (i.e. $\sigma_{obs}(n_e)^2$). For the Poisson distribution, the variance ($\sigma_{obs}(n_e)^2$) is equal to the mean of the distribution, therefore E_{obs} can be estimated from the data as F_{obs} (Bevington & Robinson 1992).

The reduced chi-squared (χ^2_ν) is given by

$$\chi^2_\nu = \frac{\chi^2}{\nu} = 1 \pm \left(\frac{2}{\nu}\right)^{1/2}, \tag{6.24}$$

where ν is the number of degrees of freedom given by

$$\nu = n_e - p, \tag{6.25}$$

where p is the number of free parameters in the model.

Appendix C

The final model of Chapter 2 was comprised of the following stages,

- splitting up the UV continuum into equal segments and calculating the intensity of each segment (I_s),
- tracing the light path of each UV continuum segment through the absorbing material to calculate a path length (S),
- splitting the path length through the absorbing material up into elements and calculating the wavelength and intensity of each element to produce an intensity-wavelength profile ($I_e - \lambda_e$),
- calculating the total absorption profile by summing the profile of each element,
- fitting the model profile to the observed absorption profile,
- calculating a chi-squared error for the absorption fit,
- writing results to a file.

The following program shows the FORTRAN code **ABSOR_FIT.F** developed to produce the absorption profile. This program also calculates a chi-squared fit to the observed data, and writes the results into the file,

- **absor_fit_results.dat** - Normalised model results.

```
C*************************************************************
C MAIN PROGRAM
C*************************************************************
      PROGRAM ABSOR_FIT
C*************************************************************
C Program Name: Absor_fit
C Author      : Tracey Suzanne Poole
C Date        : 17th October 2003
C Description : The program models light from the UV continuum
C               of RW Tri as it passes through a cylindrically
C               shaped absorption material column that is
C               centered on the centre of the UV continuum.
C               The primary star and accretion disc are both
C               assumed to contribute to the UV continuum.
C Function    : BINVAL - Function to calculate the wavelength
C               bin in which the intensity of an element in
C               the absorption material should be added.
C*************************************************************
C Counters
C Counter     : A    - 1 to NUMM, counts around the maximum
C                      number of elements in along the maximum
C                      path length distance.
C               M    - 1 to NUM, counts around the main loop
C                      to iterate around each UV continuum
C                      annulus.
C               J    - 1 to NUMS, counts around the second loop
C                      to loop around the number of segments
C                      in the current annulus.
C               B    - 1 to NUMB, to loop around WAVEARY for
```

```
C                       output to screen.
C               P    - 1 to NUME, loops around the number of
C                       elements in the absorbing material.
C               I    - 1 to NUMB, to loop around in the
C                       chi-squared calculations.
C               L    - 1 to NUMO, to loop around observed data.
C               COBS - Counter to find the observed data
C                       wavelength that corresponds to the
C                       first model wavelength bin.
C*************************************************************
C Constants
C Physical    : GRAV   - Gravitational constant (dyn cm^2 g^-2).
C constants     STEFAN - Stefan's constant (erg cm^-2 K^-4 s^-1).
C               PLANCK - Planck's constant (erg.s).
C               BOLTZ  - Boltzmann's constant (erg K^1).
C               C      - Speed of light (cm s^-1).
C               PI     - pie.
C               ANGLE1 - 90 degrees in radians.
C               ANGLE2 - 270 degrees in radians.
C               ANGLE3 - 360 degrees in radians.
C System      : MASS   - Mass of the primary star (g).
C parameters    INC    - Inclination angle of the system
C                        (radians).
C               RADWD  - Primary star radius (cm).
C               RADUV  - UV continuum radius (cm).
C               RADOUT - Outer radius of the accretion disc (cm).
C               MDOT   - Accretion rate (g s^1).
C               TEMPWD - Temperature of the primary star (K).
C               DISTO  - Distance to the system from the
```

```
C                        observer (cm).
C UV/absorbing: NUM    - Number of UV continuum annuli.
C material      SEGL   - Length of an UV continuum segment (cm).
C parameters    ELES   - Length of an absorbing material element
C                        (cm).
C Wavelength  : WAVEO  - Rest wavelength (wavelength of central
C parameters             peak in Angstroms).
C               BIN    - Size of wavelength bins (Angstroms).
C               NUMB   - Number of wavelength bins.
C               WAVE1  - Start wavelength for the first bin
C                        (Angstroms).
C Input       : INR    - Inner radius of the absorbing material
C                        (cm).
C parameters    RTHICK - Radial thickness of the absorbing
C                        material (cm).
C               CONST  - Optical depth constant of the absorbing
C                        material (cm^-1).
C               PAR    - Number of free parameters.
C               NUMO   - Number of data points in the original
C                        data file.
C Calculations: OUTR   - Outer radius of absorbing material (cm).
C with          SINI   - Sine of the inclination angle.
C constants     WAVEC  - Rest wavelength divided by the speed of
C                        light (s).
C               BINHF  - Half a wavelength bin (Angstroms).
C               INTWD  - Intensity of the primary star.
C               WAVEOCM- Rest wavelength in cm.
C               CONA   - Accretion disc temperature constant.
C               CONB   - Accretion disc intensity constant.
```

```
C               CONC   - Accretion disc intensity constant.
C               MAXPL  - Maximum path length through the
C                        absorbing material.
C               NUMM   - Maximum number of elements in the
C                        absorbing material.
C***************************************************************
C Variables
C Distances   : DELR   - Thickness of an individual UV Continuum
C                        annulus.
C               R      - Radius of the an annulus from the
C                        centre of the UV continuum.
C               INVR   - Inversion of R.
C               RPERPS - Perpendicular distance of a UV
C                        continuum segment in the orbital plane
C                        of the system.
C               DISTS  - Distance around the circumference of a
C                        UV continuum annulus, to a segment in
C                        the UV continuum.
C               XVAL1  - Distance parallel to the observers line
C                        of sight from the centre of the primary
C                        star to the inner radius of the
C                        absorbing material in the orbital plane
C                        of the system.
C               XVAL2  - Distance parallel to the observers line
C                        of sight from the centre of the primary
C                        star to the outer radius of the
C                        absorbing material in the orbital
C                        plane of the system.
C               PATHOP - Path length through the absorbing
```

```
C                        material in the orbital plane of the
C                        system.
C               DISTOP - Distance from the inner radius of the
C                        absorbing material to the current
C                        element in the orbital plane.
C               RADE   - Radial distance of an element in the
C                        absorbing material.
C               INVRE  - Inversion of RADE.
C Angles      : THETA  - Angle increment of a UV continuum
C                        segment in radians.
C               SINT   - Sine of THETA.
C               SINEL  - The sine of the angle subtended from
C                        the line of sight of the observer, to
C                        the current element in the absorbing
C                        material.
C               THMAXE - Maximum SINEL value.
C UV segment  : WAVES  - Wavelength of a UV continuum segment.
C variables     TEMPS  - Temperature of a UV continuum segment
C                        in the accretion disc.
C               INTS   - Intensity of a UV continuum segment.
C               NUMS   - Number of segments in an annulus
C                        (INTEGER value).
C               NUMSR  - Number of segments in an annulus
C                        (REAL value).
C               DIFFN  - Difference between NUMS and NUMSR.
C               INVWS  - Inversion of WAVES.
C Absorbing   : NUME   - Number of elements in the absorbing
C material               material along the path length in the
C elements               direction for the observers line of
```

```
C                        sight.
C               NUMER  - NUME as a real value.
C               DIFFNE - Difference between NUME and NUMER.
C               BINE   - Wavelength bin in which an element in
C                        the absorbing material belongs.
C               WAVEE  - Wavelength of an element in the
C                        absorbing material.
C               INTE   - Intensity of an element in the
C                        absorbing material.
C Error       : MINOBS - Minimum intensity of observed data.
C analysis      MINMOD - Minimum intensity of model data.
C variables     FACTOR - Factor to multiply the intensity of
C                        the model data by.
C               CSQU   - Chi-squared value.
C               RCSQU  - Reduced chi-squared value.
C               FPAR   - Number of free parameters.
C               ECHI   - Error on the reduced chi-squared value.
C*************************************************************
C Arrays
C Observed    : OBSW      - Wavelength values of the observed
C data                      data.
C               ONSI      - Intensity values of the observed
C                           data.
C               ERROR     - Error values of the observed data.
C Model data  : ABSCOEF   - Absorption coefficient look up table
C                           array.
C               WAVEARY   - Wavelength values of the model data.
C               INTARY    - Intensity values of the model data.
C               INTARYFIN - Final intensity values of the model
```

```
C                           data after fitting to the observed
C                           data.
C Chi-squared : CHI       - Array to help calculate chi-squared.
C*************************************************************
C Defining integers, real variables and constants, and arrays.
C
      IMPLICIT NONE
C
      INTEGER A,M,J,B,P,I,L,COBS
      INTEGER NUM,NUMB,NUMS,NUMO,NUMM,NUME
      REAL*8 GRAV,STEFAN,PLANCK,BOLTZ,C,PI,ANGLE1,ANGLE2,ANGLE3
      REAL*8 MASS,INC,RADWD,RADUV,RADOUT,MDOT,TEMPWD,DISTO
      REAL*8 DELR,SEGL,ELES
      REAL*8 WAVEO,BIN,WAVE1
      REAL*8 INR,RTHICK,CONST,PAR
      REAL*8 OUTR,SINI,WAVEC,BINHF,INTWD
      REAL*8 WAVEOCM,CONA,CONB,CONC,MAXPL
      REAL*8 R,INVR,RPERPS,DISTS
      REAL*8 XVAL1,XVAL2,PATHOP,DISTOP,RADE,INVRE
      REAL*8 THETA,SINT,SINEL,THMAXE
      REAL*8 TEMPS,WAVES,INTS,NUMSR,DIFFN,INVWS
      REAL*8 NUMER,DIFFNE,BINE,WAVEE,INTE
      REAL*8 MINOBS,MINMOD,FACTOR,CSQU,RCSQU,FPAR,ECHI
      REAL*8 ABSCOEF(50000),WAVEARY(23),INTARY(23),INTARYFIN(23)
      REAL*8 OBSW(114),ONSI(114),ERROR(114)
      REAL*8 CHI(23)
C
C*************************************************************
C Defining function.
```

```
C
      INTEGER BINVAL
C
C*****************************************************************
C Define common blocks so that the Subroutines and Function can
C use the constant values as well as the main program.
C
      COMMON/CONSTANTF/WAVE1,BIN
C
C*****************************************************************
C Defining constants.
C
      GRAV=6.67259E-8
      STEFAN=5.67051E-5
      PLANCK=6.6260755E-27
      BOLTZ=1.380658E-16
      C=2.99792458E10
      PI=3.141592654
      ANGLE1=PI/2.0
      ANGLE2=3.0*PI/2.0
      ANGLE3=2.0*PI
      MASS=1.49449E33
      INC=76.86*(ANGLE3/360.0)
      RADWD=7.656E8
      RADUV=1.629E10
      RADOUT=2.79792E10
      MDOT=2.8E18
      TEMPWD=20800.0
      DISTO=1.052326E21
```

```
      SEGL=2.0E7
      ELES=2.0E7
      NUM=815
      WAVEO=1335.0
      BIN=0.59
      NUMB=23
      WAVE1=1328.445
      PAR=3.0
      THMAXE=0.0
C
C*****************************************************************
C Prompt for the inputing values needed.
C
      WRITE(*,*) "Please input the optical depth constant (cm^{-1})"
      READ(*,*) CONST
 33   WRITE(*,*) "Please input thickness of the absorbing material (cm)"
      READ(*,*) RTHICK
 22   WRITE(*,*) "Please input the inside radius of the material (cm)"
      READ(*,*) INR
C
C Calculate the outer radius of the absorbing material (OUTR).
C
      OUTR=INR+RTHICK
C
C Check that input parameters fit with limits, if not then end
C the program.
C
      IF (INR.LT.RADUV) THEN
         WRITE(*,*) "Inside radius is too small"
```

```
         GOTO 22
      ENDIF
      IF (OUTR.GT.RADOUT) THEN
         WRITE(*,*) "Thickness + Inside radius is too big"
         GOTO 33
      ENDIF
C
C*****************************************************************
C Calculate the sin value of the inclination angle (SINI), the
C rest wavelength divided by the speed of light (WAVEC), half a
C bin width (BINH), intensity of the primary star (INTWD), and
C constants for accretion disc temperature and intensity
C calculation (CONA, CONB, CONC).
C
      SINI=SIN(INC)
      WAVEC=WAVEO/C
      BINHF=BIN/2.0
      INTWD=STEFAN*(TEMPWD**4)*RADWD*RADWD/(PI*DISTO*DISTO)
      WAVEOCM=WAVEO*1.0e-8
      CONA=(3.0*GRAV*MASS*MDOT)/(8.0*PI*STEFAN)
      CONB=2.0*C*C*PLANCK
      CONC=(PLANCK*C)/BOLTZ
C
C*****************************************************************
C Calculate a look up table for the absorption coefficient
C (ABSCOEF) for the calculation of the intensity of an element
C in the absorbing material.
C
      MAXPL=SQRT((RADOUT*RADOUT)-(RADUV*RADUV))
```

```
      NUMM=MAXPL/(ELES*SINI)
C
      DO A=1,NUMM
         ABSCOEF(A)=EXP(-(A*CONST*ELES))
      ENDDO
C
C*****************************************************************
C Reading in the original data.
C
      NUMO=114
      OPEN (UNIT=1,FILE='new_profile.dat',STATUS='OLD')
      DO L=1,NUMO
         READ(1,*) OBSW(L), ONSI(L)
         ERROR(L)=1.197e-14
      ENDDO
C
C*****************************************************************
C Calculating width of a UV continuum annuls (DELR).
C
      DELR=RADUV/NUM
C
C*****************************************************************
C Main loop to iterate around each UV continuum annulus.
C
      DO M=1,NUM
C
C Calculate radius of the current annulus from the centre of the
C  UV continuum (R), and the inversion of the current radius
C (INVR).
```

```
C
         R=(M-0.5)*DELR
         INVR=1.0/R
C
C Calculate the number of segments in the current annulus (NUMS).
C
         NUMS=2*PI*R/SEGL+1
         NUMSR=2*PI*R/SEGL+1
         DIFFN=NUMSR-NUMS
         WRITE(*,*) M,R,NUMS,NUMSR
C
C Second loop to loop around the number of segments in the
C current annulus.
C
         DO J=1,NUMS
C
C Calculate the distance to the current segment around the
C circumference of the current annulus, if the current segment
C is a full segment.
C
            IF (J.LT.NUMS) THEN
               DISTS=SEGL*(J-0.5)
C
C Calculate the distance to the current segment around the
C circumference of the current annulus, if the current segment
C is a the last partial segment.
C
            ELSEIF (J.EQ.NUMS) THEN
               DISTS=((NUMS-1)*SEGL)+(DIFFN/2.0)
```

```
            ENDIF
C
C Calculate the angle increment of the current segment in
C radians (THETA).
C
            THETA=DISTS*INVR
            SINT=SIN(THETA)
C
C Calculate the perpendicular distance of the current segment
C (RPERPS) in the orbital plane of the system (make sure this
C value is positive).
C
            RPERPS=R*SINT
C
C Calculate the wavelength of the current segment (WAVES).
C
            WAVES=WAVE0+(WAVEC*SQRT(GRAV*MASS*INVR)*SINT*SINI)
            INVWS=1/WAVES
C
C Calculate the intensity of the UV continuum at the current
C segment (INTS).
C  1. Within the radius of the primary star.
C  2. In the accretion disc.
C
C 1.
            IF (R.LE.RADWD) THEN
               INTS=INTWD
            ELSE
C 2.
```

```
               TEMPS=(CONA*(INVR**3)*(1-SQRT(RADWD*INVR)))**0.25
               INTS=CONB*(INVWS**5)*(1/(EXP(CONC*INVWS/TEMPS)-1))
            ENDIF
C
C Take into account the last segment begin a fraction of a whole
C segment.
C
            IF (J.LT.NUMS) THEN
               INTS=INTS
            ELSEIF (J.EQ.NUMS) THEN
               INTS=DIFFN*INTS
            ENDIF
C
C Calculate the path length through the absorbing material in
C the orbital plane of the system (PATHOP).
C
            XVAL1=SQRT((INR*INR)-(RPERPS*RPERPS))
            XVAL2=SQRT((OUTR*OUTR)-(RPERPS*RPERPS))
            PATHOP=XVAL2-XVAL1
C
C Calculate the number of elements (NUME) along the path length
C in the direction for the observers line of sight (where path
C length is PATHOP/SINI).
C
            NUME=PATHOP/(ELES*SINI)+1
            NUMER=PATHOP/(ELES*SINI)+1
            DIFFNE=NUMER-NUME
C
C Loop around the number of element along the path length to
```

```
C calculate the intensity of each element along the path length
C (INTE) and add it to the intensity array INTARY.
C
            DO P=1,NUME
C
C Find the radial distance of the current element (RADE).
C Note that the distance from the inner radius of the absorbing
c material (INR) to the current element in the orbital plane is
C DISTOP. There are two considerations for DISTOP,
C  1. when the current element is a full element (1 to NUME-1)
C  2. when the current element is the last partial element (NUME)
C
C 1.
               IF (P.LT.NUME) THEN
                  DISTOP=(P-0.5)*ELES*SINI
C 2.
               ELSEIF (P.EQ.NUME) THEN
                  DISTOP=((P-1.5)*ELES*SINI)+(SINI*DIFFNE/2.0)
               ENDIF
C
               RADE=SQRT((RPERPS*RPERPS)+((XVAL1+DISTOP)**2))
               INVRE=1.0/RADE
C
C Calculate the sine of the angle subtended from the observers
C line of sight to the current element (SINEL). Also calculate
C the maximum SINEL (THMAXE).
C
               SINEL=RPERPS*INVRE
C
```

```
               IF (THMAXE.LT.SINEL) THEN
                  THMAXE=SINEL
               ENDIF
C
C Calculate the wavelength of the current element (WAVEE).
C
               WAVEE=WAVEO+(WAVEC*SQRT(GRAV*MASS*INVRE)*SINEL*SINI)
C
C Call a function to calculate which wavelength bin (BINE) this
C intensity should be added into.
C
               BINE=BINVAL(WAVEE)
               IF (BINE.LE.0.OR.BINE.GT.56) THEN
                  WRITE(*,*) "BINE is bad",WAVEE
               ENDIF
C
C Calculate the intensity of the current element (INTE)
C considering when,
C  1. current element is a full element (1 to NUME-1)
C  2. current element is the las partial element (NUME)
C
C 1.
               IF (P.LT.NUME) THEN
                  INTE=INTS*ABSCOEF(P)
C 2.
               ELSEIF (P.EQ.NUME) THEN
                  INTE=INTS*EXP(-CONST*((P-1)*ELES+DIFFNE))*DIFFNE
               ENDIF
C
```

```
C Add the intensity into the correct bin in the INTARY array.
C
               INTARY(BINE)=INTARY(BINE)+INTE
C
C End the loop that loops around the number of elements in the
C absorbing material.
C
            ENDDO
C
C End loop that loops around each ring.
C
         ENDDO
C
C End main loop.
C
      ENDDO
C
C*****************************************************************
C Calculate the central wavelengths for each wavelength bin and
C put them into the wavelength array WAVEARY. Print wavelength
C and relative intensity information to the screen.
C
      INTARY=-INTARY
      DO B=1,NUMB
         WAVEARY(B)=WAVE1+(BIN*(b-1))+BINHF
         WRITE(*,55) WAVEARY(B),INTARY(B)
      ENDDO
C
C
```

```
 55   FORMAT(3(E14.5),F10.2)
C
C
C*****************************************************************
C Rescaling the simulated absorption data.
C
      MINMOD=0.0
C
      DO I=1,NUMB
         IF (INTARY(I).LE.MINMOD) THEN
            MINMOD=INTARY(I)
         ENDIF
      ENDDO
C
      MINOBS=0.0
C
      DO L=1,NUMO
         IF (ONSI(L).LE.MINOBS) THEN
            MINOBS=ONSI(L)
         ENDIF
      ENDDO
C
      FACTOR=MINOBS/MINMOD
C
      DO I=1,NUMB
         INTARYFIN(I)=FACTOR*INTARY(I)
      ENDDO
C
C*****************************************************************
```

```
C Finding original data that corresponds to the first bin.
C
      DO L=1,NUMO
         IF (OBSW(L).LE.WAVEARY(1)) THEN
            COBS=L
         ENDIF
      ENDDO
      COBS=COBS+1
C
C*************************************************************
C Calculating chi-squared.
C
      CSQU=0.0
C
      DO I=1,NUMB
         CHI(I)=((ONSI(I+COBS)-INTARYFIN(I))**2.0)/
     &        (ERROR(I))**2.0
         CSQU=CSQU+CHI(I)
      ENDDO
C
C Calculating the reduced chi-squared.
C
      FPAR=FLOAT(NUMB)-PAR
      RCSQU=CSQU/FPAR
      ECHI=SQRT(2.0/FPAR)
C
C*************************************************************
C Outputting the errors to the screen.
C
```

```
      WRITE(*,*) "Chi squared is ",CSQU,"(",FPAR,")"
      WRITE(*,*) "Reduced chi squared is ",RCSQU,"+/-",ECHI
C
C Writing out factor (FACTOR) and maximum element angle (THMAXE)
c in degrees.
C
      THMAXE=ASIN(THMAXE)*360.0/ANGLE3
C
      WRITE(*,*) "Factor is ",FACTOR
      WRITE(*,*) "Maximum element angle is ",THMAXE
C
C*************************************************************
C Writing the data to the output file 'absor_fit_results.dat'.
C
      OPEN(UNIT=2,FILE='absor_fit_results.dat',STATUS='NEW')
      DO I=1,NUMB
 WRITE(2,10) I,WAVEARY(I),INTARY(I),INTARYFIN(I)
      ENDDO
C
 10   FORMAT(I2,F10.2,2(E14.5))
C
C*************************************************************
C End the main program.
C
      CLOSE(1)
      CLOSE(2)
      STOP
      END
C
```

```
C
C*****************************************************************
C*****************************************************************
C FUNCTION    - Function to calculate the wavelength bin in
C               which the current element intensity should be
C               added.
C*****************************************************************
C
      INTEGER FUNCTION BINVAL(WAVEE)
C
C*****************************************************************
C Function Name : Binval
C Author        : Tracey Suzanne Poole
C Date          : 20th October 2003
C Description   : This function calculates the wavelength bin in
C                 which an element in the absorbing material
C                 contributes too.
C Variable      : WAVEE - Wavelength of an element in the
C                         absorbing material.
C Common block  : WAVE1 - Start wavelength for the first bin
C constantf               (Angstroms).
C                 BIN   - Size of wavelength bins (Angstroms).
C*****************************************************************
C Defining external real variables and arrays.
C
      IMPLICIT NONE
C
      REAL*8 WAVEE
C
```

```
C*****************************************************************
C Defining common blocks.
C
      REAL*8 WAVE1, BIN
C
      COMMON/CONSTANTF/WAVE1,BIN
C
C*****************************************************************
C Calculate the bin value BINVAL.
C
      BINVAL=(WAVEE-WAVE1)/BIN+1.0
C
C*****************************************************************
C Exit the function.
C
      RETURN
      END
```

Appendix D

To produce the skew maps each spectrum must have a linear velocity scale. This is achieved by considering

$$\frac{\Delta v}{c} = \frac{\Delta \lambda}{\lambda}, \tag{6.26}$$

where Δv is the change in velocity, c is the speed of light (2.99×10^5 km/s), $\Delta \lambda$ is the change in wavelength, and λ is the wavelength.

Integrating both sides over the limits $0 \rightarrow v_r$ and $\lambda_o \rightarrow \lambda_{obs}$, where v_r is the radial velocity, λ_o is the rest wavelength, and λ_{obs} is the observed wavelength.

$$\int_0^{v_r} \frac{dv}{c} = \int_{\lambda_o}^{\lambda_{obs}} \frac{d\lambda}{\lambda}, \tag{6.27}$$

$$\frac{1}{c}[v]_0^{v_r} = [ln\lambda]_{\lambda_o}^{\lambda_{obs}}, \tag{6.28}$$

$$\frac{1}{c}[v_r - 0] = [ln\lambda_{obs} - ln\lambda_o], \tag{6.29}$$

$$\frac{v_r}{c} = ln\left[\frac{\lambda_{obs}}{\lambda_o}\right], \tag{6.30}$$

$$v_r = cln\left[\frac{\lambda_{obs}}{\lambda_o}\right]. \tag{6.31}$$

Appendix E

The following figures are the skew map results for the near infrared data provided by Robert Smith at the University of Sussex.

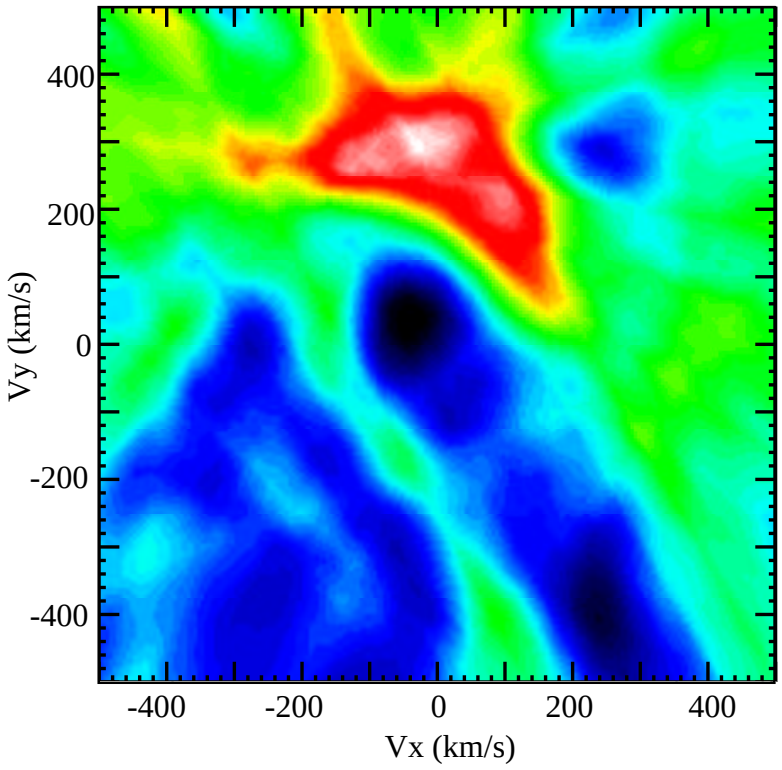

Figure 6.1: RW Tri with template gl653.

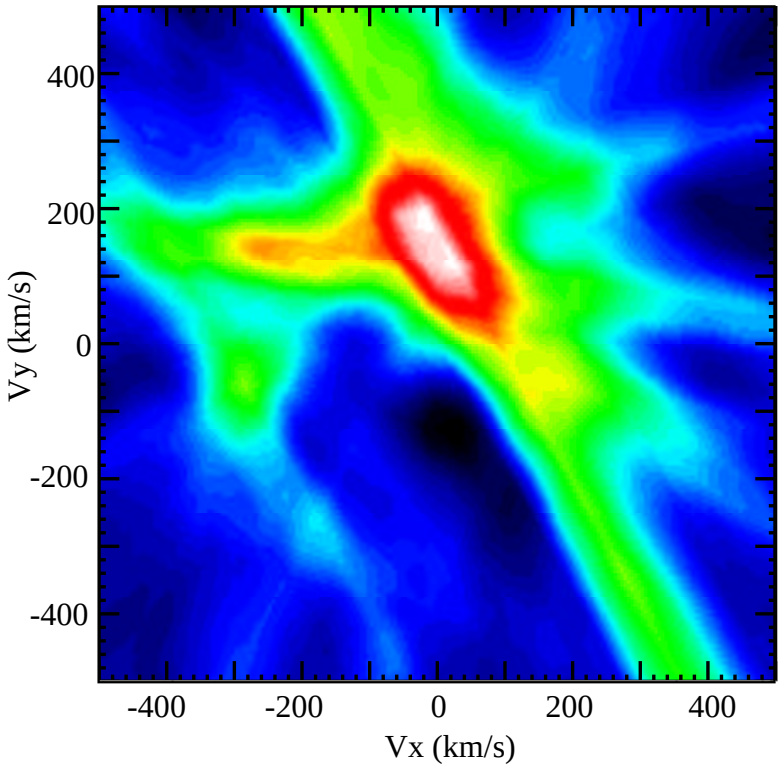

Figure 6.2: RW Tri with template gl717.

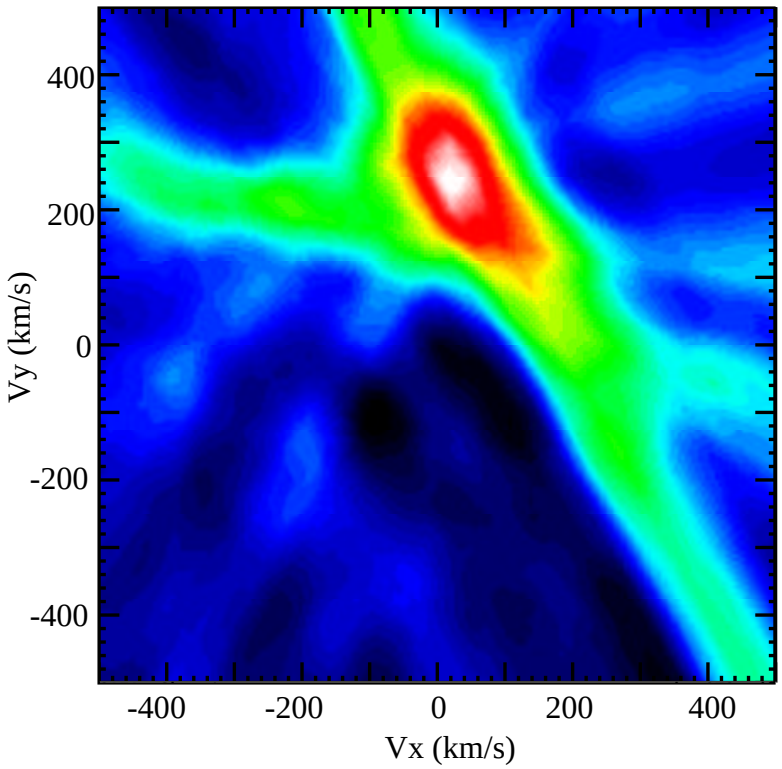

Figure 6.3: RW Tri with template gl673.

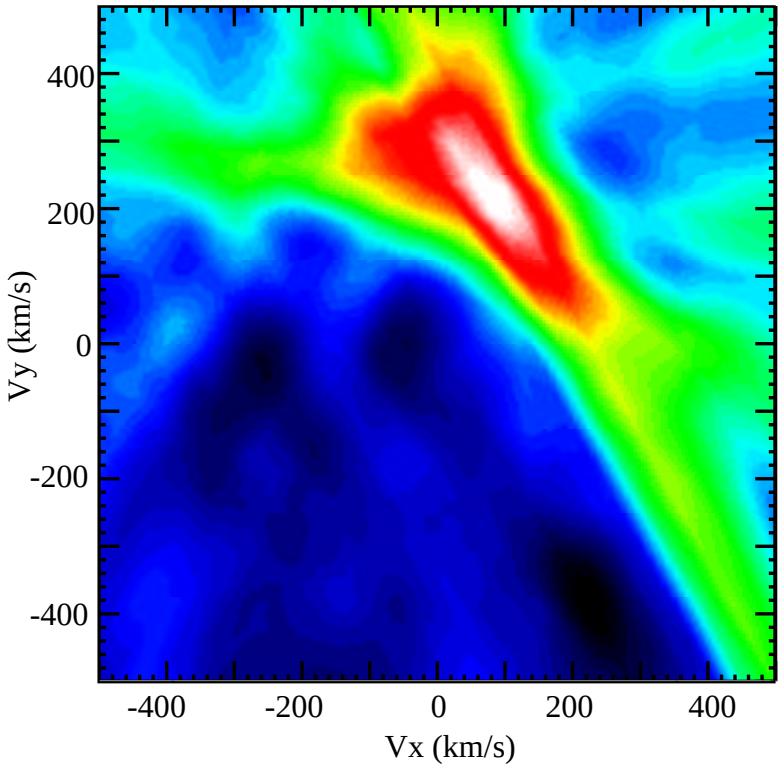

Figure 6.4: RW Tri with template gl488.

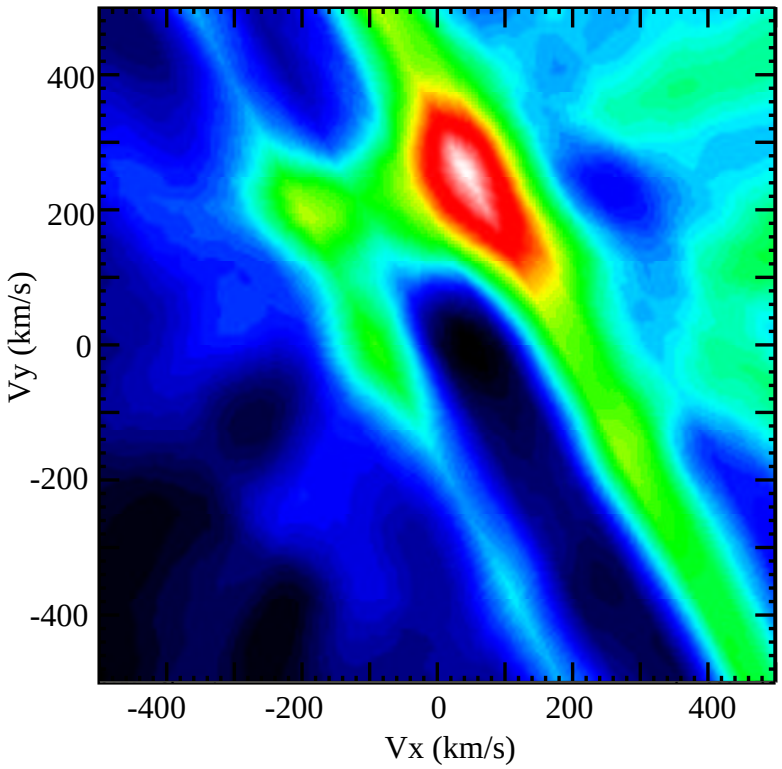

Figure 6.5: RW Tri with template gl383.

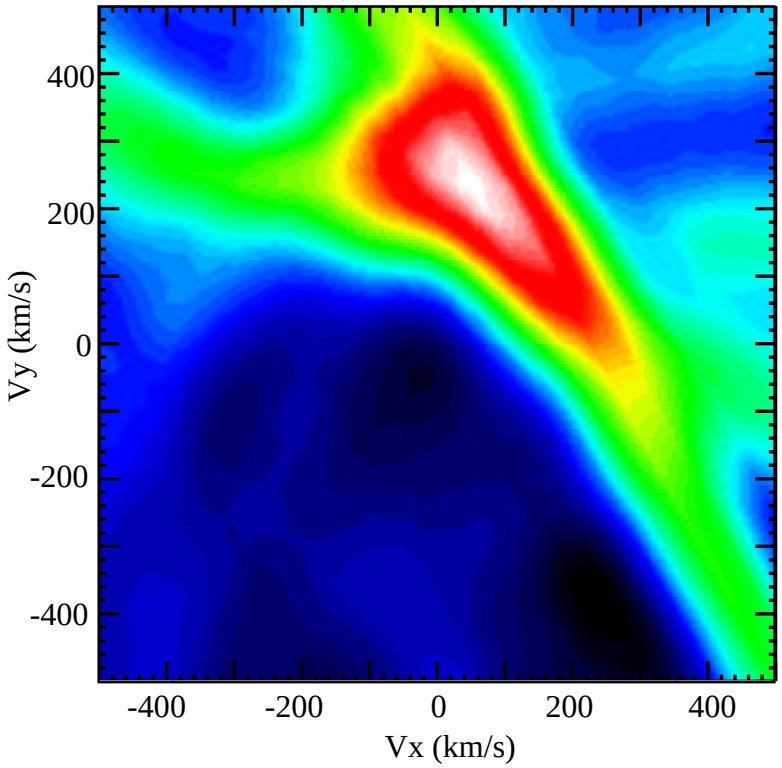

Figure 6.6: RW Tri with template gl281.

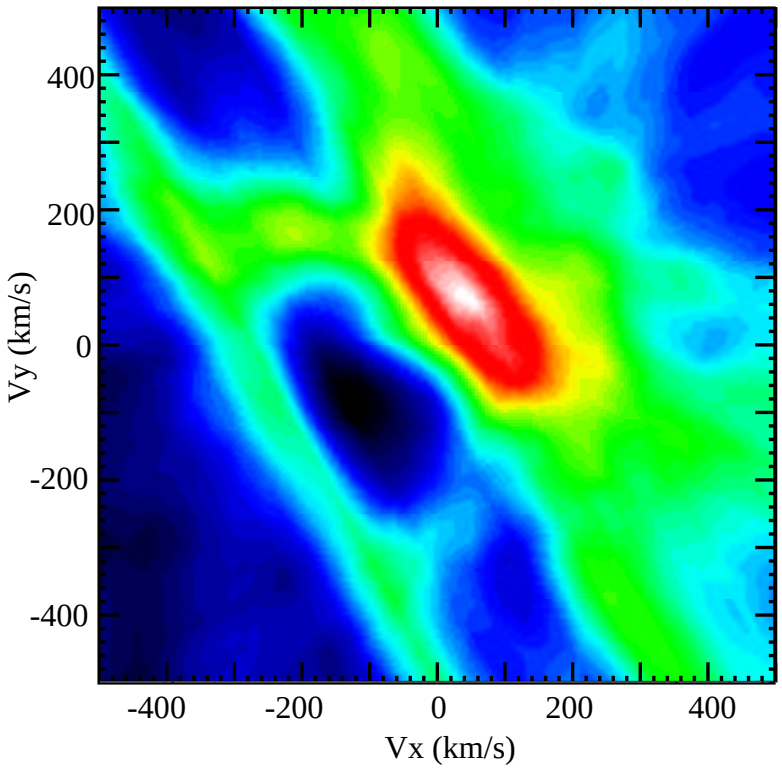

Figure 6.7: RW Tri with template gl908.

Appendix F

This derivation for the 'K-correction' is taken from Wade & Horne (1988). The value of the actual radial velocity amplitude (K_{acc}) is K_2. The observed radial velocity amplitude (K_{obs}) is displaced from the centre of mass of the secondary star due to the heating effects of the accretion disc, which alter the line strength of the secondary absorption features. The size of this displacement is defined by

$$\Delta R = fR_2, \tag{6.32}$$

were R_2 is the radius of the secondary star, and $f < 1$ is a weighting factor representing the strength of the absorption feature.

The effective centre of the secondary star will lie at $a_2 + \Delta R$ from the centre of mass of the binary system, were a_2 is the distance between the centre of mass of the binary system and the secondary star. Hence K_{obs} can be defined as

$$K_{obs} = \frac{(a_2 + \Delta R)K_2}{a_2}. \tag{6.33}$$

The 'K-correction' is the difference between the observed and actual radial velocity amplitude and is therefore given by

$$\Delta K = K_{obs} - K_{acc}, \tag{6.34}$$

$$\Delta K = \frac{(a_2 + \Delta R)K_2}{a_2} - K_2, \tag{6.35}$$

$$\Delta K = \frac{\Delta R K_2}{a_2}. \tag{6.36}$$

Using Equation 6.33, Equation 6.36 becomes

$$\Delta K = \frac{fR_2K_2}{a_2}. \tag{6.37}$$

Appendix G

The weighting factor $|f| < 1$ in the K-correction analysis of Wade & Horne (1988) is a measure of the offset of the centre of light of the star due to the absorption effects of the star. This weighting factor can be calculated by considering the disc of the secondary star, due to projection effects. From Chapter 3, Section 3.2.3, the different hemispheres of the secondary star have different absorption effects, therefore the disc of the secondary star must be split up into two semi-circles so that absorption effects can be taken into account.

The first step of this derivation is to calculate the centre of light of a semi-circle. Consider the semi-circle in Figure 6.8, where the centre of light lies on the x-axis, and is positioned at a distance of $\overline{x}$ from the y-axis. The weight per unit area of the semi-circle is w, hence the weight of the semi-circle is $w\frac{1}{2}\pi r^2$. Also, the equation of a circle is

$$x^2 + y^2 = r^2, \tag{6.38}$$

where r is the radius of the circle. From Figure 6.8 consider a strip of thickness dx and length $2y$ at a distance x from the y-axis. Therefore the weight of strip is given by $w2y\mathrm{d}x$.

Considering the moments about the y-axis gives

$$w\frac{\pi r^2}{2}\overline{x} = \sum_{x=0}^{r} w2y\mathrm{d}x\ x. \tag{6.39}$$

Expressing the right hand side of Equation 6.39 gives

$$\sum_{x=0}^{r} w2y\mathrm{d}x\ x = \int_0^r w2yx\mathrm{d}x. \tag{6.40}$$

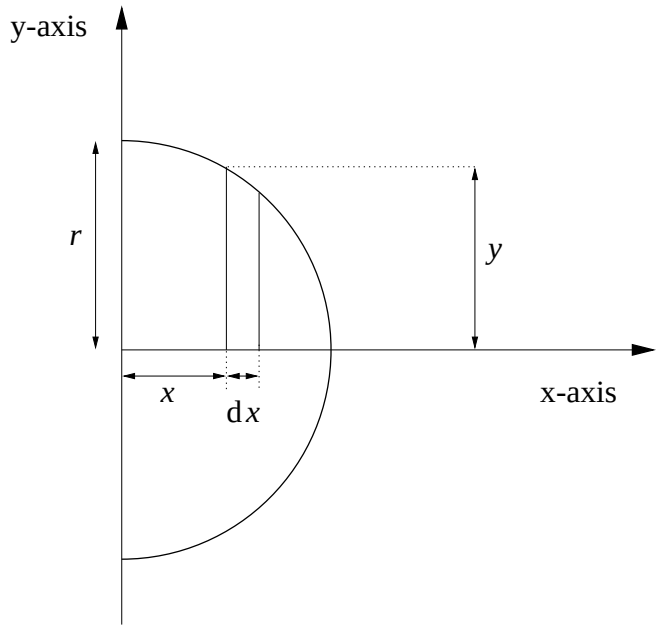

Figure 6.8: Semi-circle with the x-axis as the axis of symmetry. r is the radius of the semi circle and dx represents the thickness of a thin strip.

Substituting in

$$y = \sqrt{r^2 - x^2}, \tag{6.41}$$

from Equation 6.38, leads to

$$\sum_{x=0}^{r} w2y\mathrm{d}x \; x = w \int_0^r 2x(r^2 - x^2)^{1/2}\mathrm{d}x. \tag{6.42}$$

Defining $t = r^2 - x^2$, therefore $\frac{\mathrm{d}t}{\mathrm{d}x} = -2x$. Then Equation 6.42 becomes

$$\sum_{x=0}^{r} w2y\mathrm{d}x \; x = -w \int_0^r t^{1/2}\mathrm{d}t. \tag{6.43}$$

Integrating Equation 6.43 leads to

$$\sum_{x=0}^{r} w2y\mathrm{d}x \; x = -w \left[\frac{2t^{3/2}}{3}\right]_0^r. \tag{6.44}$$

Substituting in $t = r^2 - x^2$ gives

$$\sum_{x=0}^{r} w2y\mathrm{d}x \; x = -w \left[\frac{2}{3}(r^2 - x^2)^{3/2}\right]_0^r, \tag{6.45}$$

$$\sum_{x=0}^{r} w2y\mathrm{d}x \; x = w\frac{2}{3}r^3. \tag{6.46}$$

Substituting Equation 6.46 into Equation 6.39 gives

$$w\frac{\pi r^2}{2}\overline{x} = w\frac{2}{3}r^3, \tag{6.47}$$

$$\overline{x} = \frac{4}{3\pi}r. \tag{6.48}$$

So the centre of light of a semi-circle lies on the axis of symmetry, at a distance of $\frac{4}{3\pi}r$ from its plane face.

The second step in this derivation is to consider the absorption effects in each hemisphere of the secondary star. If the back hemisphere has an absorption effect of unity, the centre of light due to the absorption in the back hemisphere is at a distance $\overline{x}_b$ from the centre of the secondary star, and is given by

$$\overline{x}_b = \frac{4}{3\pi}r \tag{6.49}$$

using Equation 6.48. The NIR results (Chapter 3, Section 3.2.3) show that the strength of the secondary star absorption feature Ca I in the hemisphere closest to the primary star is ~ 0.4 times the strength of the absorption in the back hemisphere. Therefore the centre of light of the front hemisphere can be calculated using Equation 6.39, where the weight per unit area of the strip will be $0.4w$. So the distance to the centre of light of the front hemisphere ($\overline{x}_f$) is given by

$$w\frac{\pi r^2}{2}\overline{x}_f = \sum_{x=0}^{r}\frac{4}{10}w2y\mathrm{d}x\ x, \tag{6.50}$$

$$w\pi r^2\frac{5}{4}\overline{x}_f = \sum_{x=0}^{r}w2yx\mathrm{d}x. \tag{6.51}$$

Substituting in Equation 6.46 leads to

$$w\frac{5}{4}\pi r^2\overline{x}_f = w\frac{2}{3}r^3, \tag{6.52}$$

$$\overline{x}_f = \frac{8}{15\pi}r. \tag{6.53}$$

The third and final step in this derivation is to calculate the effective centre of light of the two hemispheres combined. Consider Figure 6.9, where X is the

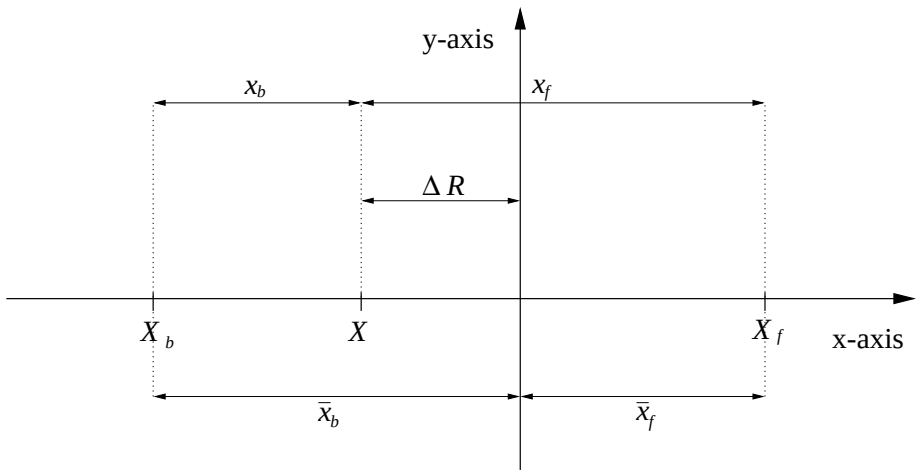

Figure 6.9: Illustration of the position of the effective centre of light (X) of the secondary star due to absorption effects. X_b and X_f are the centres of light of the back and front hemisphere respectively. x_b is the distance between the the centre of light of the back hemisphere and X. x_f is the distance between the the centre of light of the front hemisphere and X. ΔR is the displacement defined by Wade & Horne (1988).

effective centre of light of both hemispheres combined, and ΔR is the displacement between the effective centre of mass due to the absorption, and the true centre of the secondary star, as defined by Wade & Horne (1988).

From Figure 6.9, ΔR can be defined as

$$\Delta R = \overline{x}_b - x_b, \tag{6.54}$$

and

$$\Delta R = x_f - \overline{x}_f. \tag{6.55}$$

Substituting Equations 6.49 and 6.53 into Equations 6.54 and 6.55 respectively, leads to

$$\Delta R = \frac{4}{3\pi} r - x_b, \tag{6.56}$$

and

$$\Delta R = x_f - \frac{8}{15\pi} r. \tag{6.57}$$

Considering the moments about X in Figure 6.9 leads to

$$w\frac{\pi r^2}{2} x_b = \frac{4w}{10}\frac{\pi r^2}{2} x_f. \tag{6.58}$$

Hence, $x_b = \frac{4}{10}x_f$. Equating Equations 6.56 and 6.57, and substituting for x_f in terms of x_b gives

$$\frac{4}{3\pi}r - x_b = \frac{10x_b}{4} - \frac{8}{15\pi}r, \tag{6.59}$$

$$x_b = \frac{8}{15\pi}r. \tag{6.60}$$

Substituting x_b (Equation 6.60) into Equation 6.56, leads to

$$\Delta R = \frac{4}{3\pi}r - \frac{8}{15\pi}r, \tag{6.61}$$

$$\Delta R = \frac{4}{5\pi}r. \tag{6.62}$$

Therefore the weighting factor that is calculated from the results of the NIR absorption feature analysis (Chapter 3, Section 3.2.3), is $\frac{4}{5\pi}$.